Delamination Analysis of A Class of AP-PLY Composite Laminates

Zheng, Weiling

DOI
10.4233/uuid:26d1ec89-e6e6-4d5f-b4d0-2591c4aa406a

Publication date
2016

Document Version
Final published version

Citation (APA)
Zheng, W. (2016). *Delamination Analysis of A Class of AP-PLY Composite Laminates*. [Dissertation (TU Delft), Delft University of Technology]. https://doi.org/10.4233/uuid:26d1ec89-e6e6-4d5f-b4d0-2591c4aa406a

Delamination Analysis of A Class of AP-PLY Composite Laminates

Delamination Analysis of A Class of AP-PLY Composite Laminates

Proefschrift

ter verkrijging van de graad van doctor
aan de Technische Universiteit Delft,
op gezag van de Rector Magnificus Prof.ir. K.Ch.A.M Luyben,
voorzitter van het College voor Promoties,
in het openbaar te verdedigen op
dinsdag 13 december 2016 om 15.00 uur

door

Weiling ZHENG

Master of Science, Zhengzhou University, Zhengzhou, China
geboren te Henan, China

This dissertation has been approved by the
promotor: Prof. dr. C. Bisagni
copromotor: Dr. C. Kassapoglou

Composition of the doctoral committee:

Rector Magnificus	chairman
Prof. dr. C. Bisagni	Technische Universiteit Delft, promotor
Dr. C. Kassapoglou	Technische Universiteit Delft, copromotor

Independent members:

Prof. dr. ir. R. Benedictus	Technische Universiteit Delft
Prof. dr. W. van Paepegem	Ghent University, Belgium
Prof. dr. D. Saravanos	University of Patras, Greece
Dr. ir. E. Jansen	Leibniz Universität Hannover, Germany
Dr. ir. J.J.C. Remmers	Technische Universiteit Eindhoven
Prof. dr. R. Curran	Technische Universiteit Delft, reservelid

Keywords: AP-PLY Composite Laminates, Interwoven Structures, Delamination Onset, Delamination Growth, Cohesive zone element, Energy release rate.

ISBN 978-94-6186-765-0

Printed by Ridderprint drukkerij

An electronic version of this dissertation is available at
http://repository.tudelft.nl/.

To my family

Summary

A recently developed fiber placement architecture, AP-PLY, has been shown to give significantly improved damage tolerance characteristics of composite structures. The behavior of delaminations resulting from low speed impact damage is of particular concern. Major attention has been paid to expand current knowledge on the delamination response of simple AP-PLY composite structure and move towards in-depth understanding of the failure mechanisms behind the damage tolerance. This thesis presents the approaches to predict delamination onset and analyze delamination growth, in support of the search of the optimum woven pattern for AP-PLY composite laminates. The recovered interlaminar stress between layers combined with the maximum stress criterion determined the delamination onset of simple AP-PLY composite laminate under out-of-plane loads. 2D finite element models with cohesive elements inserted in the interfaces of woven layers have been built to evaluate the delamination initiation and propagation in the different woven patterns of simple AP-PLY composite beams. The parameters of the woven pattern, such as the woven angle, the number of woven plies, the number of straight filled plies, and the location of the woven patterns in through the thickness direction, were investigated and shown to have a significant effect on delamination creation and growth. An energy method based on beam theory was proposed to analyze the strain energy release rate (SERR) of an existing crack in an AP-PLY beam structure. The developed analytical method was implemented in isotropic materials and the obtained SERR of a crack was validated by reference results and finite element solutions. The general behavior of crack growth on the left or right crack tip was evaluated and basic trends leading to crack propagation on one side of the crack were established. A correction factor was introduced to improve the accuracy of the SERR of a small crack through the numerical calculation. The singularity of crack tip caused by dissimilar materials was investigated and was found that the inclusion of the singularity effect could increase the accuracy for small cracks. It has been shown that the neutral axis needs to be relocated to decouple the bending and membrane behavior of unsymmetrical composite laminates, thus to meet the requirement of minimizing the strain energy of the delaminated beam to calculate the SERR of a delaminated composite beam. The calculated SERR of a crack in a composite beam has been verified by comparing with a finite element model. The woven plies in AP-PLY composite laminate altered the layup and two conventional laminates with different stacking sequences were identified in an AP-PLY composite laminate based on the assumption that the resin areas were ignored. A step by step approach was developed to obtain the SERR of a crack that goes across different materials. The analytical SERR determined when two materials are used in sequence, sets the stage for

optimization of AP-PLY composite laminates without taking account of the effect of the resin area. The procedure of optimization of simple AP-PLY pattern was proposed and industry may benefit for many applications. An equivalent stiffness approach was used to model regions containing resin pockets and straight or inclined composite layers. A series of three point bending tests was carried out where the failure process and loading capacity were evaluated. The methodology, procedure of optimization, philosophy outlined in this thesis might also be applied to the more complicated fully woven AP-PLY composite laminates. The work in this thesis contributes to the understanding of the behavior of AP-PLY composite laminates with delaminations.

Samenvatting

Het is aangetoond dat een recent ontwikkelde vezelplaatsingsarchitectuur, AP-PLY, een grote positieve invloed heeft op de schade-tolerantie eigenschappen van composieten constructies. Met name de ontwikkeling van delaminaties door lage-snelheid impact is belangrijk. Er is veel aandacht besteed aan het uitbreiden van de huidige kennis over delaminatie-gedrag van AP-PLY composieten structuren en naar een meer fundamenteel begrip van de bezwijkmechanismes die achter schade-tolerantie zitten. Dit proefschrift laat methodes zien om het begin van delaminaties te voorspellen en de groei van de delaminatie te analyseren, ter ondersteuning van de zoektocht naar het optimale weefpatroon voor AP-PLY composieten structuren. De gevonden interlaminaire spanning tussen lagen, gecombineerd met het maximale-spanning criterium bepaalde het begin van delaminaties van eenvoudige AP-PLY composieten laminaten met krachten uit-het-vlak. 2D eindige elementen modellen met cohesieve elementen toegevoegd in de koppeling tussen gewoven lagen zijn ontwikkeld om het begin en de groei van delaminaties in verschillende weefpatronen van eenvoudige AP-PLY composieten balken te evalueren. De parameters van de weefpatronen, zoals de weefhoek, het aantal gewoven lagen, het aantal volle niet-gewoven lagen, en de plaats van de gewoven patronen in de dikte-richting, zijn onderzocht, en het is aangetoond dat deze een grote invloed hebben op het ontstaan en de groei van delaminaties. Een energie-methode gebaseerd op balkentheorie is voorgesteld om de SERR (vervormingsenergie afgiftesnelheid) van een bestaande scheur in een AP-PLY balkstructuur te berekenen. Het ontwikkelde analytisch model was gemplementeerd in isotrope materialen en de gevonden SERR van een scheur was gevalideerd door referentieresultaten en eindige elementen oplossingen. Het algemene gedrag van de scheurgroei links of rechts van de scheur is gevalueerd en basistrends die tot scheurvorming leiden aan een zijde van de scheur waren gevonden. Een correctiefactor om de nauwkeurigheid van de SERR van een kleine scheur in numerieke berekeningen te verbeteren was gentroduceerd. De singulariteit aan de tip van de scheur, ontstaan door verschillenden materialen, is onderzocht en het is aangetoond dat het meenemen van de singulariteiteffect kan leiden tot een nauwkeurigere berekening voor kleine scheuren. Het is aangetoond dat de neutrale as moet worden verplaatst om het buig- en membraangedrag van niet-symmetrische laminaten te ontkoppelen, om zo te voldoen aan de voorwaarde van het minimaliseren van de vervormingsenergie van gedelamineerde balken om de SERR van een gedelamineerde composieten balk te berekenen. De berekende SERR van een scheur in een composieten balk is geverifieerd door deze te vergelijken met een eindige elementen model. De gewoven lagen in AP-PLY composieten laminaten zorgden voor een veranderende lay-up en twee conventionele laminaten met verschillende stapelvolgordes konden gedentificeerd worden

in een AP-PLY composiet gebaseerd op de aanname dat de gebieden met hars genegeerd kunnen worden. Een stap-voor-stap methode is ontwikkeld om de SERR van een scheur die door verschillende materialen gaat te bepalen. De analytisch gevonden SERR als twee materialen naast elkaar zijn gebruikt, maakt de weg vrij voor de optimalisatie van AP-PLY composieten laminaten zonder het effect van de gebieden met hars mee te nemen. De optimalisatieprocedure van een eenvoudig AP-PLY patroon werd voorgesteld en de industrie kan baat hebben bij verschillende toepassingen. Een equivalente-stijfheidsmethode is gebruikt om regios met harszakken en rechte of hellende composiet-lagen te modelleren. Een reeks drie-punt buigtesten is uitgevoerd om het faalproces en draagvermogen te evalueren. De methode, optimalisatieprocedure en filosofie beschreven in deze thesis kunnen ook toegepast worden op ingewikkeldere volledig geweven AP-PLY composieten laminaten. Het werk in deze thesis draagt bij tot het begrijpen van het gedrag van AP-PLY composieten laminaten met delaminaties.

Abbreviations

AP-PLY	Advanced Placed Ply
2D	Two Dimensional
3D	Three Dimensional
ASTM	American Society for Testing and Materials
VCCT	Virtual Crack Closure Technology
ODB	Output Data-base
LEFM	Linear Elastic Fracture Mechanics
DCB	Double Cantilever Beam
ENF	End Notched Flexure
MMB	Mixed Mode Bending
SIF	Stress Intensity Factor
CERR	Critical Energy Release Rate
ERR	Energy Release Rate
SERR	Strain Energy Release Rate
BVID	Barely Visible Impact Damage
FEM	Finite Element Method
CZM	Cohesive Zone Model
XFEM	Extended Finite Element Method
SSTDBT	Second order Shear Thickness Deformation Beam Theory
FSDT	First order Shear Deformation Theory
CLT	Classical Laminate Theory
OM	Optical Microscopy
GA	Genetic Algorithm

Contents

Chapter 1

Introduction

The weight of structures plays an important role in the vehicle and aircraft industries. A light structure can lead to faster vehicles, fuels savings and increased range for airplanes. Compared with conventional metals, composite materials provide more options because they can be used to reduce the weight of a structure while improving on its performance. The first composite components appeared in aircraft in the 1960s with composite structures such as horizontal and vertical stabilizers. From the 1960s to the 2010s, the use of composite materials has grown significantly in the aircraft industry. Today the Boeing 787 Dreamliner is made up of more than 50% composite materials including fiberglass, carbon laminates, and carbon sandwich composites. The outstanding strength-to-weight ratio and stiffness-to-weight ratio seen with composite materials have led them to become one of the preferred materials of engineering designers, particularly transport engineers.

1.1 Laminate composites

A composite material is one which is made from at least two different constituent materials that together produce a material of which the material properties are different from the individual properties of the constituent materials. Usually composites have two phases, one is continuous matrix and the other is made up of dispersed particles or fibres. The mechanical properties of composites depend on the fibres properties, and those of the matrix used and on the ratios and geometries of those two phases.

There are many ways to classify the composites. Generally, three categories are used: particle-reinforced composites [Qiu and Weng, 1992; Ponnusami et al., 2015], fibre-reinforced composites [McCartney, 1987; Degrieck and Van Paepegem, 2001; Soutis, 2005] and structural composites [Fan et al., 2006; Akkerman, 2006]. One of the main materials forms used in the composites industry is laminated composites.

Laminated composites are assembled from layers of fibrous composite plies that can

be joined together. Each layer is composed of fibres with a high modulus and high stiffness, i.e. graphite, carbon, glass and silicon fibres which are set in a metallic, ceramic or polymeric matrix material. Changing a composite layers material properties, layup orientation(s) and layup sequence, allows designers to produce optimized laminates, and it is this in part, coupled with the other properties of composites such as low weight and flexibility of use, that makes composites a viable candidate for many applications.

The basic properties of a composite laminate such as stiffness, and strain or stress under load are usually obtained using classical lamination theory [Jones, 1999; Kassapoglou, 2010].

1.2 Woven-fabric composites

Composite laminates can be tailored for a specific application which is a definite advantage compared to more traditional materials, however, due to the relatively poor mechanical properties of composites in the thickness direction, they are prone to crack initiation and propagation along the laminar interfaces. To overcome this susceptibility to delamination, woven-fabric composites were developed to provide reinforcement in a single layer and across layers with 3D weaving. Woven-fabric composites offer the opportunity that the structure of a composite can be designed to satisfy specific requirements and to obtain specific mechanical properties in various directions.

Woven-fabric composites are formed by interlacing two or more yarn systems at an angle. In a two-dimensional, 2D, woven fabric, the lengthwise threads, called the warp and the crosswise threads, called the weft, are interlaced to produce many different patterns, called weaves.

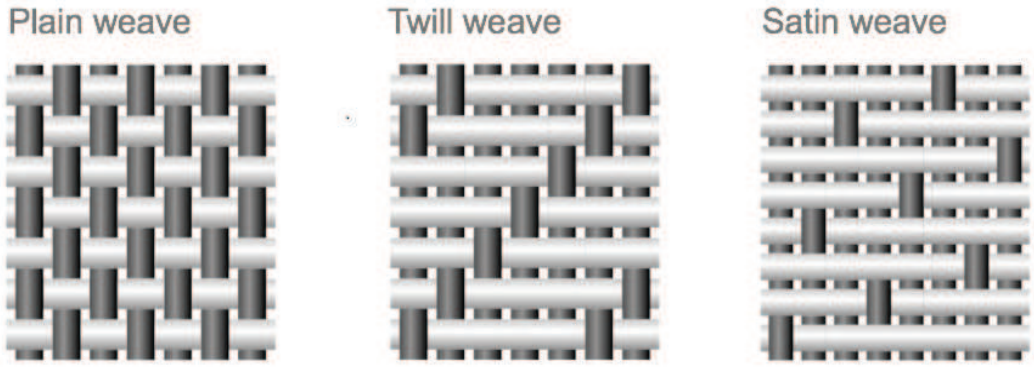

Figure 1.1: weave patterns of plain, twill and satin (www.xcomposites.com/woven.html).

The most common weaves are plain, twill and satin, see Figure 1.1. It is also possible to have three-dimensional, 3D, woven fabrics. These enhance out-of-plane strength and toughness.

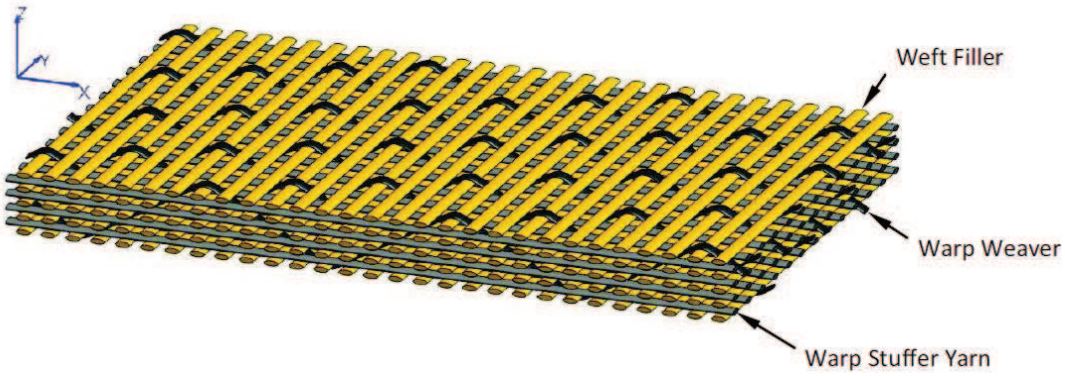

Figure 1.2: 3D woven fabric (ecre.ulster.ac.uk/research).

A woven fabric is balanced or unbalanced depending on the number of counts, i.e. number of threads used, the fineness of the yarn and the crimp necessary waviness of the warp and weft yarns. An example of a three dimensional fabric is shown in Figure 1.2.

Other types of fibre reinforcement, see Figure 1.3, used in composite are braided, z-pinned, stitched, knitted and non-crimp fabrics. Composites built with these types of reinforcement have good impact resistance but somewhat reduced in-plane compression properties because the 3-D reinforcement reduces fibre volume and/or damages in-plane fibres.

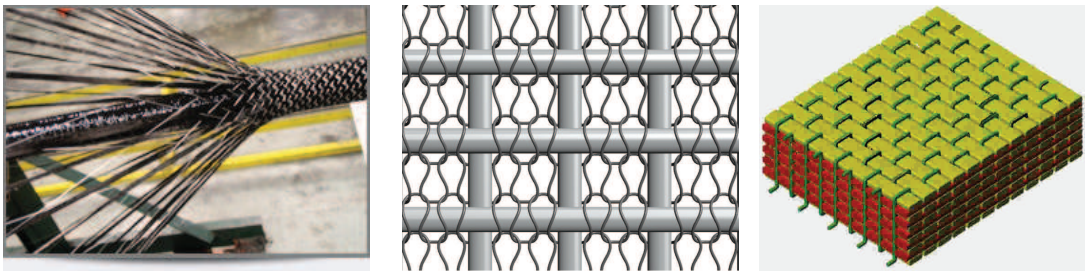

Figure 1.3: From left to right, braiding, knitting and non-crimp (fortecarbon.com/technology, innovationintextiles.com, tech.plym.ac.uk/sme/MATS324).

The fabric architecture, which decides the stiffness and strength behavior of a woven fabric composite, depends on the weave pattern(s), the density of the yarns used, the properties of the fibres used, the matrix used and the crimp angles. The disadvantages of woven-fabric composites are that they have relatively low in-plane shear resistance and undamaged compressive strength. Also reduced tensile strength lead to a lesser extent than compression or tension.

Advanced Placed Ply (AP-PLY) composites laminate [Nagelsmit et al., 2011] were developed in an attempt to combine the in-plane strength of unidirectional laminates with the out-of-plane strength of 3-D woven laminates using automated fibre placement machine.

1.3 AP-PLY composites

It is convenient to make woven-fabric composites manually or by robot for simple and small structures but not large composite structures. Automated fibre placement is a cost-effective and highly efficient technological way to make large composite structures, particularly in the aerospace and aviation industries. The obvious drawback of this technology is that the fibre placement is limited to unidirectional layers. It is difficult and costly to translate structural requirements into an optimized woven fabric material that can be manufactured by the fibre placement process. As discussed in section 1.2, reinforcement in the thickness direction can increase the damage tolerance of composite structures. How to extend the automated fibre placement technology to take the full advantage of properties of composite structures? In 2011, Naǵelsmit et al. [2011] introduce a composite structure named as AP-PLY. In this composite a new fibre architecture is used to support an automated fibre reinforcement process that produces a 3D fibre composite that is reinforced locally in the thickness direction.

1.3.1 Manufacturing process of AP-PLY

The traditional way to manufacture composite using an automated fibre placement process is to keep the tows parallel to each other and to ensure that each tow laid down is adjacent to the previous one so no space is left between the fibres on tows. This leads to the surface of each layer being made of continuous fibres, but there will be a weak out-of-plane bond between the successive layers provided by the resin. This may lead to delamination failures. Taking inspiration from weave composite fabrics, AP-PLY is formed using a process similar to weaving but not true weaving. The key point of manufacturing AP-PLY is that multiple fibre bands or tows are placed in two directions with room left between the adjacent bands rather than the bands being placed directly next to each other. The space that is left is then filled in with interchanging successive bands such that the bands are stacked. Repeating this process, as shown in Figure 1.4, gives a mimics a woven composite structure that is called AP-PLY. The interweaving tows that result from this process are very nearly straight minimizing any effects of waviness which tends to reduce in-plane properties.

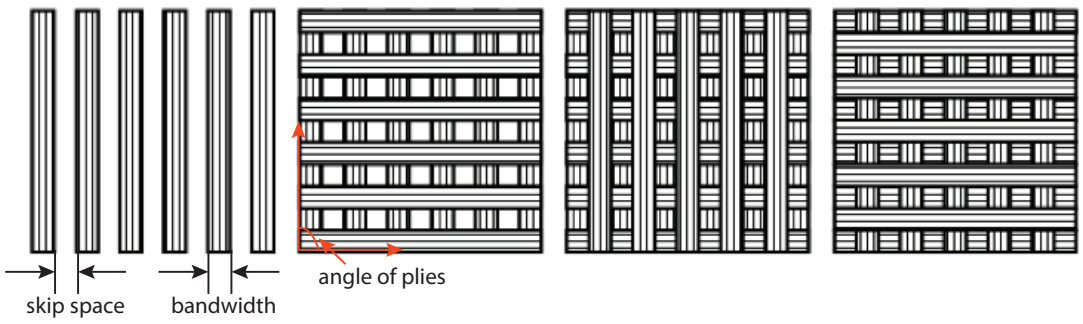

Figure 1.4: Steps to build a straight forward AP-PLY structure [Naǵelsmit, 2011].

It is also possible to make interwoven AP-PLY that are woven in plane and in the thickness direction. As can be seen from Figure 1.5, steps 1, 2 and 3 create two loosely woven plies in the 0° and 90° direction. In step 4 a new orientation is added to couple with the previous step, and interweave the third angled ply to the previous two. Step 5 will fill the space left by step 3. After that in step 6 a new fibre orientation will be added to balance the fibres in step 4. The remaining two steps will be continued as in the original pattern and used to fill the room left by step 4 and step 6. After the second package (where "package" refers to the four steps for creating the bi-directional ply of Figure 1.4) is placed, a unit of two packages with two orientation of interwoven plies was finished. For the symmetry plane of an even number of layers, it is necessary to slightly rotate (+5 or -5 degree) the adjacent originally layers with the same orientation, to make interweaving of the two possible.

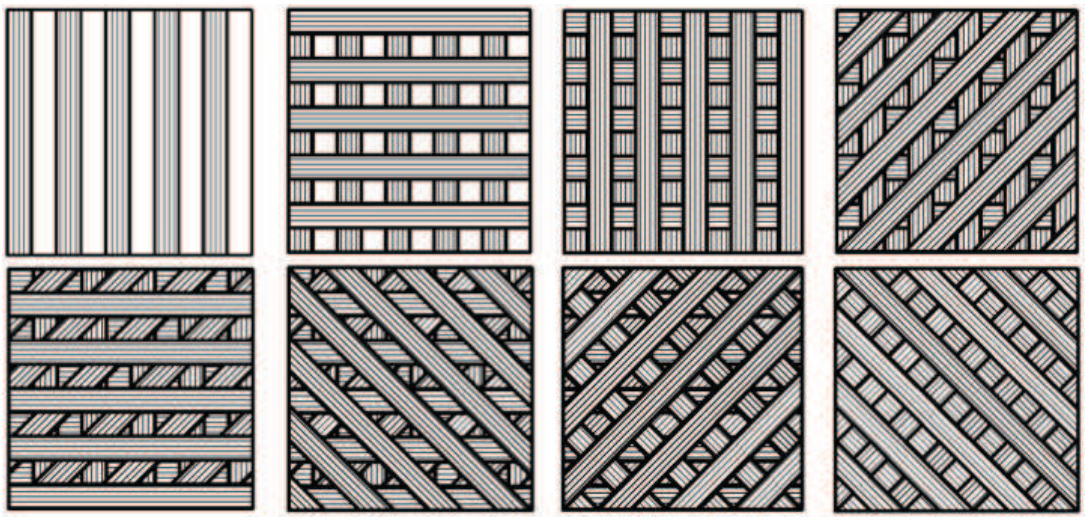

Figure 1.5: Steps to build totally interwoven AP-PLY structure [Naǵelsmit, 2013].

In addition to the straight forward and fully interwoven AP-PLY patterns discussed in section 1.3.1, there is another basic weave pattern used in AP-PLY, the alternating AP-PLY pattern. This kind of pattern is based on the straight forward pattern (see Figure 1.5) where tows are laid down only in the 0° and 90° directions but instead of placing a series of tows in one direction first, the orientation of every tow can be changed during each pass to achieve different weave patterns as shown in Figure 1.6. It can be speculated that this kind of pattern will result in somewhat longer manufacturing time and will reduce the efficiency of automated fibre placement process. It is still uncertain whether the mechanical properties of composite structure built in this way will compensate for the additional manufacturing cost.

1.3.2 Patterns of AP-PLY

The most straight forward AP-PLY, the alternating AP-PLY and the full interwoven patterns are the basic patterns of AP-PLY structure, just like plain, twill and satin form

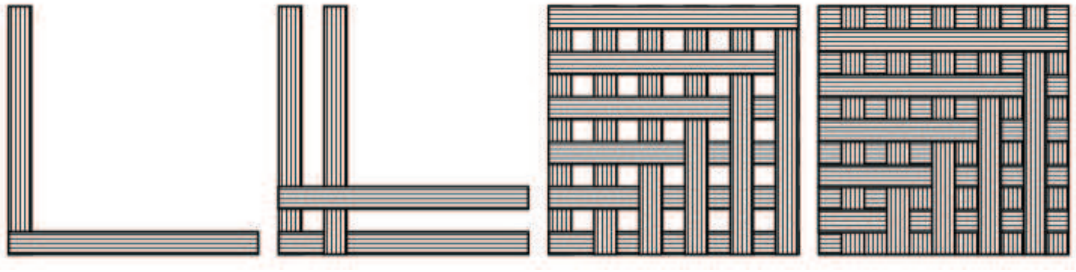

Figure 1.6: Steps to build alternating AP-PLY structure [Nagelsmit, 2013].

the basic weave patterns of a woven materials. Increasing the skip space (as shown in Figure 1.4)in the steps of manufacturing an AP-PLY makes many new and different weave patterns possible. The angles between different plies also influence the AP-PLY patterns.

Basically, any resin and fibre combination can be used to form AP-PLY composites because AP-PLY is a geometric concept that refers to the structure of the composite and not its constituent components. At present preference is given to materials that are already being used and easily obtainable in automated fibre placement process, such as thermoset prepregs, thermoplastic tapes and dry fibres. In this situation adapting the fibre placement machines to manufacture AP-PLY laminates is not necessary, but more time will be needed to manufacture AP-PLY.

When building AP-PLY composites it is the various input parameters, such as bandwidth (as shown in Figure 1.4), skip space, angle of plies, number of layers to interweave and total number of layers to be interwoven that determine an AP-PLY structures mechanical performance. Combing the conventional laminate composites and AP-PLY, it is possible to design infinite possible patterns for a fixed thickness of composite laminate.

1.4 Known advantages of AP-PLY

Composites have a long history but the AP-PLY composite structure was only developed in 2011 by Nagelsmit [2011]. Based on Nagelsmits research work, it is known that AP-PLY laminates have the following properties:

- the maximum contact force during impact of AP-PLY laminates is lower than in unidirectional laminates with the same layup
- both the interweaving laminates and sandwich panels with AP-PLY face-sheets increase by 5-10% in after impact compression strength depending on the pattern of the AP-PLY used
- the overall delamination size is decreased in AP-PLY laminates and thin tubes
- the test mode I fracture toughness is increased by 89% and mode II fracture tough-

ness is increased with 20% when an AP-PLY pattern is used

In 2014, Zhang et al. [2014] compared 3 different AP-PLY patterns with a conventional composite laminate. They found that the interlaminar shear strength of AP-PLY was 5.49%-12.54% more than that of the conventional laminate and the void content of AP-PLY is approximately 0.71%-3.07% more than that of the traditional composite laminate. The test results showed that the cracks propagated along the fibre direction and were nearly parallel in the conventional laminate while the cracks in the AP-PLY pattern crossed layers of the composite along the thickness direction. This suggests that AP-PLY composite laminates have better damage tolerance and that composites can be improved by implementing AP-PLY structure.

1.5 Thesis objective and layout

The AP-PLY fibre placement architecture has been shown to give significantly improved damage tolerance characteristics, but a detailed understanding of the mechanisms behind this improvement is still lacking. AP-PLYs behavior under impact is an especial concern. In particular, low speed impact as a result of tool drops, foot traffic, collisions is of primary interests. Prediction of damage size and type after impact is critical for aircraft because the damage may be barely visible and causes large reduction in stiffness, strength and stability of composite structures. Delamination is one of the common damage types seen after impact in fiber-reinforced composites.

As a first step to modeling the impact event, the response of AP-PLY laminates under quasi-static out-of-plane concentrated loads will be examined in this thesis. The objectives of the research reported here are: (a) to find a way to determine when and where delamination will initiate in an AP-PLY composite laminate under concentrated out-of-plane load and (b) how the delamination is going to propagate. An awareness of the behavior of delamination in AP-PLY and how the various AP-PLY patterns might influence the mechanical performance of a particular AP-PLY will help engineers and designers to optimize the structures of AP-PLY so they can meet specific design requirements. For examples, given a laminate stacking sequence optimized for other load cases, find the optimum AP-PLY pattern without changing ply orientations, to delay delamination onset and growth under out-of-plane loads.

This thesis is set out as follows: the methods used to find the critical locations in AP-PLY after impact, the initiation loads and how cracks resulting from impacts are propagating are presented in chapter 2. Stress recovery technology, cohesive element method and the methods to obtain energy release rate and the theories applied to compute strain energy release rate (SERR), are reviewed in this context. The implementation of the recovery stress technology used to find the critical location into an AP-PLY model is discussed in chapter 3. Once the critical location is known, the next step is to find the delamination initiation load. How to employ cohesive element method with commercial finite element software ABAQUS to find initiation load of different AP-PLY patterns and

simulate crack propagation are presented in detail in chapter 4. The use of energy release rate approaches is described in chapter 5. The simplified 3D AP-PLY structure into a beam structure process is addressed and the analytical solution starts from isotropic materials and then extended to composite laminates. The parametric research gives a guidance for optimization of AP-PLY composite structure. Through the optimization it is possible to tell the best option for given requirements. Some experimental validation will be described in chapter 6. This thesis is summarized in chapter 7 with conclusions from previous chapters, and recommendations for future work on the subject.

Chapter 2

Previous work

2.1 Introduction

Composites are increasingly being used in the airspace industry, they have a wide range of properties, in particular, most are lighter than conventional aerospace materials, and their ease of production through automation is making it ever easier and at lower cost to build efficient designs with complex shapes. A shortcoming of composites that must be clearly understood as we advance their use in aviation is how they respond to impact damage. In general, owing to the ductile nature of metals, a large amount of energy can be absorbed before a structure will fail. Composites, in contrast, are brittle and can absorb energy during an elastic deformation phase and can then fail suddenly when a stress or strain exceeds the limit value for that composite. It is also difficult to see damage externally as impact damage, e.g. from a dropped hammer, typically propagates internally leading to delamination and failure with little visible at the impact point on the surface of the structure. Considerable research has been done [Liu, 1987; Sjöblom et al., 1988; Choi and Chang, 1992, Kim and Kedward, 2000; Olsson, 2001; Esrail and Kassapoglou, 2014a; Esrail and Kassapoglou, 2014b] on ways to determine damage in composites caused by low-velocity and high-velocity impacts.

A structure can fail for many reasons, due to defects in the materials, an inadequate design, poor knowledge of the loads or environments the structure will be subjected to, or deficiencies in the maintenance of the structure. A designer analyzing structure failure needs to consider which kind of failure will be the main failure mode. Generally, the failure modes of a composite laminate can be classified into fibre breakage, matrix cracking, fibre-matrix debonding, and delamination. Fibre breakage and matrix cracking are respectively caused by damage to the fibres and matrix when the stress or strain in the component of interest exceeds the allowable maximum of either the fibre or the matrix. Fibre-matrix debonding is seen as the damage to the interface between fibres and matrix while delamination is caused by damage at the interface between two adjacent plies [Liu, 1987]. Thus, the failure behavior of a composite laminate is dependent on the

properties of each constituent of the laminate and in particular the stiffness mismatch. A mismatch between fibre and matrix in a laminate can induce failure in a structure and any consequent fibre-matrix debonding may lead to delamination. The fibre and matrix properties of a laminate such as fibre orientation and stacking sequence are parameters that can greatly influence the material properties of a composite laminate.

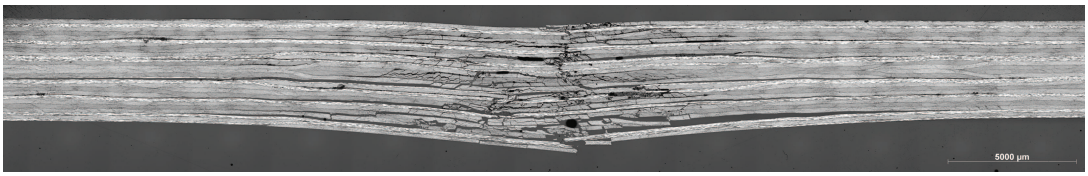

Figure 2.1: A damaged composite laminate [Nagelsmit, 2011]

Any failure of a fibre composite will typically be caused by a combination of at least two of the recognized composite failure modes as can be seen Figure 2.1. Final failure in a composite is preceded by an accumulation of different types of damages until a threshold is reached and final collapse occurs. An important case is that of residual strength after impact when a composite fails due to a small amount of fibre damage and a lot of delamination, typically this is not easily detected when viewing a structure externally [ASTM, 1973]. The weakest link in a composite structure is the out-of-plane strength because there are no fibres in the thickness direction. Delamination in a composite structure represents a potentially severe reliability and safety problem for those designing and using composite structures. Most of the time, delamination is initiated from matrix cracking or fibre-matrix debonding or manufacturing defects in the composite laminate. Being able to predict failure of a composite structure requires being able to predict the onset of delamination and how this delamination will propagate. The methods available for predicting out of plane failure are stress based [Tsai and Wu, 1971; Hashin, 1980; Christensen, 1997; Puck and Schürmann, 1998; Puck and Schürmann, 2002] or fracture mechanics based [Saghizadeh and Dharan, 1986; Benzeggagh and Kenane, 1996; Kim and Mayer, 2003; Oskouei et al., 2011]. Delamination growth can be predicted using cohesive elements, virtual crack closure technology (VCCT) or strain energy release rate.

This chapter is organized as follows. A review of the stress recovery method used in the research presented here to predict crack initiation is provided in section 2.2. Since crack growth can be simulated using VCCT or a cohesive model, the advantages and shortcomings of these two methods are discussed in section 2.3. The strain energy release rate was selected to predict whether a crack will propagate or not in the analysis model. Methods used to determine energy release rate are discussed in section 2.4, and the proposed approach to determining an analytical energy release rate is described in section 2.5.

2.2 Stress recovery technology

2.2.1 Interlaminar stress in composites

It is well known that composite laminates are sensitive to the interlaminar mode of failure: delamination. Lagace demonstrated that interlaminar stresses can lead to delamination and failure of a structure at lower loads than those predicted using in-plane failure criteria [Lagace, 1983]. Predicting delamination onset requires in-depth knowledge of the interlaminar stress fields in a composite and this means being able to determine interlaminar stress is crucial for understanding and locating places of crack initiation [OBrien, 1982]. In early research into interlaminar stress [Puppo and Evensen, 1969; Pipes and Pagano, 1970; Raju and Crews, 1981; Wang and Choi, 1982], researchers find that the singularity of interlaminar stress occurs in the vicinity of the free edge and that the size of the region where interlaminar stresses are significant is approximately equal to the laminate thickness. Interlaminar stresses in a laminate are three-dimensional thus classical laminate theory is inadequate for describing this situation. Numerous approximate methods have been used to address the problem, including high-order plate theory [Pagano, 1974], boundary layer theory [Tang and Levy, 1975], the perturbation method [Hsu and Herakovich, 1977], approximate elasticity solutions [Pipes and Pagano, 1974], the closed form solution derived using the Force Balance Method [Kassapoglou and Lagace, 1987], interlaminar shear stress continuity theory [Lu and Liu, 1992], and the layer reduction technique used layerwise theory [Lee and Chen, 1996].

Another mechanism that can give rise to interlaminar stress is in-plane stress gradients. Gradients in the in-plane stress field can be caused by notches in the composite, material characteristics or nonuniform in-plane loads in composite laminates. Bhat and Lagace [1994] propose an analytical method to evaluate the interlaminar stress at the material discontinuities. They divide the laminate into two regions around the discontinuity and the stresses are expressed in terms of eigenfunctions that satisfy equilibrium. The differential equations are then obtained using the principle of minimum complementary energy and thus the eigenfunctions in each region are solved. An analytical interlaminar stress solution for a laminate with notches or holes is difficult to obtain because such defects give rise to complex stress fields. A curved isoparametric element method is reported by Dana and Barker [1974] to investigate the interlaminar stress near the hole edge. Rybicki and Schmueser [1978] discuss the effect of stacking sequence and lay-up angle on the stresses at a free edge around a hole in a laminate plate.

The free corners in a layered composite laminate can also lead to interlaminar stresses arise. Becker et al. [1999] and Mittelstedt and Becker [2003] assess the stress at rectangular free corners of cross-ply and angle-ply laminates based on the force-balance method. The corner effect, within the context of fracture and singularities, has been studied numerically [Labossiere and Dunn, 2001; Dinitrov et al., 2001]. The following reviews, Salamon [1980], Kant and Swaminathan [2000], and Olsson [2011] are recommended for the interested reader, with respect to research into interlaminar stress.

Considerable efforts have been put into extending the finite element methods [Stanton et al., 1977; Wang and Crossman, 1977; Herakovich et al., 1979; Raju and Crews, 1980; Robbins and Reddy, 1996] as an alternative way to solve the problems of stress singularity and interlaminar stress determination discussed above. Many different finite elements like two-dimensional element [Engblom and Havelka, 1989; Kant and Menon, 1991; Bose and Reddy, 1998], three-dimensional element [Chen and Huang, 1989; Kim and Hong, 1991; Lessard et al., 1996] and the global-local model [Hirai et al., 1985; Mao and Sun, 1991; Whitcomb and Woo, 1993] have been developed to refine finite element calculation of stress singularity and interlaminar stresses.

2.2.2 Stress recovery technology

Interlaminar stresses cannot be calculated by analysis within acceptable accuracy for the complicated stress field found in a composite laminate, particularly very close to free edges, holes, notches, and free corners. A full 3D finite element analysis requires considerable computer resources and is expensive. A mixed finite element formulation based on the Hu-Washizu (HW) functional and stress recovery procedure is proposed by Mota and Abel [2000]. This work follows a series of efforts for determining reliable stress data using recovery procedures. For example, the interpolation-extrapolation of stress from super-convergent points [Barlow, 1976], L2 projection [Oden and Brauchli, 1971], stress smoothing [Hinton and Campbell, 1974 and Chen et al., 1996], and the integral stress technique [Argyris and Willam, 1974]. Fagiano et al. [2010a] propose a stress recovery procedure based on the stress recovery procedure developed by Moorthy and Reddy [1999]. This procedure can avoid stress oscillations and does not rely on extrapolation of super-convergent points. The advantages of this procedure are: (1) coarser meshes can be used to attain accurate stresses; (2) the accuracy of the stress does not depend on the stress recovery method used.

The basic theory of Fagiano et al. [2010b] stress recovery procedure can be described as follows: each ply is modelled separately, and the compatibility between the plies is enforced using the finite element tearing and interconnecting domain decomposition method. Then the traction distribution is interpolated over the complete interlaminar surface. A typical interface between two layers is shown in Figure 2.2. The linear equilibrium equations and compatibility conditions for the interface between two layers of a composite laminate can be written as:

$$\begin{bmatrix} \mathbf{D}_1 & 0 & \mathbf{B}_1^T \\ 0 & \mathbf{D}_2 & \mathbf{B}_2^T \\ \mathbf{B}_1 & \mathbf{B}_2 & 0 \end{bmatrix} \begin{bmatrix} \mathbf{u}_1 \\ \mathbf{u}_2 \\ \boldsymbol{\lambda} \end{bmatrix} = \begin{bmatrix} \mathbf{f}_1 \\ \mathbf{f}_2 \\ 0 \end{bmatrix}, \tag{2.1}$$

where $\mathbf{D}_1$ and $\mathbf{D}_2$ are the stiffness matrices of the two layers, $\mathbf{u}_1$ and $\mathbf{u}_2$ are the displacement vectors, $\mathbf{f}_1$ and $\mathbf{f}_2$ are the load vectors, $\mathbf{B}_1$ and $\mathbf{B}_2$ are the Boolean matrices imposing displacement equality conditions for the two layers, and $\boldsymbol{\lambda}$ are the Lagrange multipliers, representing the interlaminar forces used to enforce the compatibility constraints between two layers. The interlaminar forces and displacements within a interface can be obtained

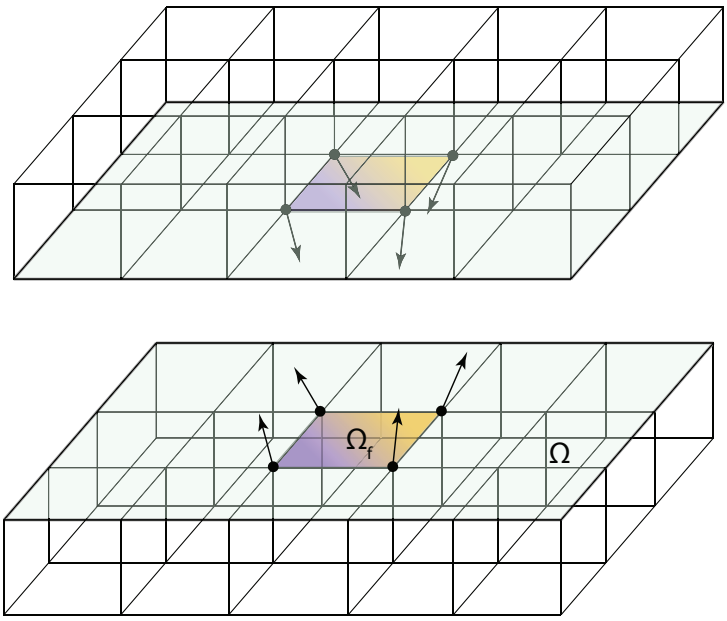

Figure 2.2: Interfacial nodes of each element in a composite model

after solving Eq. (2.1). The distributed traction $\mathbf{t}_{\Omega_e}$ over the surface of Ω_e is interpolated using C^0 iso-parametric shape functions:

$$\mathbf{t}_{\Omega_e} = \mathbf{N}\mathbf{t}_e \tag{2.2}$$

where $\mathbf{t}_e$ is the vector of the nodal traction and $\mathbf{N}$ is the matrix of C^0 shape functions. The distributed displacement $\mathbf{u}_{\Omega_e}$ over the surface of Ω_e is interpolated with the same method as the distributed traction:

$$\mathbf{u}_{\Omega_e} = \mathbf{N}\mathbf{d}_e \tag{2.3}$$

where $\mathbf{d}_e$ is the vector of the nodal displacement. The internal work W_{in} done by the traction over the surface of the element is:

$$\mathrm{W}_{in} = \int_{\Omega_e} \mathbf{t}_{\Omega_e}^T \delta\mathbf{u}_{\Omega_e} d\Omega_e = \int_{\Omega_e} (\mathbf{t}_e\mathbf{N})^T \mathbf{N}\delta\mathbf{d}_e d\Omega_e = \mathbf{t}_e^T \mathbf{A}_e \delta\mathbf{d}_e \tag{2.4}$$

where $\mathbf{A}_e$ is the matrix of areas:

$$\mathbf{A}_e = \int_{\Omega_e} \mathbf{N}^T\mathbf{N}\partial\Omega_e \tag{2.5}$$

Then, the matrices of areas of all the elements on the interlaminar surface Ω are assembled in a matrix $\mathbf{A}$:

$$\mathbf{A} = \mathbb{R}_{e=1}^{nel}\mathbf{A}_e \tag{2.6}$$

where $\mathbb{R}$ is the finite element operator. The elements connectivity on the surface can be directly established from the solid element faces. The static equivalence between the tractions and the connecting forces need to be satisfied:

$$\mathbf{t}^T\mathbf{A}\delta\mathbf{d} = \boldsymbol{\lambda}^T\delta\mathbf{d} \tag{2.7}$$

where $\mathbf{t}$ and $\mathbf{d}$ are the global vector of nodal traction and nodal displacement on the surface Ω respectively, then the following equation can be obtained:

$$\mathbf{At} = \boldsymbol{\lambda} \quad \Rightarrow \quad \mathbf{t} = \mathbf{A}^{-1}\boldsymbol{\lambda} \tag{2.8}$$

through which the interlaminar stress distribution is then retrieved over the surface Ω. This procedure can be repeated for any relevant interface.

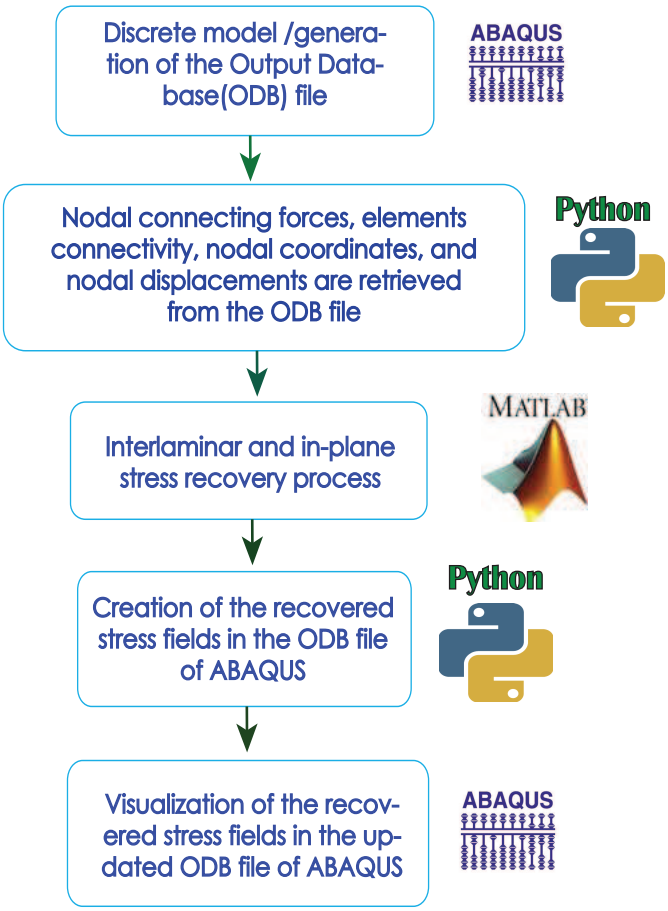

Figure 2.3: The interlaminar stress recovery procedure

The above procedure used in combination with commercial software ABAQUS is shown in Figure 2.3. The first step is to implement a discrete FE model in ABAQUS. The interlaminar boundary is modelled as a contact zone because the connecting forces are needed in subsequent steps. The second step is to recover the input variables from ABAQUS ODB file which is based on the Python programming language using the ABAQUS Scripting Interface. The third step is the recovery of the interlaminar stresses from the contact loads that satisfy the force equilibrium at the interface of any two plies using a MATLAB code. In the fourth step, the data are transferred back to the ABAQUS output database file and the retrieved stress distributions are visualized.

Fagiano et al. [2010b]'s stress recovery procedure is a good choice to analyse the interlaminar stress of a composite structure as complicated as AP-PLY. The limitation of this

method is that a stress-based failure criterion is required and it cannot be used to predict growth of delamination in a composite.

2.3 Cohesive zone model

Interlaminar stresses, combined into a failure criterion, could help to locate a critical location or the crack initiation in a laminate under loading but cannot be used to predict crack growth. The growth of a crack as a process creates two new surfaces for a 3D problem. Linear elastic fracture mechanics (LEFM) can be used to analyse a crack problem when a material is predominantly linear elastic during the failure process, however, the nonlinear behaviour of a cracks tip and the crack propagation into a sizable plastic zone cannot be addressed with LEFM. The cohesive zone model approach [Hillerborg et al., 1976; Needleman, 1987; De-Andrés et al., 1999; Turon et al., 2007b] has emerged as a powerful tool for analysing nonlinear fracture process or plasticity at a crack tip, as shown in Figure 2.4. Crack growth at a crack tip is simulated as a natural process of debonding of the cohesive zone element under various load conditions.

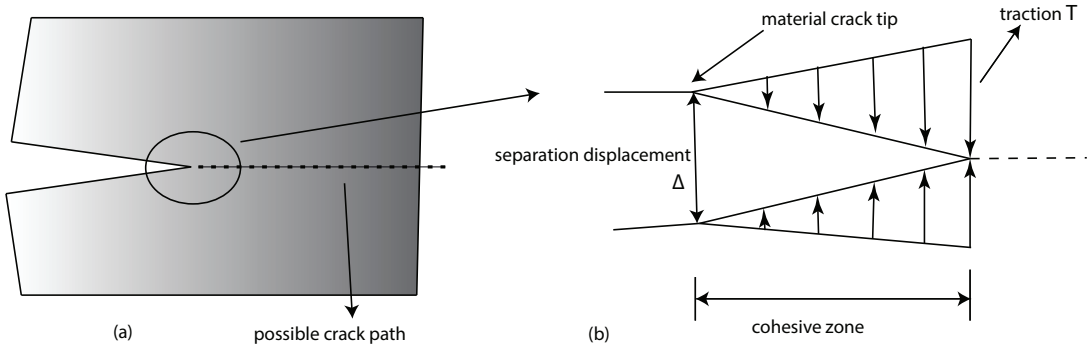

Figure 2.4: (a) cohesive zone area (b) crack tip's traction and displacement

2.3.1 Cohesive zone model

The cohesive zone model was first introduced by Dugdale [1960] and Barenblatt [1962] as a means to solve the stress singularity at the vicinity of a crack tip that is being predicted by linear elastic fracture mechanics. Subsequently, numerous researchers have extended the cohesive zone approach [e.g. Hillerborg et al., 1976; Petersson, 1981; Needleman, 1987; Hui and Kramer, 1995; De-Andrés et al., 1999; Allen and Searcy, 2001; Turon et al., 2007b; Park et al., 2009]. The cohesive zone model has been applied extensively to quasi-brittle materials such as polymers, rocks, concrete, composites and functionally graded materials [Boone et al, 1986; Xu and Needleman, 1994; De Borst, 2002; Jin et al., 2003; Song et al., 2006]. Other material systems and failure phenomena, such as bi-material interfaces [Mohamed and Lechti, 2000; Chandra et al., 2002], adhesive

bonded joints [Yang and Thouless, 2001; Khoramishad et al., 2010], the dynamic fracture problems [Falk et al., 2001; Zhang and Paulino, 2005; Kandula et al., 2005], and the fatigue crack growth under cyclic loading [Roe and Siegmund, 2003]. Su et al. [2015] also utilize the cohesive zone model for the progressive damage of open-hole composite laminates under compression. Cohesive zone models have also been used to analyze composite delamination problems [Massabo and Cox, 1999; de Borst, 2003; Borg et al., 2004; Turon et al., 2007]. In laminate problems, the cohesive zone model offers the prospect of determining important issues such as the influence of stacking sequence on delamination crack propagation, free edge delamination initiation and propagation [Turon et al., 2007a], and damage and delamination around pinned holes [Yang and Cox, 2005].

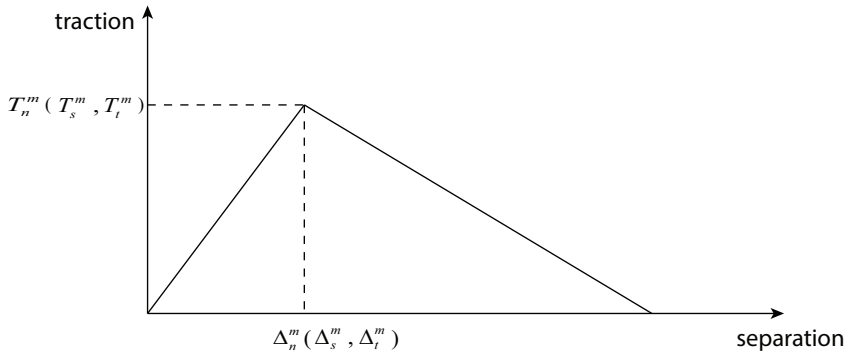

Figure 2.5: traction separation law

Crack growth in the cohesive zone model is a process which tracks the separated cohesive elements that are controlled by a traction-separation law. The cohesive elements do not have any real physical material properties, but describe the traction forces that cause the pulling apart of bulk materials. The traction-separation law, also called the cohesive-zone law, is not a physical law, it is a phenomenological model used to characterize a fracture process zone. In a cohesive zone model, the traction-separation law can be described as a softening constitutive equation related to the creation of crack surfaces during the material separation process and it is the key component to deciding whether the debonding is complete or not. The constitutive relationships of the cohesive zone model are defined as linear [Camacho and Ortiz, 1996; Maiti and Geubelle, 2005], as shown in Figure 2.5, or cubic polynomial [Tvergaard, 1990], trapezoidal [Tvergaard and Hutchinson, 1993], exponential [van den Bosch et al., 2006] and bilinear [Wittmann et al., 1988; Park et al., 2008] softening functions. If the traction in the cohesive zone exceeds the maximum value, it goes down to zero when the maximum displacement is achieved. This whole process defines a cracks propagation. Most of the traction separation laws assume a relation between normal and/or shear traction and opening and/or sliding displacement, see Figure 2.4. The area under the traction separation curve is the critical strain energy release rate that represents the energy flow taking place within the cohesive zone under external loading. For a mixed mode crack, the traction separation law will be related to normal and shear tractions and opening and sliding displacements or the traction and three different critical fracture energies. The parameters that are used to define the cohesive law may be found through simple fracture tests such as the double cantilever beam (DCB) for mode I, end notched flexure (ENF) for mode II, and mixed

mode bending (MMB) for mixed mode. Once the parameters related to the traction separation law have been obtained by particular tests, they can be used to predict the fracture of other stacking sequences or loading capacity.

In an ABAQUS cohesive zone model without a crack, damage initiation can be defined by a stress-based criterion or strain-based criterion such as maximum nominal stress criterion, maximum nominal strain criterion, quadratic nominal stress criterion, quadratic nominal strain criterion. The damage evolution, representing the formulae of a cohesive separation law, is chosen to control the damage behaviour of the cohesive elements after crack initiation. The damage evolution can be displacement-based or energy-based, and the softening constitutive can be linear, exponential or even tabulated in ABAQUS standard [ABAQUS, 2011]. Other traction softening types can be applied using a User Subroutine to define the cohesive element.

2.3.2 Virtual crack closure technique

The virtual crack closure technique is another tool that has been widely used to analyse crack growth using the finite element method. The VCCT dates back to the approach developed by Rybicki and Kanninen [1977] to determine stress intensity factors for 2D crack problems and then for 3D crack problems by Shivakumar et al. [1988]. Before the VCCT was proposed, the crack closure method based on Irwins [1958] crack closure integral was used to obtain energy release rate by a two-step finite element analysis. When using the crack closure method, the assumption is made that the energy released

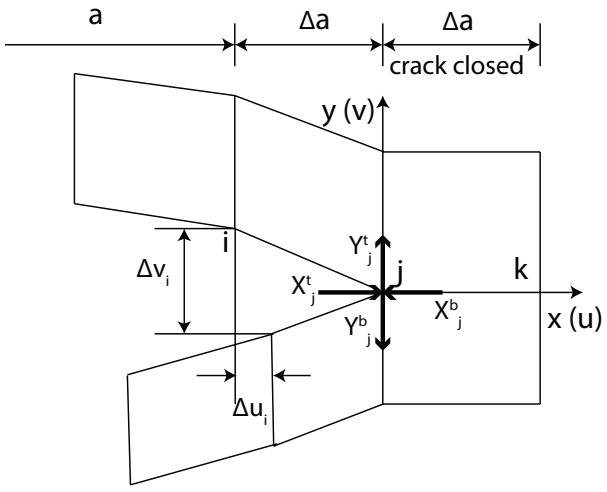

Figure 2.6: virtual crack closure technology

when a crack grows by length $\Delta + a$ and the crack is extended from a to $a + \Delta a$ is equal to the energy required to close the crack. The first step of the finite element method is to determine the nodal forces at the crack tip when the crack length is a, the second finite element analysis gives the displacement when the crack has been extended to $a + \Delta a$.

The VCCT modified the crack closure method and assumed that a crack extended from $a + \Delta a$ to $a + 2\Delta a$ does not significantly change the state at the crack tip, as shown in Figure 2.6, for a 2D four-noded element model. The released energy ΔE of extension crack length Δa is identical to the energy required to close the crack between nodal j and nodal k. The energy ΔE to close the crack can be written as:

$$\Delta E = \frac{1}{2}\left(X_j \Delta u_i + Y_j \Delta v_i\right) \tag{2.9}$$

where X_j and Y_j are the shear and opening forces at nodal point j and Δu_i and Δv_i are the shear and opening displacements at nodal point i, as shown in Figure 2.6. To meet force equilibrium at nodal j, the equilibrium equations are:

$$X_j^t = X_j^b = X_j \tag{2.10}$$

$$Y_j^t = Y_j^b = Y_j \tag{2.11}$$

where X_j^t and X_j^b are the shear forces, and Y_j^t and Y_j^b are the opening forces at nodal j for top layer and bottom layer respectively. Then the total energy release rate for 2D problems can be calculated as:

$$G = \frac{\Delta E}{\Delta A} = \frac{1}{2\Delta a}\left(X_j \Delta u_i + Y_j \Delta v_i\right) \tag{2.12}$$

where Δa is the length of the elements at the crack front and ΔA is the newly created crack surface as $\Delta A = \Delta a \times 1$ in a 2D model with a unit thickness 1. The quarter-point elements can be used to accurately simulate the $\frac{1}{\sqrt{r}}$ stress singularity at the crack tip [Barsoum, 1977]. Different elements such as eight-noded 3D solids elements [Shivakumar et al., 1988], twenty-noded 3D solids elements [Raju et al, 1988], four- and nine-noded plate elements [Wang and Raju, 1996] and shell elements [Krueger and OBrien, 2001] have been developed to solve 3D problems. It is necessary to make sure that the crack propagates in a kinematically compatible way by element-wise opening/closing instead of node-wise opening/closing because node-wise might cause incompatible interpenetration for eight-noded elements with quadratic shape functions [Buchholz, 1984]. Normally, elements in front of the crack tip and behind need to have the same length to make the calculation of energy release rate conveniently. Whereas, when simulating complex geometries using elements with different lengths or widths or arbitrarily shaped delamination front at the crack tip, typically generated by automatic mesh, the energy release rate will not be expressed as simply as in Eq. (2.12). Expressions of energy release rate for arbitrary shape elements and related references can be found in the review of Krueger [2004]. Suggested solutions for different engineering problems and related application problems for the VCCT are also discussed in Krueger [2004].

2.3.3 Choice made for crack growth modelling method

As discussed in subsections 2.3.1 and 2.3.2, the cohesive zone model and VCCT are widely used in the analysis of crack growth and both can be applied in ABAQUS. The advantages

of the cohesive method are: (1) there is no need for a priori input of a mode separation parameter for a mixed mode crack, while the phase angle is required to be input in VCCT simulations; (2) the cohesive zone model can be used to predict crack initiation without the existence of a crack. The shortcomings of the model are: (1) the cohesive element needs to be relatively fine meshed to obtain accurate results [Turon et al., 2007a]; (2) The parameters of the constitutive equations of the cohesive law need to be carefully treated [Song et al., 2008]. Yet, VCCT is convenient to obtain the energy release rate of mode I and mode II separately for a mixed mode crack problem. The limitations are: (1) the oscillation of the singularity of crack-tip stress introduces numerical instabilities and mesh-dependence in the numerical results [Dattaguru et al., 1994], this means that the element size at the crack-tip element will be restricted: it has to be between $\frac{1}{4}$ and $\frac{1}{2}$ of the ply thickness [Raju et al., 1988]; (2) the VCCT requires the existence of a pre-crack with a finite length to obtain the strain energy release rate that will vanish at zero crack length. The propagation of which has to start from an assumed crack-like flaw. For the research represented in this thesis, the structure of AP-PLY composite laminates was simulated using a model in which the structure was assumed to be intact before impact loading and the cohesive zone model will be used to predict damage initiation and growth. The interlaminar stress recovery technology combined with a stress criterion was used to predict crack initiation. The predicted crack initiation location needs to be verified using another method that can predict the crack initiation and crack growth. The cohesive zone model can be used to analyze crack growth and to predict crack initiation which made it a good choice for analyzing delamination initiation and growth and to compare to the VCCT. Within this framework, the requirement of VCCT for the existence of a pre-existing crack limits its application to the work described here.

2.4 Energy release rate

As mentioned in subsection 2.3.1, crack evolution can be defined as energy-based, where energy-based means based on the strain energy release rate which is used to determine whether a crack will propagate or not. The strain energy release rate is based on the Griffiths energy balance theory for fracture mechanics which means the crack will grow if the energy release rate G is equal or greater than the fracture energy Γ or critical energy release rate G_c for a static or quasi-static crack propagation. The energy release rate can be taken as the driving force for the extension of a crack when the structure is under loading and the fracture energy is the resistance to the growth of the crack which can represent a material property. The energy release rate is the reduction of elastic energy associated with increasing crack length per unit area:

$$G = -\frac{U(\Delta, A+dA) - U(\Delta, A)}{dA} = -\frac{\partial U(\Delta, A)}{\partial A} \tag{2.13}$$

where elastic energy U is function of displacement Δ and crack area A.

Since the early 1960s, most of the research into energy release rate and stress intensity factors has been done on isotropic materials. Some of the work on homogeneous dissimilar or

orthotropic or anisotropic materials [Suo and Hutchison, 1990; Suo, 1990; Kardomateas, 1993]. Hutchinson et al. [1987] obtain the expression for the energy release rate and stress intensity factors for a semi-infinite interface crack between dissimilar materials based on the complex intensity factor originally introduced by Rice and Sih [1965]. Here the stress singularity caused by the dissimilar materials is expressed in terms of Dundurs parameters α and β [Suo and Hutchinson, 1989]. Suo [1989] employ a superposition scheme to determine the stress intensity factors of a bimaterial interface with singularities such as point force, point moment, edge dislocation. An edge crack in a laminate [Sun and Manoharan, 1989] has been analysed using the three point bending test and an expression of energy release rate was obtained using classical laminate theory and Timoshenko beam theory. Williams [1988] derives general methods to calculate energy release rate in laminates using the crack-tip values for bending moments, normal forces and shear forces. Based on Williams method, Nairn [2006] expresses the energy release rate of a crack in a multi-layered structure including the influence of temperature and applied this equation to different geometric configurations.

2.4.1 J-integral for energy release rate

J-integral is a volume or area integral formulation used to calculate the energy required for crack growth. The path independent J-integral proposed by Eshelby [1956] and Rice[1968] extended the fracture mechanics from linear elastic behaviour to encompass plastic behaviour allowing the J-integral to be used as a fracture criterion [Begley and Landes, 1972]. For a 2D crack, as shown in Figure 2.7, an arbitrary counter-clockwise path around the crack tip, the J-integral can be written as:

$$J = \int_{\Gamma} (W \cdot n_1 - T_i \cdot \frac{\partial u_i}{\partial x_i}) ds \tag{2.14}$$

where W is the elastic strain energy density, T_i is the traction along the contour Γ with being $\mathbf{n}$ the unit normal of the contour path, and:

$$W = \frac{1}{2} \sigma_{ij} \varepsilon_{ij} \tag{2.15}$$

σ_{ij} and ε_{ij} are the stress and strain tensors respectively. The traction vector can be expressed as:

$$T_i = \sigma_{ij} \cdot n_j \tag{2.16}$$

Combing Eq.(2.14) to Eq. (2.16) together, the J-integral can be expressed analytically in terms of displacement, strain and stress fields.

Kishimoto et al. [1980] extend Rices J-integral and included a fracture process zone and the effect of plastic deformation, body forces, thermal strain and inertia of material. The J-integral can also be applied to mixed-mode dynamic fracture mechanics [Nishioka and Atluri, 1983]. Sheinman and Kardomateas [1997] obtain the total energy release rate of through width crack of the composite laminate using the J-integral for one dimensional

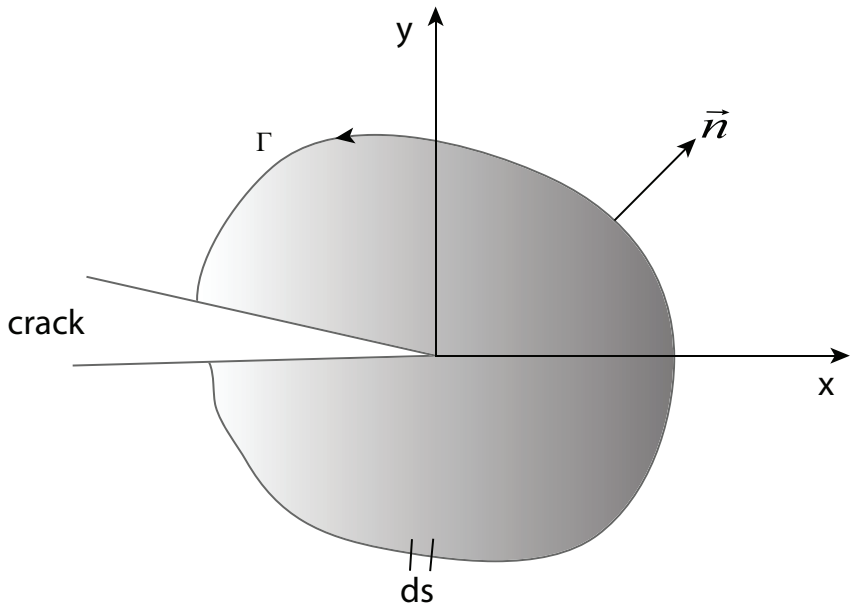

Figure 2.7: The domain of J-integral

model and decomposed it into mode I and mode II based on the orthotropic properties in the thickness direction of the anisotropic materials. Vavrik and Jandejsek [2014] directly calculate the J-integral as it is defined based on digital image correlation data and it is proven that the J-integral is independent of the integration path even though the integration paths crossed completely yielded ligament. The J-integral can also be utilized for stress intensity factor calculations based on the relationship between the energy release rate and stress intensity factor.

2.4.2 Other methods for calculating energy release rate

The strain energy release rate can be calculated using many different methods such as the compliance derivative method, VCCT and derivative of potential energy which allows the energy release rate to be calculated directly based on its definition. The compliance derivative method is popular among researchers because the energy release rate in an experiment can be determined from the compliance of the structure which can be directly obtained from the load-displacement curve. Ramkumar and Whitcomb [1985] obtain the critical Mode I strain energy release rate in static double cantilever beam test using the compliance method to deal with the test results. For a simple loaded linear elastic material system, the energy release rate can be written as:

$$G = \frac{P^2}{2B}\frac{dC}{da} \tag{2.17}$$

where C is compliance of the structure, a is the crack's length, P is the external load and B is the width of the crack.

In addition to being used for crack growth modelling, see section 2.3.2, the VCCT can

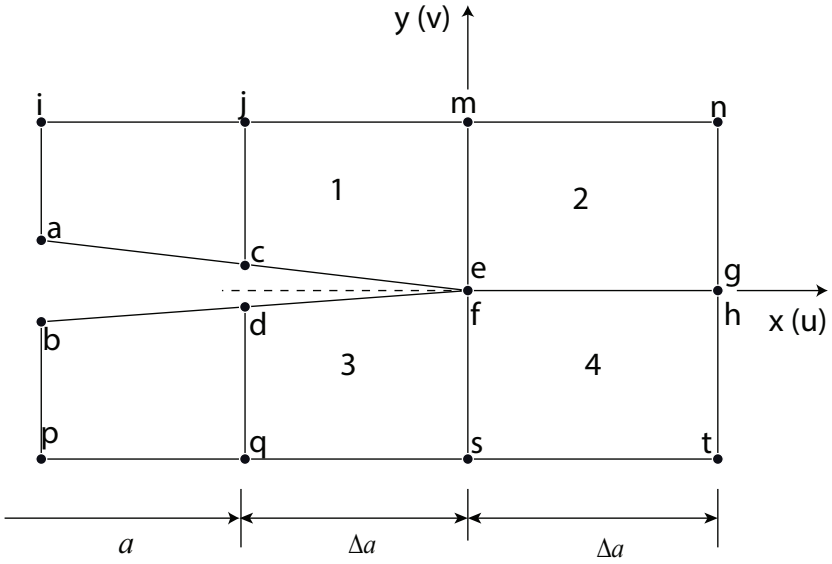

Figure 2.8: Nodes at the crack tip

be used to determine the energy release rate [Rybicki and Kanninen, 1977]. The energy release rate of mode I and mode II using VCCT as shown in Figure 2.8 can be written as:

$$G_I = \lim_{\Delta a \to \infty} \frac{1}{2\Delta a} F_c(v_c - v_d) \tag{2.18}$$

$$G_{II} = \lim_{\Delta a \to \infty} \frac{1}{2\Delta a} T_c(u_c - u_d) \tag{2.19}$$

where F_c and T_c are the nodal forces in the direction of x and y, u_c, u_d, v_c and v_d are the displacements of nodal c and nodal d. Qian and Sun [1997] evaluate the strain energy release rate using VCCT. The total energy release rate is decomposed utilizing the relation between the crack surface displacement ratio.

The various used methods to analysis energy release rate can be applied to simple structures, however, it is difficult to utilize these methods for a complex structure such as an AP-PLY composite laminate. The J-integral shows great ability in obtaining the energy release rate and there are special singularity elements in ABAQUS which can be used to solve the crack tip singularity problem. The J-integral in ABAQUS will be chosen for the research presented in this thesis to verify the energy release rate calculation using the proposed approach which will be discussed in next section.

2.5 Proposed approach

An AP-PLY composite laminate gives the advantages of lower weight and increased damage tolerance. The main objective of the research presented here was to understand the fracture mechanism of delamination in an AP-PLY composite laminate structure under

out-of-plane loading. In the present body of research on the SERR of cracks in composite laminates, three different ways are used to calculate SERR: analytical methods, finite element methods and experimental methods. Based on finite element method, Banks-Sills [1991] gives three methods that can be used to calculate SERR: the displacement extrapolation method, the stiffness derivative method and the J-integral method, all of which can be used to calculate SERR. With the continuing development of computer science and software innovations, the SERR can now be obtained directly using commercial software such as ANSYS and ABAQUS using J-integral around the crack tip with some special requirements on element meshing which can include stress singularity at the crack tip [ABAQUS, 2011]. Another common way to calculate SERR used in commercial software is to use VCCT, this allows the SERR, G_I for mode I and the SERR G_{II} for mode II to be calculated separately [Krueger, 2004]. Additionally, Cohesive Zone Model (CZM) can be used to simulate crack growth using energy-based crack evolution in which the critical SERR is taken into account. Since the SERR includes the total energy release rate G_T of a delamination, the component G_I of mode I due to interlaminar tension, the component G_{II} of mode II due to interlaminar sliding shear, and the component G_{III} of mode III due to interlaminar scissoring shear, different experimental configurations are required to calculate the SERR. The following can be used to calculate different SERR: Double Cantilever Beam (DCB) for G_I [Ozdil and Carlsson, 1999; Hamed et al., 2006; Gordnian et al., 2007], End Notched Flexure (ENF) for G_{II} [Carlsson et al., 1985; Sun and Zheng, 1996; Davidson et al., 1996] and Mixed Mode Bending (MMB) for the mixed-mode to evaluate the mixed-mode ratio [Kinloch et al., 1992; Benzeggagh and Kenane, 1996; Camanho et al., 2003].

Numerical finite element methods, such as the cohesive zone model and the VCCT were used to predict delamination onset and growth. The finite element is sensitive to element length and large models were required to assure the accuracy of the model. Even for each simple case like stack sequence changing or geometry changing, the whole computation had to be repeated. However, the advantage of an experiment is that it gives a real case, with a real structure undergoing delamination without simplification using in modeling. Using an analytical method to obtain SERR gives the flexibility to apply it to different materials and different geometries. The drawback of using an analytical method is that the SERR will be less accurate due to the simplification of the real structure and the assumption made, thus the theory used to describe a structure problem for an analytical method needs to be chosen with care. As an efficient, less costly, but perhaps not so accurate alternative, an analytical approach to determine the energy release rate was proposed in the research presented in this thesis.

Determining SERR of a crack in composite laminates using an analytical method requires two steps: the first step is to choose a proper theory to describe the structure; the second step is to choose the method used to obtain SERR. Several theories of describing composite laminates underpin the methods to obtain the SERR for delaminations which are found at the interface of different layers in composite laminate. These include beam theory such as the Eurler-Bernoulli beam theory, the Timoshenko beam theory and the second order shear thickness deformation beam theory (SSTDBT) and plate theories such as laminate plate theory. The general methods that are based on one of the above theories

described used to calculate SERR are the compliance method, the J-integral method and the derivative of potential energy which allows the SERR to be computed based on the definition of SERR as described in this chapter, section 2.4.

2.5.1 Beam theory

The delaminations in composite laminate occur at the interfaces between different layers and resulting in a structure with several sub-laminates. The beam theories, used to analyze the SERR in composite laminate, are based on the assumption that a delamination will be through the width direction of a composite laminate. Kanninen [1973] analyzes the SERR of DCB using Euler-Bernoulli beam theory and the undelaminated part of the composite laminate is expressed using the Winkler foundation as shown in Figure 2.9. The governing differential equation for the deflection of the beam w is:

$$\frac{d^4w}{dx^4} + 4\lambda^4 H(x)w = 0 \tag{2.20}$$

where $H(x)$ is Heaviside function,

$$H(x) = \begin{cases} 1, & \text{if } x > 0 \\ 0, & \text{if } x < 0 \end{cases}$$

and $\lambda^4 = \dfrac{k}{4EI} = \dfrac{3k}{Ebh^3}$. Combined with continuum conditions at the crack tip and boundary conditions, the solution of the differential equation is obtained. The energy release rate is determined using compliance method.

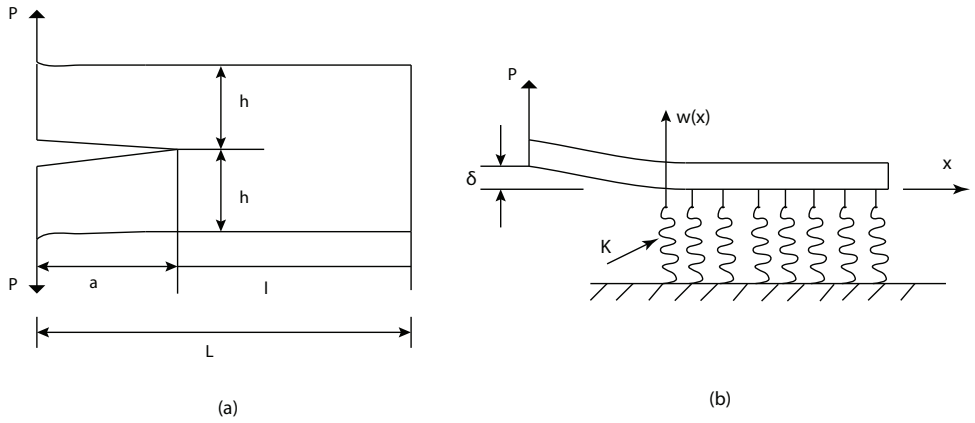

Figure 2.9: (a) DCB specimen (b) Beam on elastic foundation model of DCB specimen

Later, Kanninen [1974] extends the beam-on-elastic foundation to a dynamic analysis of unstable crack propagation, calculating the SERR of DCB, based on Timoshenko beam theory to include shear deformation. Ozdil and Carlsson [1999] analyze the energy release

rate, mode I, mode II and mixed-mode, of quasi-unidirectional and angle-ply laminate DCB specimen. The analysis is based on Bernoulli-Euler-type beam theory and compliance method, for which the uncracked part is joined together using a Winkler-type elastic foundation. Andrews et al. [2005] utilize a cantilever beam model based on classical beam theory to analyze the elastic interaction of multiple through-width delamination in laminated plates under out-of-plane loading. The length of the delaminations and the position of the delaminations influence the interaction behavior of the multiple delaminated systems and may lead to shielding or amplification of the energy release rate.

In order to include the influence of shear deformation, Carlsson et al. [1986] analyze the mode II SERR G_{II} of ENF specimen using Timoshenko beam theory and compliance method. Sun and Pandey [1994] calculate the mode I SERR G_I of the DCB test. The shear deformation effect can be included in the Timoshenko beam governing equation as done by Kanninen [1974], or in the displacement solution, which is based on Timoshenko beam theory, to get the SERR using compliance method as done by Carlsson et al. [1986].

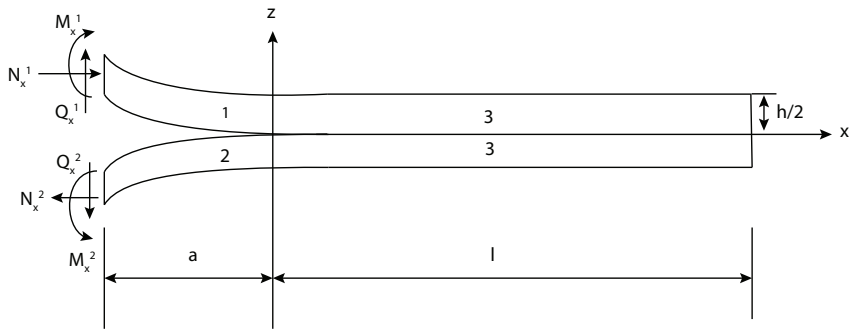

Figure 2.10: Double cantilever beam configuration

Another higher order beam theory, SSTDBT, is used to analyze delamination in composite beams including the shear and the thickness deformation effect. Take DCB as an example, the geometry is shown in Figure 2.10, the delamination is assumed in the middle plane of the beam. Based on the assumption of SSTDBT, the displacement field of each part can be expressed as:

$$u = u(x) + z\psi_x(x) + z^2\eta_x(x) \tag{2.21}$$

$$v = 0 \tag{2.22}$$

$$w = w(x) + z\psi_z(x) \tag{2.23}$$

where u, v and w are displacement components in the $x-$, $y-$ and $z-$ axes, respectively. Substituting the assumed displacement into the strain-displacement relation of elasticity, then into the stress-strain relations of a composite beam and the composite beams' constitutive relations, after that substituting the obtained results into the equilibrium equations which use the minimum total potential energy gives, finally, the equilibrium in terms of displacement equations. The displacements are then obtained by solving the differential equations combined with the boundary conditions and continuity conditions at the end and in the joint of the different parts. Hamed et al. [2006] use a displacement field based on SSTDBT and use the principle of minimum total potential energy to

obtain the equilibrium equation of angle plied composite beams with delamination, then the ERR is obtained by J-integral and decomposed to different modes. Gordnian et al. [2007] employ the same beam theory and the compliance method to calculate the energy release rate for an angle ply composite beam.

2.5.2 Laminate plate theory

The laminate plate theory is commonly used to analyze composite laminates in engineering applications especially classical laminate theory (CLT) and first-order shear deformation theory (FSDT). The CLT is an extension of Kirchhoff's classical plate theory for isotropic materials to composite laminates with a smaller thickness to width ratio. Similar to Kirchhoff plate theory, the CLT works well for thin laminates. Based on CLT, the displacement field is given by:

$$u(x,y,z) = u_0(x,y) - z\frac{dw}{dx} \tag{2.24}$$

$$v(x,y,z) = v_0(x,y) - z\frac{dw}{dx} \tag{2.25}$$

$$w(x,y,z) = w_0(x,y) \tag{2.26}$$

where u, v and w are displacement components in the $x-$, $y-$ and $z-$ axes, respectively; $u_0(x,y)$, $v_0(x,y)$ and $w_0(x,y)$ are displacement components in the midplane of the plate. O'Brien [1982] determines the SERR of graphite-epoxy laminate under static tension loading and tension-tension fatigue loading based on CLT. Raju et al. [1988] analyze the SERR of edge-delaminated composite laminates using CLT. Schapery and Davidson [1990] express ERR of mixed-mode delamination for composites in terms of the moment and shearing force at the crack tip and decompose the shearing-to-opening mode components of the ERR using a classical plate theory and virtual crack closure method. Hu and Wu [1995] analyze the energy release rate and stress intensity factors of an interface crack based on classical plate theory and the mix mode parameter is determined. Zou et al. [2001] use laminate theory and VCCT to obtain the energy release rate of a composite laminate.

Due to the lower transverse shear stiffness in composite laminates, the shear deformation is significant and can not be neglected. Therefore, a high order theory is needed to be developed for moderate thickness laminates. Zheng and Sun [1995] propose a double-plate model to calculate the SERR in a composite laminate which is similar to FSDT. Two Mindlin plates are used to model the delaminated parts of DCB laminate and contact conditions were used to constrain the separate parts to avoid penetration. A crack closure method is employed to obtain the SERR at the delamination front. For a composite laminate treated as two separate Mindlin plates, the displacement field can be written

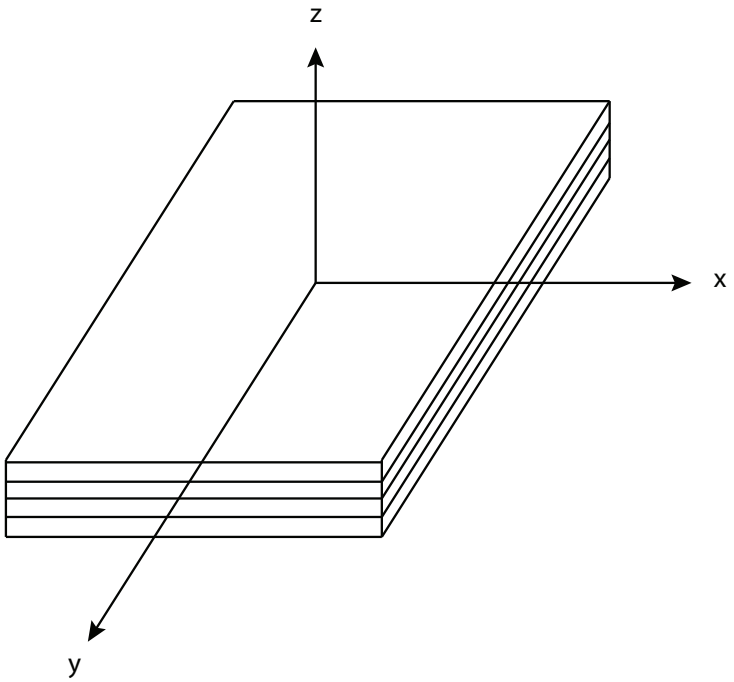

Figure 2.11: Composite laminate

as:

$$u(x,y,z) = u_0(x,y) + z\psi_x(x,y) \quad (2.27)$$

$$v(x,y,z) = v_0(x,y) + z\psi_y(x,y) \quad (2.28)$$

$$w(x,y,z) = w_0(x,y) \quad (2.29)$$

where u, v and w are displacement components in the $x-$, $y-$ and $z-$ axes, respectively; $u_0(x,y)$, $v_0(x,y)$ and $w_0(x,y)$ are displacement components in the midplane of the plate; ψ_x and ψ_y are rotations of the cross-sections. Sun and Manoharan [1989] analyze the ERR of a edge cracked 3 point bending specimen with cross-ply laminate structure utilizing classical laminate theory and Timoshenko's theory. The results show that the CLT is adequate for that case and the shear effect is negligible. Sun and Zheng [1996] analyze the energy release rate of double-cantilever beam and end-notched flexure composite specimens including the boundary layer in the width direction and the skewed G distribution across the width owing to the bending-twisting coupling by the plate finite element.

Wang [1983] obtains the fracture parameters such as stress intensity factors and energy release rate of delamination crack in composite laminates based on anisotropic laminate elasticity theory and Lekhnitskii's stress functions. Suo and Hutchinson [1989] provide a solution for energy release rate and stress intensity factors for the problem of a semi-infinite crack in a brittle substrate parallel to the film/substrate interface using longitudinal load and moment. Suo and Hutchinson [1990] obtain the energy release rate for a semi-infinite crack on the interface of two infinite isotropic elastic layers by superposition to include the singularity at the crack tip. Barbero and Reddy [1991] extend the layer-wise laminate theory to multiple delaminations between layers, in which delaminations

are modeled by jump discontinuity conditions at the interfaces. Leguillon [1999] predicts the edge delamination of composite laminates based on singularity theory. Cho and Kim [2001] develop a higher-order zig-zag theory for composite laminate plates with multiple delaminations that can be used to obtain the buckling load and natural frequency of the delaminated structure.

2.5.3 The chosen approach used in this thesis

In addition to the compliance method and J-integral method, derivative of potential energy method discussed in this chapter are also the ways to obtain SERR. Williams [1988] derives a general method to calculate the SERR for delaminated laminates from the local bending moments, normal forces and shear forces. Nairn [2006] expresses the SERR of a crack in a multi-layered structure including the influence of temperature based on Williams' [1988] method. In this thesis, beam theory and William's method will be used to determine the SERR of delaminated AP-PLY composite laminate. The use of 2D beam model for the analysis of delamination in AP-PLY composite laminate may cause a loss of accuracy but can be a very efficient method for trade studies.

Ultimately, the goal is to link the model with optimization to promote the selection of the best AP-PLY configuration for a specific structure. The analytical energy release rate of AP-PLY formed the basis of the optimization of an AP-PLY structure. The new proposed approach will employ the crack-tip values of bending moments, normal forces and shear forces [Williams, 1988] to analyze the energy release rate. The requirement of minimum complementary energy will be made to satisfy the need for compatibility between delaminated layers. Lagrange multipliers were used to determine the generalized forces at the crack tip, which were used to calculate the strain energy release rate.

Chapter 3

Characteristics of different AP-PLY patterns

3.1 Introduction

As discussed in chapter 1, the use of an AP-PLY composite laminate generally improves damage tolerance, however, we still lack detailed information about the structure of an AP-PLY's behavior under impact. The traditional composite parameters, such as stacking sequence, fibre and resin material properties, geometry and loading all influence the mechanical properties of a composite laminate. To understand the AP-PLY composite laminate better we need to determine the traditional parameters affecting composites in addition to how these parameters interact when present in an AP-PLY composite and the parameters that define the different AP-PLY patterns of 'weaving' used. These are the factors that need to be determined during any optimization process. They are width of the ply, thickness of the woven ply or the number of plies "interwoven", the angle of inclination of the woven ply, and the placing order of the plies that are the parameters that characterized an AP-PLY pattern.

The study of AP-PLY composite laminate behavior under an impact load will start from predicting delamination initiation. It is known that understanding interlaminar stress plays a key role in predicting onset delamination of composite laminate [O'Brien, 1982; Lagace, 1983]. For a structure as complicated as AP-PLY, the analytical methods cannot give accurate results and the finite element method requires very fine mesh for each structure configuration which means the simulation will be time-consuming and costly. The interlaminar stress recovery technology developed by Fagiano et al. [2010a] has been shown to be more efficient than conventional finite element models and was employed for the research described here to obtain the interlaminar stresses in an AP-PLY laminate under out-of-plane load. Combining the interlaminar stress with stress failure criteria, the crack initiation location was located for the AP-PLY and the initiation load was determined. In this chapter, a finite element model is established according to the cross

section of a simple AP-PLY composite laminate but only woven in one direction. Using the stress recovery technology, the interlaminar stresses were recovered based on the interlaminar stresses obtained using a coarse meshed finite element model in ABAQUS. The critical delamination onset locations for this simple AP-PLY pattern were determined using an interlaminar stress failure criterion.

This chapter is set out as follows: the detailed finite element model is described in section 3.2. The recovery stress procedure and the recovered stress compared with fine mesh finite element results are discussed in section 3.3. Determining the critical delamination onset is described, using maximum stress failure criteria, in section 3.4. The chapter conclusions are presented in section 3.5.

3.2 Model description

Many different patterns of AP-PLY exist and each pattern's cross-section in the xz and yz planes is different (where z is the out-of-plane direction). The structure of the finite element model when determining delamination in an AP-PLY composite is based on its cross-section. It is impossible to analyze or simulate all possible AP-PLY patterns this way and perform optimization. For the work discussed in this chapter, one specific model was chosen to capture the main characteristics of the delamination onset of AP-PLY woven plies. This specific model is composed of several layers of straight plies with woven layers in the middle.

3.2.1 Basic model information

Material Properties

A width of 6.35mm was chosen for the ply with a thickness of 0.18mm to match the size of a ply used during manufacturing process. The material properties used for the model were the same as those of HexPly AS4/8552, see table 3.1.

Young's modulus	Shear modulus	Poisson's ratio
$E_1 = 148GPa$	$G_{12} = 4.55GPa$	$\nu_{12} = 0.3$
$E_2 = 9.65GPa$	$G_{13} = 4.55GPa$	$\nu_{13} = 0.3$
$E_3 = 9.65GPa$	$G_{23} = 3.64GPa$	$\nu_{23} = 0.45$

Table 3.1: Ply's material properties

The subscripts 1, 2 and 3 are used to denote longitudinal direction, transverse direction and thickness direction, respectively. Most conventional laminate simulations only take into account the reinforcement in a composite but not the matrix. For an AP-PLY

composite laminate, the matrix volume at the woven part cannot be ignored, and matrix cracks can lead to delamination. This is the reason that matrix had to be taken into account during the simulation process. The matrix used for our model was epoxy resin 8552, with the material properties $E = 4.56GPa$ and $\nu = 0.3$.

Geometry of the model

To simplify the simulation for the model, the assumption was made that delamination could be expected during the linear deformation phase and the AP-PLY pattern was assumed to be similar to that of the symmetry layup $[0_n/90_n/0/90]_s$, where n is the number of layers determined by analyzing the deformation of the plate to make sure the deformation was linear until damage occurred. Another factor that must be determined when studying linear deformation is the load. The ideal load is the one that can lead to damage during the impact test but that still gives linear deformation. In a standard impact test, the impact energy is an input or known variable that can be adjusted by the weight of the impactor and its release height. The low-velocity impact loading was modeled as quasi-static load. The limitations of the quasi-static loading are: (1) Impact duration is longer than the time it takes for elastic waves to travel to the plate boundaries; (2) The plate is big enough so impact load can be considered a point load. The force that the impactor has imparted to the specimen can be measured using a strain gauge attached to the impactor. Naǵelsmit [2013] has done a number of impact tests for different AP-PLY specimens of $100 \times 150 \times 4$ mm to check for the Barely Visible Impact Damage (BVID) level, i.e., damage manifested by 1 mm indentation depth after impact. The maximum force produced by the impactor during the impact process was in the range of 8KN to 13KN for the different AP-PLY patterns. Taking into account Naǵelsmit's work [2013] we chose a 9KN force for our impact load for our simulation AP-PLY composite laminate model. Using classic composite laminate theory, n was determined to equal to 5, therefore, the layup of AP-PLY composite laminate was $[0_5/90_5/(0^w/90^f)/90/0/90_5/0_5]$.

The sketch of the woven part was based on the close-up of a single undulation in an AS4/8552 0/90 AP-PLY, as shown in Figure 3.1. The angle of the woven plies was 7 degrees, and this angle could be varied from 5 degrees to 25 degrees depending on the thickness of straight filled ply see Figure 3.1. In an AP-PLY model of a composite laminate woven in one direction, the angle of woven plies was 17.4 degrees, the length of the woven part was 0.575mm. The length of one unit of the AP-PLY was $26.55 \times 26.55 \times 4.32$ mm, as shown in Figure 3.2 (a). The whole model was composed of 3 units and the geometry of the model was $79.65 \times 79.65 \times 4.32$ mm. It is recognized that the straight edged angles formed by the woven layer in the simulation model is not the same as the gradual wavy shape seen in Figure 3.2 (b). Simple FE analysis of a wavy shape representative of the situation in Figure 3.2 (b) and a shape with straight line segments showed a difference of 20% in normal stresses and 14% in shear stresses at the corner. As knowing the exact wavy shape for each pattern is not possible, it was decided to stay with the straight segment shape for the rest of the work and use test results (see chapter 6) to validate or invalidate the usefulness of this approach.

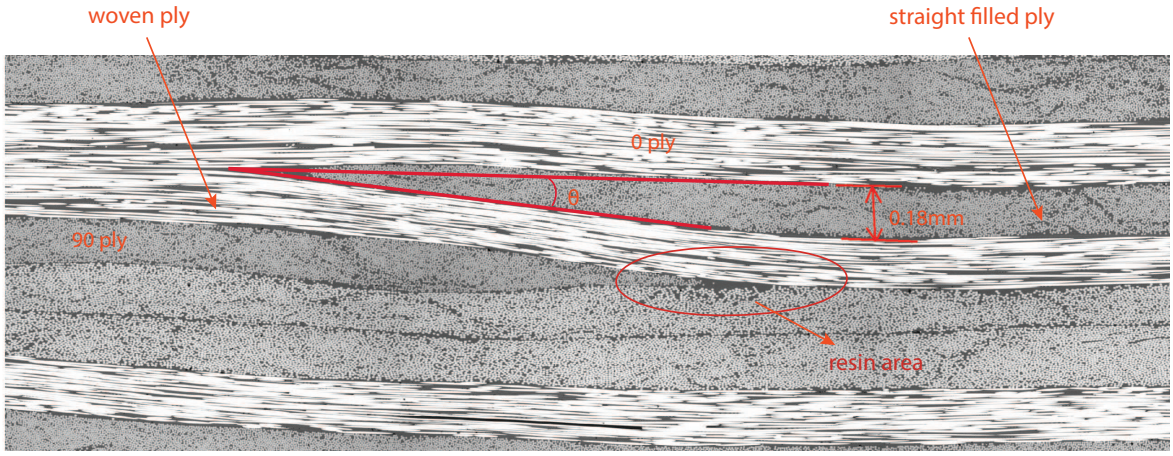

Figure 3.1: Close-up of a single undulation of 0/90

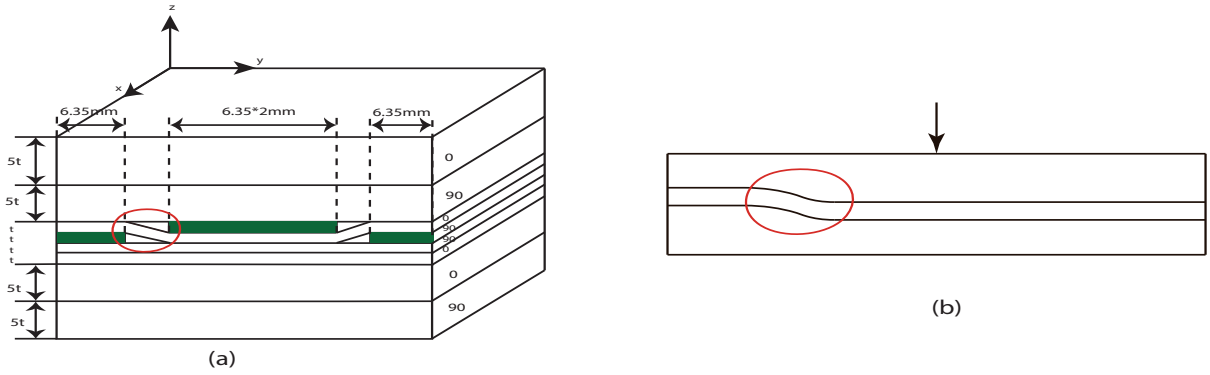

Figure 3.2: (a)One unit cell of model (b)A simple model with actual woven shape

Model simplification

It can be seen from Figure 3.1 that in the cross-section the plies are deformed slightly and are no longer straight. It is hard to capture detailed information of ply deformation during the manufacturing process, that's why the plies in the simulation model are assumed to be perfectly straight, and the resin only fills the sharp tip of the woven area. To make the mesh in the model easier and make the results conservative, the resin for our model was expanded to the whole triangle area of the woven plies see Figure 3.1, with the rest of the space filled by the ply in the other direction.

Boundary conditions

The simply supported boundary conditions for the plate, as shown in Figure 3.3 were:

$$v = w = 0, \qquad \text{at } x = 0 \text{ and } x = a_2 \tag{3.1}$$

$$u = w = 0, \qquad \text{at } y = 0 \text{ and } y = a_1 \tag{3.2}$$

where $a_1 = a_2 = 79.65mm$.

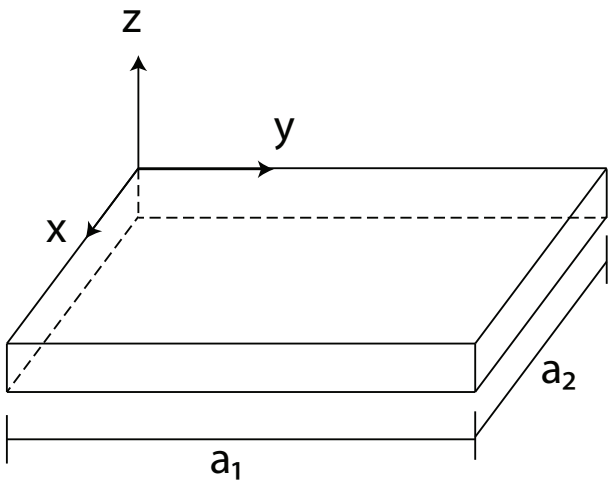

Figure 3.3: Plate with AP-PLY pattern modeled in present study

The clamped boundary conditions were described as:

$$u = v = w = 0, \qquad \text{at } y = 0 \text{ and } y = a_1 \tag{3.3}$$

3.2.2 Model mesh and stress recovery requirement

As discussed in chapter 2, each ply is modeled separately to recover the interlaminar stress between each interface. Due to the transverse shear stress field in a laminate, the area most vulnerable to delamination will be in the vicinity of the middle-plane in this model. The layup of AP-PLY composite laminate model was $[0_5/90_5/(0^w/90^f)/90/0/90_5/0_5]$, in which the 0 ply in the 11th layer was interwoven with the 90 ply in the 12th layer. To speed up the simulation and to concentrate more on the characteristics of the woven part of the AP-PLY, the top and bottom five layers of the 0 plies, the two bundles of five layers of the 90 plies, the woven 0 ply, the filled 90 ply, and the straight 1 layer of 0 and 90 plies were modeled separately. The interaction at the interfaces was defined as surface-to-surface contact and was defined using a tied contact formulation to overcome the oscillatory behaviors of the retrieved transverse stress distributions, and the small sliding was chosen for the sliding formulation. The tolerance for adjustment zone was

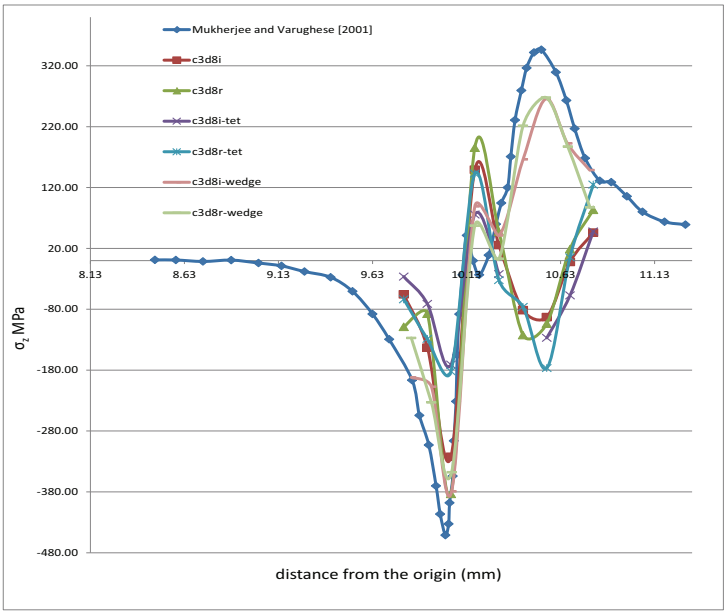

Figure 3.4: Interlaminar normal stress at the drop-off

specified as 0.01 for the contacted surfaces to avoid the slave surface penetrating into the master surface.

Depending on the geometry of the whole model, the model could be meshed with combinations of different element types. Many different element types can be chosen in ABAQUS based on different requirements. There are hex elements, wedge elements and tet elements for a three-dimensional model based on the shape, and for different element shapes, linear elements and quadratic elements (second order elements) are available based on different interpolation method. All these elements can be full integration or reduced integration. The linear hexahedral C3D8I element is an improved version of the C3D8 element. The advantages of C3D8I element are that the shear locking is removed and volumetric locking is much reduced. Accurate results can be obtained with relatively coarse mesh and C3D8I is insensitivity to distortion for a large range of length to thickness ratio. Normally, using quadratic elements will give more accurate results than using linear elements, but the incompatible mode elements perform almost as well as quadratic elements [ABAQUS, 2011]. Using the C3D8I element seemed to be a good choice for our bending composite laminate model. From Fagiano's [2010a] experience of recovering interlaminar stress of variable stiffness composite laminates, a combination of linear hexahedral C3D8I elements and linear triangular prism C3D6 elements will give accurate elements in non-conforming meshes, however it is still necessary to validate the procedure for different loadings and different non-conforming meshes.

As can be understood from the model see Figure 3.2, the woven areas of the AP-PLY composite laminate are very similar to ply drop-off location. Mukherjee and Varughese [2001] discuss the influence of the parameters related to a drop-off using a global-local approach finite element method. In our work a stress comparison of combinations of different elements using the same model size and material properties as those used by

Mukherjee and Varughese [2001] was done in the vicinity of the ply drop-off, as shown in Figures 3.4 and 3.5.

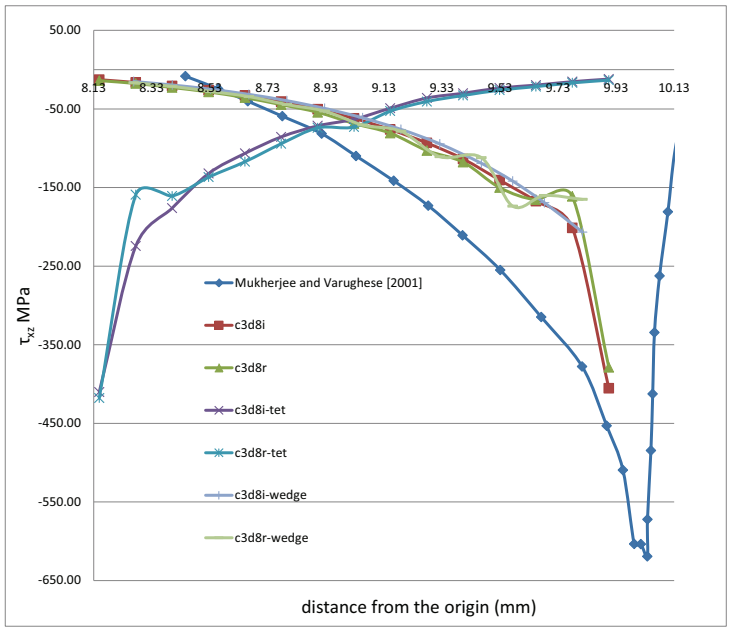

Figure 3.5: Interlaminar shear stress at the drop-off

It can be seen from Figures 3.4 and 3.5 that the model meshed with C3D8I and the model meshed with a combination of C3D8I brick and C3D6 wedge elements will give in the sense of being closest to the fine mesh used by Mukherjee and Varughese [2001], compared with the rest of the models meshed with different elements. The results will be closer to the fine meshed model of a ply drop-off to be found in the literature [Mukherjee and Varughese, 2001] where a fine meshed model was used.

3.3 Comparison

In order to gauge the applicability and accuracy of our model in recovered stress, the recovered stresses were compared to analytical results obtained for a conventional composite laminate and the fine meshed finite element results of the AP-PLY composite laminate model. These comparisons were used to establish the accuracy of the recovered stress values in a complicated structure and to help identify the problems that the recovered technology might need improvements of when dealing with complicated structures.

3.3.1 Recovered interlaminar stress compared with analytical results

The first aspect was to make sure the process of stress recovery was correct and, at the same time, to check the accuracy of the recovered stress values. This was done by comparing the recovered stress values with analytical results available for a conventional composite laminate [Pagano, 1974; Kassapoglou and Lagace, 1987]. Pagano [1974] modifies the theory of Whitney and Sun [1973] that included shear deflection and thickness stretch deformation. Pagano defines the distribution of interlaminar normal stress along the central plane of a symmetric laminate, which accounts for the material and geometric influence. Kassapoglou and Lagace [1987] derive closed form solutions of interlaminar stress field at a straight free edge for angle-ply and cross-ply composite laminates and compared the results with those obtained by Pagano. To check the interlaminar stress recovery procedure, the recovered interlaminar normal stress of a $[0/90]_s$ traditional composite laminate model was compared with the results of Pagano [1974] and results of Kassapoglou and Lagace [1987], as shown in Figure 3.6. The recovered interlaminar shear stress of a $[\pm 45]_s$ laminate model was compared with the results of Pipes and Pagano [1970] as shown in Figure 3.7.

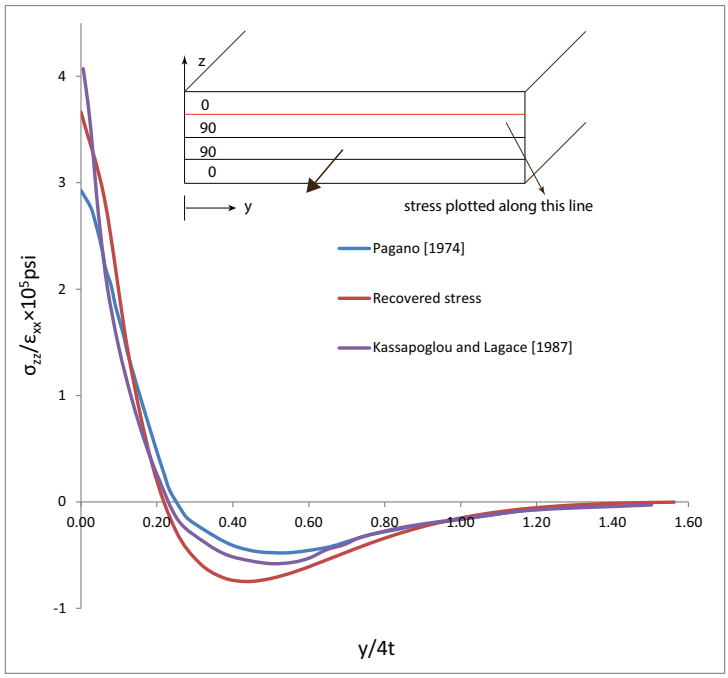

Figure 3.6: Interlaminar normal stress at 0/90 interface of a $[0/90]_s$ laminate

The recovered interlaminar stresses of the different layups were in good agreement with the results in the literature and the stress recovery procedure was considered accurate for a conventional composite laminate.

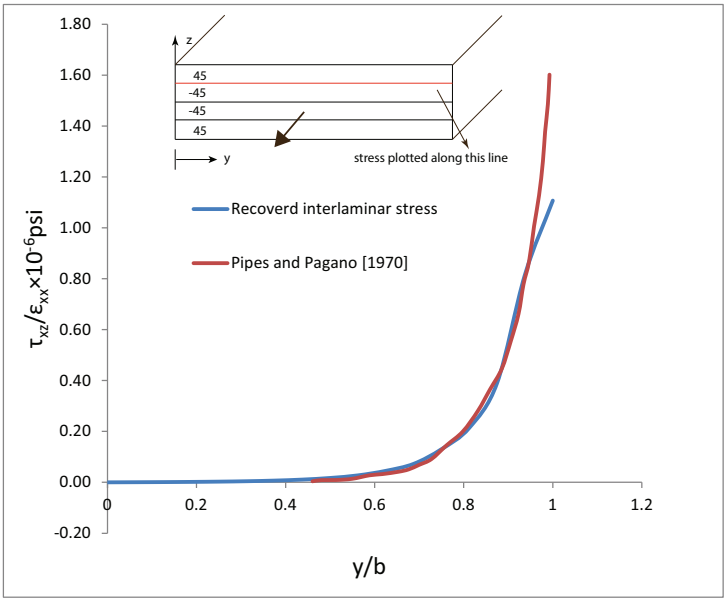

Figure 3.7: Interlaminar shear stress at $45/-45$ interface of a $[\pm 45]_s$ laminate

3.3.2 Recovered interlaminar stress compared with fine meshed FEM results

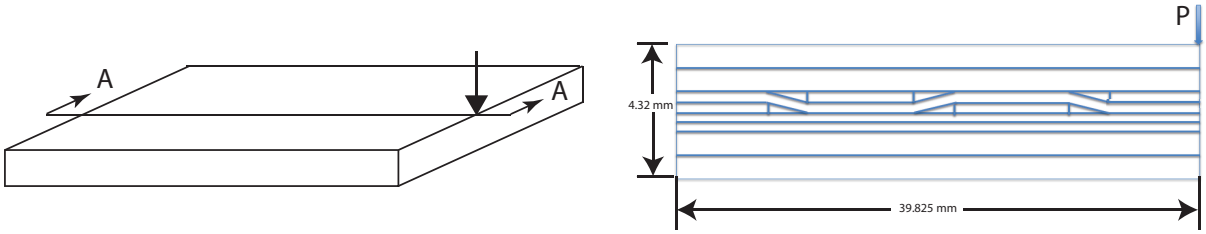

Figure 3.8: (a) Half model (b) The cross-section A-A of the half model

The recovered interlaminar stresses using stress recovery technology were accurate for conventional laminates as can be seen from subsection 3.3.1. It is still unknown whether the stress recovery technology is sufficiently accurate or not for a woven part of the AP-PLY composite laminate in which the resin pocket is probably the delamination initiation location. The recovered interlaminar stresses were compared with the results of a fine meshed finite element model to verify the accuracy of the recovered stresses. For a $79.65 \times 79.65 \times 4.32$ mm woven in one direction AP-PLY model, as shown in Figure 3.8, the model is meshed in two ways. One is a coarse mesh model with the results of which the stress recovery technology is implemented. The other is very fine mesh model that is used to verify the accuracy of the stress recovery technology in different shaped recovered areas.

The elements in the fine mesh model are a combination of C3D8I and C3D6. In the triangular resin area, the elements are C3D6, and the seed is 0.045 with 205,320 elements in the resin part. The C3D8I elements are assigned to the straight plies, the seed is 0.27,

and each layer has 4 elements in the thickness direction of the middle four layers. In total there are 2,355,288 elements in the fine meshed model.

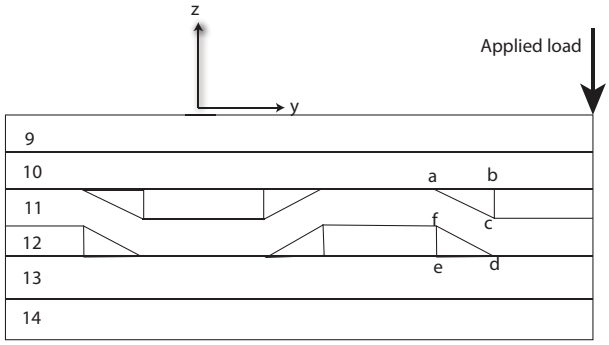

Figure 3.9: Sketch of the part whole model

The element type in the coarse mesh model is C3D8I, the seed to mesh the model of top 10 layers (0 and 90 part instances) and bottom 10 layers (0 and 90 part instances) is 0.7965, and the seed for middle 4 layers is 0.575. There are 119,094 elements in total which is around $\frac{1}{20}$ of the element number of the fine meshed model. It is possible to recover every interface of interest in the model. The model described in this chapter is symmetric in the width direction for which the stress was recovered in the left half of the model. In this model, the material properties of the resin are weaker than those of the plies. Therefore, the resin areas are the possible locations for crack initiation. The stresses obtained from the finite element results for the coarse mesh model confirmed this, the two resin areas close to the middle had the highest interlaminar stress. The stresses in these two triangular areas were recovered using the stress recovery technology. As shown in Figure 3.9, the top triangular area was represented using abc, while def was used to represent the bottom area. The coarse mesh of the resin pockets in Figure 3.9 are shown in Figure 3.10 (b).

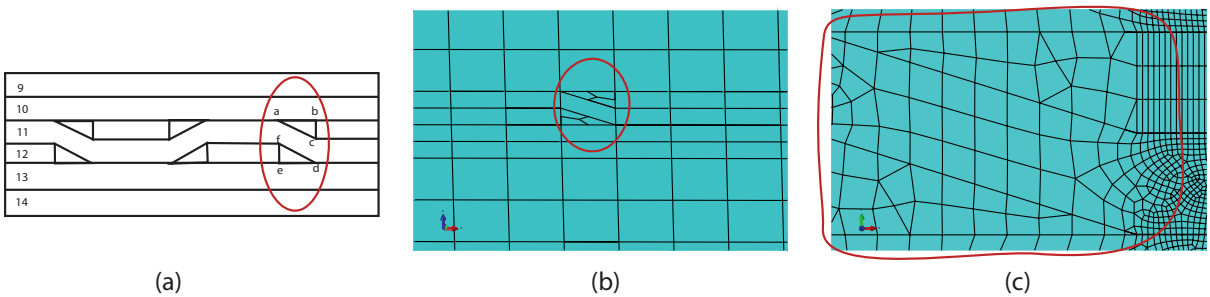

Figure 3.10: (a) the resin pocket (b) mesh used in recovered stress (c) mesh used in cohesive element model (see Chapter 4.2.2)

The recovered stresses at the relevant resin areas compared to the stresses of the resin area in the fine meshed model are shown in Figures 3.11, 3.12, and 3.13. It can be seen that the recovered stresses were close to those using the fine meshed finite element model. The results showed that the recovered interlaminar stresses give accurate trends and that

the stress recovery technology also can be used to recover the stresses of the interfaces that are not horizontal, like the sloped interface.

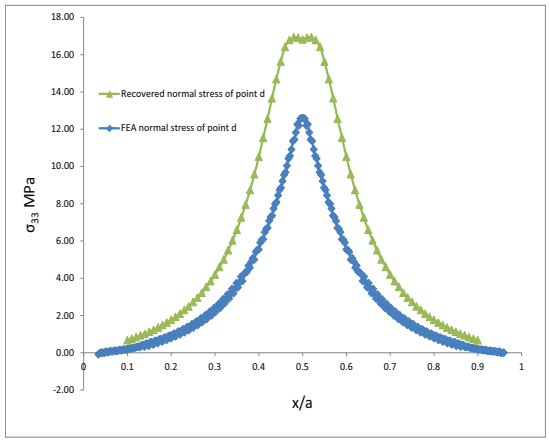

Figure 3.11: The recovery normal interlaminar stress σ_{33} of point d compare with fine meshed finite element results

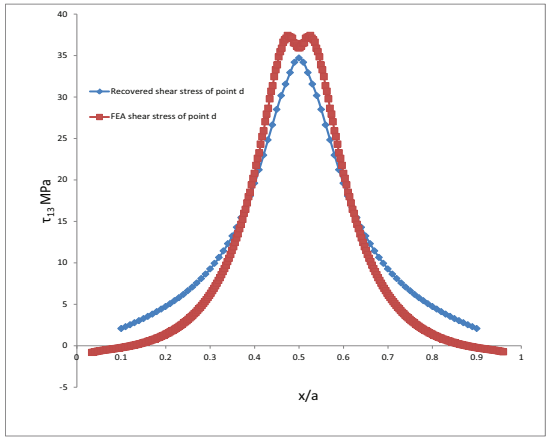

Figure 3.12: The recovery shear interlaminar stress τ_{13} of point d compare with fine meshed finite element results

3.3.3 Problems during stress recovery procedure

The problems, found during the procedure of stress recovery in the triangular resin pocket, need to be addressed in future work. The first problem is that of the smooth of the shear stress τ_{13} see Figure 3.14. At the beginning, the recovered shear stresses oscillate in the thickness direction as seen in Figure 3.14. To eliminate the fluctuations of the shear stress, the average element stress could be used instead of the nodal stress to recover the interlaminar stress during the recovery process. Secondly, the stress of the concerned point could be recovered through different surfaces. For example, the stress of point a in Figure 3.9 could be recovered from interface ab or from interface ac, this would also hold for other points of interest. The recovered stresses of points of interested are shown in Figures 3.15, 3.16 and 3.17.

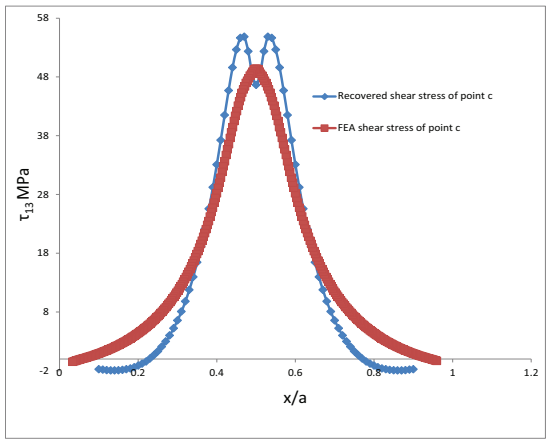

Figure 3.13: The recovery shear interlaminar stress τ_{13} of point c compare with fine meshed finite element results

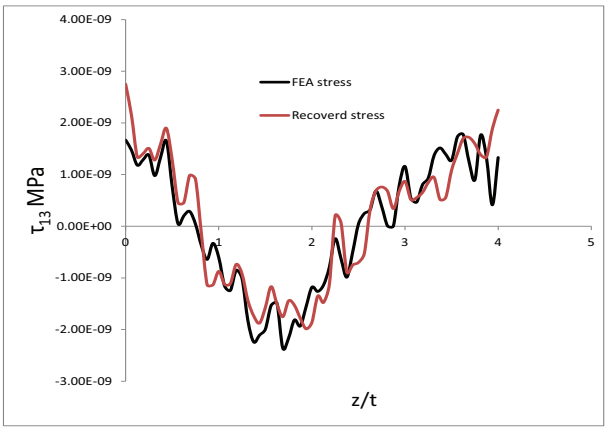

Figure 3.14: The recovery interlaminar stress in the thickness direction of 0/90 interface of a $[0/90]_s$ model

As can be seen from Figures 3.15, 3.16 and 3.17 the stresses recovered from different interfaces show considerable variation. The maximum difference can be around 2 or 3 times that of another stress value. The reason that the stresses are different at the cross point locations of two cross-lines is because of the stress singularity of these points, that is: if the stress of point A are recovered by different paths, such as AC, AD, AE and AF, as shown in Figure 3.18 the recovered stress will be varied. The singularity of the stress, see Figure 3.18 at a specific cross point makes a way to get accurate stresses at that point impossible. There are two possible ways to deal with the stress singularity of the cross point: one is to make the resin pocket boundary smoothly connected, to make the curve fillet. The other is to recover the stresses at the horizontal interface to make sure the precision of the recovered stresses is the same. Considering the reality of the model, it is impossible to avoid the singularity point. The recovered stresses for determining the critical location of the AP-PLY composite laminate in this thesis were recovered from related horizontal interfaces.

There is a further problem when recovering the stress of a non-horizontal interface and

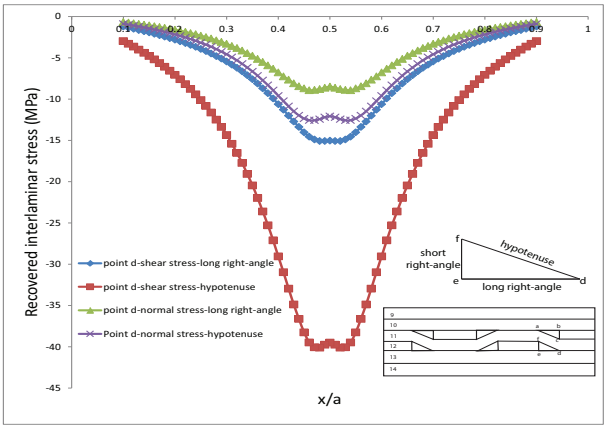

Figure 3.15: The recovery interlaminar stress of point d from different interfaces

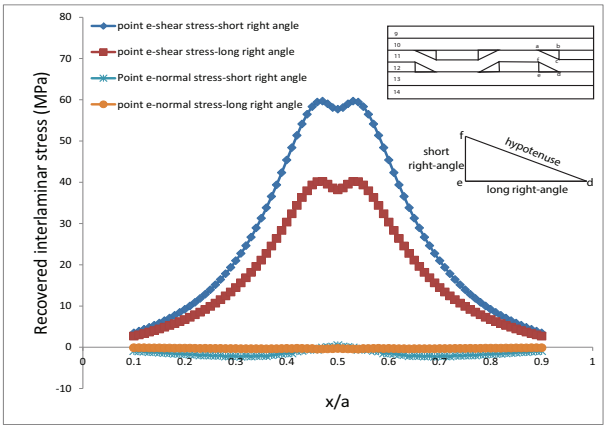

Figure 3.16: The recovery interlaminar stress of point e from different interfaces

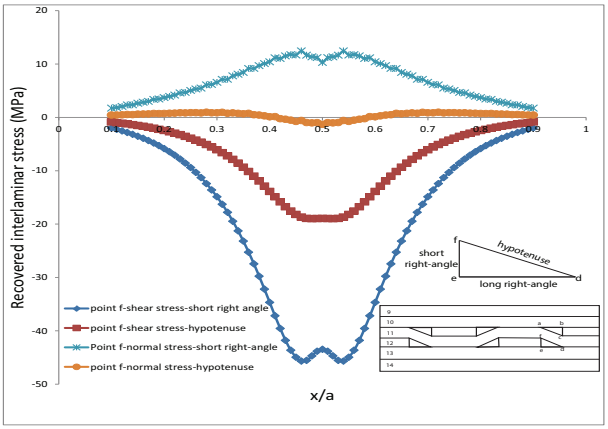

Figure 3.17: The recovery interlaminar stress of point f from different interfaces

that is about the sign of the recovered stresses. Actually, this problem can be related to the second problem. When recovering the stresses of a point of interest from the horizontal surfaces, there are still two possible paths that the stress can be recovered from, the left interface that the point of interest belongs to or the right interface the

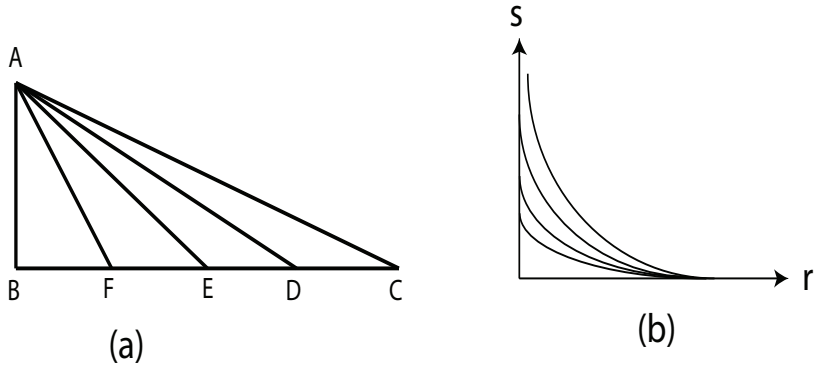

Figure 3.18: (a) different path of recover the stress of point interest; (b) stress singularity of the interest point

point belongs to. A very simple model was made to test the sign of the recovered stresses from left and right side of the point of interest. The results showed that the recovered stresses were exactly the same from both sides but that they had opposite signs. This can be explained based on the equilibrium requirement. The simple way to define the right signs of the recovered stress is to define the positive shear stress in advance and only take the value of the recovered stress.

3.4 Identification of critical location

The resin pockets that were close to the mid-point where the loading was applied were the probable crack initiation locations through the coarse meshed finite element results. The recovered stresses of the two resin pockets are shown in Figures 3.19, 3.20, 3.21 and 3.22.

Many different criteria can be used to predict the critical location of a model where a crack will begin. In this thesis, the dominant failure mode of the model subjected to impact load was mode II which means the interlaminar shear stresses were the dominant failure stress. The maximum failure stresses criterion was chosen to predict the crack initiation location. The maximum normal stress of the top resin pocket, -19MPa, was located at point b, as shown in Figure 3.19. The maximum normal stress of the bottom resin pocket was point d, as shown in Figure 3.21, the value of interlaminar normal stress is -18MPa, which was close to the maximum normal stress in the top resin pocket. From Figure 3.20 it can be seen that the maximum interlaminar shear stress of the top resin pocket, of which the value is 95MPa, is located at point a. The maximum shear stress of the bottom resin pocket was -110MPa, located at point f, as can be seen from Figure 3.22. The normal failure stress of resin used in our model was around 45MPa to 60MPa, and the shear failure stress was 125MPa. Since Mode II was the main failure mode of the model, points a and f, where shear stresses are close to the failure stress of the resin, were the critical location in the one direction woven AP-PLY structure used in our study.

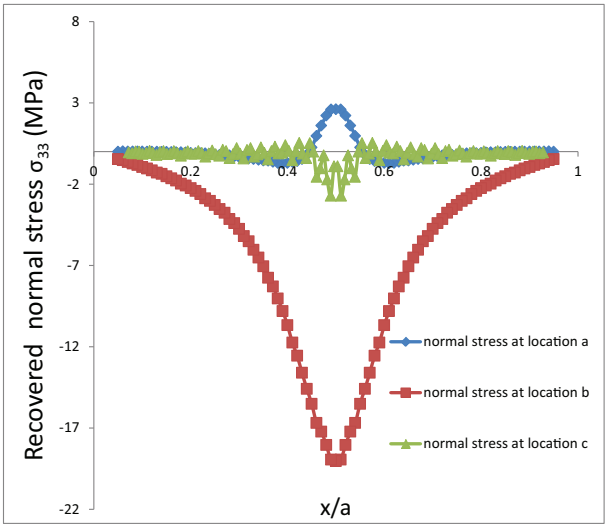

Figure 3.19: The recovery interlaminar normal stress of top resin pocket

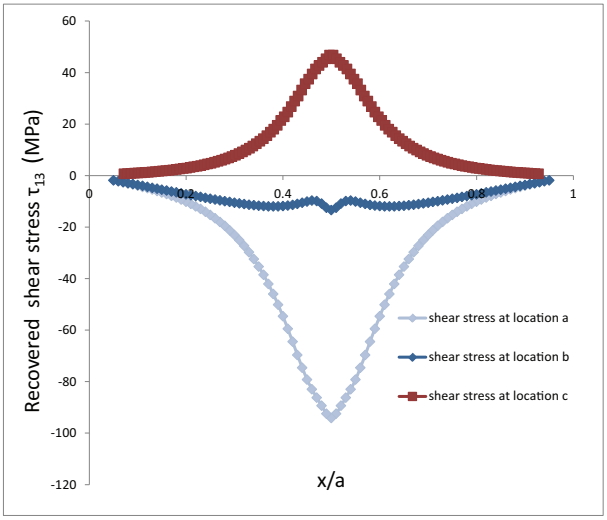

Figure 3.20: The recovery interlaminar shear stress of top resin pocket

3.5 Conclusions

The simplest way to determine the delamination onset of an AP-PLY composite laminate under impact load is to find the critical location where the interlaminar shear stress is at maximum in one of the resin pockets based on the maximum stress criterion. The available and efficient way to obtain accurate interlaminar stresses in AP-PLY laminate is to combine the convenience of a relatively coarse finite element method with interlaminar stress recovery technology. The combination of those two together assures an efficient analysis and reasonably accurate determination of the interlaminar stress. Comparisons of the obtained interlaminar stresses with the analytical results in a conventional composite laminate and the fine meshed finite element results of an AP-PLY composite laminate showed that the stress recovery technology could be applied to conventional laminate

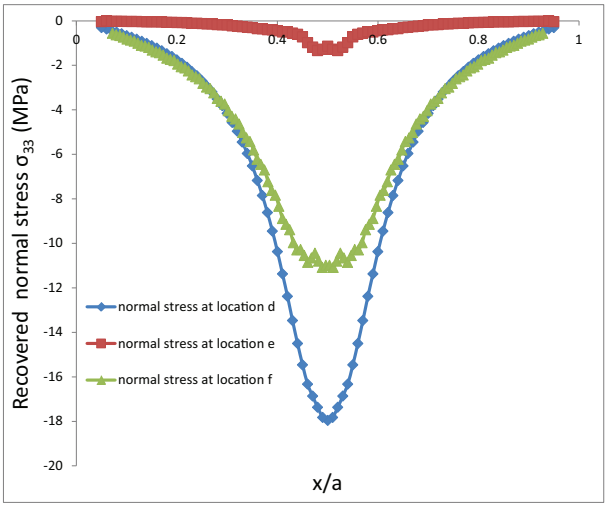

Figure 3.21: The recovery interlaminar normal stress of bottom resin pocket

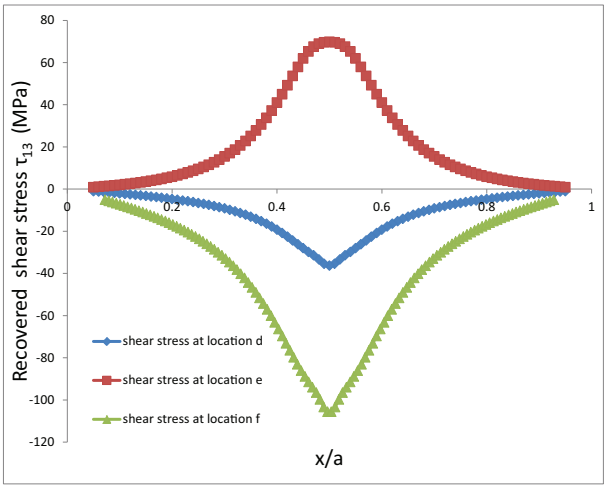

Figure 3.22: The recovery interlaminar shear stress of bottom resin pocket

and AP-PLY composite laminate. The problems of recovered stress for the triangular resin pocket were addressed, and the critical locations of an AP-PLY model woven in one direction were determined. Delamination onset is the beginning of damage in a composite laminate and this has been discussed in this chapter, the evolution of damage which is more important will be addressed in chapter 4.

Chapter 4

Use of cohesive elements to predict onset of delamination and growth for different AP-PLY patterns

4.1 Introduction

Impact damage in laminated composites is receiving considerable attention because the compression strength of a laminated composite can decrease significantly after impact even when the damage is barely visible on the surface of the laminate. Impact damage can be any combination of fibre breakage, matrix cracks and delaminations along the laminar interfaces. Over the last half century, many approaches have been proposed to analysis the effect of impact on the mechanical properties of composite structures [Sun and Chattopadhyay, 1975; Abrate, 1991; Olsson, 2003; Esrail and Kassapoglou, 2014a]. The impact damage found in composite laminates is complicated as shown in Figure 4.1, however, the impact damage in AP-PLY composite laminates is more complicated than that of conventional laminates and is even harder to predict due to the complicated structures of AP-PLY composite laminates. This complex problem of studying impact damage in AP-PLY composite laminates lends itself to the use of the finite element method (FEM). Thus FEM was chosen to simulate impact damage in AP-PLY composite laminates.

In the patterns of impact damage, delamination is one of the most common and severe form of damage that can occur to structures built of laminates due to the low out-of-plane strength of the matrix between plies. Such damage can lead to catastrophic failure of the whole structure due to a lack of reinforcement in the thickness direction of the composite laminate. The AP-PLY composite laminate has been shown to improve damage tolerance [Nagelsmit et al. 2011] but the detailed mechanism behind this improved tolerance is still not well understood. Part of the AP-PLY composite laminate structure is similar to that of a conventional laminate, which means that delamination is still a concern even for

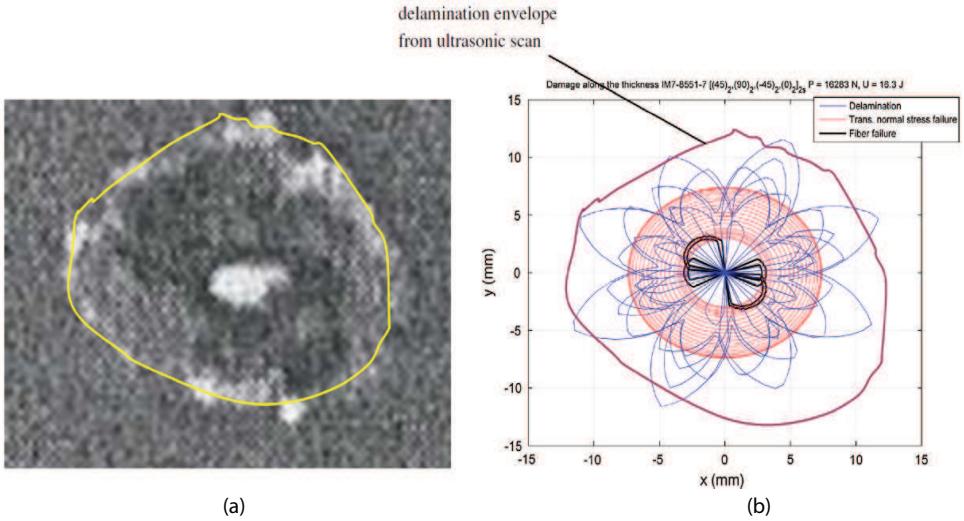

Figure 4.1: (a) Ultrosonic scan of impact damage [Abrate, 1991] (b) Predicted damage pattern [Esrail and Kassapoglou, 2014a]

AP-PLY composite laminates. For a conventional laminate, the delamination propagates at the interfaces of different layers and sometimes may propagate through the thickness direction. How crack propagation occurs for different AP-PLY patterns is unknown and will be discussed in this chapter.

It is recognized that delamination is critical for conventional composite laminates, and three general types can be found, as shown in Figure 4.2, which need to be addressed with respect to how the different crack lengths and crack locations influence the properties of the whole structure.

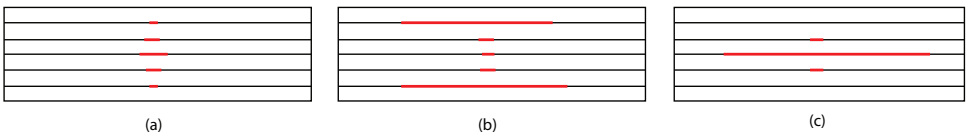

Figure 4.2: (a) smaller cracks (b) long crack on the top and bottom (c) long crack in the middle

Type a: there are some smaller cracks in the structure of the composite laminate, but these cracks do not have a big influence on the bending stiffness of the whole structure and the structure can still be loaded with significant loads. For this type of delamination, it is necessary to know how these cracks will propagate and when the structure will fail.

Type b: there are several cracks in the composite laminate and some of the cracks are long enough to influence the structure which greatly reduces the stiffness of the structure. A crack on the top or bottom will not influence the compression after impact properties a lot, however, we still need to determine which crack is the most critical one that will propagate and lead the whole structure to failure.

Type c: is the type of delamination where some of the cracks are long enough to influence

the stiffness of the structure, if the crack is in the middle, it will decrease the stiffness of the whole structure and the whole structure might fail.

In an AP-PLY composite laminate, the crack formation is more complicated than the types described above for conventional laminates. The specialty of the structure of an AP-PLY is that it has the woven areas, which are delineated by woven plies (0 ply in Figure 4.3) and the thickness of the straight plies (90 ply in Figure 4.3) in the other direction that are used to fill the intervals left by the woven layers, as shown in Figure 4.3. In the research presented here, an attempt was made to determine which combinations of ply direction and woven pattern are the best under certain requirements. The following question was proposed: How do the interwoven layers used in the various AP-PLY patterns influence the properties of an AP-PLY laminated structure?

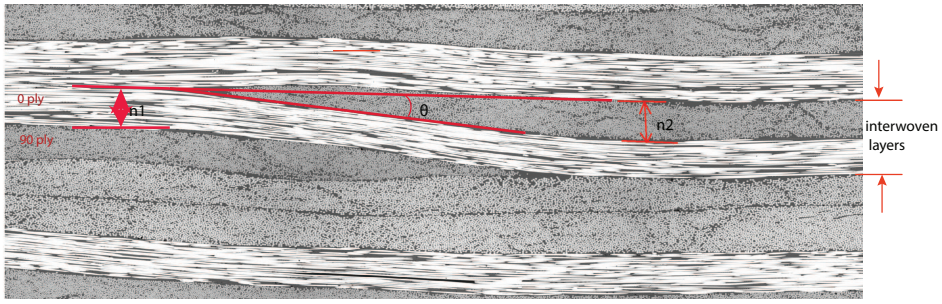

Figure 4.3: Parameters of woven plies

The study of the delamination initiation and propagation of an existing delamination are the two main aspects of delamination analysis. Understanding the initiation of delamination requires a total understanding of the interlaminar stress and stress-based criteria. In chapter 3, delamination onset was determined by determining the interlaminar stress of the interest area and the maximum stress criterion. It has been found that the resin areas of an AP-PLY composite laminate are the most probable delamination initiation locations. In the resin area, the critical location was found (see section 3.4) and was taken as the place where the first crack will appear. This was done by creating a detailed finite element model with stress recovery technology to recover the interlaminar stress which is used for the stress-based criteria. It is important and necessary to understand the initiation of crack location and initiation load, however, the more important thing is to know whether the crack is going to propagate or not, and if it propagates, the speed of the propagation and whether the propagation will stop or lead to catastrophic failure of the whole composite laminate structure. In addition, when multiple delaminations are present, it is important to determine any interaction between them which may slow down or speed up the growth of any given delamination.

The analysis of crack propagation can be achieved using fracture mechanics based methods, CZM and the extended finite element method (XFEM) in finite element methods. Based on linear elastic fracture mechanics, crack propagation can be related to fracture mechanics properties such as strain energy release rate (SERR) or stress intensity factor (SIF). In the commercial finite element software ABAQUS which has been selected for use in this program, the SERR can be obtained using the J-integral method, the VCCT, or

the compliance method. The compliance method is convenient to use for tests, however, the drawback of both the compliance method and J-integral method is that each model can only obtain the energy release rate for a specified crack length, which means as the delamination propagates, new models need to be created and analyzed. The VCCT is based on the assumption that the energy needed to extend a crack by some length will be equal to the energy required to close the crack by the same length to obtain the SERR that will vanish with zero increased crack length. The crack will propagate when the SERR at the crack tip exceeds the critical energy release rate of the material provided by the user in ABAQUS. The drawback of the VCCT is it requires the existence of a finite length crack-like flaw before the simulation can be started.

Compared to the VCCT, the CZM does not need the presence of a pre-crack which means it can be used to predict the onset of delamination and growth of delamination. The CZM can be traced back to the research work of Dugdale [1960] and Barenblatt [1962] for the stress singularity problem. In the CZM crack growth is taken to be a gradual procedure in which two adjacent virtual surfaces with zero thickness in 3D model separate and the crack growth is taken as the failure procedure of a very thin thickness of cohesive element in 2D model. In this chapter, a 2D cohesive element model of a simple AP-PLY composite laminate will be used to analyze delamination initiation and delamination growth.

This chapter is organized as follows. The choice of parameters for a cohesive zone model and 2D AP-PLY model are described in section 4.2. The influence of parameters that characterize the interwoven layers on the structure performance under out-of-plane load is examined in section 4.3. The initiation loads and delamination growth curves of different AP-PLY patterns are discussed in section 4.4. The conclusions are presented in section 4.5.

4.2 Finite element model description

4.2.1 Choice of parameters for cohesive zone model

The failure process of the cohesive element was taken to be the degradation of the material properties assigned to the cohesive elements and governed by the softening constitutive equation. The softening equation, named as traction-separation law, is controlling the creation of new crack surfaces during the failure process of the cohesive elements. The typical four types of traction-separation law are bilinear, exponential, trapezoidal and linear-parabolic as shown in Figure 4.4. Alfano [2006] discusses the influence of those four laws on the application of cohesive zone models and two conclusions are given: (1) the influence of the shape of the traction-separation law is negligible on the solution of an adequate meshed finite element model; (2) the exponential traction separation law gives the best approximation for the finite element model while the bilinear traction separation law has a better balance in terms of computational cost and accuracy of the approximation. Based on the conclusions above, the bilinear traction-separation law was

implemented in ABAQUS in the simulation of AP-PLY composite laminate model for the work reported here.

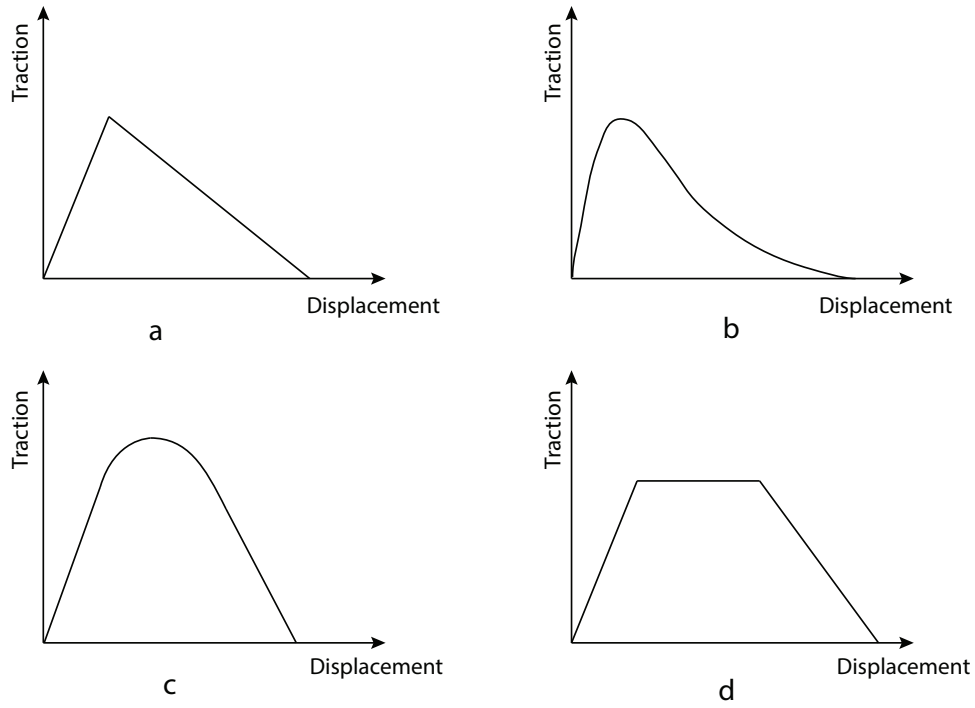

Figure 4.4: Four different shapes of traction separation law (a) Bilinear (b) Exponential (c) Linear-parabolic (d) Trapezoidal

The traction-separation law is related to the displacement of two separating nodes in the interfaces and their internal stresses. The internal stress will increase with the increasing displacement at the initiation of the crack, the slope of the internal stress versus the displacement is the penalty stiffness of the cohesive material, which will ensure the connection of the interface before delamination onset is stiff, and before the stress of the elements on the interfaces achieved the maximum stress, the penalty stiffness is always positive for mode I and can be negative for mode II and mode III. Crack initiation will take place when the traction of the cohesive elements equals to the limit strength of material properties of the composite laminates, which is called interfacial strength of the interfaces. Once the summit point of traction-separation law is reached, the softening of the cohesive element will begin and evolution of the crack will take place. At the softening stage, the penalty stiffness will be negative and the traction will decrease. Once the traction has decreased to zero, propagation of a crack will occur. The evolution of a crack can be either energy-based or displacement based. Taking the bilinear traction-separation law as an example, as shown in Figure 4.5, the shape of the law can be defined by the penalty stiffness K, the interfacial strength t_n^0, t_s^0, t_t^0 and the displacement δ_n^0, δ_s^0, δ_t^0 or the critical energy release rate G_c of that point which is equal to the area under the bilinear curve. The critical energy release rate sometimes referred to as fracture toughness which can be obtained through testing. It should be noted that the use of cohesive elements to predict onset of delamination may be sensitive to the failure stress value used in the traction separation law. Separate runs for simple out-of-plane tension of a uni-directional

laminate showed that a 30% change of failure stress in the bilinear traction separation law had 23.4% change on the failure strength. Therefore, approximating the trend as linear, a percentage change in failure stress results in 0.78 times that change as the change in strength. This 22% change can be considered indicative of the sensitivity of cohesive element predictions for onset of delamination.

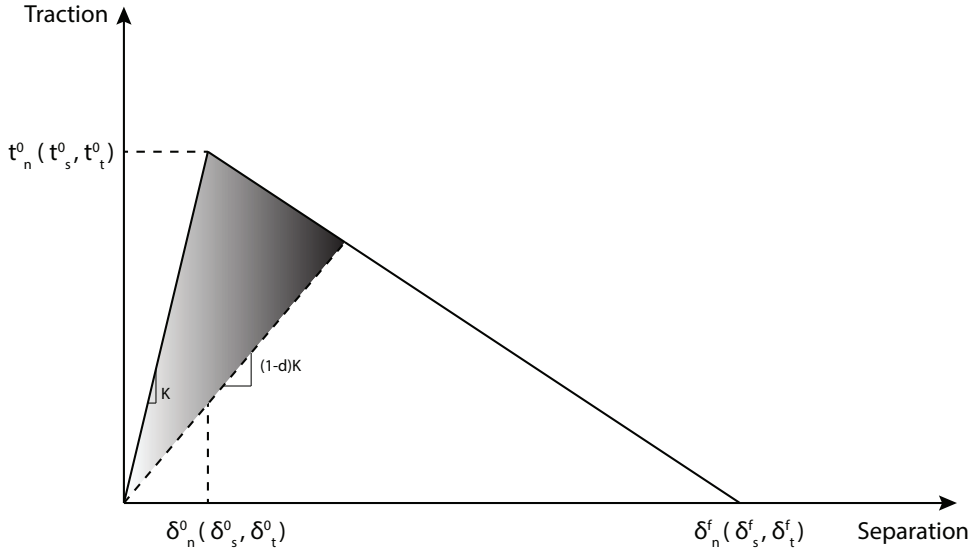

Figure 4.5: Bilinear traction separation law

In the research work of simulating the damage of composite laminates using CZM, the definition of the traction-separation law is the key point. Since there is no physical mechanism for the traction-separation law and the function of cohesive elements is to simulate the fracture, the contribution of the cohesive element to the structure's compliance before crack propagation should be small enough and the element size should be less than the length of the cohesive zone. In the parameters that shape the curve of traction-separation law, the interfacial strength and the critical energy release rate are the material properties while the penalty stiffness of the cohesive element is used for numerical reason and can not be determined from a test. To reduce the cohesive element's influence on the whole structure's compliance, the stiffness of the cohesive element should be large enough, however, the large stiffness of the cohesive layers may cause numerical problems, such as oscillation of the traction and difficulty with convergence. Therefore the stiffness of the cohesive layers should be chosen with care. Camanho et al. [2003] use the 8-node decohesive element with a penalty stiffness $K = 10^6 N/mm^3$ for a 24-ply unidirectional AS4/PEEK carbon fiber reinforced composite and obtain accurate delamination growth results. Turon et al. [2007a] give an expression of penalty stiffness such that the cohesive elements will not effect the compliance of composites when

$$\mathrm{K} = \frac{\alpha \mathrm{E}_3}{t} \tag{4.1}$$

where α is a coefficient much larger than 1 ($\alpha \gg 1$) and the stiffness change of the composite is less than 2% when α is greater than 50. E_3 is the Young's modulus of the material in the thickness direction. t is the thickness of an adjacent sub-laminate. From

Equation (4.1), the penalty stiffness $K = 2.7 \times 10^6 N/mm^3$ was obtained based on the geometry and the material properties of the AP-PLY composite laminates discussed in this thesis, however, for the AP-PLY cohesive zone model used in the research discussed in this thesis, a penalty stiffness of $K = 6 \times 10^7 N/mm^3$ was chosen to get more accurate results because the large stiffness can reduce the cohesive element's influence on the whole structure and a little larger will not increase the convergence difficulty a lot.

The separation of the surfaces or the failure of the cohesive element in a composite laminate can be represented by a scalar stiffness degradation variable parameter d, as shown in Figure 4.5. The initial value of this scalar is 0. When damage starts, scalar d will monotonically evolve from 0 to 1 with further loading. A cohesive element has totally failed when $d = 1$.

The nonlinear process of crack propagation in composite laminates and the softening laws of the decohesion element constitutive equation make the convergence of the cohesive zone model difficult. Camanho et al. [2003] suggest that the Newton-Raphson method and a "line-search" algorithm can help to get convergence results. Wang et al. [2011] discuss the convergence issues in ABAQUS when doing damage and fracture analysis. Using viscous regulation, or automatic stabilization or nondefault solution controls can help to avoid convergence difficulties. Through parameter research, Wang et al. [2011] have found that a smaller viscous parameter is better than a larger one. In ABAQUS automatic stabilization is offered to help convergence because of local instabilities. In the option of solution controls in ABAQUS, the option "discontinuous" can be chosen or the smaller time incrementation for the steps can be changed. According to Wang et al.'s [2001] parameter research, the viscous parameter of the cohesive element is 0.0005, the damping factor is 0.004. It should be noted that the damping factor and viscous parameters used result less than 1% of the energy being taken up by these effects so their influence on the results should be negligible. The automated solver setting is used, for which the next step is propagating from the previous step. The maximum number of increments is 10000, the initial increment is 0.001, the minimum increment size is 0.000001 and the maximum increment size is 0.01. These related non-default solution controls are implemented for the simulation of an AP-PLY model with cohesive elements in this thesis.

4.2.2 Description of 2D AP-PLY finite element model

As discussed in chapter 3, it is known that the deformation of a 24 layer, $79.65mm \times 79.65mm \times 4.32mm$ composite laminate is linear until the structure fails. The geometry of the AP-PLY composite laminate discussed in this chapter and used to simulate the delamination induced by impact was the same as that of the structure of AP-PLY composite laminate discussed in chapter 3, see Figure 3.2. Since the aim of the research reported here was to find out the mechanism behind the improvement in damage tolerance with respect to AP-PLY composite laminate, the research was focused on how the patterns of the AP-PLY composite laminate influence the delamination initiation and delamination growth. There are plenty of possible patterns for a specific thickness composite laminate.

To make the research feasible and to check the basic trend governed by the pattern of an AP-PLY composite laminate, a simple AP-PLY pattern where the plies were only woven in one direction was chosen.

The impact load in finite element model is treated as a point load or as distributed load in a very small area see Figure 4.6. The cohesive elements are embedded along the laminar interfaces that are close to the resin pocket. For a model where the length and the width are not on the same scale compared to the thickness, it is necessary to make the size of the elements in length and width direction not exceed the size in thickness direction by a lot to get accurate results. Therefore, quantitative 3D elements and 3D cohesive elements are unavoidable in this type of 3D model. The deformation of a cohesive element is nonlinear due to the nature of the traction-separation law. The quantitative elements and the nonlinear behavior of the cohesive elements make simulation expensive. Since the AP-PLY composite laminate was only woven in one direction, the 3D model can be simplified into a 2D model under plane stress if the applied out-of-plane load was changed into line load with the assumption that the delamination would be though the width direction. The transformation process for the AP-PLY model is shown in Figure 4.6. The characteristics of the AP-PLY pattern were kept when the out-of-plane load was changed from point load to line load. The edge effect, which will not be discussed in this chapter, was lost after the 3D line load model was transferred into a 2D plane stress model.

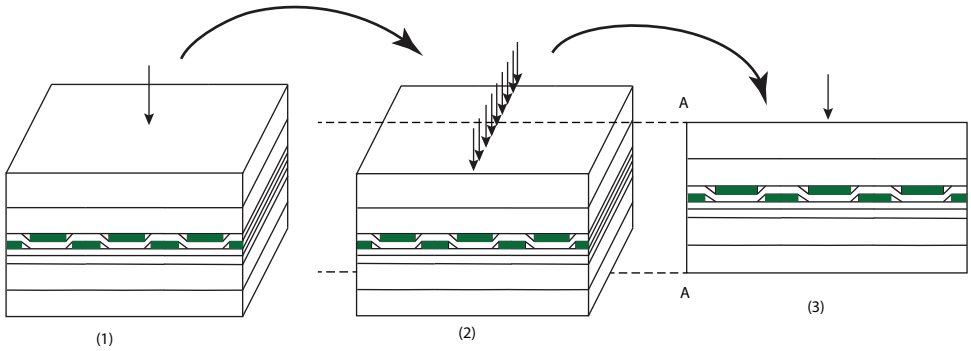

Figure 4.6: Transformation of the model (1) 3D point load (2) 3D line load (3) 2D point load

The 2D AP-PLY composite laminate was taken to be a simple supported 3 point bending beam model. The interlaminar shear stresses were the main driven forces that accelerate the formation of delaminations. From previous researcher' work [Creemers, 2009], it is known that the maximum shear stress in the thickness direction of a symmetry composite laminate is in the middle, as shown in Figure 4.7. For a symmetric 24 layers AP-PLY composite laminate, there are many different combinations of AP-PLY patterns and it is not necessary to put the woven plies everywhere in the thickness direction. To capture the woven pattern's influence and simplify the model, the 4 layers in the middle were taken to be the target for the research discussed here. Above and below these layers, conventional elements were used. The simple AP-PLY composite laminate was composed as follows: 5 layers of 0° plies and 5 layers of 90° plies, then the middle 4 layers, and then 5 layers of 90° plies and 5 layers of 0° plies. For an AP-PLY composite laminate with

2 interwoven layers, it is impossible to make a completely symmetric layup everywhere. The assumptions made for the woven plies were the same as those given in chapter 3, section 3.2.1.

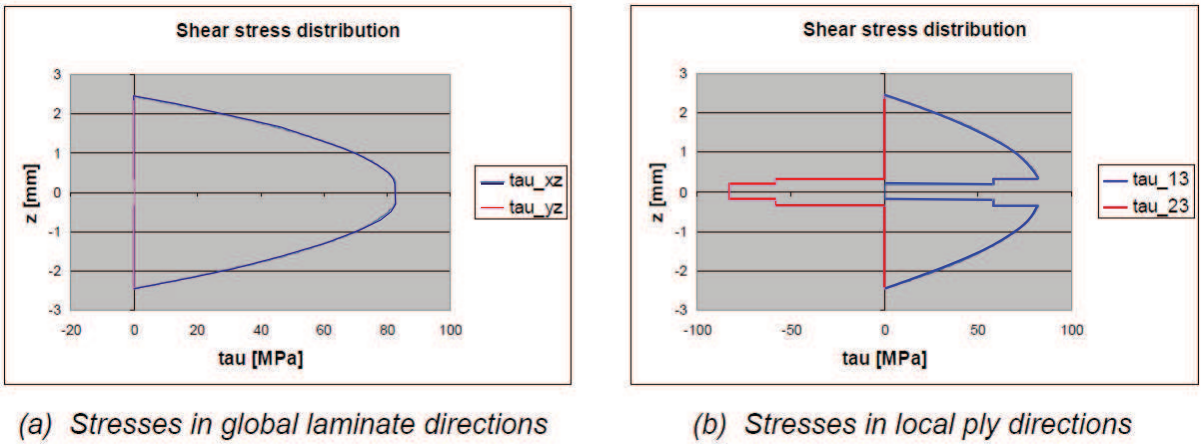

(a) Stresses in global laminate directions (b) Stresses in local ply directions

Figure 4.7: Shear stress distribution with lay-up $[0_{16}/45/90/90/90/45/0_{16}]$ in [Creemers, 2009]

From the cross-section of an AP-PLY, shown in Figure 4.3, we assumed all of the fibers were straight and the space between woven plies was filled with resin. Based on this assumption, an idealized 2D model of an AP-PLY composite laminate was created as shown in Figure 4.8. An out-of-plane load was applied in the middle of the structure, right end in Figure 3, a half finite element model, to simulate impact. The delaminations were expected to be around the resin, the black lines in Figure 4.8 are used to represent the cohesive elements that were embedded in the structure. The load magnitude at which a crack initiates and the rate of crack propagation were monitored during the simulation. The cohesive layers were divided into 3 groups from left to right and denoted A, B and C. Each group had 3 layers from top to bottom denoted A1, A2 and A3 in group A and similarly for group B, B1, B2 and B3, and group C, C1, C2 and C3. It should be noted that the cohesive zone interfaces are only along the horizontal segments A1, A2, A3, B1, etc. in Figure 4.8. Runs with the cohesive zone extending horizontally across the resin pockets showed that the initiation and growth characteristics were the same. To reduce computation time, the scheme with the separate horizontal segments of cohesive zone interfaces was selected.

The material properties of the AP-PLY composite laminates were the same as those described for AS4/8552 in chapter 3, section 3.2.1. The thickness of the cohesive layer was $0.001mm$ in a model of $4.32mm$ thickness which will not affect the stiffness of the whole structure, and the failure stress of cohesive layers was $66.2MPa$. The length of each cohesive element was $0.005mm$. This is smaller than the recommended size of 0.74 mm (see Turon et al. [2007]) and should give enough accuracy in the results. Damage evolution was controlled by the energy of the interface, i.e. fracture toughness, the value of mode II fracture energy was $1.58KJ/m^2$. Since the AP-PLY composite laminate under out-of-plane line load was represented as a pure 2D 3 point bending beam. In 3 point bending, most of the failures are shear stress driven, therefore the main fracture mode

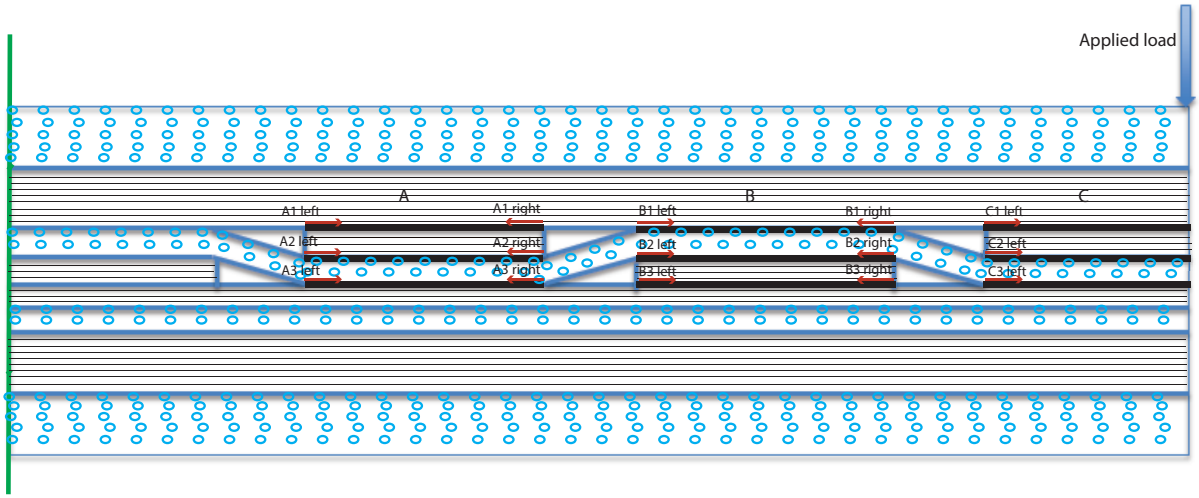

Figure 4.8: A 2D AP-PLY model with cohesive layers in the structure (arrows indicate the crack propagation direction)

was mode II and mode I could be ignored, which made it unnecessary to define a mixed mode ratio. Therefore mode-independent was chosen for the mixed mode behavior of damage evolution in ABAQUS. The mesh that close to the resin area is shown in Figure 3.10 (c) in Chapter 3.3.

4.3 Parameters examined and their effect on performance

There are many different patterns that might be used to compose a 24 layers AP-PLY composite laminate with 20 layers conventional and only 4 layers designed using an AP-PLY pattern. It is impossible to model all of the potential patterns using finite element model, therefore only representative patterns were studied and are discussed in this thesis. The number of woven plies, n_1, the number of straight plies to fill the gap that is left by the woven plies, n_2, and the angle θ in the woven area are the parameters of an AP-PLY pattern which can be seen from Figure 4.3 in section 4.1. The ply orientation of the plies in the woven area follows that of a lay up in conventional composite laminates and the locations of the woven plies in the thickness direction must be known. The layup of the interwoven layers and the locations of the interwoven layers are the other two parameters that need to be checked when doing parameter research on the patterns of AP-PLY composite laminates. The bandwidth of the woven plies and the skipped length left by the woven plies fall outside the range of the research discussed in this thesis.

The following notation is used throughout the thesis for the AP-PLY configurations with the patterns discussed in this thesis

$$[(\theta_1^{n_1 w}/\theta_2^{n_2 f})/\theta_3/\theta_4]_{ns}$$

where the round brackets denote the layers that are interwoven, n_1w denotes the number of woven plies, and n_2f denotes the number of straight plies that fill the gap left by the woven plies. In the previous case, the θ_1 and θ_2 are interwoven layers, θ_3 and θ_4 are conventional straight layers as in a conventional composite laminate. The description of the patterns starts from the left of the unit as shown in Figure 3.2 and the whole model will specify how many units were included. As shown in Figure 4.9, there are 3 units in the AP-PLY composite laminate model with a layup of $[0_5/90_5/(0^{1w}/90^{1f})/90/0/90_5/0_5]$ where 1 from 1w and 1f could be left out.

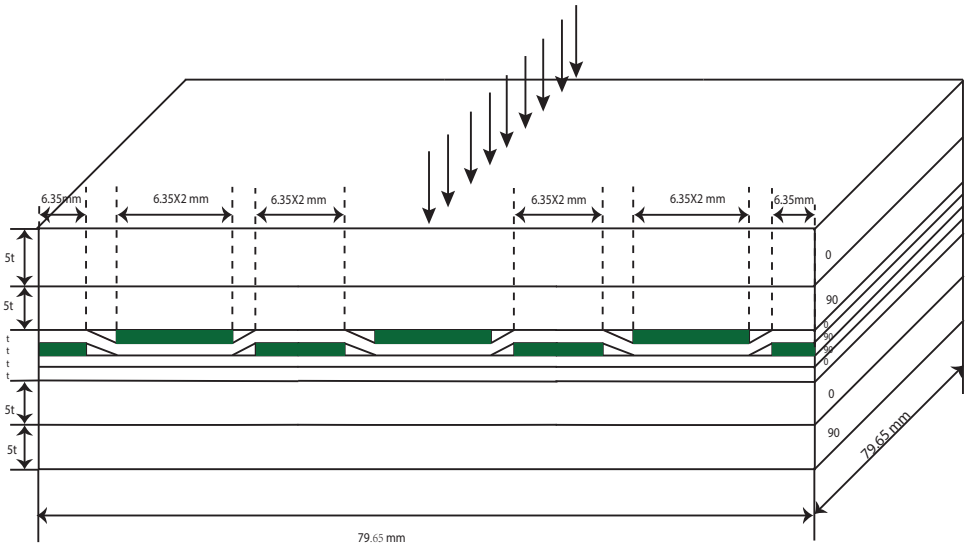

Figure 4.9: A model with 3 units, $[0_5/90_5/(0^w/90^f)/90/0/90_5/0_5]$

4.3.1 Angle of interweaving ply-angle of resin

The parameter angle, denoted θ in Figure 4.3 and the angle of the woven ply depend on the material properties of the plies and on the thickness of the plies used to fill the space left by the woven plies in an AP-PLY composite laminate. To isolate the effect of the different parameters, the assumption was made that the angle of the woven plies will remain constant when there is a change in the thickness of the straight plies which are used to fill the gap left by the woven plies. As described in section 3.2.1, the angle of interwoven $0^w/90^f$ plies in the model of AP-PLY composite laminate for this research was 7 degrees based on a close-up of a single undulation in an AS4/8552 AP-PLY composite laminate and this angle could be varied from 5 degrees to 25 degrees. It is hard to do a statistical analysis on a probability distribution of an angle, thus for the work reported in this thesis, the angle for the interwoven of θ_1^w/θ_2^f case was chosen to be 17.4 degrees. The woven layer had a thickness of $0.18mm$, the length of the woven area was $0.575mm$, which was also the length of the triangular resin area. Three angle values were chosen for the angle parameter research: 5, 17.4 and 25 degrees.

4.3.2 Woven ply thickness

The woven ply thickness variable requires two parameters to be used to determine the interwoven pattern of an AP-PLY composite laminate: the number of woven plies n_1 and the number of the straight plies n_2 needed to fill the room left by the woven plies. An AP-PLY composite laminate could be designed as totally interwoven laminates or partially interwoven laminates. The totally interwoven laminate is a laminate without any conventional layers. The AP-PLY composite laminate discussed in detail in this thesis is partially interwoven laminate. The top 10 layers and the bottom 10 layers are conventional laminate layers. Only the middle 4 layers could be designed as interwoven layers. There is a relationship for n_1 and n_2: $n_1 + n_2 \leq n_{tot}$, where n_{tot} is the number of layers that could be designed. Since in the research reported here, there were only four layers in the middle that could be designed for the AP-PLY model, the parameter of n_1 and n_2 could be chosen from any combination following:

$n_1 = 1$ and $n_2 = 1$, as shown in Figure 4.10.a

$n_1 = 1$ and $n_2 = 2$, as shown in Figure 4.10.b

$n_1 = 2$ and $n_2 = 1$, as shown in Figure 4.10.c

$n_1 = 2$ and $n_2 = 2$, as shown in Figure 4.10.d

$n_1 = 3$ and $n_2 = 1$, as shown in Figure 4.10.e

$n_1 = 1$ and $n_2 = 3$, as shown in Figure 4.10.f

The sketch of the 4 designable layers that changing the thickness of the woven plies can be seen in Figure 4.10.

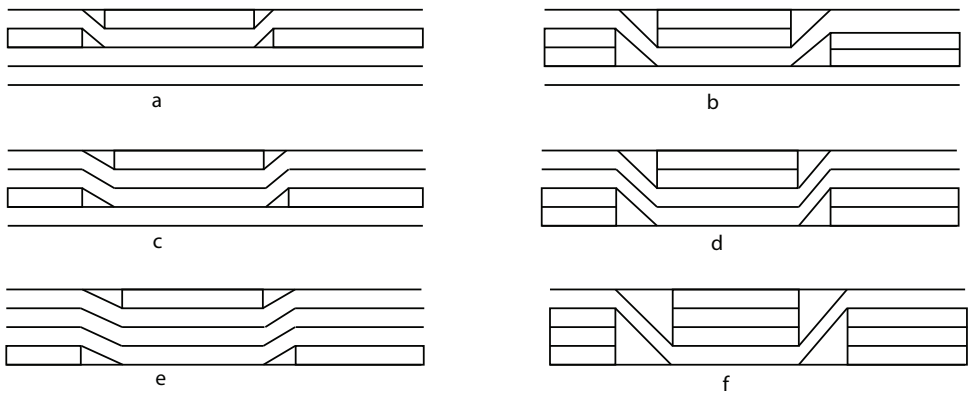

Figure 4.10: Patterns of the 4 layers in the middle of simple AP-PLY model

4.3.3 Layup

The parameter layup here is the same as the layup in the conventional laminate, with the addition of 4 layers in the middle that can be designed, thus one of the layups of the

models could be (using only multiples of 15 degrees as possible ply orientations):

$[0_5/90_5/(0^w/90^f)/90/0/90_5/0_5]$

$[0_5/90_5/(15^w/-15^f)/-15/15/90_5/0_5]$

$[0_5/90_5/(30^w/-30^f)/-30/30/90_5/0_5]$

$[0_5/90_5/(45^w/45^f)/45/45/90_5/0_5]$

$[0_5/90_5/(60^w/-60^f)/-60/60/90_5/0_5]$

$[0_5/90_5/(75^w/-75^f)/-75/75/90_5/0_5]$

4.3.4 Location of interwoven pattern in through the thickness direction

The last parameter of the model that presented in this chapter is the location of the interwoven plies in through the thickness direction. This parameter can also be expressed as the parameter layup. It is easy to check the influence of the interwoven plies in the thickness direction if the interwoven plies have moved up or down in the thickness direction. The exception to this is the parameter for the location of the interwoven plies in the thickness direction, which will vanish when $n_1 + n_2 = n_{tot}$ because there is no space left for the interwoven plies to change location in the thickness direction. Sketches of the changed location of the interwoven plies in the 4 middle layers of a simple AP-PLY model, following the sketches shown in Figure 4.10, are shown in Figure 4.11. The $a1$ and $a2$ sketches in Figure 4.11 are based on sketch a in Figure 4.10, and $b1$ and $c1$ are based on b and c, respectively. The location of the interface elements in Figures 4.10 and 4.11 is the same as in Figure 4.8. Note that A1 is the first layer of interface elements of the A group in Figure 4.8. It should not be confused with $a1$ which is a representative structure (see Figure 4.11).

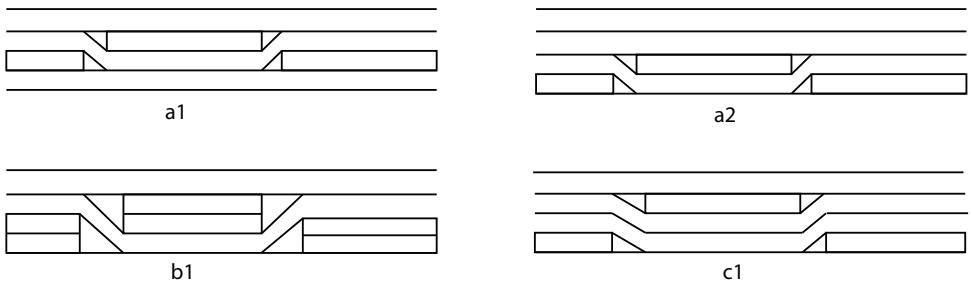

Figure 4.11: Location of the interwoven plies in the 4 middle layers of simple AP-PLY models

4.4 FE results

The different patterns of the AP-PLY composite laminates were simulated using ABAQUS, one of the models is shown in Figure 4.8. For a 2D cohesive element model, COH2D4 cohesive elements were used for the cohesive layers. The length of the cohesive element was $0.005mm$, and there were 19050 cohesive elements in one of the models. The element numbers differed slightly for different models while the size of the cohesive elements in the cohesive layers was always the same. The remaining elements used in the model were 2D continuum solid elements CPS4R, a type of quad element, and CPS3, a type of linear triangular element. The number of CPS4R elements in the finite element model was 612811 and 6127 for CPS3 elements. Normally, CPS3 element should be avoided because of accuracy problems, however, due to the sharp tip of the woven area in the structure of an AP-PLY finite element model, it is better to use some CPS3 elements than severely distorted CPS4R elements as these will cause the aspect ratio to be large possibly leading to an error or convergence problem. And the percentage of the CPS3 elements in this model was around 1% as a fraction of the total number of elements.

Due to the nonlinear behavior of the damage process of the cohesive elements in an AP-PLY model, the cost of computer time when modeling such a composite laminate is high compared to other types of simulations in ABAQUS. The minimum time required to model the above described AP-PLY composite laminate using ABAQUS was 35 hours with 16 processors on 1 node on cluster. The average time required to process one simulation model on cluster with 16 processors on 1 node was around 60 hours. It is hard to say how many hours might be required to finish one finite element model using multiple nodes on a cluster (the time for interchange data among nodes are unknown) or a personal computer. The amount of time will depend on the hardware of the computer, and on the model used.

4.4.1 Initiation load of delamination

The structure of the simple AP-PLY composite laminate studied for the research reported in this thesis had x axial symmetry and half of the AP-PLY was modeled as a 2D beam with cohesive elements in the finite element model, as shown in Figure 4.8. The cohesive elements in the model were divided into 3 groups, A, B and C from left to right in the model and each group had 3 layers of cohesive elements. For example, for A group the layers are A1, A2, A3 from top to bottom. Similarly for groups B and C. These should not be confused with a1, a2 etc. (Figure 4.11) which denote patterns. Thus there were 9 layers of cohesive elements in total with 15 different crack initiation locations for each half model. The results of the ABAQUS analysis which explain the influence of the woven angle in an AP-PLY on the initiation load of different cohesive locations are given in Tables 4.1, 4.2 and 4.3.

To determine the influence of the parameter of different woven angle in the models, the layup, $[0_5/90_5/(0^w/90^f)/90/0/90_5/0_5]$, used for the different AP-PLY composite models

Parameter name	Initiation load of cohesive element group A					
	A1 left	A1 right	A2 left	A2 right	A3 left	A3 right
angle=5	141N	196N	236N	186N	206N	221N
angle=17.4	126N	217N		219N	176N	201N
angle=25	116N	207N		196N	148N	157N

Table 4.1: Initiation loads for group A, different woven angles

Parameter name	Initiation load of cohesive element group B					
	B1 left	B1 right	B2 left	B2 right	B3 left	B3 right
angle=5	142N	136N	186N	166N	171N	191N
angle=17.4	124N	118N	219N	181N	191N	217N
angle=25	163N	151N	197N	145N	163N	184N

Table 4.2: Initiation loads for group B, different woven angles

was kept always the same.

From Table 4.1 it can be seen that, for the different woven angle AP-PLY composite laminate models, the location of A1 left, A3 left and A3 right have the biggest initiation load with a woven angle $\theta = 5$, and the location of A1 right and A2 right have the biggest initiation load when the woven angle $\theta = 17.4$. There is no crack at location of A2 left when $\theta = 17.4$ and $\theta = 25$. From Table 4.2 and 4.3 it can be seen that the locations of B2 left, B2 right, B3 left, B3 right, C2 left and C3 left have the biggest initiation load when $\theta = 17.4$ compared to $\theta = 5$ and $\theta = 25$, and B1 left and B1 right have the high initiation loads when the woven angle is 25 degree. From Table 4.3 it can be seen that there is no crack initiated from C1 left and that the cracks of the C1 cohesive layers of different woven angles are initiated from the middle of the C1 layers. The results indicated that the best choice of woven angle was $\theta = 17.4$, and the next best would be $\theta = 5$, thus for the research work on other parameters of the AP-PLY models discussed here, the woven angle was fixed as $\theta = 17.4$.

The results of initiation load are presented in Tables 4.4, 4.5 and 4.6 for the models of the combined different thicknesses of woven ply and straight filled ply. From Table 4.4 it can be seen that the AP-PLY composite laminate model, which had a woven pattern with one layer woven ply and one layer filled, straight ply, had the largest initiation load at the different locations of group A except for the location A3 left. The model with 2 layers of woven plies and 2 layers of straight, filled plies had the smallest initiation load when

Parameter name	Initiation load of cohesive element group C			
	C1 left	C2 left	C3 left	C1 middle
angle=5		156N	109N	291N
angle=17.4		176N	161N	277N
angle=25		145N	124N	242N

Table 4.3: Initiation loads for group C, different woven angles

Parameter	layup	Initiation load of cohesive element group A					
		A1 left	A1 right	A2 left	A2 right	A3 left	A3 right
$n_1 = 1$,$n_2 = 1$	$[(0^w/90^f)/90/0]$	126N	217N		219N	176N	201N
$n_1 = 1$,$n_2 = 2$	$[(0^w/90^{2f})/0]$	79N	121N	136N	139N	115N	139N
$n_1 = 1$,$n_2 = 3$	$[(0^w/90^{3f})]$	76N	116N	106N	136N	109N	139N
$n_1 = 2$,$n_2 = 1$	$[(0^{2w}/90^f)/90]$	116N	166N		166N	181N	176N
$n_1 = 3$,$n_2 = 1$	$[(0^{3w}/90^f)]$	116N	166N	211N	161N	181N	176N
$n_1 = 2$,$n_2 = 2$	$[(0^{2w}/90^{2f})]$	52N	82N	103N	91N	88N	97N

Table 4.4: Initiation load of group A, different thickness of filled straight plies and woven plies

Parameter	layup	Initiation load of cohesive element group B					
		B1 left	B1 right	B2 left	B2 right	B3 left	B3 right
$n_1 = 1$,$n_2 = 1$	$[(0^w/90^f)/90/0]$	124N	118N	219N	181N	191N	217N
$n_1 = 1$,$n_2 = 2$	$[(0^w/90^{2f})/0]$	142N	139N	145N	118N	115N	100N
$n_1 = 1$,$n_2 = 3$	$[(0^w/90^{3f})]$	139N	127N	133N	118N	112N	82N
$n_1 = 2$,$n_2 = 1$	$[(0^{2w}/90^f)/90]$	176N	176N	166N	166N	161N	136N
$n_1 = 3$,$n_2 = 1$	$[(0^{3w}/90^f)]$	181N	186N	161N	206N	166N	116N
$n_1 = 2$,$n_2 = 2$	$[(0^{2w}/90^{2f})]$	97N	85N	94N	100N	82N	52N

Table 4.5: Initiation load of group B, different thickness of filled straight plies and woven plies

Parameter	layup	Initiation load of cohesive element group C			
		C1 left	C2 left	C3 left	C middle
$n_1 = 1$,$n_2 = 1$	$[(0^w/90^f)/90/0]$		176N	161N	C1 277N
$n_1 = 1$,$n_2 = 2$	$[(0^w/90^{2f})/0]$	202N	124N	145N	
$n_1 = 1$,$n_2 = 3$	$[(0^w/90^{3f})]$	169N	178N	133N	
$n_1 = 2$,$n_2 = 1$	$[(0^{2w}/90^f)/90]$	266N	141N	171N	
$n_1 = 3$,$n_2 = 1$	$[(0^{3w}/90^f)]$	292N	141N	176N	
$n_1 = 2$,$n_2 = 2$	$[(0^{2w}/90^{2f})]$	160N	88N	97N	

Table 4.6: Initiation load of group C, different thickness of filled straight plies and woven plies

Parameter	layup	Initiation load of cohesive element group A					
		A1 left	A1 right	A2 left	A2 right	A3 left	A3 right
1layer top	$[(0^w/90^f)/90/0]$	126N	217N		219N	176N	201N
1layer middle	$[90/(0^w/90^f)/0]$	69N	89N	97N	97N	108N	101N
1layer bottom	$[90/0/(0^w/90^f)]$	67N	61N	53N	79N	72N	76N
2layer top	$[(0^{2w}/90^f)/90]$	116N	166N		166N	181N	176N
2layer bottom	$[90/(0^{2w}/90^f)]$	141N	161N	161N	171N	176N	166N
2t top	$[(0^w/90^{2f})/0]$	79N	121N	136N	139N	115N	139N
2t bottom	$[90/(0^w/90^{2f})]$	97N	118N	109N	148N	124N	142N

Table 4.7: Initiation loads in group A, for different woven locations in the thickness direction of AP-PLY

compared with the initiation load of other models with different thicknesses of woven ply and straight filled ply. The initiation load of the different locations of group A in two models, one in which the two had 2 layers of woven ply with 1 straight, filled ply and the other had 3 layers of woven ply with 1 layer of straight, filled ply, were almost equal and followed the biggest initiation load. The model with the pattern that had 3 layers of straight, filled plies had a larger initiation load than the model with the pattern that had 2 layers of straight, filled plies. From Table 4.5 it can be seen that for the locations of B2 left, B3 left and B3 right, the model with the one layer of woven ply and one layer of filled straight ply had the largest initiation load and the model with 3 layers of woven plies and 1 layer of straight filled ply had the largest initiation load at the rest of the locations in group B. The initiation loads in location group B of the pattern that with 2 layers of woven plies and 1 layer of filled straight plies was very close to the pattern with 3 layers of woven plies and 1 layer of straight ply. The initiation load for group C in Table 4.6 had the same tendencies as those found for group B.

From the data given in Tables 4.4, 4.5 and 4.6, the following conclusions can be drawn: (1) the fewer the number of straight, filled plies used in an AP-PLY laminate, the higher the initiation load of delamination; (2) if one model has the same number of straight filled plies, with different layers of woven plies, it is hard to determine which configuration of AP-PLY pattern has the biggest initiation load at different locations. In our models with one layer straight filled ply, the initiation loads of the model with the pattern of 3 layers woven plies were higher than that of the model with the pattern of 2 layers woven plies. And there are some locations which had the largest initiation load for 3 layer woven plies pattern while more than half of the biggest initiation load locations come from the 1 layer woven ply model.

The location of the interwoven layers in through the thickness direction of an AP-PLY is another factor that is going to influence the mechanical properties of AP-PLY composite laminates. The results of 3 different woven patterns at different locations in the thickness direction of AP-PLY composites are presented in Table 4.7, 4.8 and 4.9. The first three rows of results in Table 4.7, 4.8 and 4.9 are initiation loads of the AP-PLY model with the same woven pattern, i.e. 1 layer of woven ply and 1 of layer straight ply, at different

Parameter	layup	Initiation load of cohesive element group B					
		B1 left	B1 right	B2 left	B2 right	B3 left	B3 right
1layer top	$[(0^w/90^f)/90/0]$	124N	118N	219N	181N	191N	217N
1layer middle	$[90/(0^w/90^f)/0]$	92N	96N	104N	104N	84N	69N
1layer bottom	$[90/0/(0^w/90^f)]$	88N	98N	69N		66N	35N
2layer top	$[(0^{2w}/90^f)/90]$	176N	176N	166N	166N	161N	136N
2layer bottom	$[90/(0^{2w}/90^f)]$	147N	163N	115N		109N	58N
2t top	$[(0^w/90^{2f})/0]$	142N	139N	145N	118N	115N	100N
2t bottom	$[90/(0^w/90^{2f})]$	160N	166N	133N	148N	121N	85N

Table 4.8: Initiation loads in group B, for different woven locations in the thickness direction of AP-PLY

Parameter	layup	Initiation load of cohesive element group C			
		C1 left	C2 left	C3 left	C middle
1layer top	$[(0^w/90^f)/90/0]$		176N	161N	C1 277N
1layer middle	$[90/(0^w/90^f)/0]$	128N	104N	108N	
1layer bottom	$[90/0/(0^w/90^f)]$	57N		76N	C2 146N
2layer top	$[(0^{2w}/90^f)/90]$	266N	141N	171N	
2layer bottom	$[90/(0^{2w}/90^f)]$	95N		126N	C2 242N
2t top	$[(0^w/90^{2f})/0]$	202N	124N	145N	
2t bottom	$[90/(0^w/90^{2f})]$	142N	205N	136N	

Table 4.9: Initiation loads in group C, for different woven locations in the thickness direction of AP-PLY

locations in the thickness direction, such as at the top of the 4 designable layers, the middle, and the bottom. The next two rows of data in Table 4.7, 4.8 and 4.9 are the initiation loads of the AP-PLY model with the 2 layers of woven plies and 1 layer of straight ply pattern and where the woven pattern was located at different places in the thickness direction. The woven pattern of the model used in the last two rows was 1 layer of woven ply with 2 layers of straight filled ply. From the three Tables, Tables 4.7, 4.8 and 4.9, it can be seen that, for the pattern in the first 3 rows of AP-PLY model results, the model with the interwoven layers at the top of the 4 layers had the biggest loads for all of the delamination initiation locations of the cohesive element layers. The results for the two models with the pattern of 2 layers woven plies and 1 straight filled ply in the next two rows in Table 4.7, 4.8 and 4.9 show the same tendency for the delamination initiation loads in the model with interwoven layers at the top of the 4 layers to be larger than those of where the woven pattern is at the bottom of the 4 layers. The model with the pattern of 1 layer woven ply and 2 layers straight filled ply at the top location in the 4 designable layers sustained $\frac{2}{5}$ of the total number of the highest initiation loads in the A, B and C groups and the remaining larger initiation loads were seen in the model of interwoven layers at the bottom of the 4 layers.

4.4.2 Crack growth curves

Crack propagation in an AP-PLY composite laminate can be traced in the finite element models of AP-PLY laminates as with increasing load, more and more cohesive elements will fail. This failure of the cohesive elements represents the formation of cracks. If the load is not increasing, but the crack length is increasing, this indicates that a crack is unstable. With a constant load, or a load that is increasing very slowly, a crack will continue to propagate quickly, this gives the critical load of the interface of the structure. The crack growth curves for different woven angles of the simple AP-PLY composite laminates with the same layup are shown in Figures 4.12, 4.13 and 4.14.

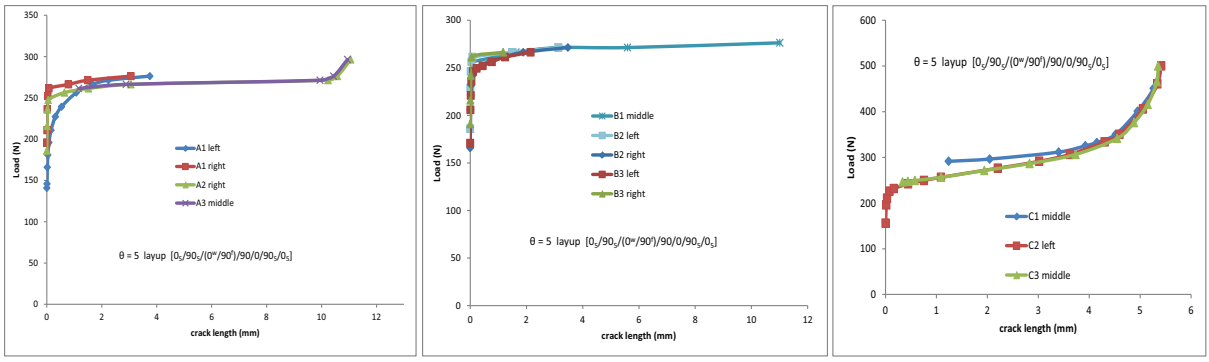

Figure 4.12: Crack growth curves of the woven angle=5 with layup $[0_5/90_5/(0^w/90^f)/90/0/90_5/0_5]$

The horizontal axis for all the figures shown in this section is crack length, and the vertical axis is load. Take Figure 4.12 as an example, the 3 constituent figures from left to right

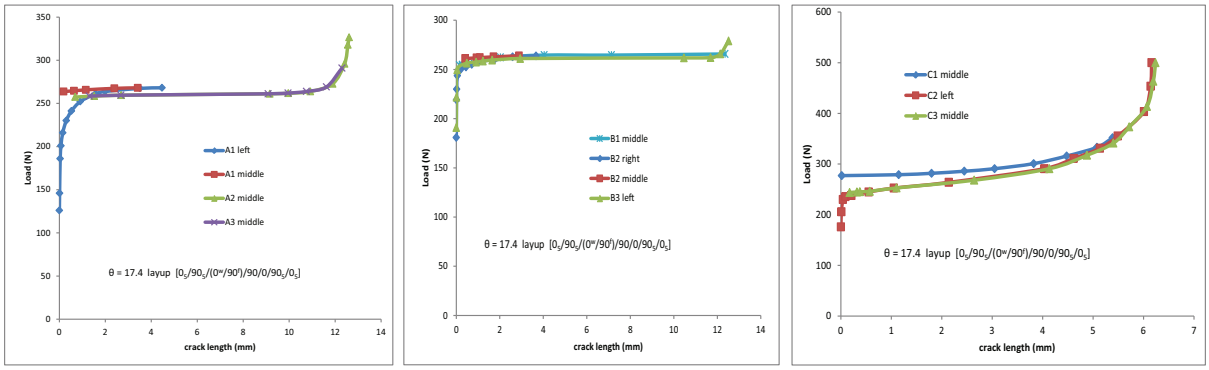

Figure 4.13: Crack growth curves of the woven angle=17.4 with layup $[0_5/90_5/(0^w/90^f)/90/0/90_5/0_5]$

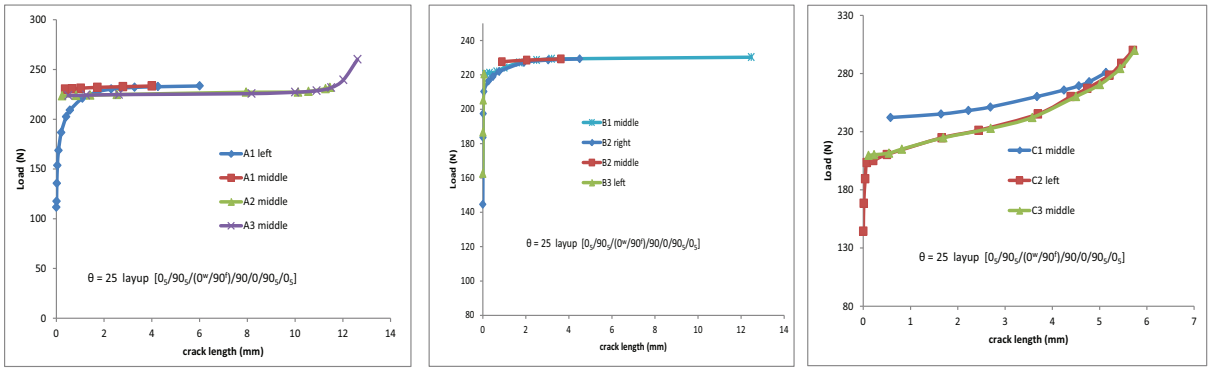

Figure 4.14: Crack growth curves of the woven angle=25 with layup $[0_5/90_5/(0^w/90^f)/90/0/90_5/0_5]$

show the crack growth curves for the cohesive layers of groups A, B and C of the AP-PLY composite laminates with layup $[0_5/90_5/(0^w/90^f)/90/0/90_5/0_5]$. It can be seen that after initiation of the crack, the crack initially propagates slowly then the crack propagates without increasing the load for the cohesive layers of group A and group B. The load at which a crack length keeps increasing in an unstable fashion is referred to here as the critical load. In Figures 4.12, 4.13 and 4.14, the critical load is the load at which the slope of crack growth curve is zero. The cracks in the C group propagate slowly at the beginning, then fast and finally they begin to propagate slowly again. The reason that the cracks at group C propagate finally slowly is because the cracks are very close to the middle of the beam which also is the boundary condition of the half finite element model. It can be seen from Figures 4.12, 4.13 and 4.14 that the crack growth curves of A, B and C groups for different woven angle are very similar, and that the critical loads of different crack curves for the same group are the same. The crack growth curves of group A in Figures 4.12, 4.13 and 4.14 indicate that the resin area can influence the crack propagation when the crack grows very close to the resin area.

The critical loads of the different groups for different woven angles are presented in Table 4.10.

Parameter name	Critical load of different cohesive element group		
	Group A	Group B	Group C
angle=5	270N	270N	300N
angle=17.4	265N	262N	285N
angle=25	232N	228N	280N

Table 4.10: Critical load of different woven angle

Parameter	layup	Critical load of different cohesive element group		
		Group A	Group B	Group C
$n_1 = 1, n_2 = 1$	$[(0^w/90^f)/90/0]$	265N	262N	285N
$n_1 = 1, n_2 = 2$	$[(0^w/90^{2f})/0]$	233N	235N	250N
$n_1 = 1, n_2 = 3$	$[(0^w/90^{3f})]$	230N	232N	245N
$n_1 = 2, n_2 = 1$	$[(0^{2w}/90^f)/90]$	263N	264N	300N
$n_1 = 3, n_2 = 1$	$[(0^{3w}/90^f)]$	270N	272N	290N
$n_1 = 2, n_2 = 2$	$[(0^{2w}/90^{2f})]$	176N	176N	192N

Table 4.11: Critical load of different thickness of filled straight plies and woven plies

From Table 4.10 it can be seen that the critical load of cohesive layer group A is almost equal to that of group B and the critical load of group C is larger than that of groups A and B. It can be concluded that with a decreasing angle, the critical loads of the groups A, B and C will increase.

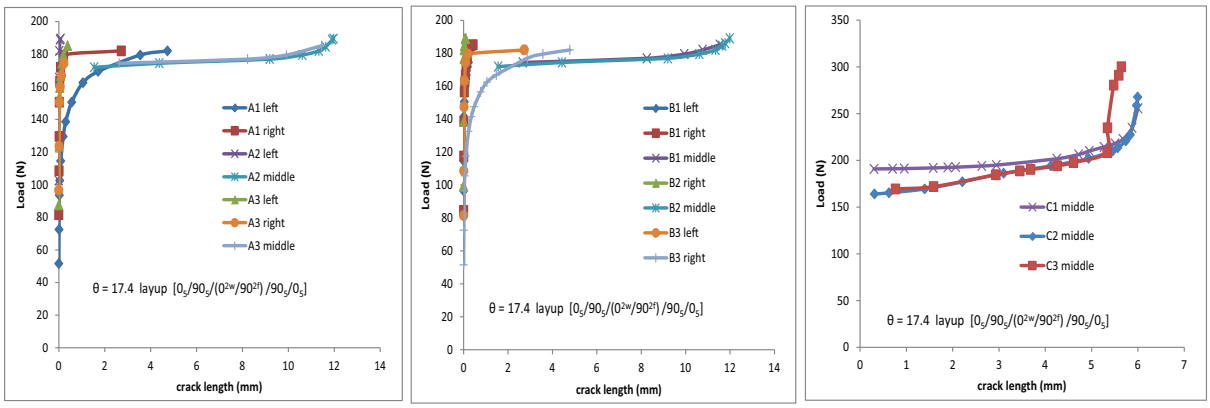

Figure 4.15: Crack growth curves of layup $[0_5/90_5/(0^{2w}/90^{2f})/90_5/0_5]$

Most of the crack growth curves are similar to the curves in Figure 4.12 for the model of the pattern with the parameter-woven ply thickness. The similar crack growth curves are presented in Appendix A. From Figure 4.15 it can be seen that the critical load of group A is close to that of group B. The interesting curves are the crack growth curves of group C. The crack growth curve of C3 middle shows that crack C3 has nearly stopped growing when crack length $a = 5.7mm$ and the other two curves, C1 middle and C2 middle, stopped growing when crack length $a = 6.05mm$. The crack growth curves of group C clearly show the influence of the symmetry boundary.

Parameter	layup	Critical load of different cohesive element group		
		Group A	Group B	Group C
1layer top	$[(0^w/90^f)/90/0]$	265N	262N	285N
1layer middle	$[90/(0^w/90^f)/0]$	143N	143N	146N
1layer bottom	$[90/0/(0^w/90^f)]$	142N	142N	145N
2layer top	$[(0^{2w}/90^f)/90]$	263N	264N	300N
2layer bottom	$[90/(0^{2w}/90^f)]$	263N	235N	245N
2t top	$[(0^w/90^{2f})/0]$	233N	235N	250N
2t bottom	$[90/(0^w/90^{2f})]$	235N	235N	265N

Table 4.12: Critical load of different woven location in thickness direction

The critical loads of the different cohesive layer groups in the AP-PLY composite laminate models with different patterns including the parameter of woven ply thickness are presented in Table 4.11. It can be seen from Table 4.11 that the largest critical loads of groups A, B and C are found in the model with the AP-PLY pattern of 3 layers of woven plies and 1 layer of straight filled ply, which is $n_1 = 3$, $n_2 = 1$. The smallest critical loads are seen in the model with the pattern of 2 layers of woven plies and 2 layers of straight filled plies, $n_1 = 2$,$n_2 = 2$. From Table 4.11 it can be seen that with an increasing number of straight filled plies, the critical loads will decrease. In the models with 1 layer of straight filled ply, the critical loads of the models with different numbers of woven plies are very close and the differences of the critical loads in these three models can be neglected.

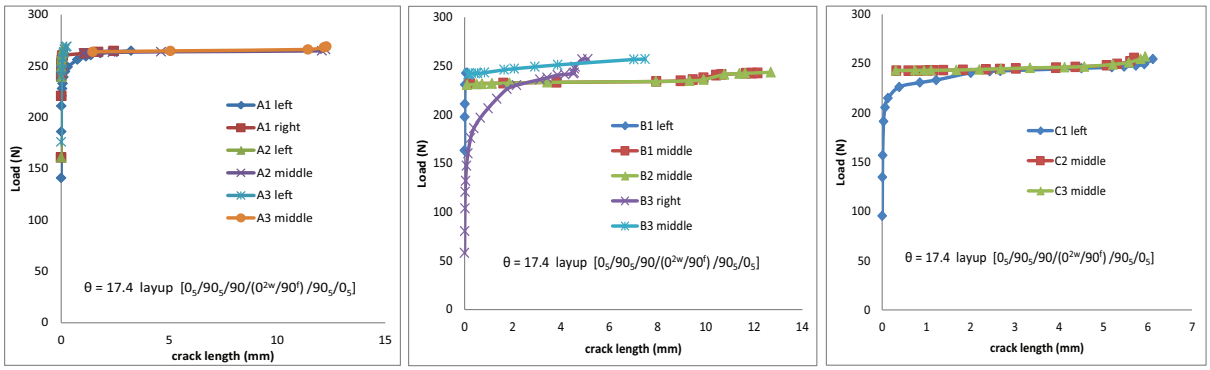

Figure 4.16: Crack growth curves of layup $[0_5/90_5/90/(0^{2w}/90^f)/90_5/0_5]$

The crack growth curves that relate to the parameter of interwoven layers location in the thickness direction of the simple AP-PLY composite laminates with the same woven angle can be seen in Figure 4.16 and the remaining crack growth curves are in Appendix A. The crack growth curves for the AP-PLY model, with woven angle $\theta = 17.4$ and the pattern of 2 layers woven plies with 1 layer straight fill ply in the bottom of the 4 middle layers are shown in Figure 4.16. It can be seen from Figure 4.16, the cracks of group C are continuously propagating even when the cracks are very close to the symmetry boundary, which indicates that the cracks will propagate through the whole laminate and the whole structure will fail.

The critical loads of the different cohesive layer groups in the AP-PLY composite laminate models as the location of the AP-PLY pattern changes in the thickness direction are presented in Table 4.12. From Table 4.12 it can be seen that the interwoven layers at the top of the 4 layers have higher critical loads than the critical loads at other locations in the thickness direction of AP-PLY laminate from those seen in the model 1 layer of woven ply and 1 layer of straight filled ply and the model with 2 layer of woven plies and 1 layer of straight filled ply. The models with the pattern of 1 layer of woven ply and 2 layers of straight filled plies were a little bit different: the critical load at group C for the interwoven layers at the bottom of the 4 layers was larger than that for the interwoven layers at the top of the 4 designable layers in AP-PLY model.

4.5 Conclusions

A simple woven pattern, in which the plies were woven in one direction, was employed for a 3D AP-PLY composite laminate model under simulated impact load to explain the mechanism behind the improvement of damage tolerance of the AP-PLY composite laminate. The impact load was modeled as a static out-of-plane line load to simplify the complicated AP-PLY model. The structure of the 3D simple AP-PLY composite laminate under out-of-plane line load was simplified to a 2D plane stress model based on the characteristics of the AP-PLY woven pattern used in the AP-PLY composite laminate. The delamination behavior was observed using 2D finite element AP-PLY models with cohesive elements inserted into the interfaces of the interwoven layers. This parametric investigation indicated: the fewer the number of straight filled plies used in a laminate the larger will be the delamination initiation load and critical load. In the models of a pattern with 1 layer of straight filled ply, the model with 3 layers woven plies showed larger initiation loads than the model with 2 layers of woven plies while the one with 1 layer of woven ply showed the largest initiation loads. The more layers of woven plies present in the AP-PLY model, the larger the critical loads of delamination growth seen, the precondition for this is a pattern with same number of straight filled plies. With respect to the location of the interwoven layers, patterns where the woven patterns are on the top of the 4 designable layers have higher delamination initiation loads and critical loads. And the crack growth curves showed that the resin area influences on crack propagation when the cracks propagate closely to that area. A limited number of models was chosen to research the parameters related AP-PLY woven patterns, and the isolation of these parameters could not be separated totally from the other parameters. Since finite element simulations are, computer, time-consuming, it is necessary to analyze delamination propagation analytically not only to reduce the time but also for the convenience of future optimization work.

Chapter 5

Analytical solutions to obtain energy release rate

5.1 Introduction

Composite laminates are widely used in the aerospace industry due to their good performance with respect to damage tolerance when properly designed, high stiffness and strength, low density and their tailorability to meet the requirements of specific applications. However, composites are very sensitive to delamination when out-of-plane loads are present because of their weak interlaminar strength in the transverse direction. Delamination can be initiated from manufacturing defects, matrix cracks or fiber breaks, or by out-of-plane loads, which make delamination one of the most frequently occurring types of damage in composite laminates. The presence of delamination in a composite laminate may significantly decrease the stiffness of the whole structure and growth of the delamination will probably lead to the failure of the composite laminate. Delamination propagation studies in composite laminates commonly employ fracture mechanics, in which the strain energy release rate (SERR), or energy release rate (ERR), and stress intensity factors (SIF) are the parameters that need to be determined. According to fracture mechanics, a criterion can be used to determine whether a delamination will propagate or not. This criterion states that if the strain energy release rate G of the crack tip is greater than or equal to the critical energy release rate G_c the delamination will grow. The critical energy release rate (CERR) is a material property and is independent of the geometry of the structure.

The finite element methods, experimental methods and analytical methods to analyze the strain energy release rate (SERR) in composite laminates are discussed in chapter 2. The disadvantage of using a finite element method or an experimental method to obtain the SERR is relatively low efficiency and increased computation time because one model or one test with a certain crack length will give only a SERR for a specific structure configuration with a specific material. Due to the drawbacks of the finite element method

and experimental method, an efficient analytical approach to determine the energy release rate was proposed. Beam theory and William's method [1988] are used to determining the SERR of delaminated AP-PLY composite laminate. The use of beam theory for determination of SERR in AP-PLY composite laminate may cause a loss of accuracy but can be a very efficient method for trade studies.

This chapter is structured as follows. The basic characteristics of the 2D beam model will be described in section 5.2. The special cases of the isotropic material will be discussed in section 5.3. The method to determine SERR of delamination will be extended to composite materials in section 5.4. The application of analytical SERR model to AP-PLY composite laminate will be presented in section 5.5.

5.2 Basic characteristics of the model

The laminate architecture that is of interest in this thesis is AP-PLY composite laminate, that is woven in one direction. This would mean that the structure of AP-PLY composite laminates can be simplified into a 2D problem based on the cross-section as described in chapter 4, section 4.2.2. To obtain the SERR of AP-PLY composite laminate, beam theory was chosen to describe the behavior of a 2D AP-PLY model under out-of-plane loads. Among the methods to calculate SERR analytically, Williams [1988] offers a simple way to derive the SERR based on linear elastic fracture mechanics, in which only the generalized forces at the crack tip are used to calculate SERR and can give accurate results. A general case, as shown in Figure 5.1, was a delamination, or a crack, in a sheet of thickness $2t$ and width b. The distance from the top surface to the crack is t_1. The loading is considered as uniform in the thickness direction, therefore the loading conditions at the crack front are uniform. The crack length will be $a + \delta a$ after the crack propagates from line AB to CD, and the SERR can be defined as:

$$G = \frac{1}{b}\frac{dU^*}{da} \tag{5.1}$$

where U^* is the complementary energy, which is equal to U_s, the strain energy, for the linear case.

5.2.1 Internal loads and internal equilibrium

In a 3D plate, cracks can be located anywhere and with arbitrary shapes. Figure 5.1 is a general case of a crack in a plate under line load. It can be simplified into a 2D beam with a line crack based on the assumption that the crack is through the width of the plate. The simplified beam model can be taken as a 3-point bending beam. The crack

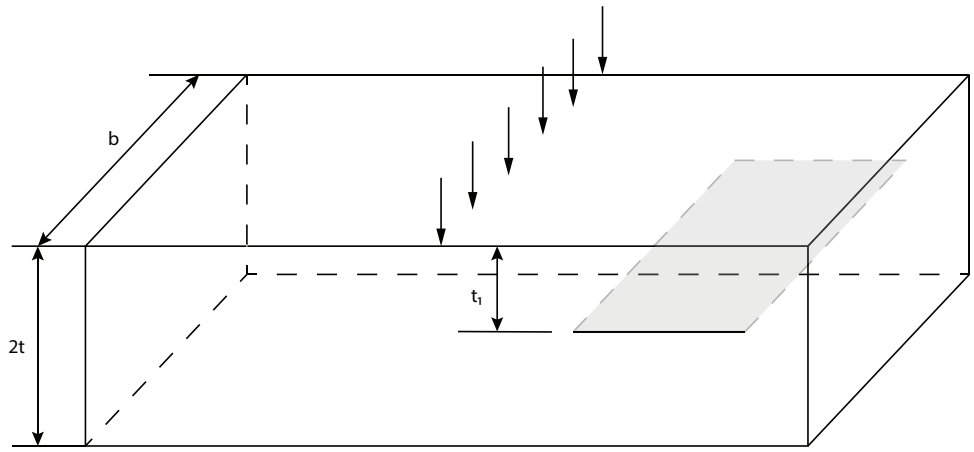

Figure 5.1: A crack in a plate

can be also at the edge, which is transferred to an ENF beam after simplification but that is out of our discussion in this thesis.

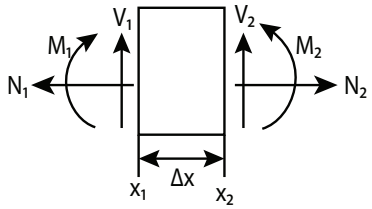

Figure 5.2: Internal forces analysis of beam segment

The equilibrium needs to be satisfied for each segment for the structure of a beam model with a crack. The analysis of internal generalized forces for a beam segment without loading is shown in Figure 5.2. The equilibrium equations are:

$$\Sigma F_x = 0 \tag{5.2}$$

$$\Sigma F_y = 0 \tag{5.3}$$

$$\Sigma M = 0 \tag{5.4}$$

The Eq. 5.2 implies that:

$$N_1 = N_2 \tag{5.5}$$

The Eq. 5.3 implies that:

$$V_1 = V_2 \quad \Rightarrow \quad \frac{dV}{dx} = 0 \tag{5.6}$$

Eq. 5.4 implies that:

$$M_1 + V_1 \Delta x = M_2 \quad \Rightarrow \quad V_1 = \frac{M_2 - M_1}{\Delta x} \tag{5.7}$$

$$\Rightarrow V = \frac{dM}{dx} \quad \text{when} \quad \Delta x \to 0 \tag{5.8}$$

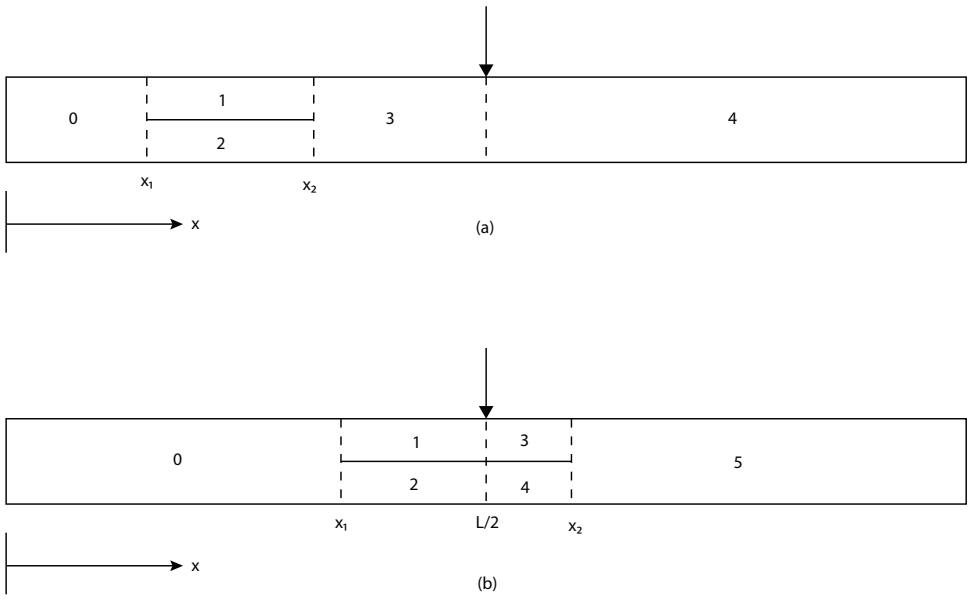

Figure 5.3: Dividing the beam into several parts (a) the crack not under the loading point (b) the crack under the loading point

A 2D three-point beam model with one crack inside is shown in Figure 5.3. The beam model was divided into several different parts depending on the number of cracks and whether the crack goes across the load point or not. For the model with a crack that does not go across the load point, there are 4 parts, while for the case that the crack goes across the load point, there is one more part need to be dealt due to the singularity of the load point, as shown in Figure 5.3. Each part of the beam was taken as a single beam and the equilibrium of force and moment need to be satisfied for each segment.

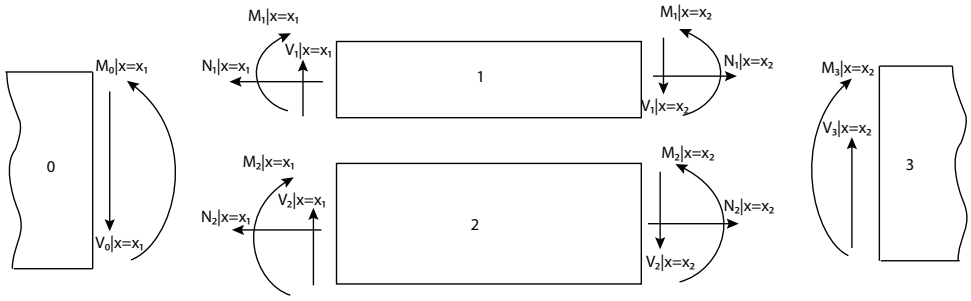

Figure 5.4: Generalized forces at the interfaces

Taking the case that the crack does not go across the loading point as an example, the internal generalized forces for each part are shown in Figure 5.4. $M_1|_{x=x_1}$, $V_1|_{x=x_1}$ and

$N_1|_{x=x_1}$ are the bending moment, shear force and normal force of beam part 1 at the section $x = x_1$. The subscript represents the number of the part and the right part at the vertical line represents the location of the generalized forces acting. The continuity conditions for isotropic materials at the interface $x = x_1$ are:

$$N_1|_{x=x_1} + N_2|_{x=x_1} = 0, \text{ at } x = x_1 \quad (5.9)$$

$$V_1|_{x=x_1} + V_2|_{x=x_1} - V_0|_{x=x_1} = 0, \text{ at } x = x_1 \quad (5.10)$$

$$M_1|_{x=x_1} + M_2|_{x=x_1} - N_1|_{x=x_1}\frac{t_1}{2} + N_2|_{x=x_1}\frac{t_2}{2} - M_0|_{x=x_1} = 0, \text{ at } x = x_1 \quad (5.11)$$

The continuity conditions of interface $x = x_2$ can also be obtained similarly and are shown as follows:

$$N_1|_{x=x_2} + N_2|_{x=x_2} = 0, \text{ at } x = x_2 \quad (5.12)$$

$$V_1|_{x=x_2} + V_2|_{x=x_2} - V_0|_{x=x_2} = 0, \text{ at } x = x_2 \quad (5.13)$$

$$M_1|_{x=x_2} + M_2|_{x=x_2} - N_1|_{x=x_2}\frac{t_1}{2} + N_2|_{x=x_2}\frac{t_2}{2} - M_3|_{x=x_2} = 0, \text{ at } x = x_2 \quad (5.14)$$

where t_1 and t_2 are the thickness of the sub-beams 1 and 2 and $t_1+t_2 = t$. The equilibrium of sub-beam 1 in x direction is:

$$\Sigma F_x = 0 \quad \Rightarrow \quad N_1|_{x=x_1} = N_1|_{x=x_2} \quad (5.15)$$

Eq. 5.9 gives that $N_1|_{x=x_1} = -N_2|_{x=x_1}$, together with Eq. 5.15 gives that:

$$N_1|_{x=x_1} = N_1|_{x=x_2} = N \quad (5.16)$$

$$N_2|_{x=x_1} = N_2|_{x=x_2} = -N \quad (5.17)$$

where N is the value of the normal force caused by the presence of the crack.

The generalized forces expression of the intact beam parts are:

$$M_0(x) = \frac{P}{2}x, \quad M_3(x) = \frac{P}{2}x, \quad M_4(x) = \frac{P}{2}(L-x) \quad (5.18)$$

$$V_0(x) = \frac{P}{2}, \quad V_3(x) = \frac{P}{2}, \quad V_4(x) = -\frac{P}{2} \quad (5.19)$$

From Eqs. 5.16, 5.17, 5.18 and 5.19, the moment continuity equations 5.11 and 5.14 can be rewritten as:

$$M_1|_{x=x_1} + M_2|_{x=x_1} - N\frac{t}{2} - \frac{P}{2}x_1 = 0 \quad (5.20)$$

$$M_1|_{x=x_2} + M_2|_{x=x_2} - N\frac{t}{2} - \frac{P}{2}x_2 = 0 \quad (5.21)$$

5.2.2 Energy minimization to get internal loads

The strain energy of the beam equals the complementary energy of the model for linear elastic deformation. The complementary energy of the beam model in Figure 5.3 is:

$$\begin{aligned} U^* &= \frac{1}{2}\Bigg(\int_0^{x_1} \frac{M_0^2(x)}{E_0 I_0} dx + \int_0^{x_1} \frac{V_0^2(x)}{\alpha_s G_0 A_0} dx + \int_{x_1}^{x_2} \frac{M_1^2(x)}{E_1 I_1} dx + \int_{x_1}^{x_2} \frac{V_1^2(x)}{\alpha_s G_1 A_1} dx \\ &+ \int_{x_1}^{x_2} \frac{N^2}{E_1 A_1} dx + \int_{x_1}^{x_2} \frac{M_2^2(x)}{E_2 I_2} dx + \int_{x_1}^{x_2} \frac{V_2^2(x)}{\alpha_s G_2 A_2} dx + \int_{x_1}^{x_2} \frac{N^2}{E_2 A_2} dx \\ &+ \int_{x_2}^{\frac{L}{2}} \frac{M_3^2(x)}{E_3 I_3} dx + \int_{x_2}^{\frac{L}{2}} \frac{V_3^2(x)}{\alpha_s G_3 A_3} dx + \int_{\frac{L}{2}}^{L} \frac{M_4^2(x)}{E_4 I_4} dx + \int_{\frac{L}{2}}^{L} \frac{V_4^2(x)}{\alpha_s G_4 A_4} dx \Bigg) \end{aligned} \tag{5.22}$$

There is no explicit expression of generalized forces for the two delaminated sub-beams. The moments at $x = x_1$ and $x = x_2$ are $M_1|_{x=x_1}$ and $M_1|_{x=x_2}$, respectively. Therefore, the moment of sub-beam 1 can be expressed as:

$$M_1(x) = M_1|_{x=x_1} + k(x - x_1) \tag{5.23}$$

where $k = \dfrac{M_1|_{x=x_2} - M_1|_{x=x_1}}{x_2 - x_1}$. Eq. 5.23 can be rewritten as:

$$M_1(x) = M_1|_{x=x_1}(1 - \xi) + M_1|_{x=x_2}\xi, \qquad \xi \in [0, 1] \tag{5.24}$$

where $\xi = \dfrac{x - x_1}{x_2 - x_1}$. The integration part of the moment in the sub-beam 1 can be rewritten as:

$$\begin{aligned} \int_{x_1}^{x_2} \frac{M_1^2(x)}{E_1 I_1} dx &= \frac{x_2 - x_1}{E_1 I_1} \int_0^1 \left[M_1|_{x=x_1}(1 - \xi) + M_1|_{x=x_2}\xi \right]^2 dx \qquad (5.25) \\ &= \frac{a}{E_1 I_1} \left[\frac{1}{3}(M_1|_{x=x_1})^2 + \frac{1}{3}(M_1|_{x=x_2})^2 + \frac{1}{3}(M_1|_{x=x_1})(M_1|_{x=x_2}) \right] \end{aligned}$$

where the crack length $a = x_2 - x_1$. Similarly, the integration part of the moment in sub-beam 2 is:

$$\int_{x_1}^{x_2} \frac{M_2^2(x)}{E_2 I_2} dx = \frac{a}{E_2 I_2} \left[\frac{1}{3}(M_2|_{x=x_1})^2 + \frac{1}{3}(M_2|_{x=x_2})^2 + \frac{1}{3}(M_2|_{x=x_1})(M_2|_{x=x_2}) \right] \tag{5.26}$$

Based on beam theory, the shear forces of the sub-beams are:

$$V_1(x) = \frac{M_1|_{x=x_2} - M_1|_{x=x_1}}{x_2 - x_1} = \frac{M_1|_{x=x_2} - M_1|_{x=x_1}}{a} \tag{5.27}$$

$$V_2(x) = \frac{M_2|_{x=x_2} - M_2|_{x=x_1}}{x_2 - x_1} = \frac{M_2|_{x=x_2} - M_2|_{x=x_1}}{a} \tag{5.28}$$

After integrating the explicit expression of generalized forces in the complementary energy and substituting Eqs. 5.25, 5.26, 5.27 and 5.28, the complementary energy of the beam model is:

$$\begin{aligned} U^* = & \frac{P^2 x_1^3}{24} + \frac{P^2 x_1}{8\alpha_s G_0 A_0} + \frac{a}{6E_1 I_1}\left[(M_1|_{x=x_1})^2 + (M_1|_{x=x_2})^2 + (M_1|_{x=x_1})(M_1|_{x=x_2})\right] \\ & + \frac{1}{2a\alpha_s G_1 A_1}\left[(M_1|_{x=x_1})^2 + (M_1|_{x=x_2})^2 - 2(M_1|_{x=x_1})(M_1|_{x=x_2})\right] + \frac{N^2 a}{E_1 A_1} \\ & + \frac{a}{6E_2 I_2}\left[(M_2|_{x=x_1})^2 + (M_2|_{x=x_2})^2 + (M_2|_{x=x_1})(M_2|_{x=x_2})\right] \\ & + \frac{1}{2a\alpha_s G_2 A_2}\left[(M_2|_{x=x_1})^2 + (M_2|_{x=x_2})^2 - 2(M_2|_{x=x_1})(M_2|_{x=x_2})\right] + \frac{N^2 a}{E_2 A_2} \\ & + \frac{P^2(\frac{L}{2} - x_2)^3}{12E_3 I_3} + \frac{P^2(\frac{L}{2} - x_2)}{4\alpha_s G_3 A_3} + \frac{P^2 L^3}{96E_4 I_4} + \frac{P^2 L}{8\alpha_s G_4 A_4} \end{aligned} \tag{5.29}$$

In the expression of the strain energy of Eq. 5.30, the first two terms and the last four terms are known and will be zeros after calculating the derivative with respect to the crack length a. Eq. 5.30 implies that the energy release rate G is related to the generalized forces at the crack tip.

The principle of minimum potential energy should be satisfied and the Lagrange Multipliers method was used to find out the solution of the unknowns $M_1|_{x=x_1}$, $M_1|_{x=x_2}$, $M_2|_{x=x_1}$, $M_2|_{x=x_2}$ and N in Eq. 5.30. Therefore, the problem is reduced into obtaining the minimum strain energy of the delaminated beam under the constraints of the two continuity conditions at the interfaces of $x = x_1$ and $x = x_2$. The objective function is:

$$\begin{aligned} & \mathbf{F}(M_1|_{x=x_1}, M_1|_{x=x_2}, M_2|_{x=x_1}, M_2|_{x=x_2}, N) = \\ & \frac{a}{6E_1 I_1}\left[(M_1|_{x=x_1})^2 + (M_1|_{x=x_2})^2 + (M_1|_{x=x_1})(M_1|_{x=x_2})\right] \\ & + \frac{1}{2a\alpha_s G_1 A_1}\left[(M_1|_{x=x_1})^2 + (M_1|_{x=x_2})^2 - 2(M_1|_{x=x_1})(M_1|_{x=x_2})\right] + \frac{N^2 a}{E_1 A_1} \\ & + \frac{a}{6E_2 I_2}\left[(M_2|_{x=x_1})^2 + (M_2|_{x=x_2})^2 + (M_2|_{x=x_1})(M_2|_{x=x_2})\right] \\ & + \frac{1}{2a\alpha_s G_2 A_2}\left[(M_2|_{x=x_1})^2 + (M_2|_{x=x_2})^2 - 2(M_2|_{x=x_1})(M_2|_{x=x_2})\right] + \frac{N^2 a}{E_2 A_2} \end{aligned} \tag{5.30}$$

The constraint functions which should be zero are:

$$\mathbf{g}_1(M_1|_{x=x_1}, M_1|_{x=x_2}, M_2|_{x=x_1}, M_2|_{x=x_2}, N) = M_1|_{x=x_1} + M_2|_{x=x_1} - N\frac{t}{2} - \frac{P}{2}x_1 \tag{5.31}$$

$$\mathbf{g}_2(M_1|_{x=x_1}, M_1|_{x=x_2}, M_2|_{x=x_1}, M_2|_{x=x_2}, N) = M_1|_{x=x_2} + M_2|_{x=x_2} - N\frac{t}{2} - \frac{P}{2}x_2 \tag{5.32}$$

Lagrange multipliers λ_1 and λ_2 are introduced and the Lagrange function is defined as:

$$\begin{aligned}\mathbf{L}(M_1|_{x=x_1}, M_1|_{x=x_2}, M_2|_{x=x_1}, M_2|_{x=x_2}, N, \lambda_1, \lambda_2) = \\ \mathbf{F}(M_1|_{x=x_1}, M_1|_{x=x_2}, M_2|_{x=x_1}, M_2|_{x=x_2}, N) \\ +\lambda_1\mathbf{g}_1(M_1|_{x=x_1}, M_1|_{x=x_2}, M_2|_{x=x_1}, M_2|_{x=x_2}, N) \\ +\lambda_2\mathbf{g}_2(M_1|_{x=x_1}, M_1|_{x=x_2}, M_2|_{x=x_1}, M_2|_{x=x_2}, N)\end{aligned} \tag{5.33}$$

The gradient of Lagrange function is:

$$\begin{aligned}\nabla_{M_1|_{x=x_1}, M_1|_{x=x_2}, M_2|_{x=x_1}, M_2|_{x=x_2}, N, \lambda_1, \lambda_2}\mathbf{L}(M_1|_{x=x_1}, M_1|_{x=x_2}, M_2|_{x=x_1}, M_2|_{x=x_2}, N, \lambda_1, \lambda_2) = \\ \left(\frac{\partial\mathbf{L}}{\partial M_1|_{x=x_1}}, \frac{\partial\mathbf{L}}{\partial M_1|_{x=x_2}}, \frac{\partial\mathbf{L}}{\partial M_2|_{x=x_1}}, \frac{\partial\mathbf{L}}{\partial M_2|_{x=x_2}}, \frac{\partial\mathbf{L}}{\partial N}, \frac{\partial\mathbf{L}}{\partial\lambda_1}, \frac{\partial\mathbf{L}}{\partial\lambda_2}\right)\end{aligned} \tag{5.34}$$

The Lagrange multiplier method requires that:

$$\nabla_{M_1|_{x=x_1}, M_1|_{x=x_2}, M_2|_{x=x_1}, M_2|_{x=x_2}, N, \lambda_1, \lambda_2}\mathbf{L}(M_1|_{x=x_1}, M_1|_{x=x_2}, M_2|_{x=x_1}, M_2|_{x=x_2}, N, \lambda_1, \lambda_2) = 0 \tag{5.35}$$

The minimum energy and all the unknowns could be obtained after solving Eq. 5.35.

The solved unknowns are listed as following:

$$M_1|_{x=x_1} = \frac{C_1\lambda_1 - C_2\lambda_2}{C_1^2 - C_2^2} \tag{5.36}$$

$$M_2|_{x=x_1} = \frac{C_3\lambda_1 - C_4\lambda_2}{C_3^2 - C_4^2} \tag{5.37}$$

$$M_1|_{x=x_2} = \frac{C_1\lambda_2 - C_2\lambda_1}{C_1^2 - C_2^2} \tag{5.38}$$

$$M_2|_{x=x_2} = \frac{C_3\lambda_2 - C_4\lambda_1}{C_3^2 - C_4^2} \tag{5.39}$$

$$N = \frac{-(\lambda_1 + \lambda_2)c}{\frac{a}{E_1A_1} + \frac{a}{E_2A_2}} \tag{5.40}$$

$$\lambda_1 = \frac{P(x_1C_5 + x_2C_6)}{2(C_5^2 - C_6^2)} \tag{5.41}$$

$$\lambda_2 = \frac{P(x_1C_6 + x_2C_5)}{2(C_5^2 - C_6^2)} \tag{5.42}$$

where the constants are listed as below:

$$\begin{aligned}
c &= \frac{h}{2} \\
C_0 &= \frac{c^2}{\frac{a}{E_1A_1} + \frac{a}{E_2A_2}} \\
C_1 &= \frac{a}{3E_1I_1} + \frac{1}{aG_1A_1} \\
C_2 &= \frac{a}{6E_1I_1} - \frac{1}{aG_1A_1} \\
C_3 &= \frac{a}{3E_2I_2} + \frac{1}{aG_2A_2} \\
C_4 &= \frac{a}{6E_2I_2} - \frac{1}{aG_2A_2} \\
C_5 &= C_0 + \frac{C_1}{C_1^2 - C_2^2} + \frac{C_3}{C_3^2 - C_4^2} \\
C_6 &= -C_0 + \frac{C_2}{C_1^2 - C_2^2} + \frac{C_4}{C_3^2 - C_4^2}
\end{aligned} \tag{5.43}$$

Remark 1 *The expression of the unknowns at the crack tips are correct for a crack in a three point bending beam model, where the crack is only present in the left or in the right side of the load point, as shown in Figure 5.3 (a). For the crack that goes across the load point in the middle, as shown in Figure 5.3 (b), there are different expressions. The expression of unknowns and the constants can be obtained following the same procedure as the case that a crack in one side, which are shown in Appendix B.*

Remark 2 *There is another method to compute the generalized forces at crack tips based on the displacement which is presented Appendix C. The expression of displacement of different parts is obtained after integrating the governing equations. The constants in the displacements are determined from the continuity conditions and boundary conditions. The generalized forces are obtained once the expressions of displacement and rotations are obtained.*

The energy release rate G, which is the derivative of the strain energy, can be computed after all the unknowns are obtained. For the crack as shown in Figure 5.3, the energy release rate of a crack with length a is the sum of the energy release rate contributions from the left and right crack tips. It is necessary to distinguish the energy release rate of the left crack tip and the right tip to determine whether the crack is going to propagate, followed by the direction in which it is going to propagate to. The strain energy release rate of the left crack tip G_L was determined by the generalized forces $M_1|_{x=x_1}$, $M_2|_{x=x_1}$, $M_0|_{x=x_1}$, $V_1|_{x=x_1}$, $V_2|_{x=x_1}$, $V_0|_{x=x_1}$ and N at the crack's left tip. It is the same for the strain energy release rate G_R of the right crack tip. The expression of G_L and G_R can be written as:

$$\begin{aligned} G_L(x) &= \frac{1}{2}\Bigg[\frac{(M_1|_{x=x_1})^2}{E_1I_1} + \frac{(M_2|_{x=x_1})^2}{E_2I_2} - \frac{(M_0|_{x=x_1})^2}{E_0I_0} + \frac{(V_1|_{x=x_1})^2}{\alpha_s G_1A_1} + \frac{(V_2|_{x=x_1})^2}{\alpha_s G_2A_2} \\ &\quad - \frac{(V_0|_{x=x_1})^2}{\alpha_s G_0A_0} + \frac{N^2}{E_1A_1} + \frac{N^2}{E_2A_2}\Bigg] \end{aligned} \tag{5.44}$$

$$\begin{aligned} G_R(x) &= \frac{1}{2}\Bigg[\frac{(M_1|_{x=x_2})^2}{E_1I_1} + \frac{(M_2|_{x=x_2})^2}{E_2I_2} - \frac{(M_3|_{x=x_2})^2}{E_3I_3} + \frac{(V_1|_{x=x_2})^2}{\alpha_s G_1A_1} + \frac{(V_2|_{x=x_2})^2}{\alpha_s G_2A_2} \\ &\quad - \frac{(V_3|_{x=x_2})^2}{\alpha_s G_3A_3} + \frac{N^2}{E_1A_1} + \frac{N^2}{E_2A_2}\Bigg] \end{aligned} \tag{5.45}$$

Remark 3 *The analytical model presented makes use of the generalized forces and moments acting in the vicinity of the crack tip. The details of the stress field at the crack tip are not included. This suggests that there may be cases where the crack growth and thus the energy release rate require detailed knowledge of the stress field at the crack tip. This means that the detailed effects of the stress singularity are not explicitly included in the present model.*

5.2.3 Typical results and comparison with finite element results

Double cantilever beam model

The performance of the proposed analytical solution of SERR with regard to reliability and accuracy is discussed in this section. A DCB model with a crack in the middle, as shown in Figure 5.5, under a single point load P at the tip, creates a mode II situation for which the SERR was obtained by Williams [1988] as:

$$G_{II} = \frac{9}{4}\frac{P^2a^2}{b^2Eh^3} \tag{5.46}$$

where P is the applied load, a is the crack length, b is the width of the beam, E is the Young's modulus of the material, h is half of the thickness. The expression of the energy release rate of a crack in a DCB model using the minimum energy method in the last section is the same as the one in the reference of Williams [1988].

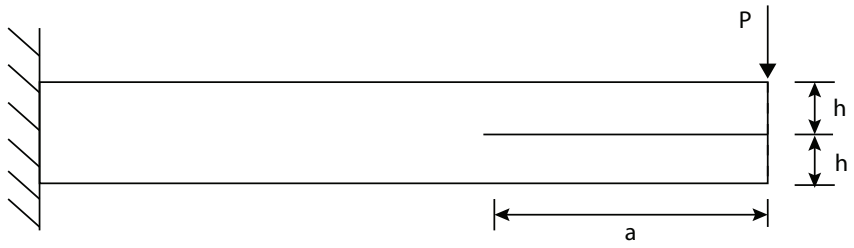

Figure 5.5: DCB model using Williams' method

Two different finite element models were built to validate Williams' method for two different through the thickness locations of the crack. One model was the same as Figure 5.5, which had a crack in the middle. The applied load was $P = 50N$, the length of the beam was $L = 39.825mm$ and the thickness was $t = 4.32mm$. The energy release rate of the finite element DCB model was computed using the J-integral method in ABAQUS. The finite element results were compared to the reference solution provided by Williams [1988] and are shown in Figure 5.6. It can be seen from Figure 5.6 that the results of the finite element analysis agreed very well with the referenced analytical solution. The other model is a model, where a crack was at the location of $t_1/t = 1/3$ in the thickness direction. Here t_1 is the distance from the crack to the top of the beam and t is the thickness of the beam. The applied load and the thickness of the beam in this model are the same as in the first model. The full length of this model is $L = 79.65mm$. The comparison between the finite element results and the analytical solution just presented above is shown in Figure 5.7. The computed finite element SERR is in good agreement with the analytical solution using Williams' method. It can be concluded that Williams' method to obtain the SERR is sufficiently accurate and can be used to analyze SERR of a crack in a beam.

Three point bending beam model

A crack in a DCB model could only propagate to one direction, whereas it can grow to two directions in a 3 point bending model. To verify the obtained SERR of a crack in a 3 point bending beam structure, a finite element half beam model was built. A crack is in the middle of the beam in the length direction, therefore this is a symmetric 3 point bending beam model with isotropic material and the structure of the half beam model is similar to DCB model in Figure 5.5. The differences are the simply supported boundary

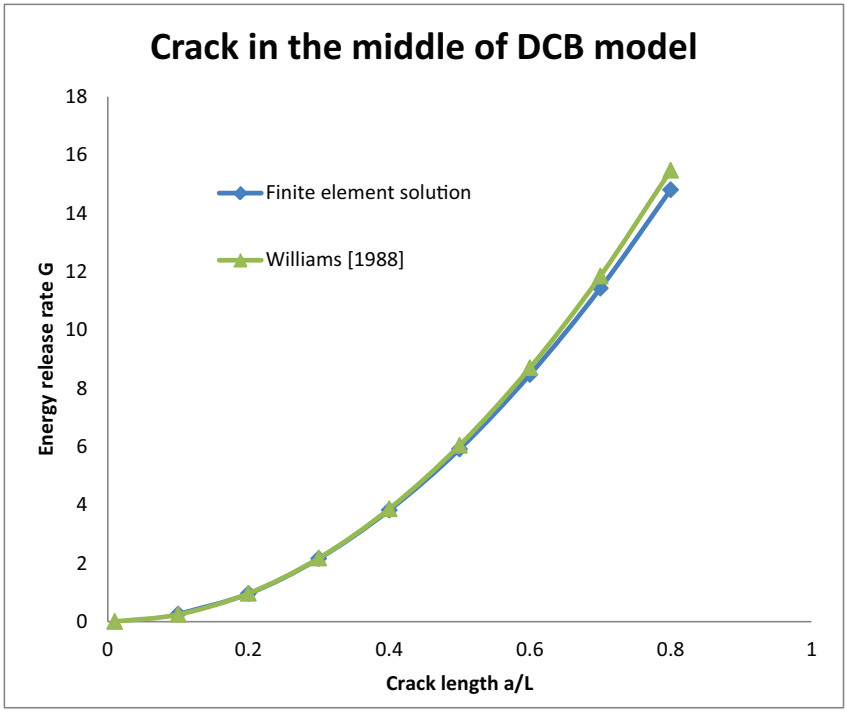

Figure 5.6: SERR of DCB model for the crack in the middle

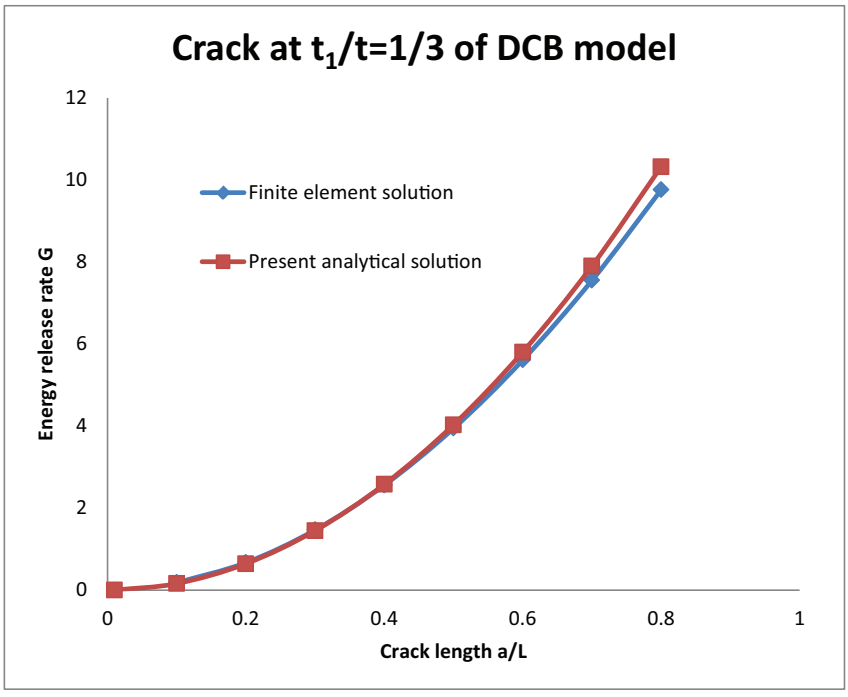

Figure 5.7: SERR of DCB model for the crack not in the middle of the thickness

condition at the left edge and the symmetric condition at the right edge. The length of the half beam model is $L = 39.825mm$, the thickness is $t = 4.32mm$, the applied load is $P = 50N$, the crack is located at 1/3 of the thickness direction. The analytical SERR at the crack tip was obtained using Euler beam theory and Timoshenko beam theory. The expressions of SERR at the left crack tip and the right crack tip in section 5.2.2 are based on Timoshenko beam theory, which included the shear deformation of short beam. The SERR of the crack based on Euler beam theory could be acquired when all the constants and parameters related to shear forces set to zero. The analytical results based on two different beam theories are compared with the finite element results in Figure 5.8. In general, the analytical solutions agreed very well with the finite element results for the case that the crack length $a \geq 0.2L$. With the increase in the crack length, the difference between the analytical SERR based on Euler beam theory and the SERR based on Timoshenko beam theory is decreasing, which is expected. It can be seen from the magnified SERR curves in Figure 5.8 for the case where $a \leq 0.2L$ that: the smaller the crack, the SERR calculated with Timoshenko beam theory is more accurate than that with Bernoulli-Euler theory. Therefore, in this thesis, the SERR is calculated based on Timoshenko beam theory.

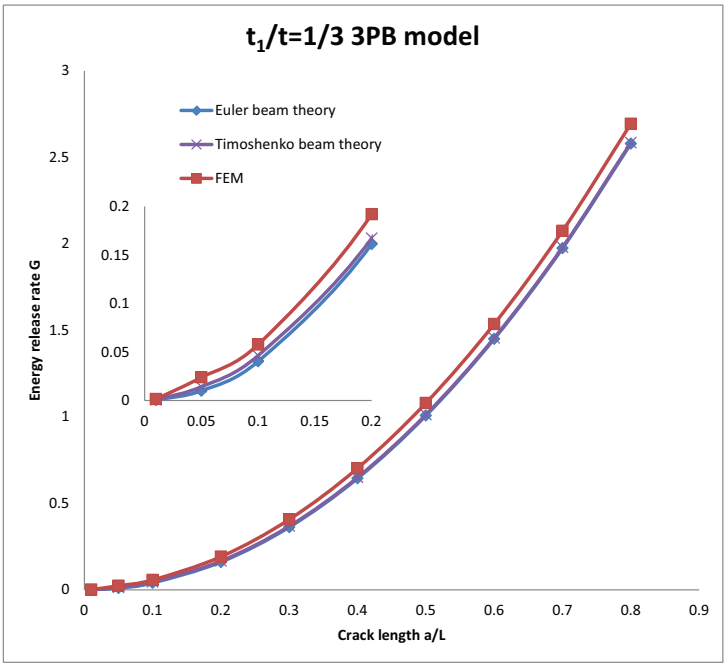

Figure 5.8: SERR of 3 point bending model

To clearly show the influence of the two different beam theories, the errors in energy release rate due to the used theories are shown in Figure 5.9. The error is calculated as:

$$\delta = \frac{G_{analyze} - G_{FEM}}{G_{FEM}} \times 100\% \tag{5.47}$$

where $G_{analyze}$ is the analytical SERR and G_{FEM} is the SERR obtained from finite element model. The shear effect could not be ignored especially when the crack $a \leq 0.5L$. The

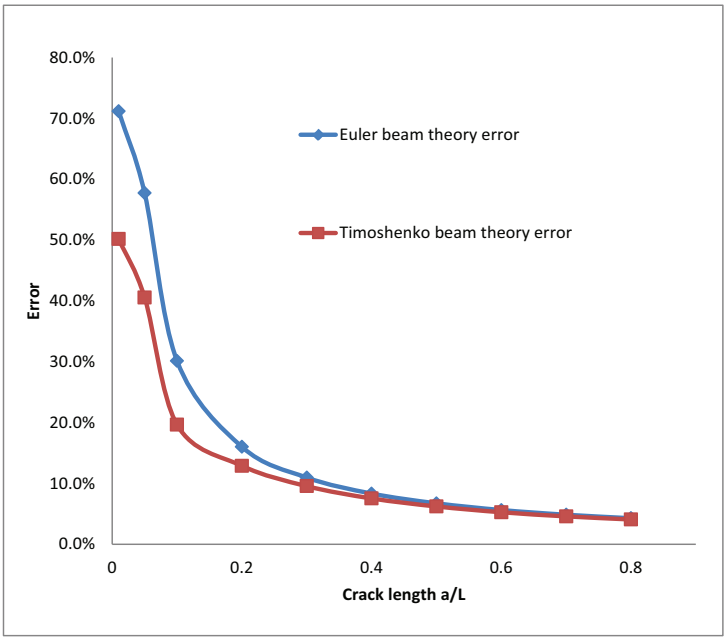

Figure 5.9: Error of the two different theories

smaller the crack length, the bigger the error of the computed SERR. The error of the SERR is bigger than 10% for the case that the crack $a \leq 0.2L$. The error is 20% for the case that the crack length $a = 0.1L$. The reason is that the beam theory is inadequate for a smaller crack and the singularity of the crack tip a much more pronounced effect on the SERR when the crack length is very close to zero.

The cracks discussed above, where there is propagation in one direction only or the SERR is the same for both crack tips, are special cases where the SERR is monotonically increasing. In the more general case, shown in Figure 5.3, where a crack could propagate at either end depending on the respective SERR. The length of a crack in a beam model is $a = x_2 - x_1$, x_1 and x_2 are the coordinates of the left crack tip and right crack tip, respectively. A thin beam model was created to find out the SERR tendency of the left and right crack tip. The crack was located at 1/3 of the thickness and the left tip of the crack was located at $x_1 = 0.1L$. The length of the beam was $L = 79.65mm$, the thickness was $t = 1.44mm$, the applied load was $P = 1N$. The SERR were evaluated for different crack lengths for both the left crack tip and the right crack tip, and compared with the SERR computed from finite element analysis, as shown in Figures 5.10 and 5.11. It is observed that the SERR obtained from analysis were in an overall good agreement with the finite element results. The depicted curve of the left crack tip's SERR versus crack length a is unlike the SERR curves for the symmetry cracks in 3PB model and DCB model, in which the SERRs are monotonically increasing. The SERR of the left crack tip is decreasing after reaching the peak point at $a \approx 0.55L$. The SERR curve of the right crack tip is more complicated than the curve of the left tip's SERR. As shown in Figure 5.11, the peak value of SERR of the right crack tip occurred at $a = 0.4L$, for which case $x_2 = 0.5L$, and the minimum SERR is almost zero when SERR of the left tip reached a maximum. After the SERR of the right crack tip reaches a minimum, it increases again.

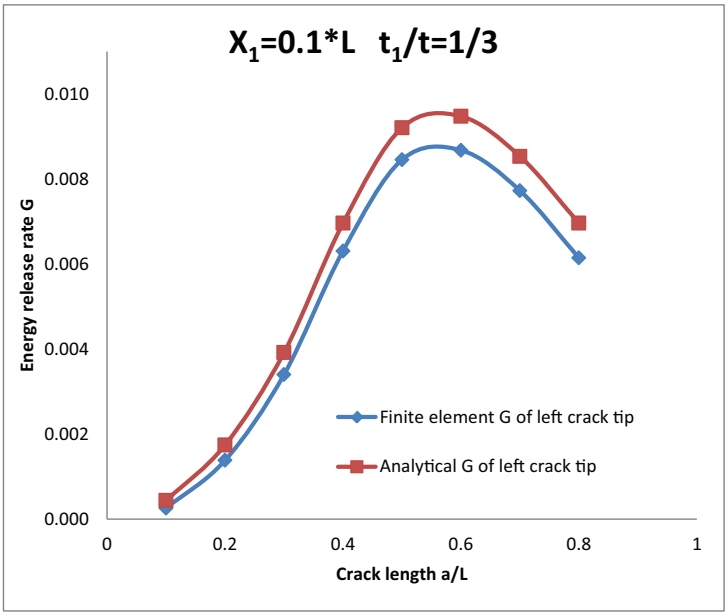

Figure 5.10: SERR of the left crack tip for isotropic beam for $x_1 = 0.1L$ and $t_1/t = 1/3$

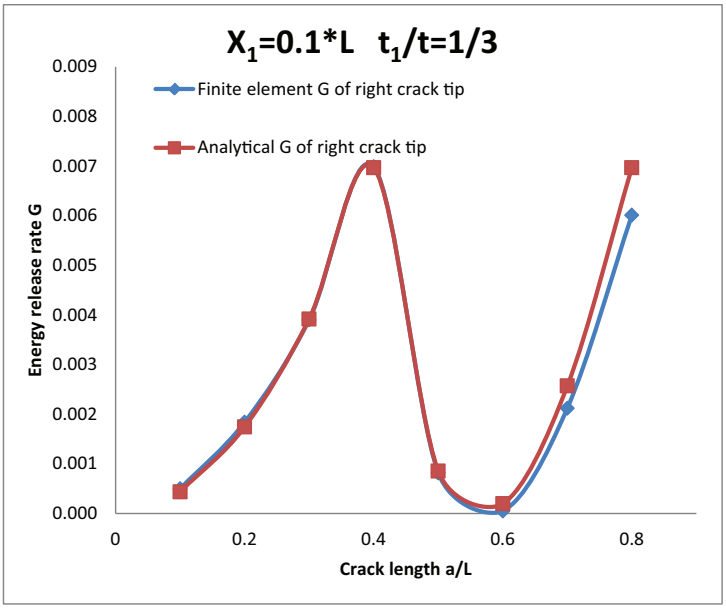

Figure 5.11: SERR of the right crack tip for isotropic beam for $x_1 = 0.1L$ and $t_1/t = 1/3$

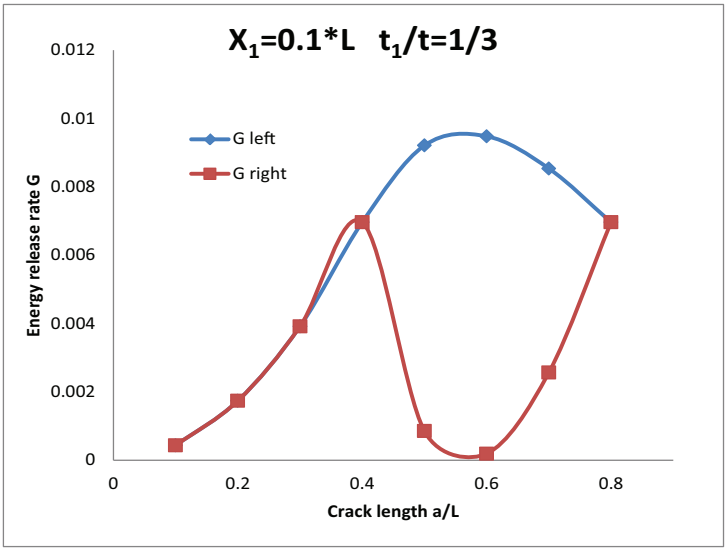

Figure 5.12: Analytical SERR for isotropic beam for $x_1 = 0.1L$ and $t_1/t = 1/3$

It is valuable to note that the SERR values for the two crack tips are equivalent when the whole crack is at the left or at the right of the load point, which means the crack can propagate to both sides before it goes across the load point. And the SERR of left crack tip equals to SERR of right tip for $a = 0.8L$ because the structure is symmetric when $x_1 = 0.1L$ and $x_2 = 0.9L$.

5.3 The special case of isotropic material

The verification of the analytical SERR of crack tip was conducted in the last section. In the following we will discuss the SERR of a crack in an isotropic beam model, as shown in Figure 5.3, in relation to different parameters, i.e. the position of the crack in the thickness direction t_1/t_2 or t_1/t, the location of the crack in the axial directions x_1 and x_2 and the isotropic material properties of the sub-beams after delamination initiation. We further discuss the possible problems of the analytical method to obtain SERR and possible reasons for discrepancies are discussed.

5.3.1 Parametric study

A three point bending beam model, the same as the one described in section 5.2.3, is employed for the parametric study. The length of the beam model is $L = 79.65mm$, the thickness is $t = 1.44mm$ and the applied load is $P = 1N$. A crack in the beam is located at $x_1 = 0.1L$ in the axial direction and the position of the crack in the thickness direction is varied to study its effect. The influence of the crack's position in the thickness direction on the SERR of the crack tip is shown in Figures 5.13 and 5.14.

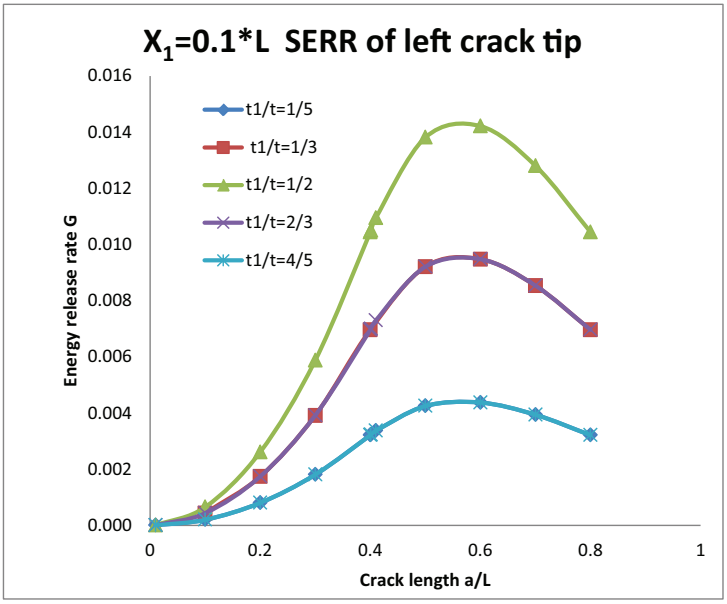

Figure 5.13: The influence of parameter t_1/t on SERR of left crack tip for isotropic beam $x_1 = 0.1L$

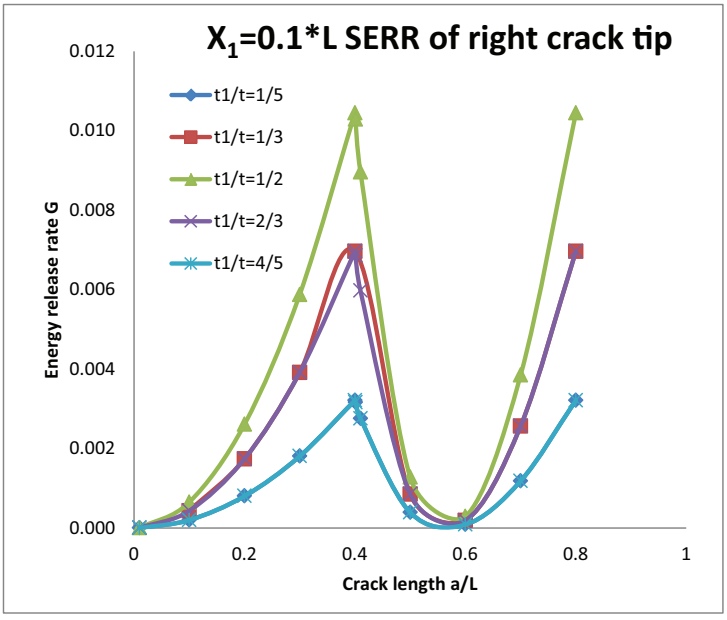

Figure 5.14: The influence of parameter t_1/t on SERR of right crack tip for isotropic beam $x_1 = 0.1L$

As demonstrated before, the increasing SERR of the left crack tip decreased after reaching the peak value and the curve shape of the right crack tip' SERR versus crack length is follows an inclined S shape. It is clearly shown in Figures 5.13 and 5.14 that the SERR of a crack located at t_1/t is equal to the SERR of a crack located at $1 - t_1/t$. The bigger the t_1/t $(0 < t_1 \leq 0.5t)$, the bigger the SERR of the crack.

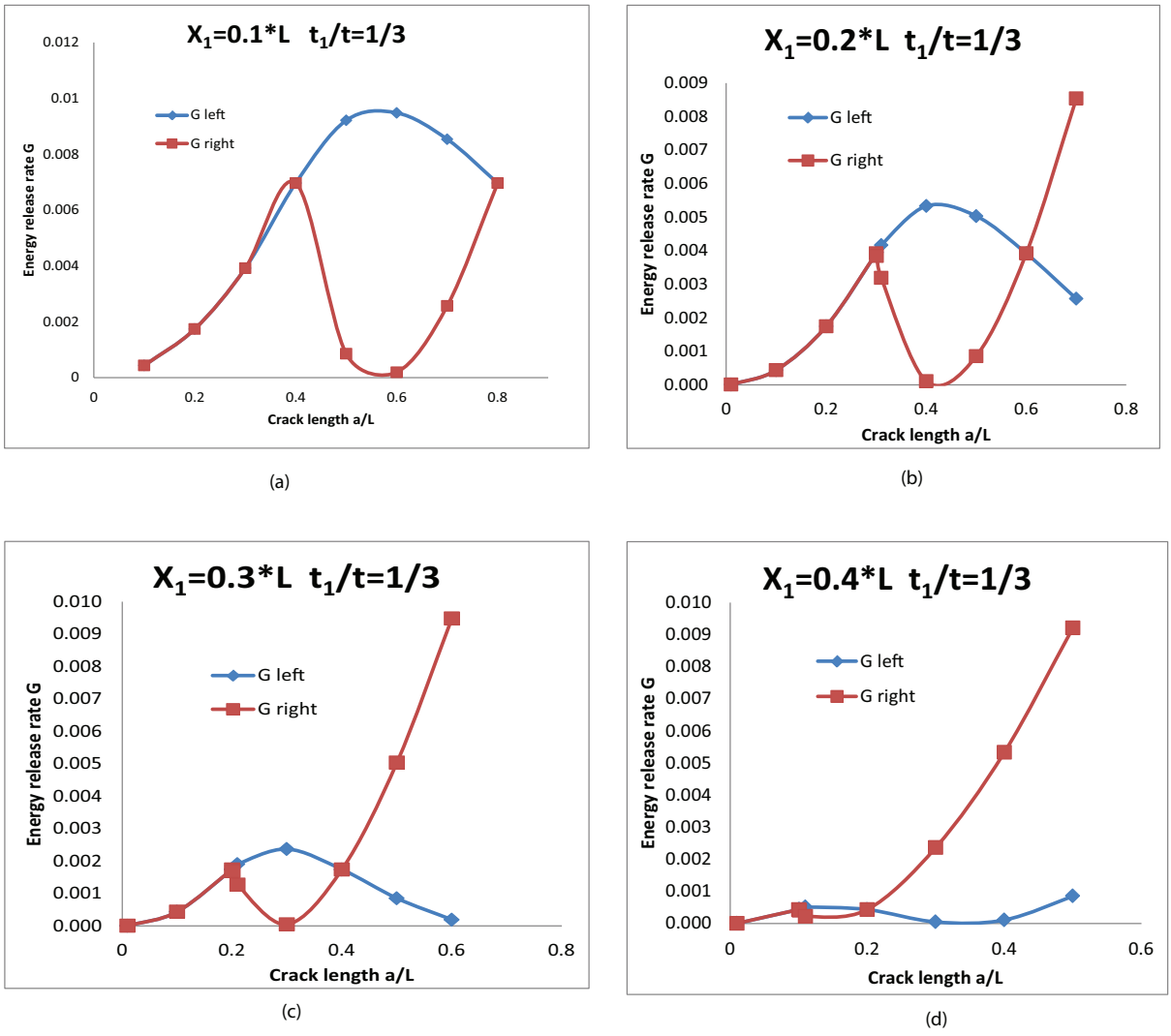

Figure 5.15: The influence of parameter x_1 on SERR for isotropic beam $t_1/t = 1/3$: (a) $x_1 = 0.1L$ (b) $x_1 = 0.2L$ (c) $x_1 = 0.3L$ (d) $x_1 = 0.4L$

In Figure 5.15, we show the influence of the crack tip location x_1 on the SERR of the crack tip. It is clearly seen that the SERR of left crack tip is bigger than or equal to that of right crack tip until the whole structure becomes symmetric in a 3PB beam model for the case that the crack is initiated from the left side of the loading point.

In Figure 5.16, we show the influence of crack tip location x_1 on the SERR of left crack tip. The position of the crack in the thickness direction is fixed as $t_1/t = 1/3$. The SERR of the left crack tip is the same for the equivalent crack length before the crack goes across the load point as shown in Figure 5.16 (a), and it is the same for the SERR of the

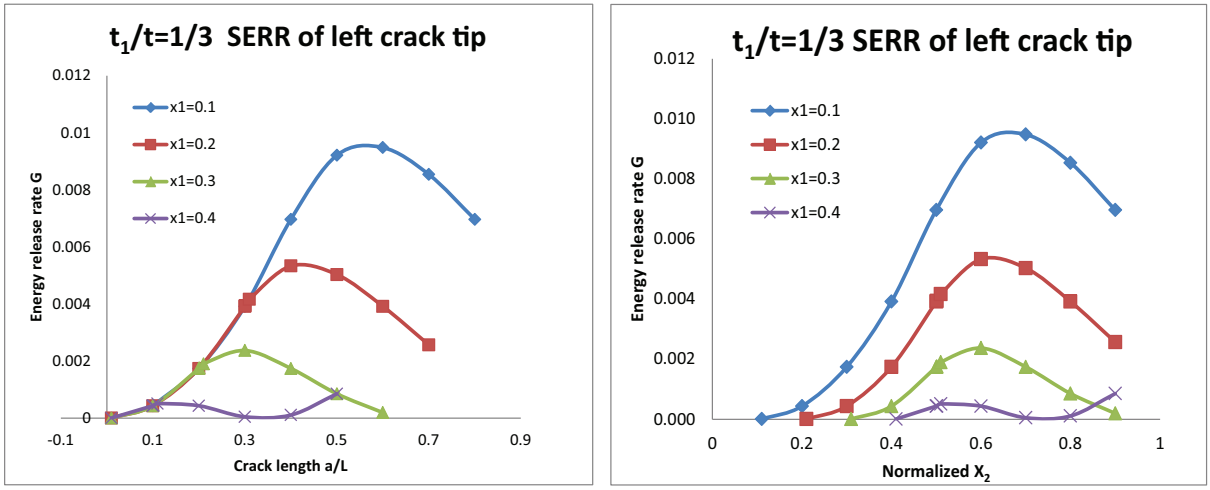

Figure 5.16: The influence of parameter x_1 on SERR of left crack tip for isotropic beam $t_1/t = 1/3$: (a) SERR versus crack length; (b) SERR vesus normalized x_2

right crack tip which can be seen in Figure 5.17 (a). The peak SERR of the left tip is at $x_2 \approx 0.55L$ from Figure 5.16 (b), whereas the maximum SERR of the right crack tip is at $x_2 = 0.5L$, as seen in Figure 5.17 (b).

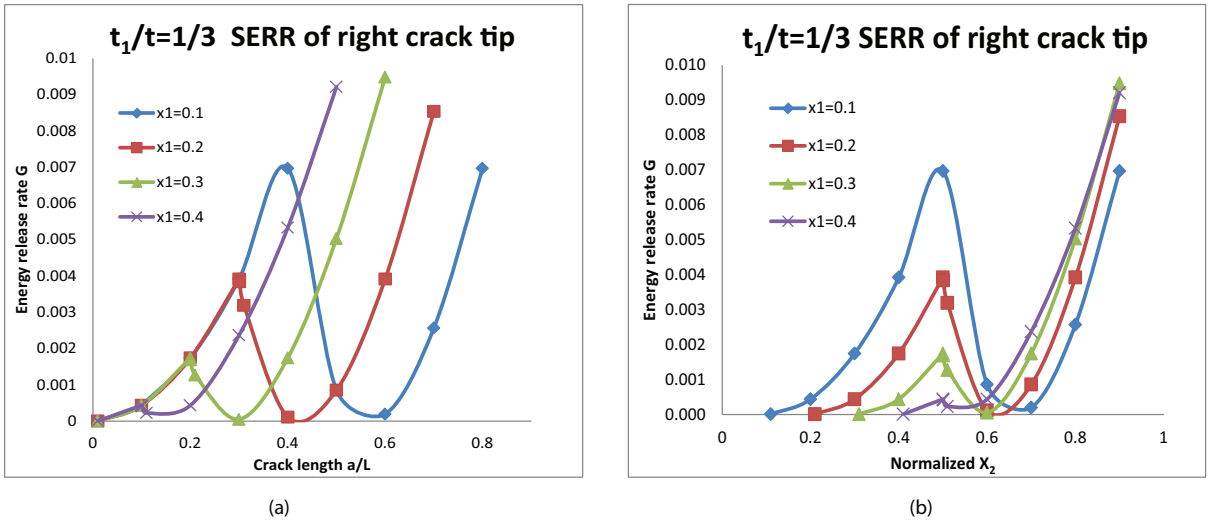

Figure 5.17: The influence of parameter x_1 on SERR of right crack tip for isotropic beam $t_1/t = 1/3$: (a) SERR versus crack length (b) SERR versus normalized x_2

Based on the parametric study, it can be concluded that: (1) as the crack is located closer to the top or the bottom of the beam, the SERR decreases; (2) the SERR of left crack tip and right tip are the same for a crack that does not go across the load point; (3) the SERR of the crack is only depending on the crack length and is not affected by the position of the crack in length direction as long as the crack is not under the load point; (4) the SERR of the left crack tip is bigger than or equal to that of right crack tip until the whole structure is symmetric for the case that the crack initiated from the left

side of the loading point; (5) the loading point is the peak point and changes the trend of the SERR of the right crack tip.

5.3.2 Results for large cracks, medium cracks and small cracks

The two theories, Euler beam theory and Timoshenko beam theory, are discussed in section 5.2.3 and the obtained SERR using these two theories are compared with the finite element solution. The errors of the two theories are shown in Figure 5.9, according to which the crack was categorized into three different types: large crack; medium crack and small crack, as shown in Figure 5.18.

$$\text{A crack is a} \begin{cases} \text{large crack ,} & \text{if } 0.5L \leq a < L \\ \text{medium crack ,} & \text{if } 0.2L \leq a \leq 0.5L \\ \text{small crack ,} & \text{if } 0 < a \leq 0.2L \end{cases}$$

A large crack is the one for which the Euler beam theory can be used to calculate the SERR and can meet the requirement of accuracy. If the shear effect could not be ignored or Timoshenko beam theory is necessary for a crack, then this crack is called medium crack. For a small crack, the beam theory is invalid and with decreasing of the crack length, the error of SERR obtained using beam theory is increasing. The error of the SERR is 70% for a small crack $a = 0.01L$, and the error could be even bigger depending on the location and the length of the crack.

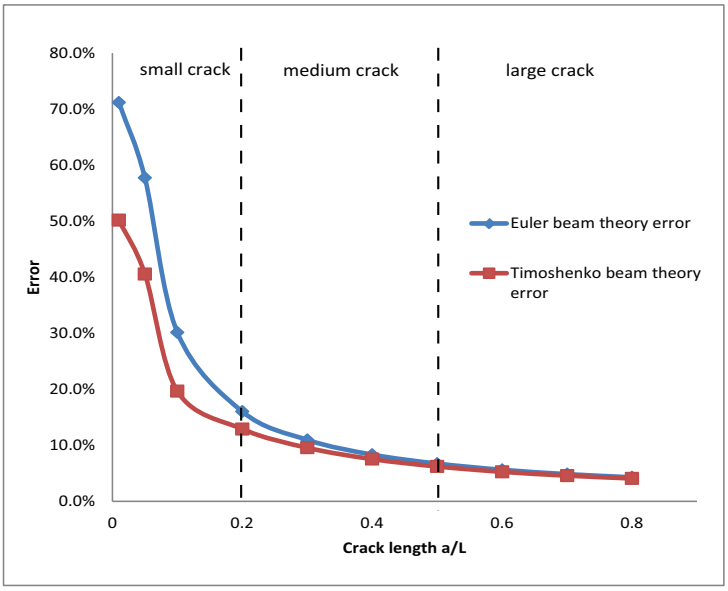

Figure 5.18: Three types of crack

There are two possible reasons that might explain the bigger error of the small crack. One reason is that the error is due to the beam theory: a small crack could not be considered as dividing the structure into two beam portions, therefore the beam theory is

not applicable to the case of small crack and a new theory is necessary to be used, which is out of the scope of this thesis. The other reason is that the error might come from the singularity of the crack tip. Based on linear fracture mechanics, for a small crack in an infinite body, the stress intensity factor $K_{II} = \tau\sqrt{\pi a}$ and the SERR that includes the singularity of the crack tip is $G = \dfrac{K_{II}^2}{E}$. Substituting τ into the expression of SERR, yields $G = \beta\dfrac{P^2 a}{Et^2}$, where β is an unknown coefficient for a crack in a finite elastic plane. For the structure in this thesis, the superposition method is employed, therefore it is assumed that the SERR is the sum of the SERR based on beam theory and the SERR because of the singularity of the crack tip. Thus the SERR of a small crack in a beam model is written as: $G = k\dfrac{P^2a^2}{Et^3} + \beta\dfrac{P^2a}{Et^2} = \dfrac{P^2a}{Et^2}(k\dfrac{a}{t} + \beta)$. The difficulty to calculate the SERR due to the singularity of the crack tip is that the coefficient β for the size effects of a crack in a finite specimen is unknown.

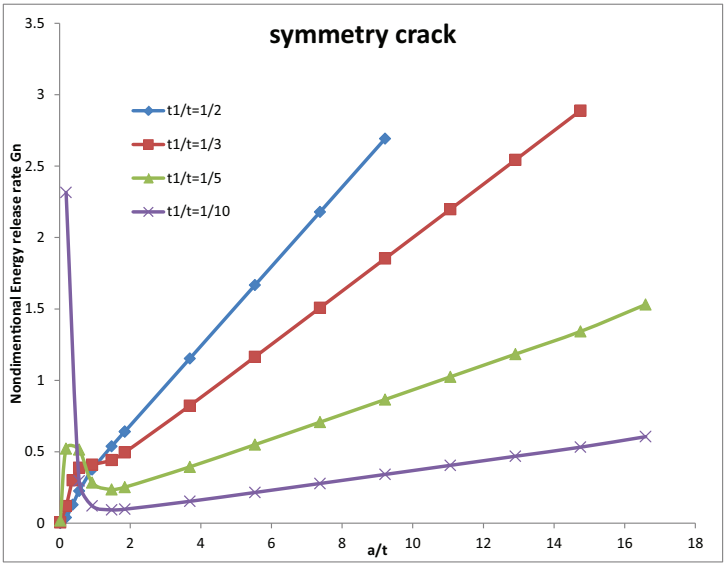

Figure 5.19: Nondimentional crack versus nondimentional crack length

It was found that variation of the nondimensional SERR with respect to the nondimensional crack length, shown in Figure 5.19, is linear for a symmetric crack in a whole model. The nondimensional SERR is defined as $G_n = \dfrac{G}{\dfrac{P^2a}{Et^2}}$, where P is the applied load, E is the Young's modulus of the material, a is crack length and t is the thickness of the model. The length of the whole model in Figure 5.19 is $L = 79.65mm$, the thickness is $t = 4.32mm$ and the load is $P = 100N$ in the middle of the model. With the crack closer to the load point in the thickness direction, the effect of the load point on the SERR of the crack tip for a very small crack is more pronounced. The error of a small crack, as defined $a \leq 0.2L$, which is the same expressed as $a \leq 4t$, is big compared with the medium crack and the large crack. The differences of the analytical SERR and the finite element results of SERR for small crack are shown in Figure 5.20 (a) and the error is

around 30%. The general analytical solution of SERR for symmetric crack is $G = k\frac{P^2a^2}{Et^3}$, therefore the nondimensional SERR is $G_n = k\frac{a}{t}$, k is the slope of the analytical SERR in Figure 5.20 (a). A constant correction factor C_n was introduced to increase the accuracy of small crack and was determined after fitting the curves in Figure 5.20 (a) and the expression of the corrected SERR is $G_{nc} = k\frac{a}{t} + C_n$. The corrected SERR of small crack agreed very well with the SERR obtained from finite element model as shown in Figure 5.20 (b).

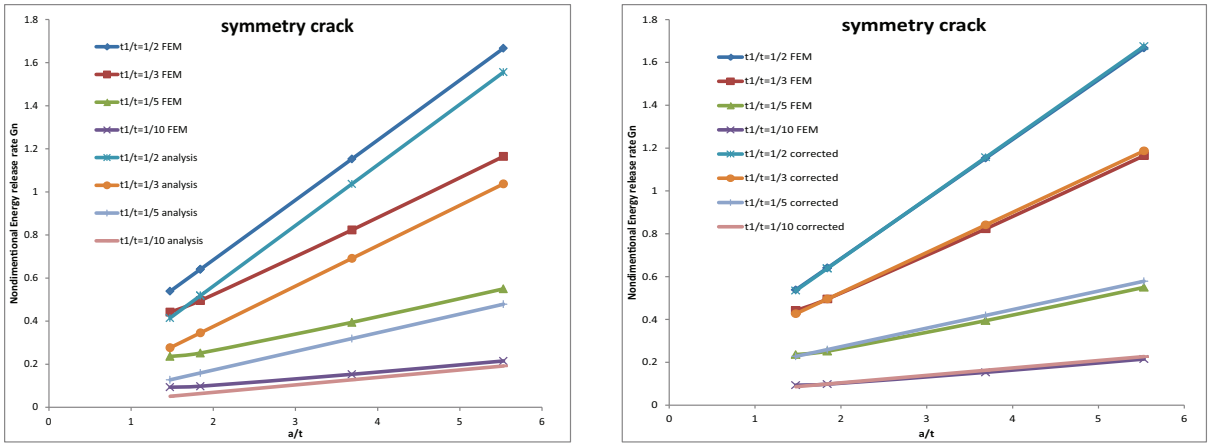

Figure 5.20: Nondimensional G_n versus nondimensional crack length a/t: (a) comparison between analytical SERR and finite element SERR results; (b) comparison between finite element SERR and corrected SERR

The correction factor C_n versus the nondimensional crack position $\frac{t_1}{t}$ is depicted in Figure 5.21, with two local maximum and a minimum, which is for a symmetry crack in a 3PB beam model. The correction factors are the same for crack located at $\frac{t_1}{t}$ and $1 - \frac{t_1}{t}$, which showed the same trend as the SERR of a crack. The correction factor for a crack that is not symmetric in the longitudinal direction is shown in Figure 5.22. The SERR of a crack that does not go across the load point is always the same for a crack with the same length that lies completely only in the left or the right side of the load point, therefore the crack location in the length direction is not related to the correction factor. The accuracy of SERR for a small crack was increased after the correction factor was implemented, whereas the error of SERR for the right crack tip may be greater, especially when the SERR value close to zero. A comparison of the finite element result, analytical solution and the corrected results of SERR is shown in Figure 5.23. The corrected SERR is much bigger than the SERR value from the finite element analysis for the case that SERR of the right crack tip is very small. The higher SERR is viewed as better than lower SERR since it would be conservative in a design situation.

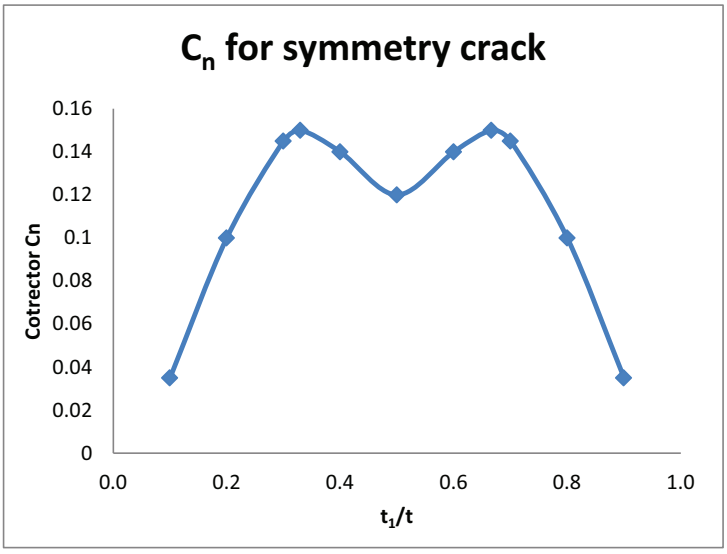

Figure 5.21: Correction factor C_n for symmetric crack

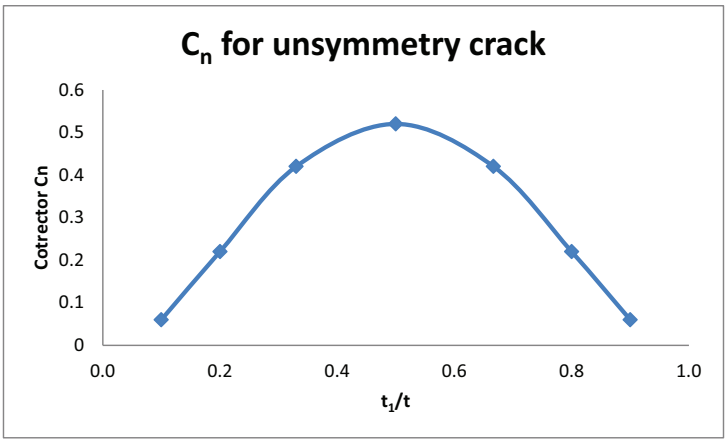

Figure 5.22: Correction factor C_n for unsymmetry crack

5.3.3 Problematic areas and possible reasons

The SERR of a crack was obtained and was classified into 3 different types based on which kind of theory is applied and the accuracy of the obtained SERR. Euler theory can be used for a large crack and Timoshenko beam theory is for a medium crack where shear effect could not be neglected. The error of the small crack is bigger than 10% and with decreasing of the crack length, the error increases. Two possible reasons caused the error of a small crack: (1) a small crack model can not be taken as a beam and a different theory needs to be developed which is out of the scope discussion of this thesis; (2) local effects at the crack tip caused by the singularity might be necessary to be included for a small crack, but because of the parameters for a finite crack in a certain body are unavailable, the singularity of the crack tip could not be included in calculating the SERR of a crack. Inspired by the non-dimensional SERR for analyzing the singularity of the crack tip, a correction factor was obtained that increased the accuracy of SERR for a

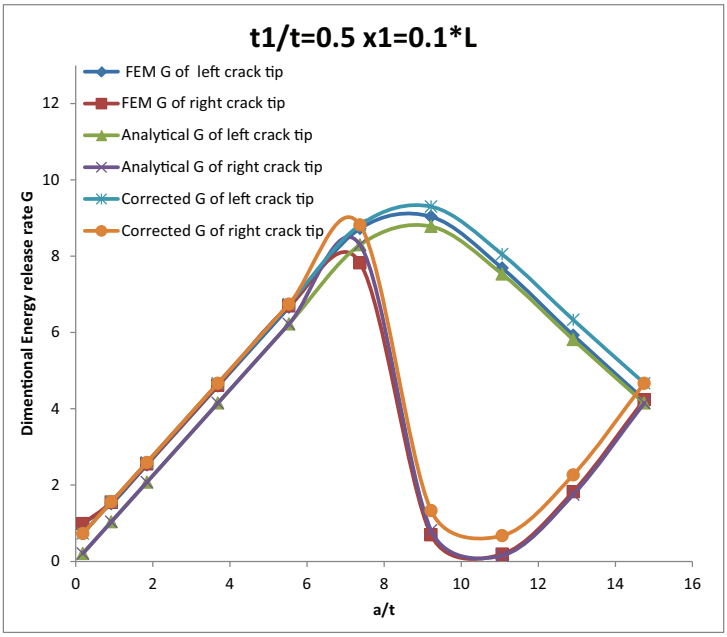

Figure 5.23: Comparison of the SERR for unsymmetrical crack

small crack, which is related to the location of the crack in the thickness direction. The used correction factor led to overestimation of SERR for a medium or large crack in cases where the SERR is very close to zero. In general, the overestimated SERR was accepted because it can be taken as a conservative value in the analysis of crack propagation.

5.4 Extension to a composite laminate

Composites are materials made of two or more constituents, the properties of which are different, such as matrix and fibers. Failures can occur as a result of many factors in composite laminates, including loads exceeding the load capability of the composite, uncertainties in the loading or environment, defects in the materials, inadequacies in design, and deficiencies in construction or maintenance. One of the most common failure modes in composite laminates is delamination between different layers. It is a concern in design of composite structures because of its susceptibility to growth and subsequent early failure of the structure. Therefore the ability to assess whether an existing delamination is going to propagate or not is critical for the safety assessment of the structure. In the following sections, the previously presented approach to obtain the SERR of a crack tip in a three-point-bending specimen is used to analyze the delamination in composite laminates. Due to the different properties of composite materials and isotropic materials, the analysis of SERR of a crack in composite laminate is more complicated than a crack in isotropic material.

5.4.1 Interfacial crack

The delamination in a composite laminate can also be called interlaminar damage, which is at the interface between different plies and can cause the degradation of the stiffness of the whole structure. For a crack on the interface, researchers [Wang and Choi, 1983; Rice, 1988; Hutchinson et al., 1987; Suo and Hutchinson, 1990] discuss the linear elasticity singularity of the crack tip region. The energy release rate of a semi-infinite crack at the interface of two different elastic materials [Suo and Hutchinson, 1990] is

$$G = \frac{C}{16}\left[\frac{P^2}{Ah} + \frac{M^2}{Ih^3} + 2\frac{PM}{\sqrt{AI}h^2\sin\gamma}\right] \tag{5.48}$$

where P and M are equivalent loads after superposition method applied, C is the compliance parameter relate to Poisson's ratio and shear modulus, h is the thickness of the top layers, A and I are positive dimensionless numbers that relate to Young's modulus of the two materials and geometry of the delaminated layers, γ is an angle that is restricted to $|\gamma| \leq \pi/2$ for the solution to exist.

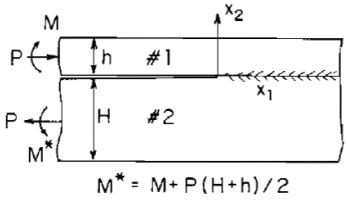

Figure 5.24: The geometry in Suo and Hutchinson [1990]

A model was built to check the effect of the singularity of crack tip on SERR. The length of the whole model is $L = 79.65mm$, thickness is $t = 4.32mm$ and the load is $P = 100N$ in the middle of the model, a symmetric crack is located in the middle of thickness direction at $\frac{t_1}{t} = 1/2$. It was found that the SERR at the interface between dissimilar materials is constant in a specific model and is independent of the length of crack $\frac{a}{L}$. A comparison of the finite element results, analytical solution without and analytical solution with the singularity of the crack tip was plotted in Figure 5.25, in which *alpha* is the same as Dundurs' parameter $\alpha = \frac{E_1 - E_2}{E_1 + E_2}$. With the increase in the crack length, the effect of crack tip's singularity decreases. For the model with a smaller crack length $\frac{a}{L} = 0.1$, the error is reduced from 25.6% to 17.1% after singularity of the crack tip was included for the case of $\alpha = 0.5$, and is reduced from 35.8% to 28.5% for the case of $\alpha = -0.5$. Including the singularity of the crack tip can increase the accuracy of the SERR. However, the error of the SERR is still big for small cracks using beam theory. The conclusion is that the correction factor in section 5.3.2 does not only include the effect of singularity of the crack tip but also a contribution accounting for the limitations of beam theory.

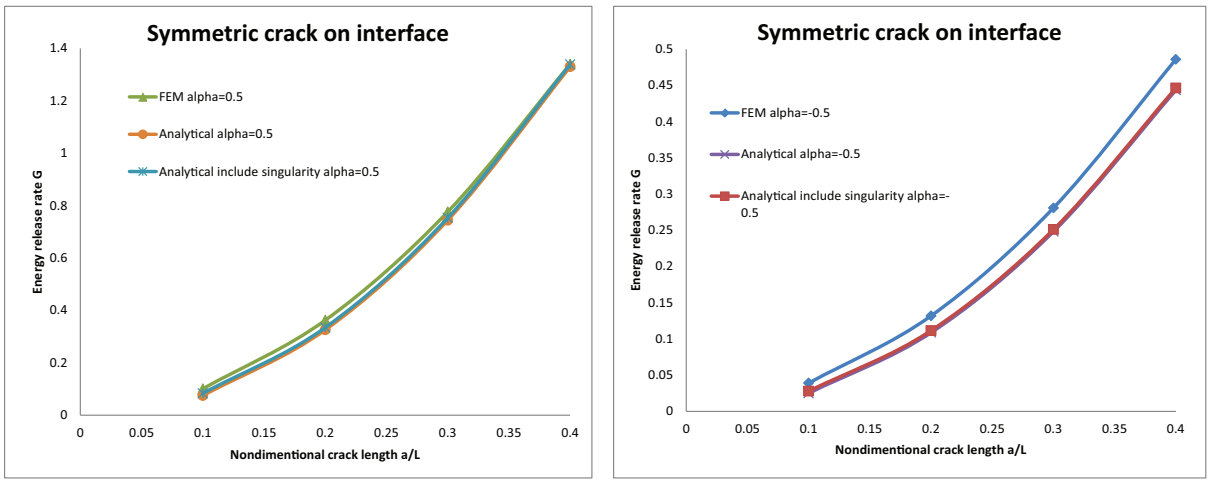

Figure 5.25: Comparison of the SERR from dissimilar material

5.4.2 Material formulation for 2D model

The composite laminates are classified into symmetric laminates, balanced laminates, cross-ply laminates, angle-ply laminates and quasi-isotropic laminates in practice. A delamination will change material properties of the whole structure and divide the laminate into two different laminates. The classical laminated plate theory [Kassapoglou, 2010] is employed to analyze the delaminated and undelaminated laminates. The materials used in this thesis are confined to orthotropic materials. A 3D AP-PLY composite laminate model under out-of-plane line loads was simplified into a 2D plane stress composite beam model, as shown in chapter 4.2.2, Figure 4.6.

For a composite laminate with a symmetric stacking sequence, the layup may be unsymmetrical after a delamination occurred. The B portion of the ABD is no longer zero, therefore the bending and the membrane behavior of the laminate are coupled. For a symmetric layup beam model, the complementary energy is:

$$\begin{aligned} U^* &= \frac{1}{2}\begin{Bmatrix} N \\ M \end{Bmatrix}^T \begin{Bmatrix} a_{11} \\ d_{11} \end{Bmatrix} \begin{Bmatrix} N \\ M \end{Bmatrix} \\ &= \frac{1}{2}(a_{11}N^2 + d_{11}M^2) \end{aligned} \tag{5.49}$$

where N and M are force and moment resultants, T is the transpose of the matrix, a_{11} and d_{11} are corresponding entries of the compliance matrix abd, which is the inverse of ABD matrix. For the delaminated composite laminates with unsymmetrical stacking sequence, the complementary energy is:

$$U^* = \frac{1}{2}a_{11}N^2 + \frac{1}{2}d_{11}M^2 + b_{11}MN \tag{5.50}$$

To decouple the moment and longitudinal force in the complementary energy, a new neutral line is formed, shown in Figure 5.26. After relocating the neutral line, N contributes

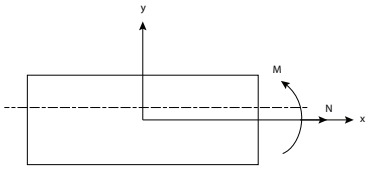

Figure 5.26: Decouple the force and moment

to the moment M. The distance from the old neutral line to the new neutral line is t_d. Thus the complementary energy can be reformed as:

$$\begin{aligned} U^* &= \frac{1}{2}a_{11}N^2 + \frac{1}{2}d_{11}M^2 + b_{11}NM \\ &= \frac{1}{2}a_{11}N^2 + \frac{1}{2}d_{11}(M + Nt_d)^2 + b_{11}N(M + Nt_d) \\ &= \frac{1}{2}(a_{11} + d_{11}t_d^2 + 2b_{11}t_d)N^2 + \frac{1}{2}d_{11}M^2 + (d_{11}MNt_d + b_{11}MN) \end{aligned} \tag{5.51}$$

The term $d_{11}MNt_d + b_{11}MN$ should equal zero to meet the decoupling requirement, which leads to:

$$t_d = -\frac{b_{11}}{d_{11}} \tag{5.52}$$

Substituting Eq. 5.52 into Eq. 5.51 gives:

$$U^* = \frac{1}{2}(a_{11} - \frac{b_{11}^2}{d_{11}})N^2 + \frac{1}{2}d_{11}M^2 \tag{5.53}$$

The new membrane stiffness is:

$$E_{1m} = \frac{1}{h(a_{11} - \frac{b_{11}^2}{d_{11}})} \tag{5.54}$$

and the bending stiffness is:

$$E_{1b} = \frac{12}{h^3 d_{11}} \tag{5.55}$$

A finite element composite laminate model with stacking sequence of $[90_5/0_5/90/0]_s$ was created to verify the calculated SERR of a crack in conventional laminates. The length of the model is $L = 79.65mm$, thickness is $t = 4.32mm$ and the load is in the middle of the beam. The left of the crack tip is fixed at either 0.1L or at 0.2L The locations of the right crack tips is allowed to change for different crack length a. The comparison of finite element results and analytical solution of SERR of left crack tip and right crack tip are shown in Figures 5.27 and 5.28. For the analytical predictions of the SERRs of a crack in a composite laminate, the approach is the same as for isotropic materials after removing the neutral axis and obtaining the new equivalent membrane and bending stiffness.

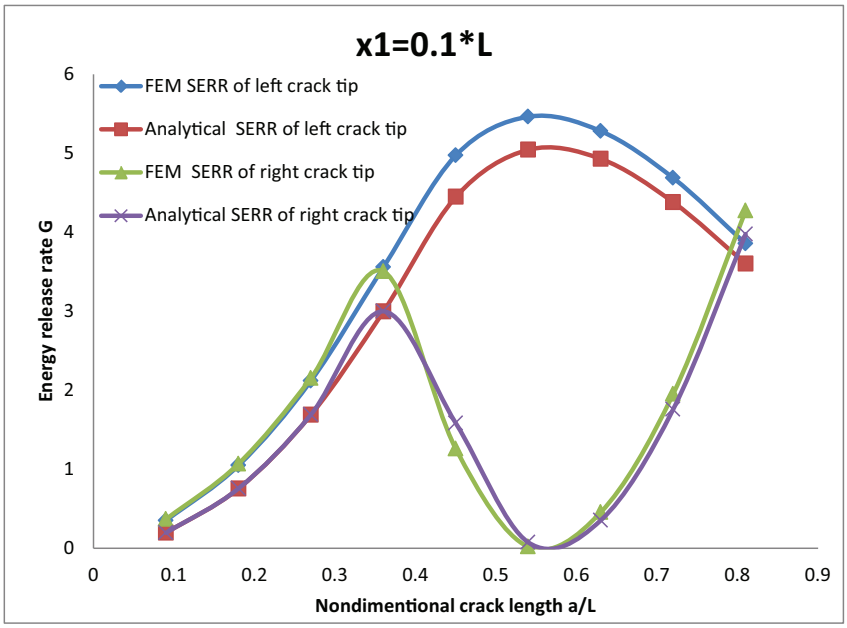

Figure 5.27: Comparison of SERR for composite laminate $x_1 = 0.1L$

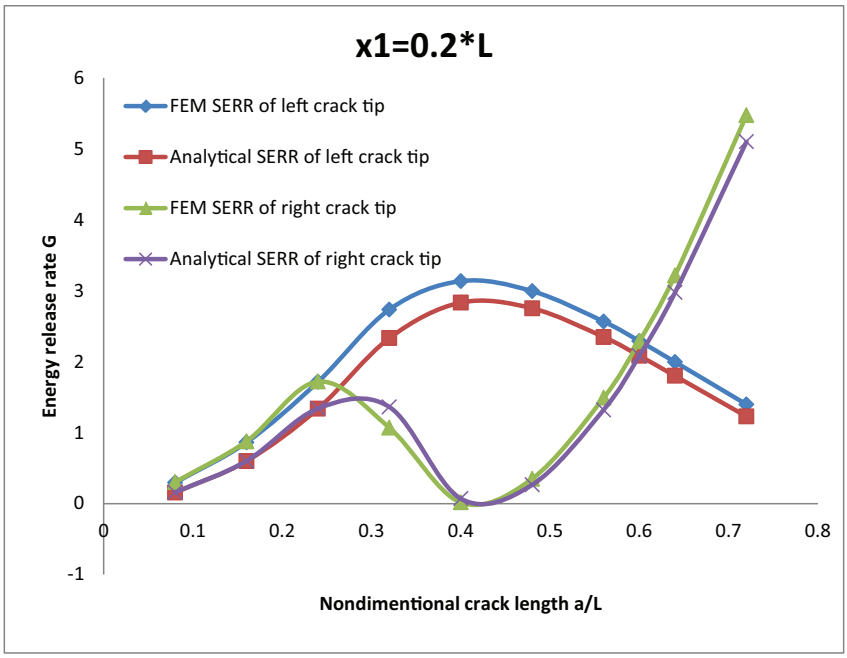

Figure 5.28: Comparison of SERR for composite laminate $x_1 = 0.2L$

It can be seen that as the crack length increases, the difference between the analytical SERR and the finite element results decreases. For the same crack length, the error of SERR of a crack in a composite laminate is bigger than that in an isotropic structure of the same geometry. The reason is that the description of material properties of isotropic structure is more accurate than that of composite laminates.

5.4.3 Extension to AP-PLY composite laminates

The energy method to calculate the SERR is applied to AP-PLY composite laminates what follows. A 2D AP-PLY composite laminate with a delamination in the structure is shown in Figure 5.29. In the structure, the green plies are the straight plies that are used to fill the gap left by the woven ply, and the red line represents the delamination in the structure. A delamination separates the laminates into sub-laminates and the material properties of sub-laminates need to be taken into account. For the unsymmetrical layup of composite laminates, the neutral line is moved to decouple the membrane and bending behavior as described in section 5.4.2. The woven ply and the resin divided the whole structure into different parts in the longitudinal direction and there are 4 different laminates for an intact AP-PLY composite laminate structure.

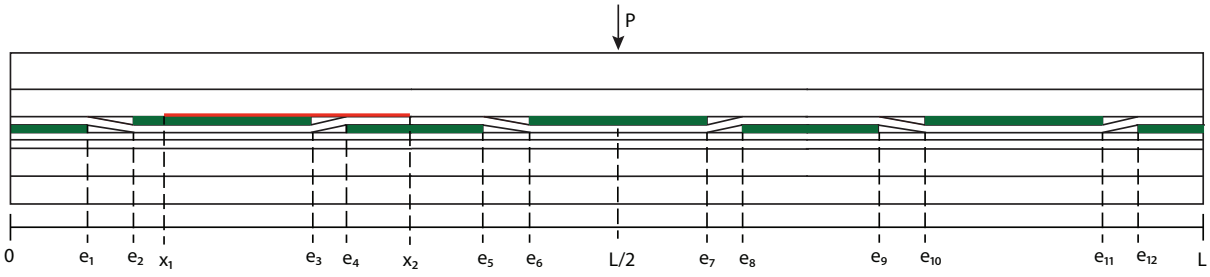

Figure 5.29: A delamination inside a 2D AP-PLY structure

Before examining the AP-PLY case in detail, a situation with different isotropic materials is examined with a crack crossing from one material to the next as it grows.

A crack goes across different isotropic materials

To find out how to determine the SERR of a crack in an AP-PLY composite laminate, a crack in a beam model that crosses different materials was modeled, shown in Figure 5.30, in which the red line represents the crack. Due to the different materials, the delaminated area was divided into 6 parts, x_1 is the location of the left crack tip, x_2 is the location of the right crack tip, and sub-beams were separated by transition points e_1 and e_2. For isotropic materials, the neutral lines of the 3 top sub-beams and the 3 bottom sub-beams

are at the same location, respectively. Here a general case was assumed, which is that the neutral lines of the 6 sub-beams are at different locations, as shown in Figure 5.30. The distance from the neutral lines of 3 top sub-beams to that of the 3 bottom sub-beams are c_1, c_2 and c_3, respectively.

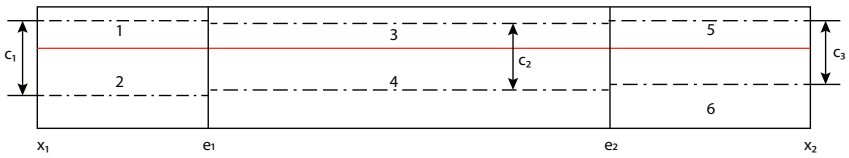

Figure 5.30: A crack across different materials

The internal axial forces, moments and shear forces for the different parts are shown in Figure 5.31. From the equilibrium of forces in the x direction, it was obtained that:

$$N_1|_{x=x_1} = N_1|_{x=e_1} = N_3|_{x=e_1} = N_3|_{x=e_2} = N_5|_{x=e_2} = N_5|_{x=x_2} = N \tag{5.56}$$

$$N_2|_{x=x_1} = N_2|_{x=e_1} = N_4|_{x=e_1} = N_4|_{x=e_2} = N_6|_{x=e_2} = N_6|_{x=x_2} = -N \tag{5.57}$$

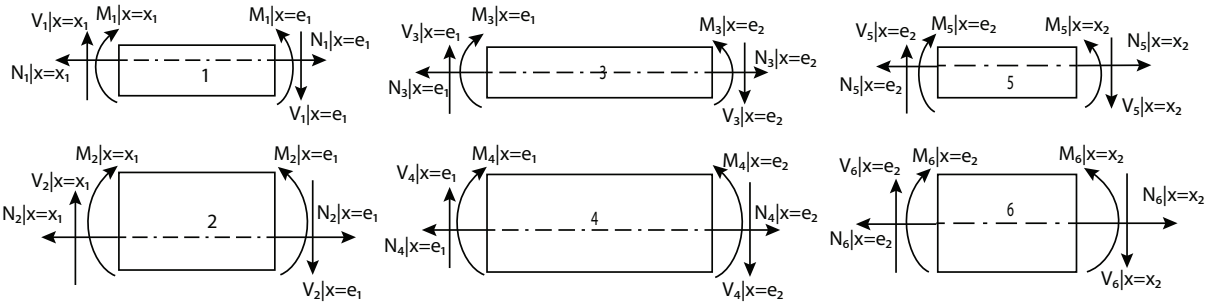

Figure 5.31: internal forces of different parts

Following the same procedure in section 5.2.2 to obtain the complementary energy of a delaminated beam, the complementary energy of the delaminated beams, which also is the objective function in Lagrange multiplier method to calculate the minimum energy

of delaminated beams, can be written as:

$$\begin{aligned}
U^* &= \frac{N^2}{2}\left(\frac{e_1-x_1}{E_1A_1}+\frac{e_1-x_1}{E_2A_2}+\frac{e_2-e_1}{E_3A_3}+\frac{e_2-e_1}{E_4A_4}+\frac{x_2-e_2}{E_5A_5}+\frac{x_2-e_2}{E_6A_6}\right)\\
&+\frac{1}{2}\Bigg\{\frac{e_1-x_1}{3E_1I_1}\left[\left(M_1|_{x=x_1}\right)^2+\left(M_1|_{x=e_1}\right)^2+\left(M_1|_{x=x_1}\right)\left(M_1|_{x=e_1}\right)\right]\\
&+\frac{e_1-x_1}{3E_2I_2}\left[\left(M_2|_{x=x_1}\right)^2+\left(M_2|_{x=e_1}\right)^2+\left(M_2|_{x=x_1}\right)\left(M_2|_{x=e_1}\right)\right]\\
&+\frac{e_2-e_1}{3E_3I_3}\left[\left(M_3|_{x=e_1}\right)^2+\left(M_3|_{x=e_2}\right)^2+\left(M_3|_{x=e_1}\right)\left(M_3|_{x=e_2}\right)\right]\\
&+\frac{e_2-e_1}{3E_4I_4}\left[\left(M_4|_{x=e_1}\right)^2+\left(M_4|_{x=e_2}\right)^2+\left(M_4|_{x=e_1}\right)\left(M_4|_{x=e_2}\right)\right]\\
&+\frac{x_2-e_2}{3E_5I_5}\left[\left(M_5|_{x=e_2}\right)^2+\left(M_5|_{x=x_2}\right)^2+\left(M_5|_{x=e_2}\right)\left(M_5|_{x=x_2}\right)\right] \qquad (5.58)\\
&+\frac{x_2-e_2}{3E_6I_6}\left[\left(M_6|_{x=e_2}\right)^2+\left(M_6|_{x=x_2}\right)^2+\left(M_6|_{x=e_2}\right)\left(M_6|_{x=x_2}\right)\right]\Bigg\}\\
&+\frac{\left(M_1|_{x=e_1}-M_1|_{x=x_1}\right)^2}{2(e_1-x_1)\alpha_sG_1A_1}+\frac{\left(M_2|_{x=e_1}-M_2|_{x=x_1}\right)^2}{2(e_1-x_1)\alpha_sG_2A_2}+\frac{\left(M_3|_{x=e_2}-M_3|_{x=e_1}\right)^2}{2(e_2-e_1)\alpha_sG_3A_3}\\
&+\frac{\left(M_4|_{x=e_2}-M_4|_{x=e_1}\right)^2}{2(e_2-e_1)\alpha_sG_4A_4}+\frac{\left(M_5|_{x=x_2}-M_5|_{x=e_2}\right)^2}{2(x_2-e_2)\alpha_sG_5A_5}+\frac{\left(M_6|_{x=x_2}-M_6|_{x=e_2}\right)^2}{2(x_2-e_2)\alpha_sG_6A_6}
\end{aligned}$$

The continuity conditions at $x = x_1$, $x = e_1$, $x = e_2$ and $x = x_2$, which are also the constraint conditions for the Lagrange Multipliers method to obtain the minimum complementary energy of the delaminated beam, are as follows:

$$M_1|_{x=x_1} + M_2|_{x=x_1} - Nc_1 = \frac{P}{2}x_1 \qquad (5.59)$$

$$M_1|_{x=e_1} + M_2|_{x=e_1} - Nc_1 = \frac{P}{2}e_1 \qquad (5.60)$$

$$M_3|_{x=e_1} + M_4|_{x=e_1} - Nc_2 = \frac{P}{2}e_1 \qquad (5.61)$$

$$M_3|_{x=e_2} + M_4|_{x=e_2} - Nc_2 = \frac{P}{2}e_2 \qquad (5.62)$$

$$M_5|_{x=e_2} + M_6|_{x=e_2} - Nc_3 = \frac{P}{2}e_2 \qquad (5.63)$$

$$M_5|_{x=x_2} + M_6|_{x=x_2} - Nc_3 = \frac{P}{2}x_2 \qquad (5.64)$$

The number of the constraint conditions is the same as the number of the introduced Lagrange multipliers. The Lagrange multipliers are λ_1 to λ_6. Differentiating the Lagrangian with respect to N gives:

$$\begin{aligned}
N\left(\frac{e_1-x_1}{E_1A_1}+\frac{e_1-x_1}{E_2A_2}+\frac{e_2-e_1}{E_3A_3}+\frac{e_2-e_1}{E_4A_4}+\frac{x_2-e_2}{E_5A_5}+\frac{x_2-e_2}{E_6A_6}\right) &= \\
-c_1(\lambda_1+\lambda_2)-c_2(\lambda_3+\lambda_4)-c_3(\lambda_5+\lambda_6) \qquad (5.65)
\end{aligned}$$

Differentiating the Lagrangian with respect to each of the moments gives a system of equations:

$$\begin{bmatrix} C_{11} & 0 & C_{12} & 0 & 0 & 0 & 0 & 0 & 0 & 0 & 0 & 0 \\ 0 & C_{21} & 0 & C_{22} & 0 & 0 & 0 & 0 & 0 & 0 & 0 & 0 \\ C_{12} & 0 & C_{11} & 0 & 0 & 0 & 0 & 0 & 0 & 0 & 0 & 0 \\ 0 & C_{22} & 0 & C_{21} & 0 & 0 & 0 & 0 & 0 & 0 & 0 & 0 \\ 0 & 0 & 0 & 0 & C_{31} & 0 & C_{32} & 0 & 0 & 0 & 0 & 0 \\ 0 & 0 & 0 & 0 & 0 & C_{41} & 0 & C_{42} & 0 & 0 & 0 & 0 \\ 0 & 0 & 0 & 0 & C_{32} & 0 & C_{31} & 0 & 0 & 0 & 0 & 0 \\ 0 & 0 & 0 & 0 & 0 & C_{42} & 0 & C_{41} & 0 & 0 & 0 & 0 \\ 0 & 0 & 0 & 0 & 0 & 0 & 0 & 0 & C_{51} & 0 & C_{52} & 0 \\ 0 & 0 & 0 & 0 & 0 & 0 & 0 & 0 & 0 & C_{61} & 0 & C_{62} \\ 0 & 0 & 0 & 0 & 0 & 0 & 0 & 0 & C_{52} & 0 & C_{51} & 0 \\ 0 & 0 & 0 & 0 & 0 & 0 & 0 & 0 & 0 & C_{62} & 0 & C_{61} \end{bmatrix} \begin{bmatrix} M_1|_{x=x_1} \\ M_2|_{x=x_1} \\ M_1|_{x=e_1} \\ M_2|_{x=e_1} \\ M_3|_{x=e_1} \\ M_4|_{x=e_1} \\ M_3|_{x=e_2} \\ M_4|_{x=e_2} \\ M_5|_{x=e_2} \\ M_6|_{x=e_2} \\ M_5|_{x=x_2} \\ M_6|_{x=x_2} \end{bmatrix} = \begin{bmatrix} \lambda_1 \\ \lambda_1 \\ \lambda_2 \\ \lambda_2 \\ \lambda_3 \\ \lambda_3 \\ \lambda_4 \\ \lambda_4 \\ \lambda_5 \\ \lambda_5 \\ \lambda_6 \\ \lambda_6 \end{bmatrix} \tag{5.66}$$

where the constants are:

$$C_{11} = \frac{e_1 - x_1}{3E_1I_1} + \frac{1}{(e_1 - x_1)G_1A_1}, \quad C_{12} = \frac{e_1 - x_1}{6E_1I_1} - \frac{1}{(e_1 - x_1)G_1A_1} \tag{5.67}$$

$$C_{21} = \frac{e_1 - x_1}{3E_2I_2} + \frac{1}{(e_1 - x_1)G_2A_2}, \quad C_{22} = \frac{e_1 - x_1}{6E_2I_2} - \frac{1}{(e_1 - x_1)G_2A_2} \tag{5.68}$$

$$C_{31} = \frac{e_2 - e_1}{3E_3I_3} + \frac{1}{(e_2 - e_1)G_3A_3}, \quad C_{32} = \frac{e_2 - e_1}{6E_3I_3} - \frac{1}{(e_2 - e_1)G_3A_3} \tag{5.69}$$

$$C_{41} = \frac{e_2 - e_1}{3E_4I_4} + \frac{1}{(e_2 - e_1)G_4A_4}, \quad C_{42} = \frac{e_2 - e_1}{6E_4I_4} - \frac{1}{(e_2 - e_1)G_4A_4} \tag{5.70}$$

$$C_{51} = \frac{x_2 - e_2}{3E_5I_5} + \frac{1}{(x_2 - e_2)G_5A_5}, \quad C_{52} = \frac{x_2 - e_2}{6E_5I_5} - \frac{1}{(x_2 - e_2)G_5A_5} \tag{5.71}$$

$$C_{61} = \frac{x_2 - e_2}{3E_6I_6} + \frac{1}{(x_2 - e_2)G_6A_6}, \quad C_{62} = \frac{x_2 - e_2}{6E_6I_6} - \frac{1}{(x_2 - e_2)G_6A_6} \tag{5.72}$$

where E_iI_i and G_iA_i are the bending stiffness and shear stiffness of the ith part, respectively.

All of the unknowns related to the generalized forces in a delaminated beam and the Lagrange multipliers were obtained after solving Eqs. 5.59-5.64, Eq. 5.65 and the system of equations 5.66. Then the SERRs of each of the crack tips were calculated using Eqs. 5.44 and 5.45. We selected a half beam model that was composed of different isotropic material parts, shown in Figure 5.32, to demonstrate the performance of the proposed method.

The length of the simply supported 3 point bending half beam model is $L = 39.825mm$, the thickness is $t = 4.32mm$ and the applied load for the half model is $P = 50N$. The transition points from one material to the other are e_1 and e_2 and the coordinates of these

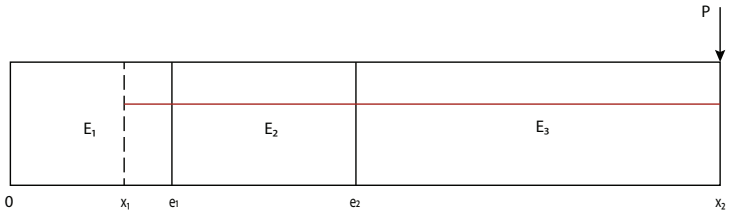

Figure 5.32: A half model with 3 different isotropic materials

two transition points were $0.2L$ and $0.5L$, respectively. A crack is located at through the thickness location of $\frac{t_1}{t} = \frac{1}{3}$, where t_1 is the thickness of the top layer and t is the total thickness of the intact beam. As the crack length increases, the crack goes across different materials. Different cases were examined with different property combinations for the materials used. The Young's moduli of the materials used in the first case were $E_1 = 10GPa$, $E_2 = 20GPa$, $E_3 = 30GPa$, and in the second case, $E_1 = 36.616GPa$, $E_2 = 10GPa$, $E_3 = 30GPa$. The Poisson's ratio for all materials was $\nu = 0.3$. The predicted SERRs of a crack in these two situations of different materials in succession, and a comparison with the simulation SERR results, are shown in Figures 5.33 and 5.34.

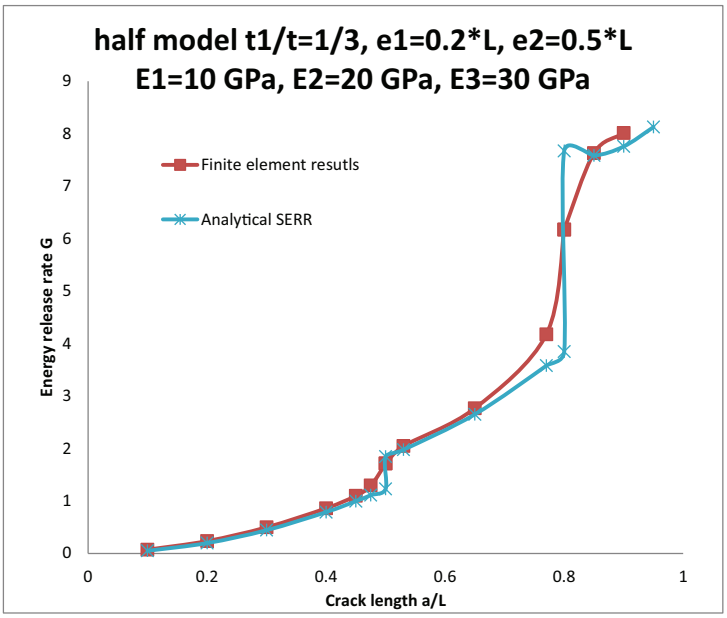

Figure 5.33: SERR of model with isotropic materials $E_1 = 10GPa$, $E_2 = 20GPa$ and $E_3 = 30GPa$

It is necessary to point out that there are two different analytical SERR values for the transition point from one material to the next in Figures 5.33 and 5.34. In the analytical method, the singularity at the transition from one material to the next does not allow calculation of the SERR at that location. To solve this problem, the upper-bound and lower-bound of SERR are obtained based on the two materials separately by calculating SERR approaching the transition from the left using properties of the material on the

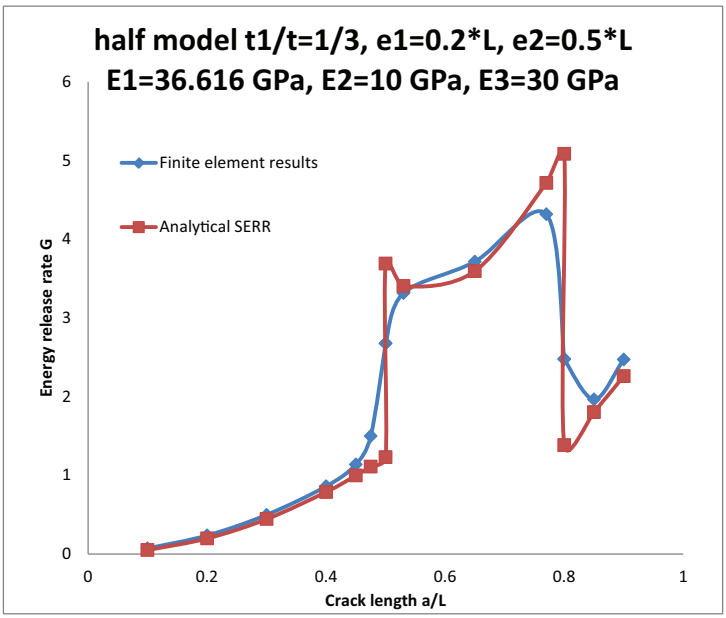

Figure 5.34: SERR of model with isotropic materials $E_1 = 36.616GPa$, $E_2 = 10GPa$ and $E_3 = 30GPa$

left and from the right using properties of the material from the right. The SERR of the transition point from the finite element simulation is between the SERRs calculated based on the two materials. The error of the analytical SERR for a smaller crack is the same as described in section 5.3.2. The closer the crack tip to the transition point, the lower the accuracy of the computed SERR. Fenner [1976] analyze the stress singularities in composite materials when a propagating crack encounters an interface with a different material, which can explain the low accuracy when the crack tip close to the transition point and is not included in the analytical solution. It can be seen from the two Figures 5.33 and 5.34 that the stiffer material has lower SERR. The analytical solution of SERR agreed very well with the finite element results, except when the crack tip is located at the transition point which cannot be treated by the analytical method.

A crack across different parts of AP-PLY

To obtain the SERR of a crack that goes across AP-PLY, it is necessary to determine the material properties of different parts. The bending stiffness and the membrane stiffness were calculated by computing the neutral axis of different portions. The neutral axis and the membrane, bending and shear stiffness can be calculated for the parts including the resin area as shown in Figure 5.35. The part that includes the resin area can be taken as 3 areas: one with the two triangular resin areas, the second is the woven ply portion, and the third is the laminate with stacking sequence $[0/90/0_5/90_5]$. The stiffness of the laminate and the new neutral line, NA_2, as shown in Figure 5.35, which was used to decouple the moment and axial load, can be computed as described in section 5.4.2 for the unsymmetrical layup of composite laminates. For the two triangular resin areas and

the woven ply area, the neutral axis, NA_1, was approximately calculated and was taken to be at the middle of the two layers. The neutral line of the part including the resin

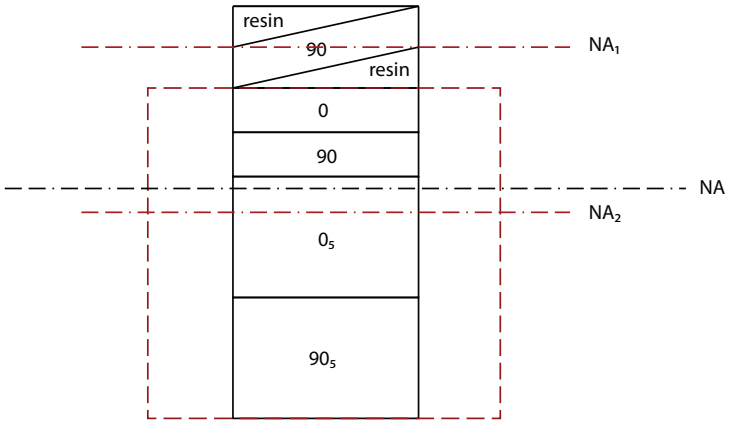

Figure 5.35: The structure of the part including resin area

area, woven ply and laminate, can be obtained using the equation below:

$$\bar{y} = \frac{\sum (EAy)_i}{\sum (EA)_i} \tag{5.73}$$

where E is membrane modulus of the material, A is the cross-sectional area, y is the distance from the bottom line to the neutral line.

Based on the Parallel Axis Theorem, the moment of inertia of the part, shown in Figure 5.35 is given by:

$$I_{xx} = I_c + Ad^2 \tag{5.74}$$

where I_{xx} is the moment of inertia with respect to xx axis, I_c is the moment of inertia with respect to the centroid line, A is the area of the cross section and d is the distance from the centroid line to xx axis.

Finally, the membrane stiffness of the part including the resin area is the sum of the membrane stiffness of the woven ply, the two triangular areas and the laminate $[0/90/0_5/90_5]$. The calculation of the bending stiffness and the shear stiffness followed the same procedure as for membrane stiffness.

The SERR of a crack in an AP-PLY composite laminate is calculated following the procedure described in subsection 5.4.3 after the stiffness of different parts is determined. For a crack that goes across n types of different materials, there are $2n$ parts of delaminated sub-beams and $n + 1$ points from the left crack tip to the right crack tip including the two points of the crack front. Taken Figure 5.30 as an example, a crack growth across 3 different materials, thus there are 6 parts of sub-beams and 4 points, x_1, e_1, e_2 and x_2 that need to be analyzed. Using Lagrange multipliers, the unknown moments, tension and shear forces in different parts are obtained after solving a series of equations in the

form shown below with $i \in [1, n]$:

$$N \sum_{i=1}^{n} \left(\frac{x_{i+1} - x_i}{(EA)_{2i-1}} + \frac{x_{i+1} - x_i}{(EA)_{2i}} \right) = -\sum_{i=1}^{n} c_i(\lambda_{2i-1} + \lambda_{2i}) \tag{5.75}$$

$$\begin{bmatrix} C_{(2i-1)1} & 0 & C_{(2i-1)2} & 0 \\ 0 & C_{(2i)1} & 0 & C_{(2i)2} \\ C_{(2i-1)2} & 0 & C_{(2i-1)1} & 0 \\ 0 & C_{(2i)2} & 0 & C_{(2i)1} \end{bmatrix} \begin{bmatrix} M_{2i-1}|_{x=x_i} \\ M_{2i}|_{x=x_i} \\ M_{2i-1}|_{x=x_{i+1}} \\ M_{2i}|_{x=x_{i+1}} \end{bmatrix} = \begin{bmatrix} \lambda_{2i-1} \\ \lambda_{2i-1} \\ \lambda_{2i} \\ \lambda_{2i} \end{bmatrix} \tag{5.76}$$

$$M_{2i-1}|_{x=x_i} + M_{2i}|_{x=x_i} - Nc_i = \begin{cases} \dfrac{P}{2} x_i, & x_i \leq \dfrac{L}{2} \\ \dfrac{P}{2}(L - x_i), & x_i \geq \dfrac{L}{2} \end{cases}$$

$$M_{2i-1}|_{x=x_{1+1}} + M_{2i}|_{x=x_{i+1}} - Nc_i = \begin{cases} \dfrac{P}{2} x_{i+1}, & x_{i+1} \leq \dfrac{L}{2} \\ \dfrac{P}{2}(L - x_{i+1}), & x_{i+1} \geq \dfrac{L}{2} \end{cases}$$

where x_i is the coordinate of the i point, c_i is the distance from neutral line of part $2i-1$ to that of part $2i$, and the constants are:

$$C_{(2i-1)1} = \frac{x_{i+1} - x_i}{3(EI)_{2i-1}} + \frac{1}{(x_{i+1} - x_i)(GA)_{2i-1}} \tag{5.77}$$

$$C_{(2i-1)2} = \frac{x_{i+1} - x_i}{6(EI)_{2i-1}} - \frac{1}{(x_{i+1} - x_i)(GA)_{2i-1}} \tag{5.78}$$

As is shown in Figure 5.29, an AP-PLY beam model with stacking sequence $[90_5/0_5/(90^w/0^f)/0/90/0_5/90_5]$ was created to demonstrate the process so as to determine the analytical SERR of a crack. The length of the beam is $L = 79.65mm$, the thickness is $t = 4.32mm$, the applied load is $P = 100N$, and the crack is located at $\frac{t_1}{t} = \frac{5}{12}$. In addition, the material properties of the ply and resin are the same as what is described in section 3.2.1. The obtained analytical solution was compared with finite element results as is shown in Figure 5.36. The error of analytical SERR of small crack in AP-PLY composite laminate is bigger than 25%, the error of medium crack is between of 15% and 25% and the error of large crack is bigger than 10% but lower than 15%. In general, the error of analytical SERR of AP-PLY is bigger than that of composite laminate, which is bigger than that of isotropic material. The error might be attributed to the limitation of the beam theory, the singularity of the crack tip as well as the approximation of material properties of the part including the resin pockets.

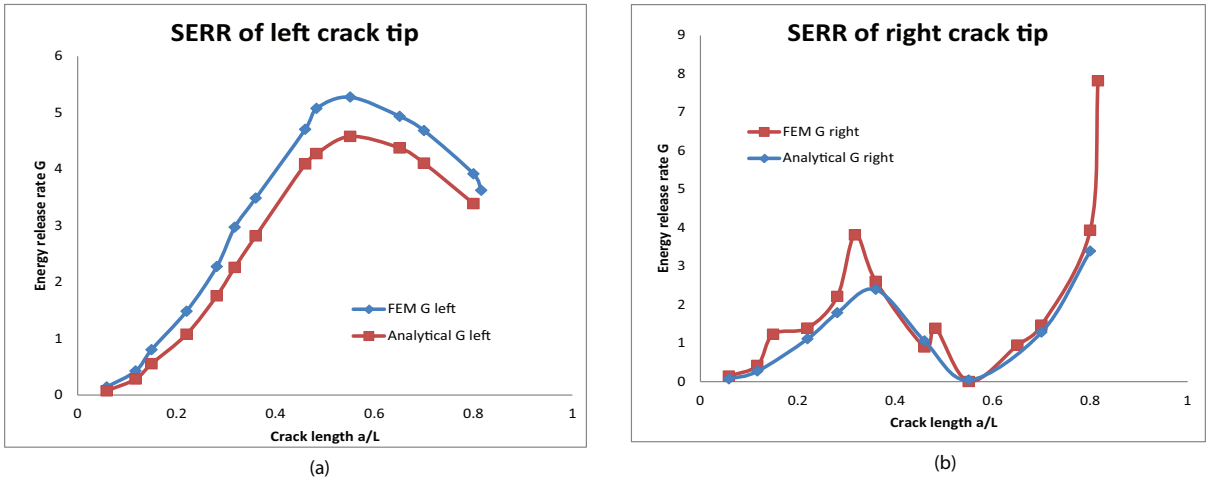

Figure 5.36: SERR of AP-PLY composite laminates (a) SERR of left crack tip (b) SERR of right crack tip

5.4.4 Parametric research of a case when a crack grows across different parts

As an interesting follow-on to the results of a crack that grows across different materials, we proceed to examine the behavior of a crack in a structure which is composed by several parts of two isotropic materials. The number of segments and the pattern of the two materials in the structure are parameters that could influence the SERR of a crack. A beam model was designed for the purpose of parametric research in three point bending test. The thickness of the beam is t=3mm, and the length is L=20t. A crack is located at the thickness location $\frac{t_1}{t} = \frac{1}{3}$, where t_1 is the thickness of the top layer. The left tip of the crack is at $x_1 = 0.1L$.

The beam was divided into 4 equal parts, and two different isotropic materials were assigned to the 4 parts. Young's moduli of the two materials are E_1 and E_2, and $E_2 = 2E_1$. Three patterns were analyzed including $E_1E_2E_2E_1$, $E_2E_1E_1E_2$ and $E_1E_2E_1E_2$. The analytical SERR of the crack tips are shown in Figure 5.37.

From Figure 5.37 we can conclude that both the SERR of the left crack tip and the right crack tip of the three patterns fell into the range of the SERR of a crack only in one material with E_1 or E_2. The best pattern is the one with the smallest peak value of SERR of the left crack tip, which is $E_2E_1E_1E_2$ as shown in Figure 5.37. Since the left crack tip was fixed at $x_1 = 0.1L$, the right crack tip location x_2 differed according to the variation of crack length. The SERR of the right crack tip is not significantly different from the three patterns. The closer the right crack tip x_2 is to the transition point of the two different materials, the greater influence of the other material is exerted on the obtained SERR. Due to the stiffness discontinuity of the transition point, it is impossible to compute the SERR at that point. That's why there are two SERR values of the right crack tip located at the transition point based on the two materials. The true value of

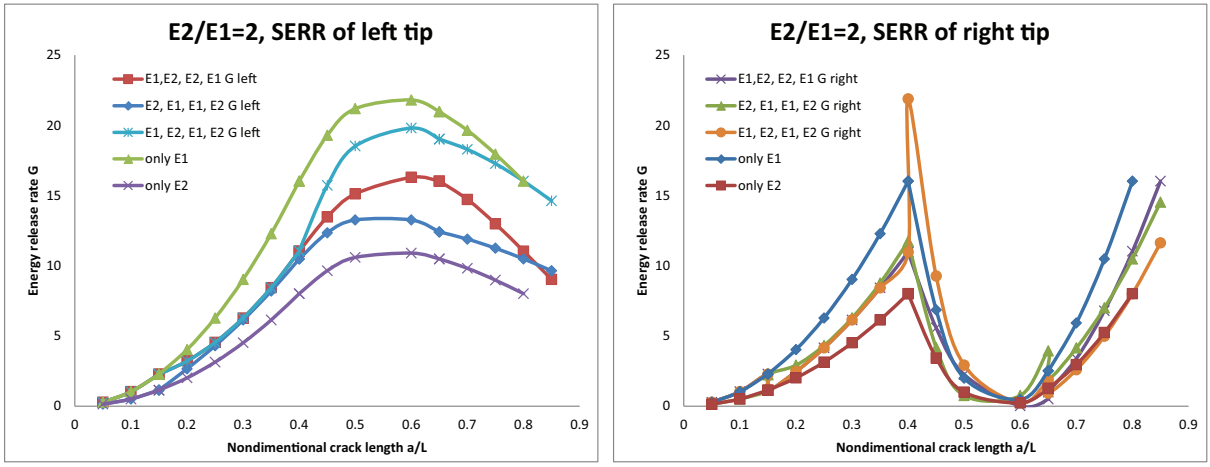

Figure 5.37: SERR of crack tips for the 4 parts with 2 different materials

SERR at the transition point falls into the range of the SERR at that point using the two materials.

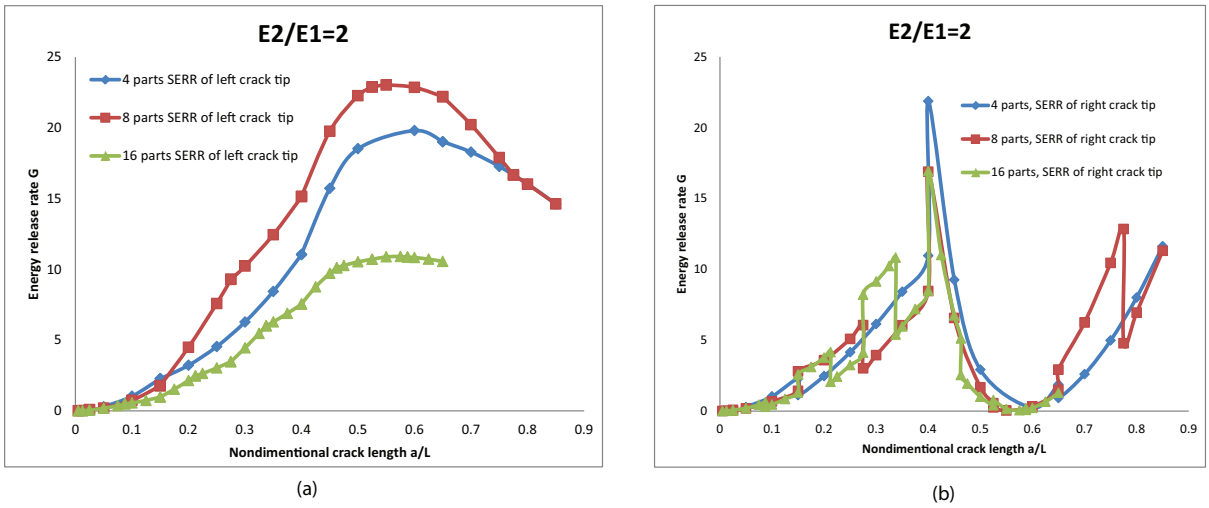

Figure 5.38: SERR of a crack in a beam divided into different parts (a) SERR of left crack tip (b) SERR of right crack tip

Another parameter worth investigating is the number of the divided parts in a structure. The analytical SERR of a crack in a beam that was divided into 4, 8 and 16 portions is presented in Figure 5.38. The material for the portions is expressed in terms of the repeating block of E_1E_2. For example, the material pattern of a beam that had 8 portions is $E_1E_2E_1E_2E_1E_2E_1E_2$. The calculated SERRs of a crack in the 3 different models are presented in Figure 5.38. The depicted curves in Figure 5.38 (a) show that the maximum SERR of the left tip of a crack is the one in the beam that was partitioned into 8 parts and the minimum SERR of a crack is the one in the beam divided into 16 parts. The value of SERR of the right crack tip depends on the location and the assigned material. It is difficult to compare the SERR of the right crack tip of the three patterns, as can be seen from Figure 5.38 (b). As such, finite element models were established to verify the

accuracy of the obtained SERR of a crack in a beam divided into 8 parts and 16 parts. The analytical SERR of a crack in a beam of 8 portions is compared with the finite element result, which is shown in Figure 5.39 (a). A comparison of analytical SERR of a crack in a beam composed of 16 parts and SERR obtained from FEM is given in Figure 5.39 (b). The analytical SERR of a crack in a beam composed of 8 parts and 16 parts both agreed well with the SERR of a crack calculated from FEM.

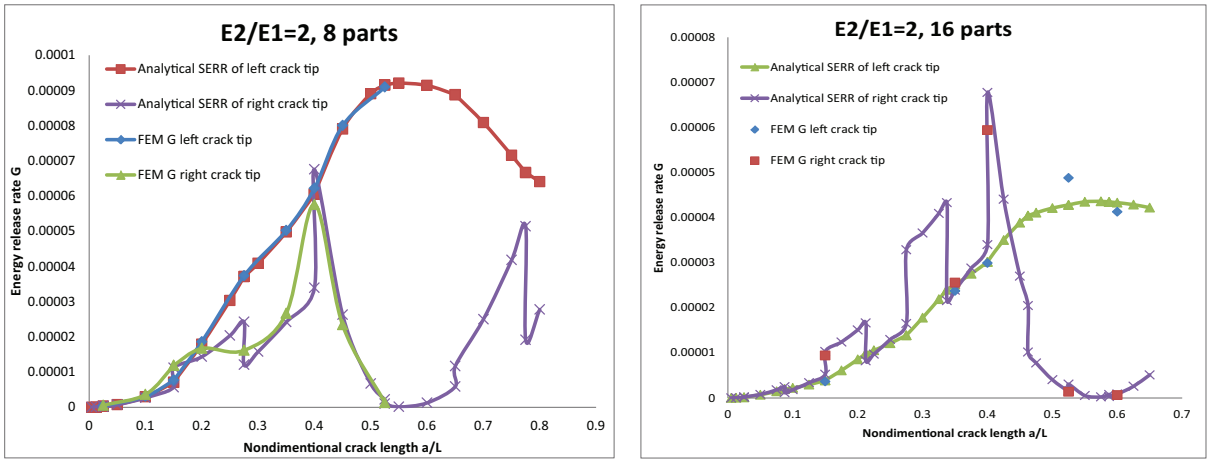

Figure 5.39: Comparison the analytical SERR of crack tips and FEM results

Towards optimizing simple AP-PLY composite laminates

The delamination behavior in a beam composed of two isotropic materials was analyzed in the previous section. To sum up, the patterns of material and the number of segments can affect the SERR of a crack in a beam structure in a three point bending beam test. A simple AP-PLY composite laminate, which is woven in one direction, is considered as mainly composed of two conventional composite laminates. This is based on the assumption that the resin area is small enough to have a negligible effect on the material properties of the whole structure. For an AP-PLY composite laminate with stacking sequence $[0_2/45/-45/(0^{2w}/90^{2f})/0]_s$, the two main materials are two conventional composite laminates whose stacking sequences are $[0_2/45/-45/0_2/90_2/0]_s$ and $[0_2/45/-45/90_2/0_2/0]_s$. While the membrane stiffness of the two composite laminates is the same, their bending stiffness is different, which plays an important role in a three point bending test. As a result, the scope of an AP-PLY laminate optimization problem in this section is limited to the question of using genetic algorithms (GA) finding an AP-PLY configuration that could meet the following requirements: (1) a specific membrane stiffness; (2) the bending stiffness of one layup is twice that of the other layup, and the two different layups can be connected by the woven layers.

The material properties of the ply used in this optimization effort are: $E_x = 140GPa$, $E_y = E_z = 11GPa$, $G_{xy} = G_{xz} = 5.1GPa$ and $\nu_{xy} = \nu_{xz} = 0.29$, and the thickness of the ply is 0.15mm. The thickness of the designed AP-PLY composite laminate is 3mm. The objective of the optimization is to use traditional orientations plies, 0°, ±45°,

$EI_1 = 120000$	$EI_2 = 240000$	AP-PLY
$[90_2/-45/0_2/45/0_4]_s$	$[0_2/45/0_2/90_2/-45/0_2]_s$ $[0/45/0_4/90_2/-45/0]_s$	$[(90_2/-45)^f/(0_2/45/0_2)^w/0_2]_s$ $[(90_2/-45/0)^f/(0/45/0_4)^w]_s$
$[90_2/45/0_2/-45/0_4]_s$	$[0_2/-45/0_2/90_2/45/0_2]_s$ $[0/-45/0_4/90_2/45/0]_s$	$[(90_2/45)^f/(0_2/-45/0_2)^w/0_2]_s$ $[(90_2/45/0)^f/(0/-45/0_4)^w]_s$
$[90/-45/90/0_2/45/0_4]_s$	$[0_2/45/0_2/90/-45/90/0_2]_s$ $[0/45/0_4/90/-45/90/0]_s$	$[(90/-45/90)^f/(0_2/45/0_2)^w/0_2]_s$ $[(90/-45/90/0)^f/(0/45/0_4)^w]_s$
$[90/45/90/0_2/-45/0_4]_s$	$[0_2/-45/0_2/90/45/90/0_2]_s$ $[0/-45/0_4/90/45/90/0]_s$	$[(90/45/90)^f/(0_2/-45/0_2)^w/0_2]_s$ $[(90/45/90/0)^f/(0/-45/0_4)^w]_s$

Table 5.1: The matched stacking sequences by woven plies

90°, to find a 20 layer, symmetric and balanced AP-PLY composite laminate whose membrane stiffness is 270000 N/mm, the two bending stiffness are 120000 $N \cdot mm$ and 240000 $N \cdot mm$, and depend on the stacking sequence. An additional requirement is 10% robustness constraint, which is the basic design rule of composite laminates. This means that each of the principal directions, 0°, 45°, −45°, and 90° has at least 10% of the fibers.

The following optimization procedures were taken in order to find the AP-PLY that can satisfy the requirements. The first step was to find a symmetric, balanced and 10% rule implemented stacking sequence that satisfies the requirements of the membrane stiffness, thus the number of 0°, ±45° and 90° plies were determined. In the second step, the number of the 4 traditional orientation plies was taken as input and the fitness function was used to work out the required normalized bending stiffness, thus the stacking sequence that could meet the 240000 bending stiffness was determined. The next step was to find a layup with the bending stiffness of 120000. Lastly, the obtained two stacking sequences were blended through woven plies. Many stacking sequences were obtained which could meet all the requirements within 5% approximation. The optimized stacking sequences that can be matched by weaving certain plies are listed in Table 5.1. The eight different AP-PLY composite laminates are presented after optimization. Moreover, other stacking sequences of AP-PLY composite laminate are likely to meet all the requirements. This is due to one of the shortcomings of GA that GA may converge towards local optima rather than the global optimum.

Sections of the optimized AP-PLY that can meet the requirements are shown in Figure 5.40, which demonstrates how to integrate the two optimized conventional laminates into AP-PLY composite laminates.

An analytical model was built to validate the optimized AP-PLY composite laminate and the chosen stacking sequence, which is $[(90_2/45)^f/(0_2/-45/0_2)^w/0_2]_s$. The length of the AP-PLY beam model is 60mm, the thickness is 3mm, a crack is located at $t_1/t = 2/5$ in the thickness direction, and the left crack tip is located at $x_1 = 0.1L$. The resin area was ignored, thus the resin was not included in the procedure of analytical SERR and the

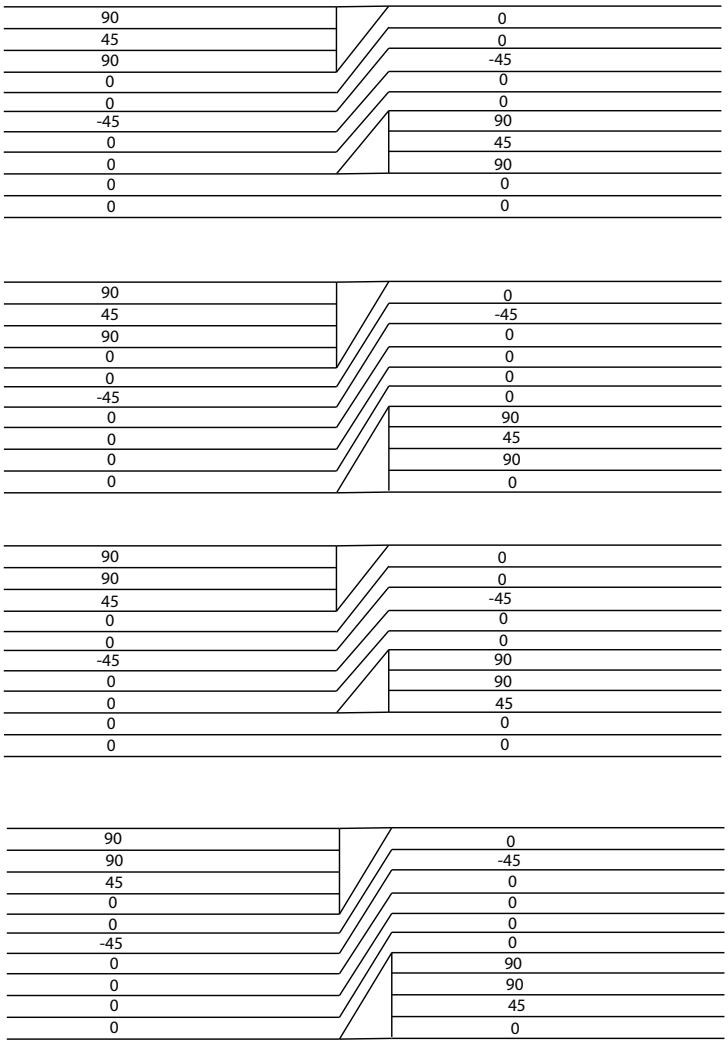

Figure 5.40: Half stacking sequence of the structure of optimized AP-PLY

material properties of the two divisions are the same as that of conventional laminates $[90_2/45/0_2/-45/0_4]_s$ and $[0_2/-45/0_2/90_2/45/0_2]_s$.

A finite element model, which is the same structure as the analytical model, was built to verify the analytical SERR of a crack. The width of the ply is 3.175mm. The resin areas are included and modeled as triangular shape with the length of 0.575mm and the thickness of 0.45mm. The locations of the crack of different crack lengths in the optimized AP-PLY composite structure $[(90_2/45)^f/(0_2/-45/0_2)^w/0_2]_s$ are shown in Figure 5.41. The analytical solution of SERR of the crack was compared with the SERR obtained from finite element model, as is shown in Figure 5.42. The difference between the two calculated maximum SERR of left crack tip is 22.4%, and the difference between the two maximum SERR of right crack tip is 14.3%. Generally speaking, the computed SERR from the finite element model is bigger than what is determined by the analytical solution. This is because the stiffness of the structure in the finite element model including the resin pockets is weaker than that of the analytical model which ignores the resin pockets, therefore the SERR is higher than the analytical SERR.

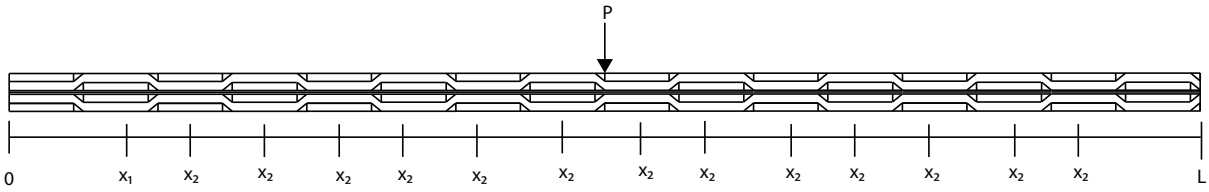

Figure 5.41: Crack locations in the optimized AP-PLY composite laminates

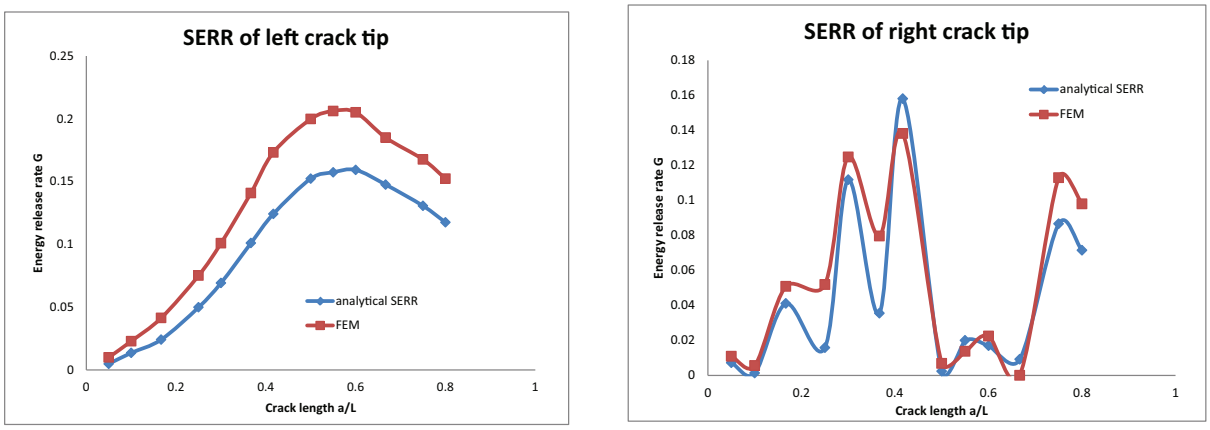

Figure 5.42: Comparison between analytical SERR of a crack in optimized AP-PLY and FEM results

5.5 Conclusion

An energy-based method to calculate the SERR of a crack in a 3 point bending beam model was developed and discussed in this chapter, which enabled us to draw upon either Euler-Bernoulli beam theory or Timoshenko beam theory to analyze the SERR of a crack

within different regions of a structural model. The energy-based analytical method was compared to an existing solution of DCB model and was found to be in good agreement with both the crack in the middle and the crack located at $\frac{t_1}{t} = \frac{1}{3}$.

According to the parametric research on isotropic materials, the SERR of a crack, in the middle of the thickness direction, is greater than that of a crack in any other location in the thickness direction. The SERR decreases when the top or bottom of the beam is approached. If a crack does not go across the load point in a 3PB model, the SERR of the left tip is equal to that of the right tip. For the crack that goes across the load point, the maximum SERR of the left crack tip is obtained when the right crack tip is at $x_2 \approx 0.55L$ and the maximum SERR of the right crack tip is calculated when the right tip is exactly below the load point. After the crack goes across the load point, the SERR of the right tip first decreases and then increases rapidly.

Based on the accuracy of the analytical SERR, a crack can be classified into 3 different types: a crack, bigger than $0.5L$ (equals to $10t$), where $L/t = 20$, is a large crack for which Euler-Bernoulli beam theory is applicable; a medium length crack, $0.2L \leq a \leq 0.5L$ (equals to $4t \leq a \leq 10t$), is the one for which transverse shear effects cannot be neglected and using Timoshenko beam theory can lead to accurate SERR; whereas a smaller crack is the one that neither of the two beam theories gives accurate results and the error is greater than 15%. Inspired by the stress intensity factor and the resulting singularity at the crack tip, a correction factor was developed to correct the SERR of a small crack. The SERR of small crack agreed very well with the finite element results after a correction coefficient was included in calculating the SERR. The correction coefficient, the same as the SERR, is symmetric for a crack located in thickness direction $\frac{t_1}{t}$ and $1 - \frac{t_1}{t}$.

Before extending the energy method to the analysis of SERR of a crack in composite laminate, a crack on the interface of two isotropic materials in a 3PB model was analyzed and the linear elasticity singularity of crack tip caused by dissimilar materials was included. The study showed that the SERR of a crack including its singularity effect increases the accuracy of the SERR of a small crack. We demonstrated that the neutral axis needs to be moved to decouple the bending and membrane behavior of unsymmetrical composite laminate, so as to meet the requirement of minimizing the strain energy of the delaminated beam in order to calculate the SERR. The analytical SERR of a crack in a composite laminate followed the same tendency as that of a crack in isotropic material. The accuracy of the analytical SERR of a crack in a composite laminate is lower than that in an isotropic material. We compared the calculated SERR of a crack in composites to the results obtained from the finite element model, and the result was found to exhibit overall good agreement.

In addition, the SERR of a delamination that goes across different materials was examined and a series of equations were obtained to solve this problem. The results demonstrated that after a crack goes across a soft material, the SERR rapidly increased and while it decreased rapidly when crossing into a stiffer material. As a result, a stiffer material can be used to prevent or delay the propagation of a crack in industrial application. AP-PLY

configurations can be tailored to give the desired behavior with lower energy release rates but with the same in-plane stiffness.

The closer a crack propagates to the transition point of the two materials, the bigger the error of the predicted SERR. In addition, the energy method to compute the SERR of a crack in an AP-PLY composite laminate is presented. The bending stiffness of the delaminated parts including the resin area, was approximately calculated using the Parallel Axis Theorem. The analytical SERR of a crack in an AP-PLY model overall showed the same trend as the finite element results.

Based on the parametric research of a crack that goes across different parts, it was found that the smallest maximum value of the SERR of the left crack tip occurred in the pattern of $E_2E_1E_1E_2$ for a 4 parts beam model. The beam model composed of 16 parts generated the smallest maximum value of SERR of the left crack tip compared with the other two models. Two finite element models were built to verify the analytical SERR of a crack in the 8 parts beam model and in the 16 parts model. The comparisons showed that the analytical solution of SERR agreed very well with the finite element results. An optimization process using GA method for simple AP-PLY composite laminate was proposed based on the results of the parametric study. An optimized simple AP-PLY composite laminate was determined in accordance with the requirements of the design.

Work by Nagelsmit [2013] has shown that for most AP-PLY patterns tested to date the effect of the pattern on in-plane properties (strength and stiffness) is, typically, within experimental scatter. Of course, it is expected that extreme patterns with higher weave angles and more interwoven layers will have an effect as they will start approaching more conventional plain weave and five or eight harness satin materials.

Chapter 6

Testing of AP-PLY composite laminate under out-of-plane load

6.1 Introduction

In order to fully understand the delamination behavior of AP-PLY composite laminates under out-of-plane loads, a series of tests was performed. This chapter provides the information associated with mode II delamination test for which the composite laminate is woven in only one direction, including the preparation of specimens, experimental set-ups, measurement techniques and experimental procedures. The specimen configuration is a special case of AP-PLY which avoids interaction of the weaving pattern in one direction with that in another. In particular, the procedure to prepare the specimens is presented in section 6.2. In section 6.3, the testing methods including experimental set-ups, measurement techniques and experimental procedures are described. The testing results are analyzed in section 6.4 and the conclusions based on tests results are presented in section 6.5.

6.2 Specimen preparation

6.2.1 Manufacturing Process

This thesis highlights AP-PLY composite laminates woven in only one direction. In this way, unnecessary complexity can be avoided and our understanding of the simpler configuration can be heightened. Therefore the manufacturing process was similar to the process described in section 1.3.1 without being completely identical. The first step and the third step in manufacturing the AP-PLY specimen of the woven parts were the same as the first and the third steps in Figure 1.4. However, the second and the fourth steps

were modified so that the produced AP-PLY is only woven in one direction, as shown in Figure 6.1.

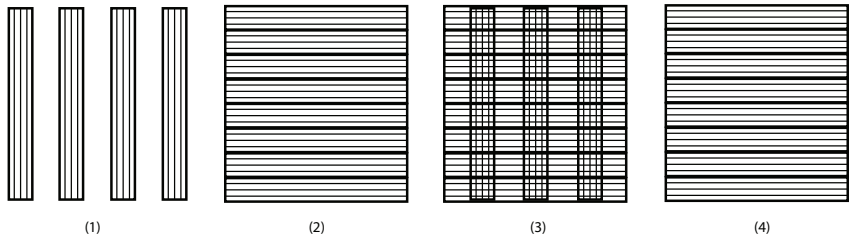

Figure 6.1: The process of manufacturing AP-PLY that woven in one direction

A 24-layers AP-PLY composite laminate made of carbon fiber AS4 and epoxy resin 8552, was manufactured using a specific program with automated fiber placement machine at NLR. The properties of fiber and resin are the same as those described for AS4/8552 in chapter 3, section 3.2.1. The geometry of the manufactured AP-PLY composite laminate is $L_1 = 202mm$, $L_2 = 191.5mm$ and $t = 4.59mm$ and the lay-up is $[90_5/0_5/(0^w/90^f)/90/0/0_5/90_5]$ in which the 0° ply is woven with the 90° ply using a plain pattern. The fabricated laminate was cured in an autoclave according to the material manufacturer's specifications.

6.2.2 Cutting process

The resulting AP-PLY composite laminate was cut into smaller specimens by a STRUERS Secotom-10 cutting machine with water-jet cutting equipment.The used diamond blade was specifically designed to cut carbon fibre reinforced composite laminates.

The first 2 tests were performed with specimens of 24 layers AP-PLY composite laminate. The remaining 7 tests used specimens of 14 layers AP-PLY composite laminate, which were made by removing the top 5 layers and bottom 5 layers from the 24 layers AP-PLY composite laminate. This modification was based on the results of the first 2 tests where the top and bottom 90_5 plies failed early. The failure of the top 5 layers was due to cracking resulting from crushing loads of the loading tab while the failure of the bottom 5 layers was due to transverse tension. The 5 top layers and 5 bottom layers were removed using a DECKEL cutting machine. It should be noted that since the plies in the specimens were not totally straight or flat, it was impossible to remove all of the 5 top layers and 5 bottom layers and over portions of the surface of some specimens, patches of a very thin layer of 90 fibers were left. The surface is shown in Figure 6.2 after top and bottom layers were removed.

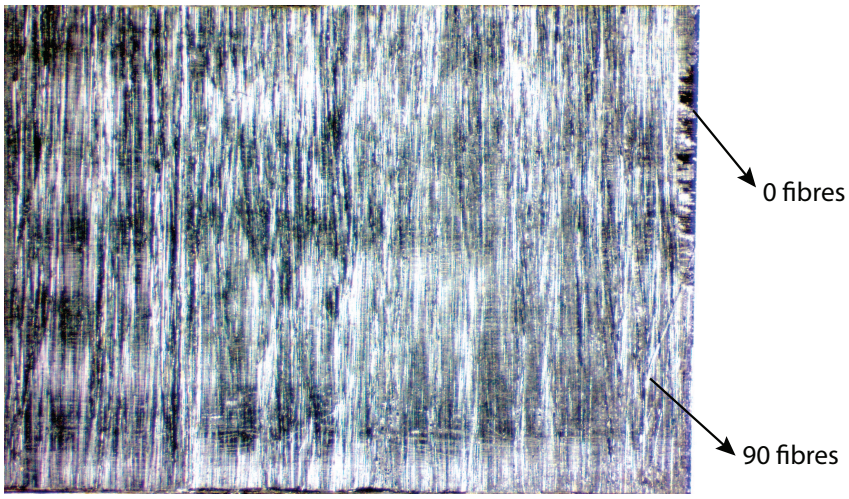

Figure 6.2: The surface after removing 5 outermost layers

6.2.3 Strain gauges

The strain gauges were used to measure the strain on the top and bottom surface of a coupon during the experiment. The strain gauges used for the test in this chapter were the KFG-5-120-C1-23 type of strain gauges with $2.12 + 1.0\%$ gauge factor from KYOWA company. Two strain gauges were placed on the top surface at $\frac{1}{4}L$ and $\frac{3}{4}L$, and three were placed on the bottom, at $\frac{1}{4}L$, $\frac{1}{2}L$ and $\frac{3}{4}L$ in the longitudinal direction, as is shown in Figure 6.3.

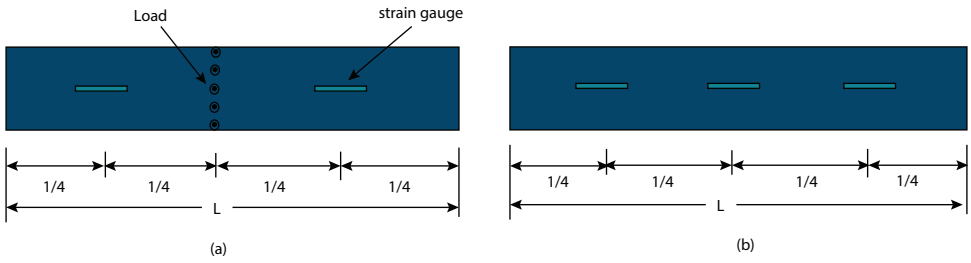

Figure 6.3: Strain locations in AP-PLY specimen (a) top surface (b) bottom surface

6.2.4 Painting

In order to check by naked eye and/or a high resolution digital camera whether a delamination has started or not, the edges of the specimens were painted flat white. This is shown as the high-lighted surface in Figure 6.4, which shows the woven structure of the AP-PLY.

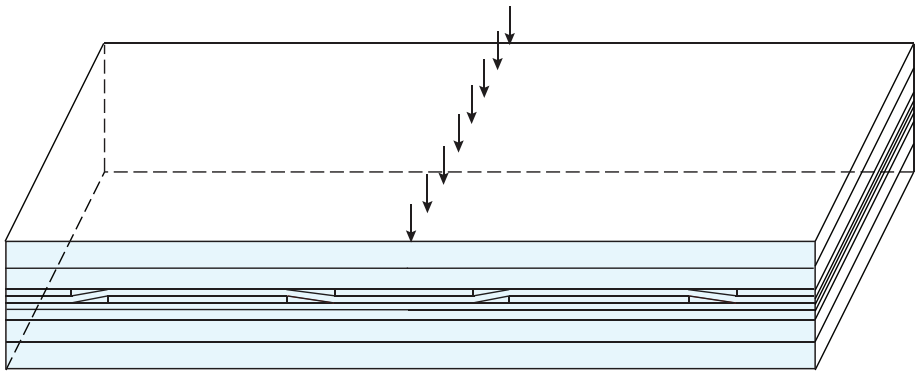

Figure 6.4: The paint of front surface and back surface

6.2.5 Moisture elimination

To remove any moisture absorbed during previous operations, in particular water jet cutting, the painted coupon was put into an oven at the temperature of $60°C$ for 72 hours.

The weight of each of the four specimens was measured before placing in and after taking out from the oven, see table 6.1, where $wm1$ is the weight of specimen before putting in oven, $wm2$ is the weight after taking out from oven, $\delta wm = wm1 - wm2$ and $ratio = \frac{\delta wm}{wm2}$. The specimen in test 1 had 24 layers, that's why it is much heavier than the other 3 specimens in test 7, 8 and 9. Moreover, the reason why the specimens have different weights in test 7, 8 and 9 is that the widths of these specimens are slightly different. The average ratio of the moisture uptake across all specimens was 0.116%.

Name	test 1	test 7	test 8	test 9
wm1	$12603.5mg$	$8328.9mg$	$7804.1mg$	$8893.4mg$
wm2	$12587.2mg$	$8321.3mg$	$7795.9mg$	$8881.3mg$
δwm	$16.3mg$	$7.6mg$	$8.2mg$	$12.1mg$
ratio	0.1295%	0.0913%	0.1052%	0.1362%

Table 6.1: Weight of different specimens

6.3 Test

Due to the novelty of the AP-PLY structure, there is no known standard for the testing of mode II delamination of AP-PLY composite laminates. It is uncertain whether a delamination occurs before the fibers break or before transverse cracks develop in the matrix. In addition, the weaving pattern is expected to have a large effect on delamination onset and growth. Hence, first a pilot experiment was designed and the subsequent test

was designed on the basis of the performance of the pilot test. Therefore the preparation work of the specimen, except the manufacturing process of the laminated plate used to cut individual specimens from, was done step by step and repeated after consideration of the results of the previous test. The testing method includes two parts: mechanical tests and evaluation of specimen surfaces under the microscope.

6.3.1 Mechanical Test

A mechanical test provides the needed information on material properties, which are essential in understanding physical behavior and serve as inputs to the finite element analysis and numerical analysis. In this thesis, three-point bending specimens were prepared. Due to the complexity of the AP-PLY structure, it was hard to meet the requirement of the standards [ASTM, 2006a; ASTM, 2006b; ASTM, 2007], which are the standards describe the three-point bending test shown in Figure 6.5. Therefore, there were no standards that applied to the test in this thesis.

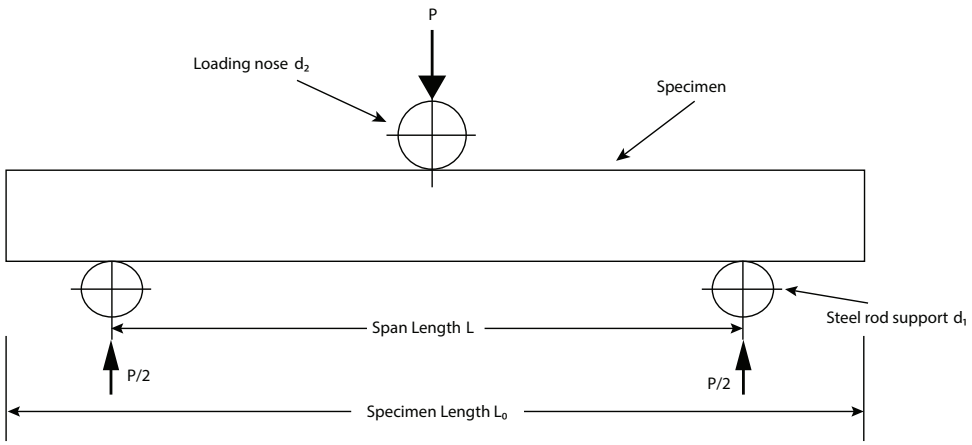

Figure 6.5: Three point bending diagram

In the present work, the span length is $L = 50.4mm$, the diameter of the two support steel rods is $d_1 = 30mm$, the specimen length L_0 is slightly different,the diameter of loading nose is d_2, which will be described later, and the structure is symmetric with respect to the load point in the x direction. Since there is no standard in the test, two parameters can be adjusted: the diameter of the loading nose and the number of silicon pads used between the loading nose and the specimen. Two different sizes of loading nose and three options for silicon pad were checked in the tests.

Two loading noses with different diameter

Loading nose 1: diameter $d_2 = 15mm$

Loading nose 2: diameter $d_2 = 25mm$

Cases related to silicon pad

Case 1: without silicon pad

Case 2: with 1 silicon pad

Case 3: with 2 silicon pads

The thickness of the silicon pad is $t = 0.54mm$. It is necessary to indicate the two changeable parameters, which are the diameter of the loading nose and the case related to silicon pad in each test. The silicon pads were put exactly under the loading nose.

Test setup

The three point bending test setup is shown in Figure 6.6. The loading nose should be ensured to be located equidistant between the steel rod supports and perpendicular to the specimen. If the loading nose is longer than the width of the specimen, the specimen must be centered with respect to the loading nose. The location of the specimen and steel rod supports were fixed during the entire test. Two high resolution digital cameras controlled by a computer were used to monitor the behavior of the structure under loading by automatically recording images of the front and back surfaces of the specimen every 1 second. The information of load and displacement was transferred to a computer and stored in an Excel file which facilitates data analysis after the test. The behavior of woven surface of the specimen during the tests was projected on a monitor through the two cameras shown in Figure 6.6. All the three point bending tests were conducted on 10kN tensile & compression Zwick machine except that one was carried out on a 20kN Zwick machine.

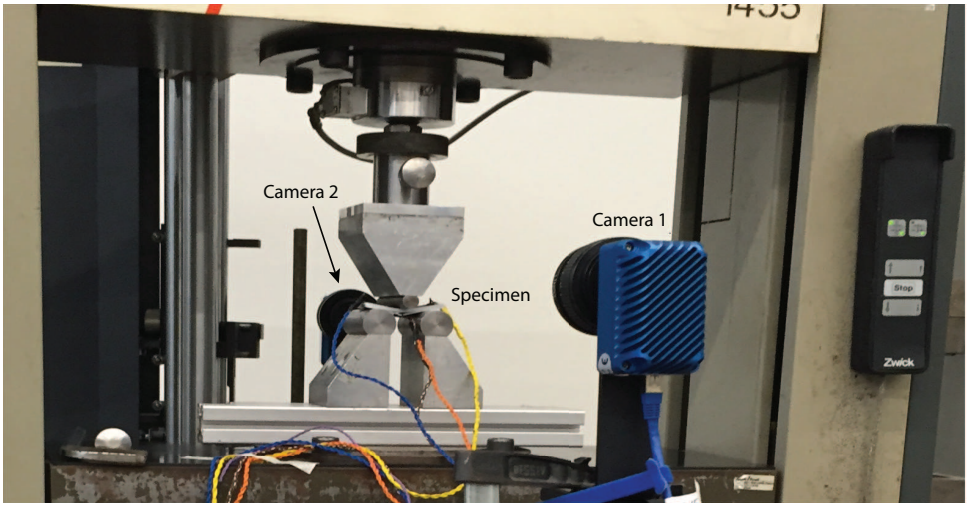

Figure 6.6: Three point bending test setup

Loading procedure

The main purpose of the tests was to identify the delamination damage behavior of the structure of AP-PLY composite under applied loads. Therefore it was important to observe the delamination during the test procedures. With the fixed displacement rate, the load was applied as a stepwise function of time during load holds it was checked whether there is delamination or not through naked eyes and the images captured by the cameras and projected on the monitor. The tests were performed under displacement control with an applied displacement rate of 0.5mm/min.

In composite laminates, the material properties of the resin are lower than those of the fibres and it was determined in chapters 3 and 4 that the resin areas are the most probable location of delamination initiation. Considering the reasons mentioned above, a 2D AP-PLY composite laminate finite element beam model, similar to Figure 4.8, was created to provide insight into the expected behavior of the specimens. The load at which a crack first initiated in the 2D AP-PLY model obtained from the finite element model was used as prediction load for the test. And then the predicted delamination initiation load of a 3D composite beam will be $F_{ini} = b \times P_{pre}$, where b is the width of the 3D composite beam, P_{pre} is the predicted onset of delamination load in 2D finite element beam model.

There are two different loading procedures of the tests in this thesis for 24 layers specimens and 14 layers specimens, respectively. For the 24-layer specimen, the procedure was as follows: A line load is applied increasing from 0 to the anticipated delamination initiation load at the rate of 0.5 mm/min. Once the expected initiation load was reached, the load was kept constant for 1 minute. Subsequently, the load was increased with $0.05F_{ini}$ and was kept unchanged for 1 minute. This was repeated until the load reached $1.75F_{ini}$. If no damage was observed, the load was increased in 300N increments, holding every time for 1 minute till the load reached 6300N. After that the test continued monotonically until 10000 N when the test was terminated.

The loading procedure for 14 layers specimens kept the same displacement rate, but the applied load increased from 0 to 2500N and the load was held for 20 seconds. Subsequently, load was increased in 250N increments until the load reached 3500N. After that, the increased load in every step was 100N till the applied load reached 7000N. And then the load was increased monotonically until 10000N, and the test was terminated. It should be noted that the test was stopped when any noises were heard, suggesting that damage had occurred. As an example, the loading procedure in test 7 is shown in Figure 6.7.

6.3.2 Microscopy

Microscopy was used to check the fracture behavior of a specimen, and was carried out following the mechanical test. Two different microscopes were used to observe the painted surfaces after the mechanical 3PB test. One was ZEISS AxioCam ERc5S camera

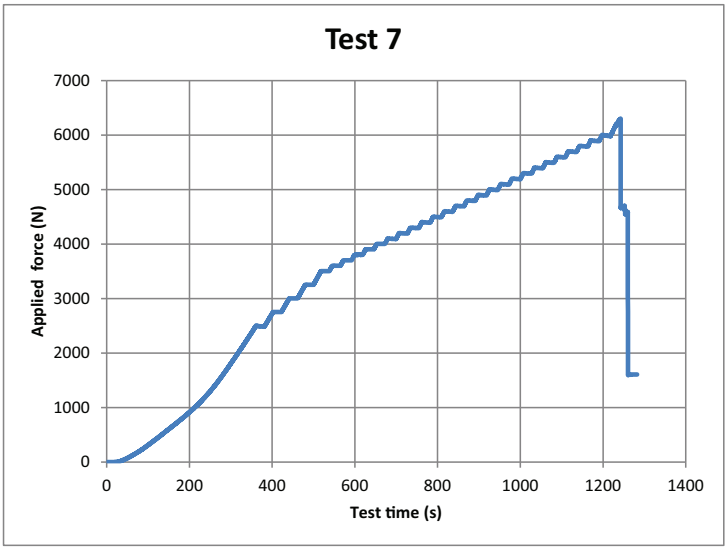

Figure 6.7: Loading procedure in test 7

with maximum magnification 8×, which was used to directly observe the surface of the deformed structure or, after test, was used to examine the polished surface. Polishing was done using sandpaper. The other was a Leica DM LM system of Optical Microscope with maximum magnification 100× and the observed samples had to be mounted. The samples were embedded in green epoxy compound with the cross section of the sample towards the bottom to make sure the cross-section can be kept flat in embedded materials. The embedded samples, as is shown in Figure 6.8, were ready to be observed under optical microscopy after the process of curing, grinding and polishing.

6.4 Test results

6.4.1 Test results of 24 layers specimens

The objective of the tests was to observe the delamination in three point bending AP-PLY composite laminate. The first two tests of 24 layer AP-PLY composite specimens were done using the loading block of $d_2 = 15mm$ without silicon pad between the loading rod and the specimen. After a noise was heard, the first test was terminated whereas the second test was terminated after complete failure, which means the load dropped by 50%. Both tests showed that the crack of the specimen initiated at the middle of the bottom surface, where the maximum moment occurred. The damage is shown in Figure 6.9.

Five strain gauges were attached to each specimen. The limit of the used strain gauges is 1%. The strains at top surface $\frac{1}{4}L$, $\frac{3}{4}L$ and bottom surface $\frac{1}{4}L$, $\frac{1}{2}L$ and $\frac{3}{4}L$ during the test are shown in Figure 6.10.

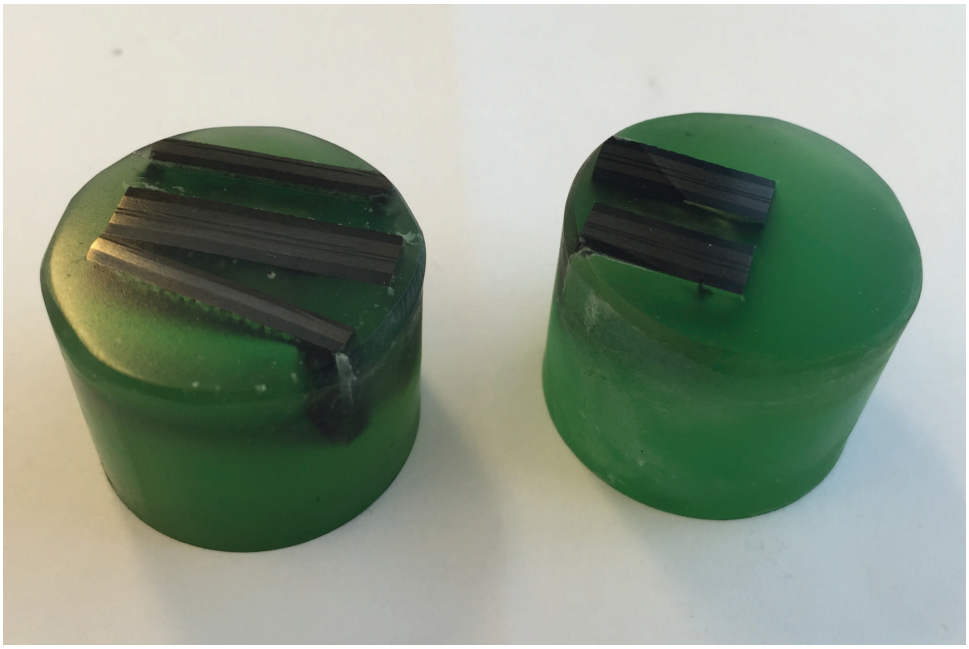

Figure 6.8: Embedded tested samples

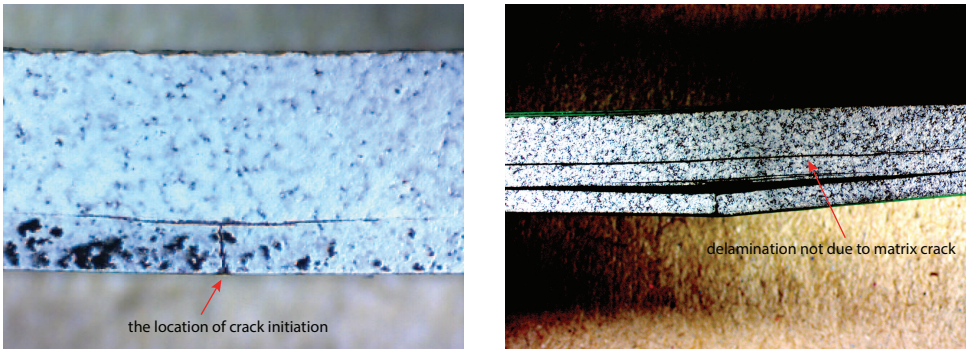

Figure 6.9: damage of the specimens after test (a) specimen 1 (b) specimen 2

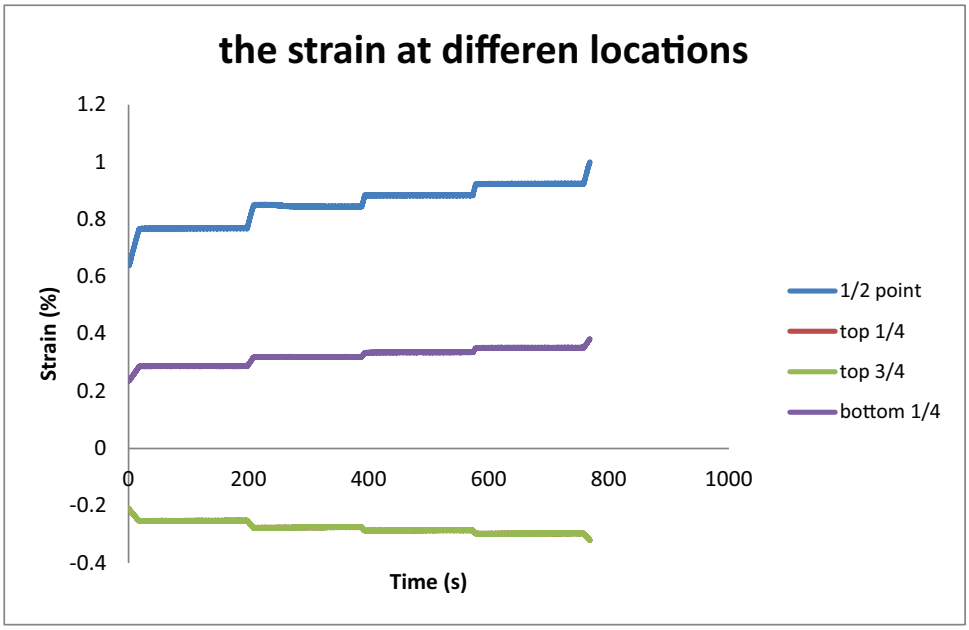

Figure 6.10: Strains of different location

The maximum strain occurred at the center point $\frac{1}{2}L$. Due to the symmetry of the structure of the load point, the strain at $\frac{1}{4}L$ equals the strain at $\frac{3}{4}L$, and the strain at $\frac{1}{4}L$ the top surface has different sign but almost the same value as the strain at the same location of the bottom surface because the top surface is in compression and bottom surface is in tension, all of which were in line with our expectation.

Due to the slightly different width of the specimens, the critical load of a crack initiation was normalized with respect to width $F_b = \frac{F}{b}$, where F is the crack initiation load of the test, b is the width of the specimen. The F_b from test 1 and test 2 is 47.93 N/mm and 49.435 N/mm, respectively. And we found that due to the layup of the top layer and the bottom layers, which are 90_5 layup, a transverse matrix crack initiated at the bottom surface instead of delamination initiating at the interface of different layers.

It is impossible to examine by naked eye whether there is damage at other locations or not, except the broken fibers and the delamination induced by the transverse crack reaching the 90/0 ply interface. As a result, the specimens were cut into 4 equal pieces. The cut pieces were firstly examined under the ZEISS microscope. Owing to the smaller magnification of ZEISS microscope and the unpolished tough surface, it is hard to determine whether there is a crack at the resin area or not. Subsequently the embedded smaller pieces were examined under optical microscopy (OM) as shown in Figure 6.11.

We found that the delamination in specimen 1 was induced by the transverse matrix failure in the bottom 5 layers, which are 90_5 plies. Without the increase of applied load after the transverse matrix failure of the bottom 5 layers, another delamination not due to matrix failure was seen in specimen 2, as shown in Figure 6.9 (b). To avoid the transverse failure of 90 plies in specimens, the top 5 layers of 90_5 and the bottom 5 layers of 90_5

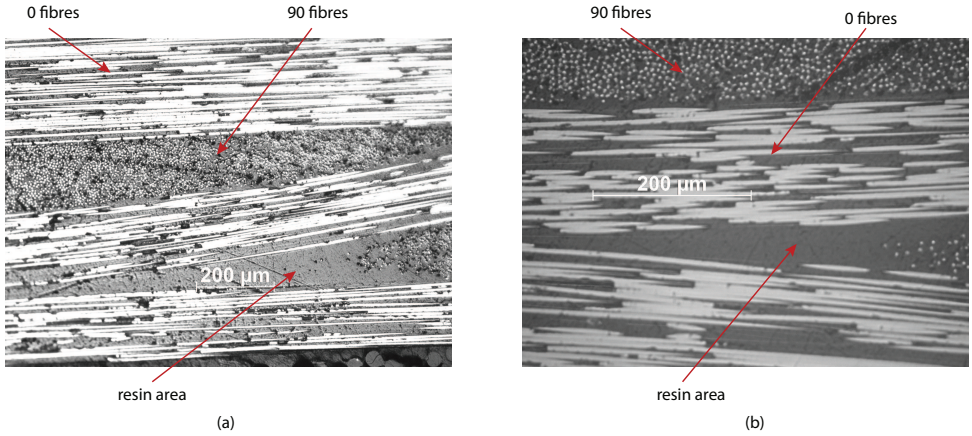

Figure 6.11: The embedded samples under optical microscopy (a) 10× (b) 20×

were removed, thus the rest specimens became 14 layers of AP-PLY composite laminate with the nominal thickness of 2.52mm.

6.4.2 Test results of 14 layer specimens

In the remaining 7 tests, the specimens had 14 layers and two of them in an AP-PLY pattern. From test 3, it was found that the displacement was larger than the thickness of the specimen when a damage occurred and the measured strains exceeded the range of strain gauges. In the following tests, the strain gauges were not employed anymore. The structure of specimens for test 3 and 4, labeled as structure A, is the same as shown in Figure 6.4. The structure of specimens used in test 5, 7, 8 and 9, which is labeled as structure B, is displayed in Figure 6.12 (a) while the structure of specimen used in test 6, which is structure C, is shown in Figure 6.12 (b). The structure B is the flip of structure A, and the structure C is the specimen that is cut from another location whereas the structural symmetry is maintained.

There are two parameters regarding the remaining 7 tests: the diameter of the loading nose and the number of the silicon pads used between the loading nose and specimens. The parameters, damage initiation loads and the damage locations are presented in table 6.2. Taking the test 3 as an example, the diameter of the loading nose is 15mm and no silicon pads were used in test 3. Also, the damage initiated from the top layer and the initiation load is 115.2 N/mm.

	diameter of loading nose	number of silicon pads	initiation load	damage location
test 3	15mm	0	115.2 N/mm	top
test 4	25mm	1	151.1N/mm	top

Table 6.2: Test results of specimens with structure A

It can be observed from table 6.2 that the loading nose with 15mm diameter led to the

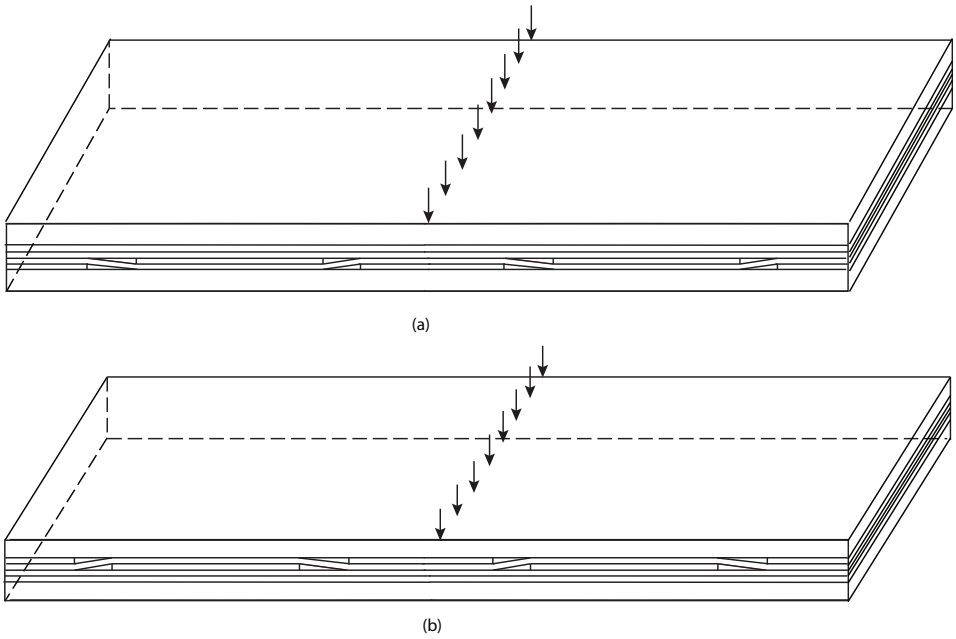

Figure 6.12: The structure of specimens (a) Structure B (b) Structure C

breakage of the fibers of the top 5 layers, which indicates that the smaller radius of the loading nodes causes higher stress concentrations in the load area. In test 4, the 25mm loading nose penetrated the silicon pad and the fibers in the top layers broke.

	diameter of loading nose	number of silicon pads	initiation load	damage location
test 5	25mm	1	148.99 N/mm	top
test 7	25mm	2	208.40 N/mm	bottom
test 8	15mm	2	164.49 N/mm	top
test 9	25mm	2	198.78N/mm	bottom

Table 6.3: Test results of specimens with structure B

The results of test 4 with structure A is very close to that of test 5 with structure B, as can be seen in table 6.3. Comparing the results of test 5 and test 7, we see that the silicon pads absorbed a certain amount of energy so that the damage initiation load of the test with thicker silicon pads is higher. In addition, the initiation load for nominally between the same structure using 1 silicon pad and 2 silicon pads is $59N/mm$.

Comparing the results of test 8 and test 9, it is seen that the size of loading nose also affects the damage initiation load and damage location. Smaller loading nose is associated with higher stress concentration in the loading area. The stress concentration in test 8 is higher than that in test 9, and the fibers at the top layers would fail when the maximum stress was reached in test 8. In addition, the fibers were broken at the bottom layers in test 9 because the tension stress was equal to or larger than the tension failure strength of the fibers.

The comparison between test 7 and test 9 shows a difference of around 4.5%. Since the damage locations are different, it is difficult to qualitatively determine the effect of the loading nose on damage initiation load by comparing test 8 and 9. Fibers were broken at the bottom surface due to tension only in specimens using 25mm loading nose and 2 silicon pads. Because the concentration of stress in the loading area and the fibers reaches the maximum compression load, the fibers were also broken at the top surfaces in test 3, 4, 5 and 8. It is important to note that there are not enough tests of the same type in order to evaluate the effect of loading nose size and tab thickness with statistical significance. In addition, the failure mode differences may be within experimental scatter. The discussion here serves to mostly identify trends.

	diameter of loading nose	number of silicon pads	initiation load	damage location
test 4	25mm	1	$151.123 N/mm$	top
test 5	25mm	1	$148.99\ N/mm$	top
test 6	25mm	2	$139.58\ N/mm$	top

Table 6.4: Test results of structure A, B and C (from top to bottom)

The specimens of configurations A, B and C were tested using the 25mm loading nose and 1 or 2 silicon pads. It can be seen from table 6.4 that the fibers in configuration C were broken earlier than configurations A and B, even when one more silicon pad was used and led to a higher damage initiation load. Since there is only one test related to structure C, we can arrive at the conclusion that the structure is likely to be one of the reason.

The size of the loading nose and the number of silicon pads used in the test influence the damage initiation load and the location of the initiation. Using smaller loading nose and less silicon pads lead to damage initiation at the top layer as shown in Figure 6.13. The structure failed soon after the top 5 layers of fibers were broken due to these induced delamination in test 4 and 6. The location of the broken fibers clearly reveals the influence of the size of loading nose and the number of silicon pads used during the tests.

One particular characteristic of test 5 is that there are two locations of fibres breakage and after that a delamination connected them together. The distances between these two locations is smaller than the diameter of the loading nose. Other delaminations, not followed the broken fibres, on the interface of two layers occurred due to the shear stress after the fibres were broken. The images were taken through microscopy to focus on delamination close to the resin areas in test 5, as shown in Figures 6.14. The propagation path of the delamination on the interface followed the woven ply.

The delamination that initiated from resin area after the fibres were broken was luckily captured by the camera during test 5, as demonstrated in Figure 6.15, in which the damages are marked in red. The damages marked in the red circles are broken fibers, in which eclipsed delamination can be seen. Figure 6.15 (b) was taken one second after Figure 6.15 (a).

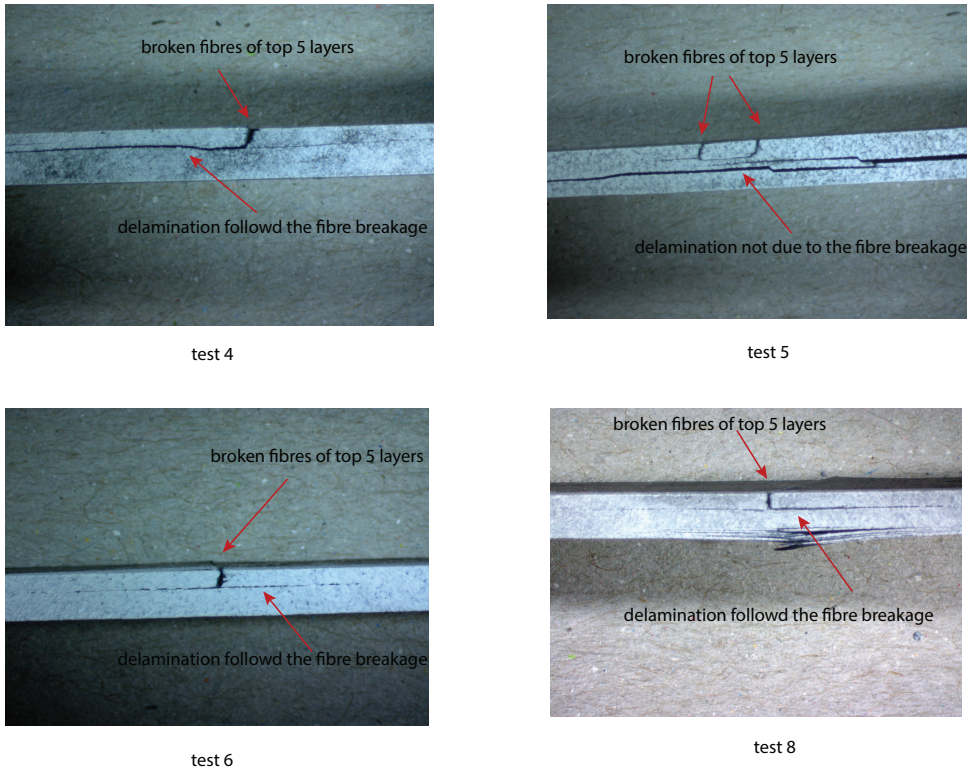

Figure 6.13: Tested specimen that damaged at top layers

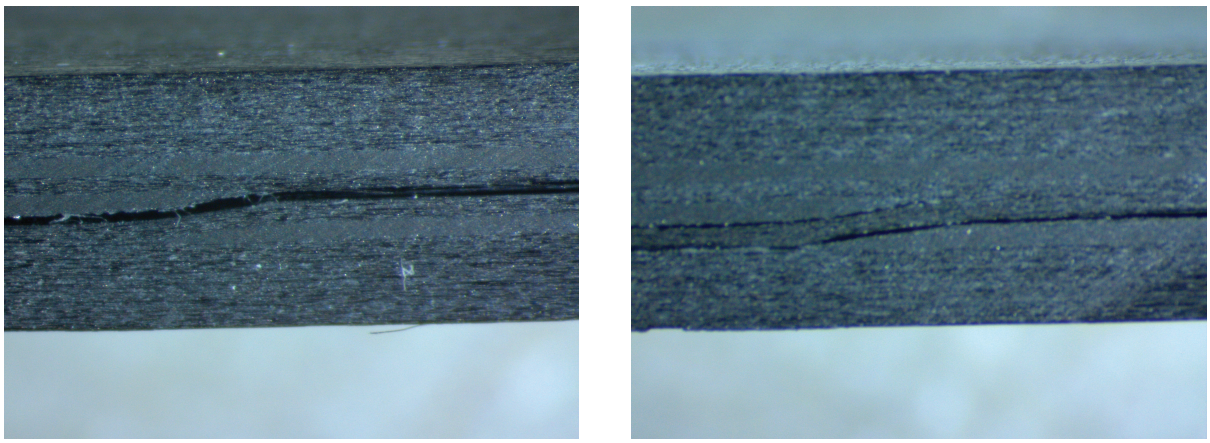

Figure 6.14: Delamination at the resin area in test 5

It was this delamination emanating from the resin pocket that was the goal of the test program in the first place. The matrix cracks occurring in other tests were an unwanted by-product of the test method and sensitivity of the specimens to small changes in loading and geometry. Modeling the matrix cracks was not part of this research.

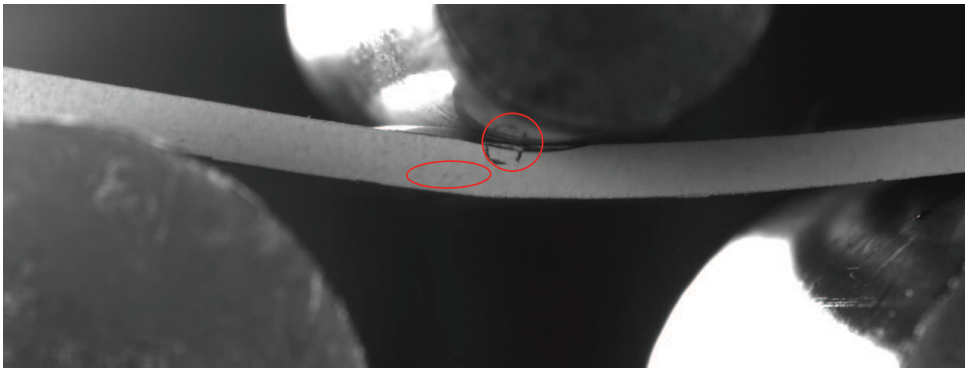

(a)

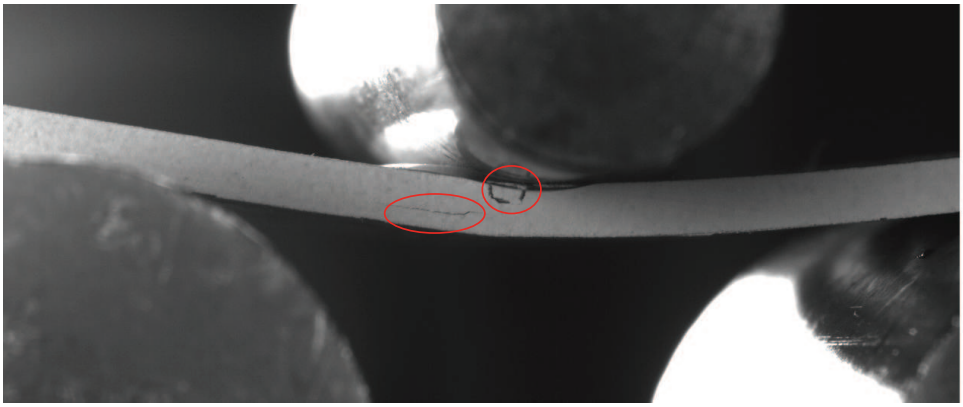

(b)

Figure 6.15: Delamination initiation in test 5

The damaged specimens in test 7 and 9 are shown in Figure 6.16. Test 7 and 9 were not stopped after the first noise was heard, which indicates that after the fibers were broken, the applied load decreased and the test continued until the structure failed. It was found out that the failure of matrix in 90 ply was due to transverse shear stress and the angle of crack is 45°. From test 7 it can be concluded that the matrix failure of 90° plies is the main driver of delamination propagation.

6.5 Comparisons with simulations

Several different finite element models were created to simulate the tests in this chapter. A 24 layer finite element model was created to model transverse matrix failure in the bottom layers and the induced delamination that followed, in which 0.001mm cohesive elements were created in the middle of specimen at the bottom, which is under the loading

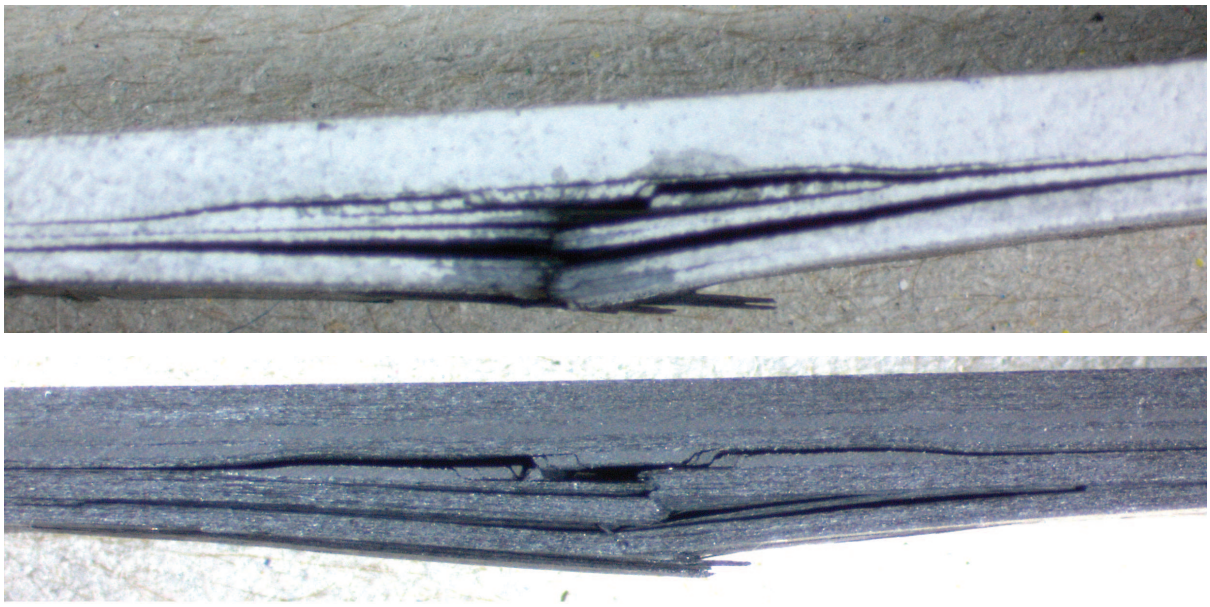

test 7

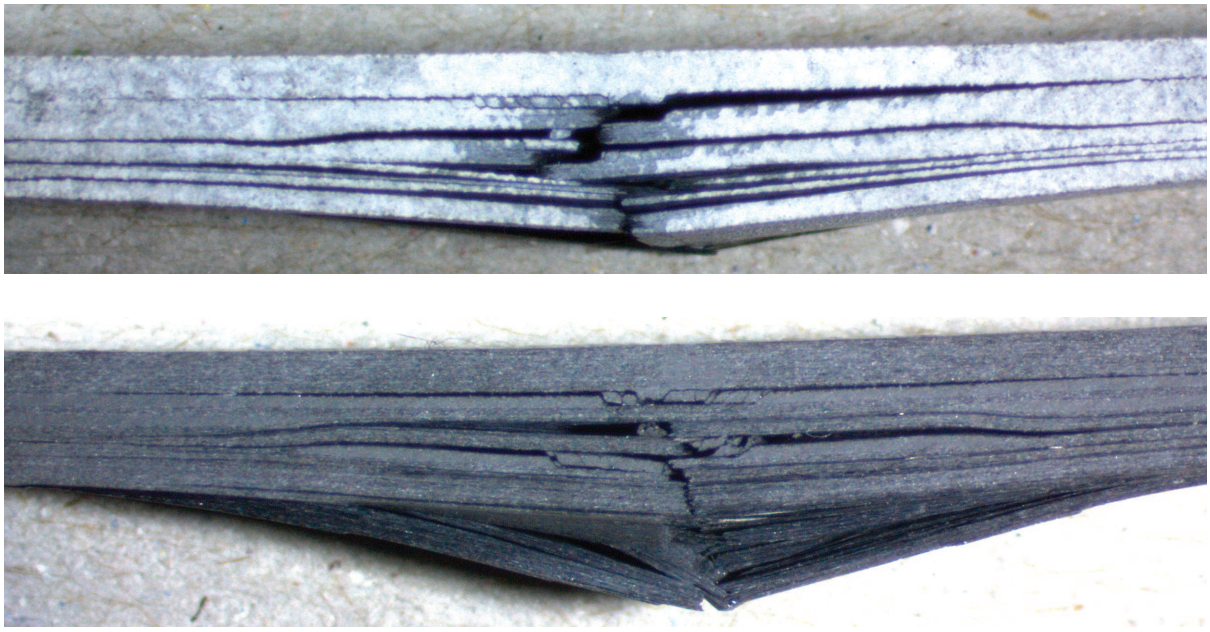

test 9

Figure 6.16: The tests in which the damage initiated from bottom layers

point, and on the interface between bottom 0_5 and 90_5 layers. It is assumed that the traction separation law of cohesive elements that simulates matrix cracks in tension is identical to that of a mode I delamination. The predicted initiation of transverse matrix failure was 60N, and the initiation load of matrix in test 1 and 2 were 47.93N and 49.435N, respectively at the same location. The predicted failure load is higher than that of the test due to the assumption that there are no defects. Damage onset prediction using cohesive elements may be inaccurate due to sensitivity on K and G_{IIc}. In addition, there are not enough test results to consider the test values as statistically significant.

In the test shown in Figure. 6.15, the load was 149N/mm when the delamination length is a=1mm. In the finite element, the load was 121.04N/mm when the same delamination size appeared at the same location. The predicted damage initiation load is about 19% lower than that of the test. This 19% difference is attributed to a combination of inaccuracies in the test method and the approximation of the geometry of the woven ply discussed in section 3.2.

The finite element models for the test of 14 layers specimens had to deal with two issues: (1) the specimens undergo large deformations when the fiber break and these were not modeled in the simulation; (2) the failure analysis of fibers needs more representative cohesive elements. Although geometry nonlinear analysis is not problematic in nature, when nonlinear deformation and cohesive elements are combined, the finite element analysis takes a long time and does not always converge. The focus of the present work is onset and growth of delamination at AP-PLY patterns. This can be studied within a linear framework first to isolate parameters of interest. Nonlinear effect is at this stage undesirable. The longitudinal tensile strength can be used to define in damage initiation, but the longitudinal tensile fracture energy parameter in the definition of damage evolution is unknown. The modelling of failure of the specimens can be improved. One approach would be to investigate the use of user-defined cohesive elements. For future work, it is worth investigating to use user defined cohesive elements in the analysis of the broken fibers if the associated traction separation law is known.

6.6 Conclusion

In this chapter, a series of tests were done to observe delamination initiation and propagation in a woven AP-PLY composite beam under out-of-plane load. After the first two tests were done, it was found that specimens with 90 layers on the outside failed early by transverse matrix cracking and compression failure under the loading tabs. The outer 90 layers were removed from the remaining specimens. Different test set-ups were used to determine which one would best interrogate onset and growth of failure in these configurations. These tests are viewed as pilot trials in the attempt of finding the configuration in which failure would start as a delamination at the resin pocket of the AP-PLY pattern.

The two parameters in the tests were the size of loading nose and the number of silicon pads used between loading nose and specimens, both of which influence the damage

initiation load and damage initiation location. The 15mm diameter loading nose leads to the breakage of fibers on the top surface even when 2 silicon pads were used in the test. In the test that uses 25mm loading nose and 1 layer silicon pads, the fibers were broken in the top layers. The used silicon pads absorbed a certain amount of energy of the load, thus the damage initiation load of the test that used more silicon pads was higher than that of the test that used fewer silicon pads. Bigger loading nose leads to higher damage initiation load. The critical load for fiber broken under tension in the three point bending test was obtained corresponding to a specific geometry and test setup.

In the tests, the damage observed was a combination of transverse matrix failure, delamination induced by fiber breakage and delamination caused by transverse shear stresses. It was difficult to distinguish the mode II delamination from all forms of damage. In one of the tests, the desired failure mode, with a delamination following the woven path of the AP-PLY pattern was observed but it occurred simultaneously with this fiber failure. It is necessary to perform more tests to figure out the delamination behavior of AP-PLY composite beam in the three point bending test.

Chapter 7

Conclusions and Recommendations

The different aspects of delamination in a simple AP-PLY composite laminate which is woven in one direction were covered in this thesis. Generally, the research work was concentrated on delamination onset and growth. Two approaches were implemented to predict the delamination onset: the first method was the combination of stress recovery technology in combination with a maximum stress criterion; the second method uses cohesive elements in a finite element simulation to model delamination initiation and in which delamination growth was also included. An analytical procedure to obtain the strain energy release rate of a delamination was developed for the analysis of delamination growth. Finally, a series of tests were completed to identify an appropriate set-up for measuring delamination onset and growth. The main developments and results are provided in this chapter. Recommendations and future challenges are presented to improve the current research work.

7.1 Conclusions and highlights

The work presented in this thesis characterizes the delamination onset and growth in a simple AP-PLY composite laminate under out-of-plane loads. This study demonstrates the methods to predict the load capacity and feasibility of optimization of an AP-PLY composite laminate according to specific requirements. The main conclusions and highlights are briefly summarized below.

7.1.1 Prediction of delamination onset based on stress criterion

In this thesis, the prediction of delamination onset of an AP-PLY composite laminate under impact load based on the maximum stress criterion was implemented using stress recovery technology and coarse meshed finite element model, which ensured an efficient analysis and reasonably accurate determination of the interlaminar stress. The critical

location of an AP-PLY pattern is where a delamination initiates at the resin pocket periodically repeating the pattern. It is noted that the stress recovery technology can be used to successfully recover interlaminar stress even in a plane that is not horizontal.

7.1.2 Cohesive zone model analysis of delamination onset and growth

A 3D simple AP-PLY composite laminate under impact was transformed into a 2D model including the essential characteristic of the woven pattern, in which the 3D impact load was first transferred to line load and then a static out-of-plane point load in a 2D model. Thus a 2D finite element AP-PLY model with cohesive elements inserted into the interfaces of the interwoven layers around the resin area has been presented to analyze the delamination behavior of simple AP-PLY composite laminates. The parameters of the woven patterns were examined and the basic trends are summarized as follows:

- The woven angle $\theta = 17.4$ had more highest initiation loads among different configurations with θ varying from 5 to 25. The delamination onset prediction agreed well with the one using the maximum stress criterion based on the recovered interlaminar shear stress.

  Most of the initiation loads in the model with the woven angle $\theta = 25$ were smaller than that in the other configurations. The growth curves related to the woven angles indicated that the critical loads of delamination growth in the model with $\theta = 25$ are the lowest whereas the model $\theta = 5$ had the biggest critical loads.

  Both the delamination onset and growth analysis demonstrated that a bigger woven angle leads to smaller initiation loads and critical loads, which indicates that more filled straight plies in the preliminary design of AP-PLY composite laminates should be avoided.

- The patterns that characterize the interwoven layers in AP-PLY composite laminate were introduced and the evaluated results revealed that for a pattern with the same woven layers, more filled straight plies lead to smaller initiation loads and critical loads.

  In the models with the same number of filled straight plies, the number of higher initiation loads in the models with fewer woven plies is greater than that in the models with more woven plies. The smallest initiation load occurs in the model with more woven layers. More layers of woven plies present in the AP-PLY model, result in lower critical loads of delamination growth seen in the model whose pattern has the same number of straight filled plies.

  In the study of patterns in which maximum 4 layers could be woven, the smallest initiation loads and the smallest critical loads of delamination growth are in the model with the pattern of two layers woven plies and two layers filled straight plies.

- With respect to the location of the interwoven layers, less interwoven layers produces bigger influence of the pattern location. Configurations where the woven patterns close to the top loading surface possess higher delamination initiation loads and critical loads.

7.1.3 Analytical solution of delamination growth

Based on LEFM, the critical SERR can be used in determining whether a crack is going to propagate or not. In chapter 5, an energy based method has been developed for the analysis of SERR of a crack in an AP-PLY composite laminate. First, the energy minimization based on beam theory has been carried out to obtain the SERR of a delamination at different thickness locations in an isotropic beam. This approach validated by comparing the calculated SERR to results in the references.

The obtained SERRs based on Euler beam theory and Timoshenko beam theory were compared with finite element results. For smaller cracks, the error was appreciable exceeding 20% when the crack length was less than 0.1L with L the length of the beam. A crack can be classified into 3 types based on the accuracy of the obtained SERR: a crack, bigger than $0.5L$, is a large crack that Euler-Bernoulli beam theory is and the error is less than 10%; a medium crack, $0.2L \leq a \leq 0.5L$, is the one that shear effect cannot be neglected and using Timoshenko beam theory accurate SERR can be obtained (error less than 15%); whereas a smaller crack is the one that using the two beam theories cannot obtain accurate results.

The SERR of a symmetric crack in a symmetric three point bending structure is monotonically increasing. The more general case is that a crack could be initiated from anywhere in a structure. The SERR of the left crack tip decreases after reaching the peak value at $a \approx 0.55L$ for a crack that initiated from the left side of the loading location in the three point bending test. The SERR of the right crack tip decreases to almost zero at the point $a = 0.6L$ after the maximum SERR of the right crack tip is reached at the load point, and then the SERR increases monotonically. The obtained SERR of a crack in isotropic beam is demonstrated as follows:

- the closer a crack is to the top or the bottom of the structure, the smaller is the SERR
- the SERR of left crack tip and right tip are the same as a crack that does not go across the load point
- the SERR of the crack is only dependent on the crack length and has no relationship with the position of the crack in the length direction in terms of the crack not under the load point
- the SERR of left crack tip is higher than or equal to that of right crack tip until the whole structure is symmetry in the case that the crack initiated from the left

side of the loading point

A correction factor was introduced to improve the accuracy of SERR of a small crack. The SERR of small cracks agreed very well with the finite element results after a correction coefficient was included in the analyzed nondimensional SERR. The corrector, which tendency is the same as the SERR, is symmetric for a crack located in the thickness direction $\frac{t_1}{t}$ and $1-\frac{t_1}{t}$, where t_1 and t are the thickness of the top delaminated layer and the whole thickness of the beam, respectively.

A crack on the interface of two isotropic materials in a 3PB model was analyzed to see the effect of dissimilar materials and anticipate the behavior of AP-PLY laminates where the stiffness changes as the woven pattern changes. The study showed that the SERR of a crack including the singularity effect increases the accuracy of the SERR of a small crack.

Moving the neutral axis is a fairly standard approach for non-symmetric laminates. The calculated SERR of a crack in composites was compared with the results obtained from the finite element model and good agreement was observed.

The materials of different parts in an AP-PLY composite laminate could be considered as two materials based on the assumption that the resin area is small and does not affect the material properties of that part. Therefore the SERR of a delamination that goes across different materials was studied and a series of equations were derived to solve this problem. The results demonstrated that after a crack goes across a soft material, the SERR rapidly increases and after it goes across a stiff material it decreases. As such, the stiffer material can be used to prevent or delay the propagation of a crack in an industrial application. It should be noted that the closer a crack is propagating to the transition point of two materials, the bigger is the error of the predicted SERR. The method based on energy minimization developed for isotropic beams was extended to AP-PLY configurations. The analytical SERR of a crack in an AP-PLY model agreed reasonably well with the finite element results.

Two parameters, the relative stiffness of different beam sections and the number of sections with different stiffness were studied again with AP-PLY variable stiffness properties in mind. The analytical solution was compared with the finite element results and displayed good agreement. An optimization process using a GA method for simple AP-PLY composite laminates was proposed based on the results of the parametric study and subsequently, an optimized simple AP-PLY composite laminate was obtained in accordance with the requirements of the design.

The analytical model only works for cases where deflections are small. For such cases, simpler models help define a range of values of parameters (stiffness, layup, AP-PLY pattern) which have promise. Then, a more detailed simulation is needed for higher accuracy.

7.1.4 Lessons learned from test

A series of three point bending test on simple AP-PLY composite laminate beam have been carried out. The 10 layers of 90 plies on top and bottom surfaces were removed after the transverse matrix crack was found in the first two tests. The tests demonstrate that the parameters in the set-up, such as the size of loading nose and the silicon pads used between the loading nose and the coupons affected the damage mode, damage location and damage initiation load. Smaller loading nose and thinner silicon pads led to breakage of fibers on the top surface which was not the desired failure mode. A bigger loading nose would result in a higher damage initiation load due to a more uniform distribution of applied loads. In the tests, the damage of the specimens was the combination of transverse matrix failure, broken fibers, fiber breakage induced delamination and mode II delamination resulting from shear. A section cut of a tested specimen showed that the delamination in the resin area followed the woven path. It is necessary to carry out more tests to figure out the delamination behavior of AP-PLY composite beam in the three point bending test.

7.2 Recommendations for future work

The recovered interlaminar stress was determined using the combination of the stress recovery technology and a coarse meshed finite element model. Therefore 4 steps were carried out manually during the whole process. Although the implementation of the stress recovery technology in the finite element software is out of the scope of this thesis, the further investigation remains necessary to make the whole process more efficient and time-saving. Furthermore, choosing another appropriate onset of failure criterion to determine the delamination onset leads to a more accurate prediction of delamination initiation location.

CZM has been applied in this thesis to predict the damage initiation and propagation in AP-PLY composite laminates. The cohesive element approach used in FEM for AP-PLY composite laminates needs to be further improved, as there were only cohesive elements at the interfaces around the resin pocket due to the convergence issues and duration of each run. Under certain conditions, a delamination will start and will propagate between plies in a direction following the woven path of the pattern and will branch from one interface to the next. These drawbacks may be remedied by inserting more cohesive elements or using an explicit computation scheme.

In the finite element model, a point load was applied to simulate the impact load. The numerical problem caused by the point load is that severe stress concentration and severe deformation of the elements occur close to the load point, which might reduce the accuracy of the solution. A more realistic model should simulate more accurately the specimen contact area over which loading is exerted. The predicted damage initiation loads and critical loads may be further improved and become more accurate by modifying this

loading area.

The beam theory employed in the energy method to analyze the SERR of a crack in a structure is not valid for small cracks $a \leq 0.1L$ or equally $a \leq 2t$. Further investigation on a newly developed theory to determine the SERR of a small crack is necessary to improve the accuracy of the present methodology.

The presented energy method demonstrates the process to determine the SERR of a crack in an AP-PLY composite laminate structure. Nevertheless, it has been found from the damaged structures that there are multiple delaminations inside which interact with each other. In this regard, a more in-depth exploration of the prediction of multi-delamination growth remains a topic of future research.

Appendix A

Figures of crack growth in the model of different layups using cohesive elements

This appendix list the figures of parametric research of crack growth using cohesive elements in chapter 4.

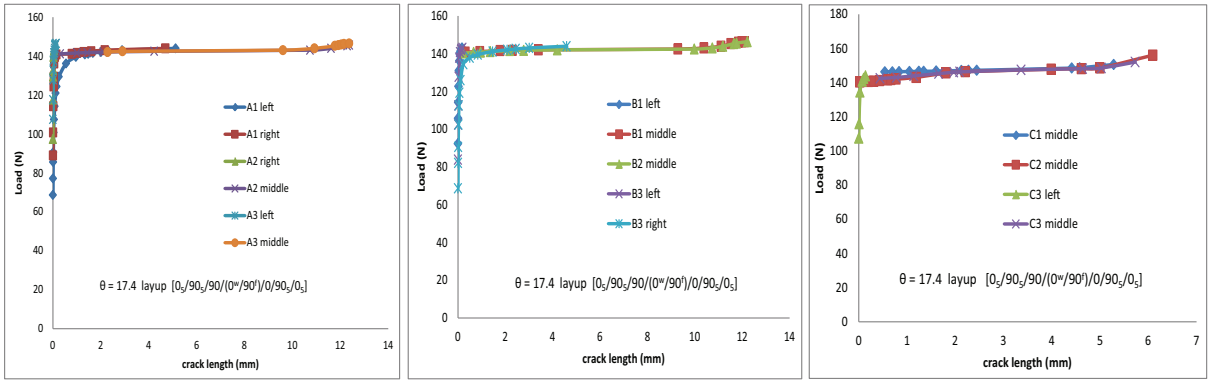

Figure A.1: Crack growth curves of layup $[0_5/90_5/90/(0^w/90^f)/0/90_5/0_5]$

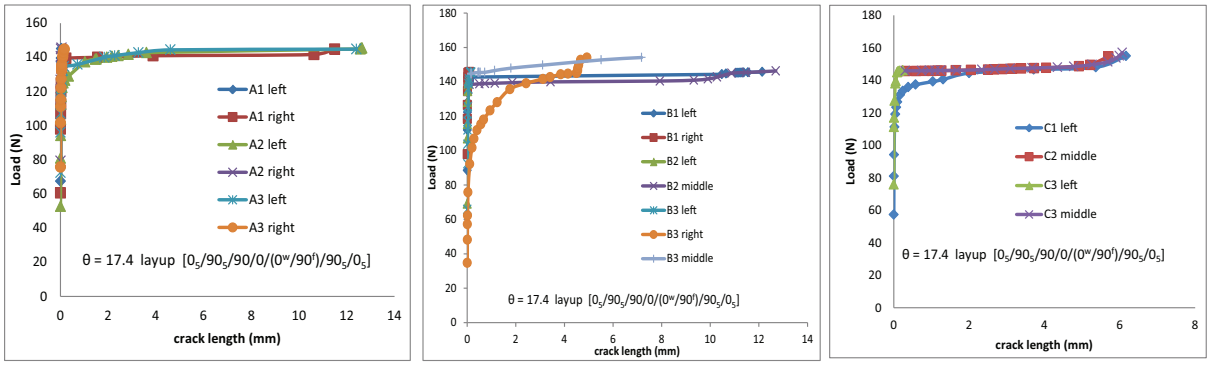

Figure A.2: Crack growth curves of layup $[0_5/90_5/90/0/(0^w/90^f)/90_5/0_5]$

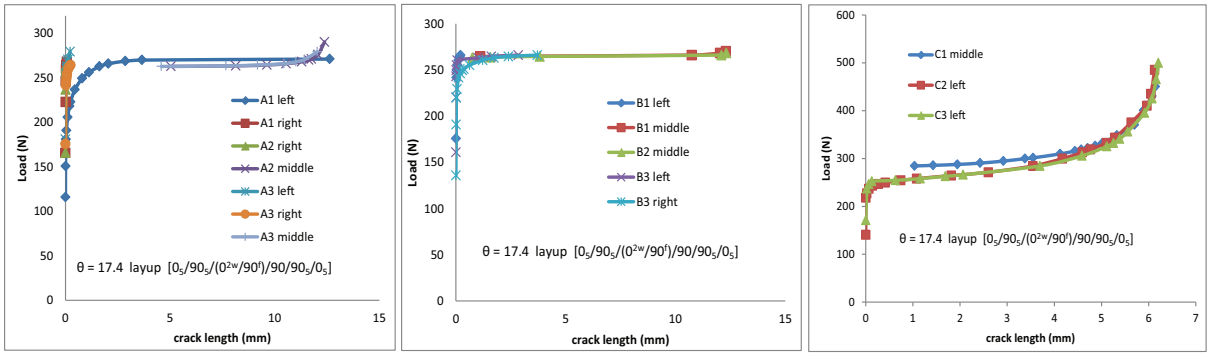

Figure A.3: Crack growth curves of layup $[0_5/90_5/(0^{2w}/90^f)/90/90_5/0_5]$

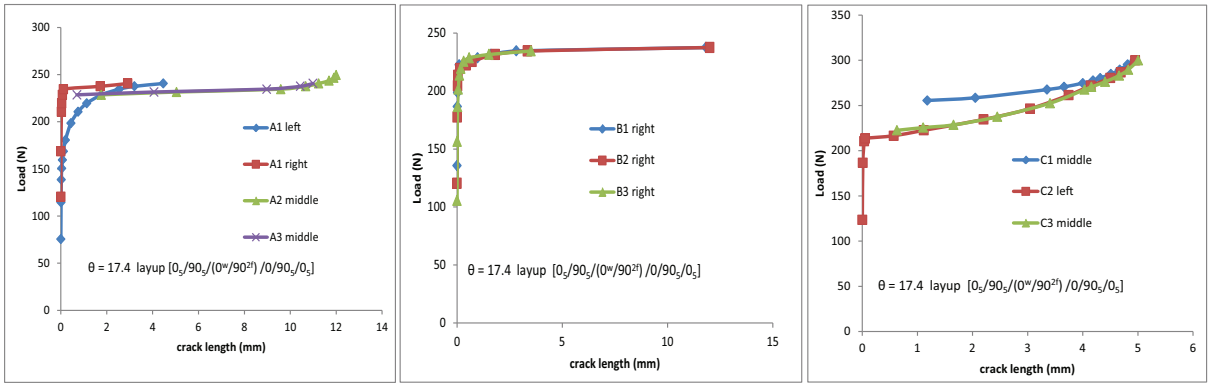

Figure A.4: Crack growth curves of layup $[0_5/90_5/(0^w/90^{2f})/0/90_5/0_5]$

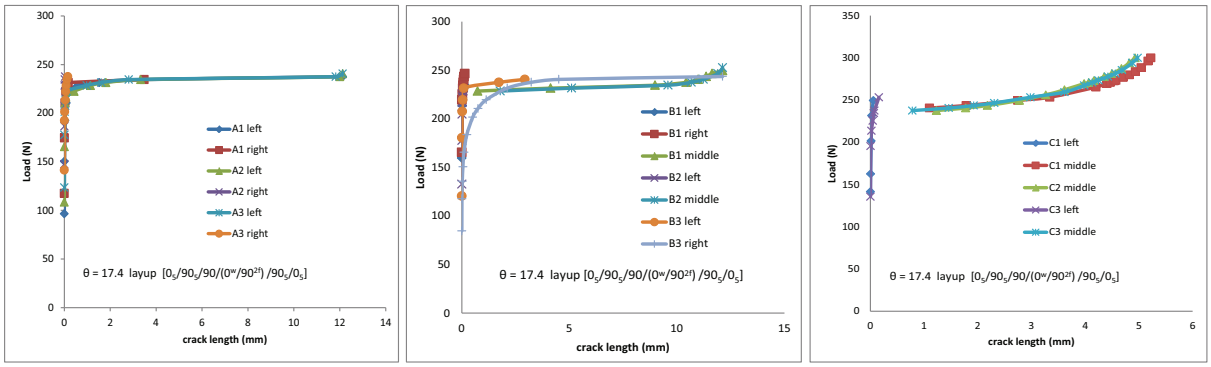

Figure A.5: Crack growth curves of layup $[0_5/90_5/90/(0^w/90^{2f})/90_5/0_5]$

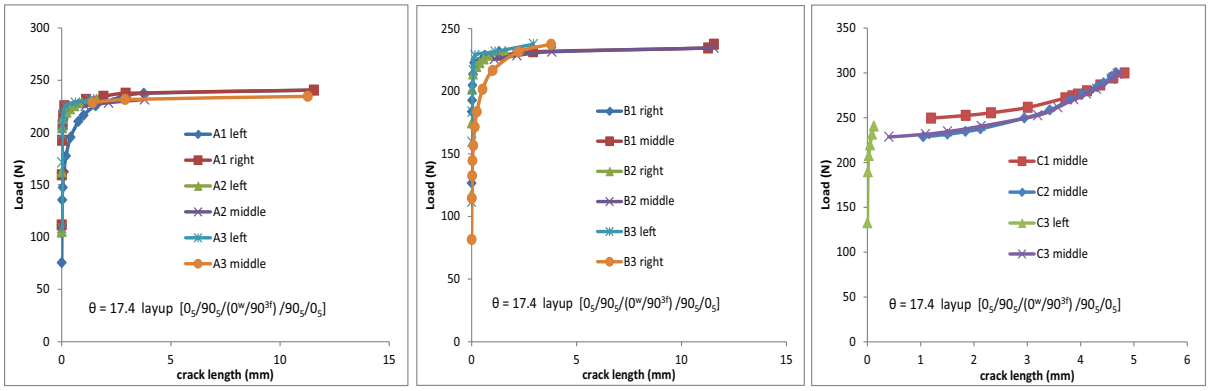

Figure A.6: Crack growth curves of layup $[0_5/90_5/(0^w/90^{3f})/90_5/0_5]$

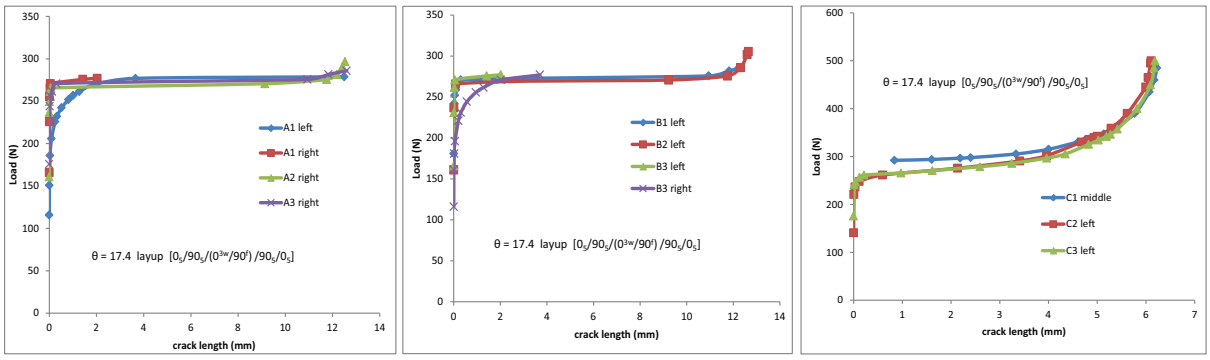

Figure A.7: Crack growth curves of layup $[0_5/90_5/(0^{3w}/90^f)/90_5/0_5]$

Appendix B

The constants and generalized forces to obtain the SERR of a crack that goes across the load point using an energy method

The basic procedure to obtain the analytical SERR of a crack that goes across the load point is the same as the procedure of a crack that is only on the left or the right of the load point. The difference is that there are one more segments in the beam of a crack that goes across the load point, as shown in Figure 5.3. Therefore the constants and generalized forces at the crack tips of a crack that goes across the load point need to be recalculated.

The constants for a crack goes across the load point are listed as below:

$$\begin{aligned}
C_1 &= \frac{\frac{L}{2}-x_1}{3E_1I_1}+\frac{1}{(\frac{L}{2}-x_1)G_1A_1} \\
C_2 &= \frac{\frac{L}{2}-x_1}{6E_1I_1}-\frac{1}{(\frac{L}{2}-x_1)G_1A_1} \\
C_3 &= \frac{x_2-\frac{L}{2}}{3E_1I_1}+\frac{1}{(x_2-\frac{L}{2})G_1A_1} \\
C_4 &= \frac{x_2-\frac{L}{2}}{6E_1I_1}-\frac{1}{(x_2-\frac{L}{2})G_1A_1} \\
C_5 &= \frac{\frac{L}{2}-x_1}{3E_2I_2}+\frac{1}{(\frac{L}{2}-x_1)G_2A_2} \\
C_6 &= \frac{\frac{L}{2}-x_1}{6E_2I_2}-\frac{1}{(\frac{L}{2}-x_1)G_2A_2}
\end{aligned} \tag{B.1}$$

$$
\begin{aligned}
C_7 &= \frac{x_2 - \frac{L}{2}}{3E_2I_2} + \frac{1}{(x_2 - \frac{L}{2})G_2A_2} \\
C_8 &= \frac{x_2 - \frac{L}{2}}{6E_2I_2} - \frac{1}{(x_2 - \frac{L}{2})G_2A_2}
\end{aligned}
$$

The Lagrange Multipliers are determined after solving the equations:

$$
\begin{aligned}
A_1\lambda_1 + A_2\lambda_2 + A_3\lambda_3 &= \frac{P}{2}x_1 \\
A_2\lambda_1 + A_4\lambda_2 + A_5\lambda_3 &= \frac{P}{2}\frac{L}{2} \\
A_3\lambda_1 + A_5\lambda_2 + A_6\lambda_3 &= \frac{P}{2}(L - x_2)
\end{aligned}
\tag{B.2}
$$

where the constants are:

$$
\begin{aligned}
A_1 &= \frac{1}{C_1} + \frac{1}{C_5} + (\frac{C_2}{C_1})^2\frac{1}{\frac{C_1^2-C_2^2}{C_1} + \frac{C_3^2-C_4^2}{C_3}} + (\frac{C_6}{C_5})^2\frac{1}{\frac{C_5^2-C_6^2}{C_5} + \frac{C_7^2-C_8^2}{C_7}} + \frac{c^2}{\frac{a}{E_1A_1} + \frac{a}{E_2A_2}} \\
A_2 &= -(\frac{C_2}{C_1}\frac{1}{\frac{C_1^2-C_2^2}{C_1} + \frac{C_3^2-C_4^2}{C_3}} + \frac{C_6}{C_5}\frac{1}{\frac{C_5^2-C_6^2}{C_5} + \frac{C_7^2-C_8^2}{C_7}} - \frac{c^2}{\frac{a}{E_1A_1} + \frac{a}{E_2A_2}}) \\
A_3 &= \frac{C_2}{C_1}\frac{C_4}{C_3}\frac{1}{\frac{C_1^2-C_2^2}{C_1} + \frac{C_3^2-C_4^2}{C_3}} + \frac{C_6}{C_5}\frac{C_8}{C_7}\frac{1}{\frac{C_5^2-C_6^2}{C_5} + \frac{C_7^2-C_8^2}{C_7}} + \frac{c^2}{\frac{a}{E_1A_1} + \frac{a}{E_2A_2}} \\
A_4 &= \frac{1}{\frac{C_1^2-C_2^2}{C_1} + \frac{C_3^2-C_4^2}{C_3}} + \frac{1}{\frac{C_5^2-C_6^2}{C_5} + \frac{C_7^2-C_8^2}{C_7}} + \frac{c^2}{\frac{a}{E_1A_1} + \frac{a}{E_2A_2}} \\
A_5 &= -(\frac{C_4}{C_3}\frac{1}{\frac{C_1^2-C_2^2}{C_1} + \frac{C_3^2-C_4^2}{C_3}} + \frac{C_8}{C_7}\frac{1}{\frac{C_5^2-C_6^2}{C_5} + \frac{C_7^2-C_8^2}{C_7}} - \frac{c^2}{\frac{a}{E_1A_1} + \frac{a}{E_2A_2}}) \\
A_6 &= \frac{1}{C_3} + \frac{1}{C_7} + (\frac{C_4}{C_3})^2\frac{1}{\frac{C_1^2-C_2^2}{C_1} + \frac{C_3^2-C_4^2}{C_3}} + (\frac{C_8}{C_7})^2\frac{1}{\frac{C_5^2-C_6^2}{C_5} + \frac{C_7^2-C_8^2}{C_7}} + \frac{c^2}{\frac{a}{E_1A_1} + \frac{a}{E_2A_2}}
\end{aligned}
\tag{B.3}
$$

The solved unknowns of generalized forces at the crack tips are listed as following:

$$
M_1|_{x=x_1} = \frac{\lambda_1}{C_1} - \frac{C_2}{C_1}\frac{\lambda_2 - \frac{C_2}{C_1}\lambda_1 - \frac{C_4}{C_3}\lambda_3}{\frac{C_1^2-C_2^2}{C_1} + \frac{C_3^2-C_4^2}{C_3}} \tag{B.4}
$$

$$
M_2|_{x=x_1} = \frac{\lambda_1}{C_5} - \frac{C_6}{C_5}\frac{\lambda_2 - \frac{C_6}{C_5}\lambda_1 - \frac{C_8}{C_7}\lambda_3}{\frac{C_5^2-C_6^2}{C_5} + \frac{C_7^2-C_8^2}{C_7}} \tag{B.5}
$$

$$M_1|_{x=x_2} = \frac{\lambda_3}{C_3} - \frac{C_4}{C_3}\frac{\lambda_2 - \frac{C_2}{C_1}\lambda_1 - \frac{C_4}{C_3}\lambda_3}{\frac{C_1^2-C_2^2}{C_1} + \frac{C_3^2-C_4^2}{C_3}} \tag{B.6}$$

$$M_2|_{x=x_2} = \frac{\lambda_3}{C_7} - \frac{C_8}{C_7}\frac{\lambda_2 - \frac{C_6}{C_5}\lambda_1 - \frac{C_8}{C_7}\lambda_3}{\frac{C_5^2-C_6^2}{C_5} + \frac{C_7^2-C_8^2}{C_7}} \tag{B.7}$$

$$M_1|_{x=\frac{L}{2}} = \frac{\lambda_2 - \frac{C_2}{C_1}\lambda_1 - \frac{C_4}{C_3}\lambda_3}{\frac{C_1^2-C_2^2}{C_1} + \frac{C_3^2-C_4^2}{C_3}} \tag{B.8}$$

$$M_2|_{x=\frac{L}{2}} = \frac{\lambda_2 - \frac{C_6}{C_5}\lambda_1 - \frac{C_8}{C_7}\lambda_3}{\frac{C_5^2-C_6^2}{C_5} + \frac{C_7^2-C_8^2}{C_7}} \tag{B.9}$$

$$N = \frac{-(\lambda_1+\lambda_2+\lambda_3)c}{\frac{a}{E_1A_1} + \frac{a}{E_2A_2}} \tag{B.10}$$

The energy release rate G of crack tips can be computed according to Eqs. 5.44 and 5.45 after all the unknowns have been obtained.

Appendix C

Derivation SERR using the displacement method based on Timoshenko beam theory

The governing equations of Timoshenko beam theory are:

$$EI\frac{d^3\phi}{dx^3} = 0 \tag{C.1}$$

$$\frac{dw}{dx} = \phi - \frac{EI}{\kappa AG}\frac{d^2\phi}{dx^2} \tag{C.2}$$

where ϕ is the angle of rotation of the beam, w is the displacement, E is the Young's modulus, I is the second moment of area, A is the cross section area, G is the shear modulus and κ is the Timoshenko shear coefficient, which depends on the geometry and $\kappa = \frac{5}{6}$ for a rectangular section. The moment M and shear force Q can be written as:

$$M = -D\frac{d\phi}{dx} \tag{C.3}$$

$$Q = S(\frac{dw}{dx} - \phi) \tag{C.4}$$

where D is the bending stiffness of the beam and $D = EI$, S is the shear stiffness and $S = \kappa AG$.

For a crack in the left side of the loading point, shown in Figure 5.3 (a), the whole beam was divided into 5 parts and the part 0, 3 and 4 are intact beams whereas part 1 and part 2 are sub-beams. For the intact beam parts, the moments can be computed using Eq.C.3. The moment of part 0 and part 3 can be expressed as:

$$M = -D\frac{d\phi}{dx} = \frac{P}{2}x \tag{C.5}$$

Integrating Eq. C.5 leads to:

$$\phi = -\frac{Px^2}{4D} + C_1 \tag{C.6}$$

Substituting Eq. C.6 into Eq. C.2 and then integrating once results in:

$$w = -\frac{Px^3}{12D} + (C_1 + \frac{P}{2S})x + C_2 \tag{C.7}$$

The expression of ϕ and w of part 4 can be obtained following the same procedure whereas the moment $M = \frac{P}{2}(L - x)$.

The moment distribution in sub-beams are unknown, therefore the expressions of rotation and displacement in sub-beams 1 and 2 are obtained by integrating Eq. C.1 three times and integrating Eq. C.2 once after ϕ was substituted in Eq. C.2:

$$\phi = C_0 + C_1 x + C_2 x^2 \tag{C.8}$$

$$w = C_3 + (C_0 - 2\frac{D}{S}C_2)x + \frac{1}{2}C_1 x^2 + \frac{1}{3}C_2 x^3 \tag{C.9}$$

The rotation and displacement of the 5 parts are:

$$\phi_0 = -\frac{Px^2}{4D} + C_{01} \tag{C.10}$$

$$w_0 = -\frac{Px^3}{12D} + (C_{01} + \frac{P}{2S})x + C_{02} \tag{C.11}$$

$$\phi_1 = C_{10} + C_{11}x + C_{12}x^2 \tag{C.12}$$

$$w_1 = C_{13} + (C_{10} - 2\frac{D}{S}C_{12})x + \frac{1}{2}C_{11}x^2 + \frac{1}{3}C_{12}x^3 \tag{C.13}$$

$$\phi_2 = C_{20} + C_{21}x + C_{22}x^2 \tag{C.14}$$

$$w_2 = C_{23} + (C_{20} - 2\frac{D}{S}C_{22})x + \frac{1}{2}C_{21}x^2 + \frac{1}{3}C_{22}x^3 \tag{C.15}$$

$$\phi_3 = -\frac{Px^2}{4D} + C_{31} \tag{C.16}$$

$$w_3 = -\frac{Px^3}{12D} + (C_{31} + \frac{P}{2S})x + C_{32} \tag{C.17}$$

$$\phi_4 = \frac{P(x^2 - 2xL)}{4D} + C_{41} \tag{C.18}$$

$$w_4 = \frac{Px^3}{12D} - \frac{PLx^2}{4D} + (C_{41} - \frac{P}{2S})x + C_{42} \tag{C.19}$$

where the subscripts of ϕ and w represent the number of the parts and the same for the first subscript in constants C.

The boundary conditions are:

$$w_0|_{x=0} = 0, \qquad w_4|_{x=L} = 0 \tag{C.20}$$

The displacement and rotation related continuity conditions at $x = x_1$, $x = x_2$ and $x = \frac{L}{2}$ are:

$$\begin{aligned} w_0|_{x=x_1} &= w_1|_{x=x_1}, \qquad w_0|_{x=x_1} = w_2|_{x=x_1}, \qquad w_3|_{x=x_2} = w_1|_{x=x_2} \\ \phi_0|_{x=x_1} &= \phi_1|_{x=x_1}, \qquad \phi_0|_{x=x_1} = \phi_2|_{x=x_1}, \qquad \phi_3|_{x=x_2} = \phi_1|_{x=x_2} \end{aligned}$$

$$\begin{aligned} w_3|_{x=x_2} &= w_2|_{x=x_2}, \qquad w_3|_{x=\frac{L}{2}} = w_4|_{x=\frac{L}{2}} \\ \phi_3|_{x=x_2} &= \phi_2|_{x=x_2}, \qquad \phi_3|_{x=\frac{L}{2}} = \phi_4|_{x=\frac{L}{2}} \end{aligned} \tag{C.21}$$

The continuity moments equations at $x = x_1$ and $x = x_2$ are:

$$M_0|_{x=x_1} = M_1|_{x=x_1} + M_2|_{x=x_1} - N_1|_{x=x_1}\frac{t_1}{2} + N_2|_{x=x_1}\frac{t_2}{2} \tag{C.22}$$

$$M_3|_{x=x_2} = M_1|_{x=x_2} + M_2|_{x=x_2} - N_1|_{x=x_2}\frac{t_1}{2} + N_2|_{x=x_2}\frac{t_2}{2} \tag{C.23}$$

From section 5.2.1, we know that $N_1|_{x=x_1} = N_1|_{x=x_2} = N$ and $N_2|_{x=x_1} = N_2|_{x=x_2} = -N$. The axial equilibrium of the deformed beam is:

$$\frac{Na}{EA_2} + \frac{Na}{EA_1} = (\phi_0|_{x=x_1} - \phi_3|_{x=x_2})\frac{t_1 + t_2}{2} \tag{C.24}$$

Therefore the axial load N is obtained:

$$N = (\phi_0|_{x=x_1} - \phi_3|_{x=x_2})\frac{t}{2a}\frac{EA_1EA_2}{EA_1 + EA_2} \tag{C.25}$$

Substituting Eq. C.25 into Eqs. C.22 and C.23, the continuity moments equations can be rewritten as:

$$M_0|_{x=x_1} = M_1|_{x=x_1} + M_2|_{x=x_1} + \frac{t^2}{4a}(\phi_0|_{x=x_1} - \phi_3|_{x=x_2})\frac{EA_1 \quad EA_2}{EA_1 + EA_2} \tag{C.26}$$

$$M_3|_{x=x_2} = M_1|_{x=x_2} + M_2|_{x=x_2} + \frac{t^2}{4a}(\phi_0|_{x=x_1} - \phi_3|_{x=x_2})\frac{EA_1EA_2}{EA_1 + EA_2} \tag{C.27}$$

The displacement and rotation equations are solved and constants are known using the above boundary conditions and continuity conditions, thus the moments, shear forces and axial loads at crack tips are obtained and the energy release rate can be computed using Eqs. 5.44 and 5.45.

Bibliography

ABAQUS 6.11. *ABAQUS User Documentation*. Pawtucket, RI, USA, 2011.

S. Abrate. Impact on laminated composite materials. *Applied mechanics reviews*, 44(4): 155–190, 1991.

R. Akkerman. Laminate mechanics for balanced woven fabrics. *Composites Part B: Engineering*, 37(2):108–116, 2006.

G. Alfano. On the influence of the shape of the interface law on the application of cohesive-zone models. *Composites Science and Technology*, 66(6):723–730, 2006.

D.H. Allen and C.R. Searcy. A micromechanical model for a viscoelastic cohesive zone. *International Journal of Fracture*, 107(2):159–176, 2001.

M.G. Andrews, R. Massabò, and B.N. Cox. Elastic interaction of multiple delaminations in plates subject to cylindrical bending. *International Journal of Solids and Structures*, 43(5):855–886, 2006.

J.H. Argyris and K.J. Willam. Some considerations for the evaluation of finite element models. *Nuclear Engineering and Design*, 28(1):76–96, 1974.

ASTM. *STP568. Foreign object impact damage to composites*. 1973.

ASTM. *D 790-03. Standard Test Methods for Flexural Properties of Unreinforced and Reinforced Plastics and Electrical Insulating Materials*. 2003.

ASTM. *D 7264-06. Standard Test Method for Flexural Properties of Polymer Matrix Composite Materials*. 2006a.

ASTM. *D 2344-06. Standard Test Method for Short-Beam Strength of Polymer Matrix Composite Materials and Their Laminates*. 2006b.

L. Banks-Sills. Application of the finite element method to linear elastic fracture mechanics. *Applied Mechanics Reviews*, 44(10):447–461, 1991.

E.J. Barbero and J.N. Reddy. Modeling of delamination in composite laminates using a layer-wise plate theory. *International Journal of Solids and Structures*, 28(3):373–388, 1991.

G.I. Barenblatt. The mathematical theory of equilibrium cracks in brittle fracture. *Advances in applied mechanics*, 7(1):55–129, 1962.

J. Barlow. Optimal stress locations in finite element models. *International Journal for Numerical Methods in Engineering*, 10(2):243–251, 1976.

R.S. Barsoum. Triangular quarter-point elements as elastic and perfectly-plastic crack tip elements. *International Journal for numerical Methods in engineering*, 11(1):85–98, 1977.

W. Becker, P.P. Jin, and P. Neuser. Interlaminar stresses at the free corners of a laminate. *Composite structures*, 45(2):155–162, 1999.

J.A. Begley and J.D. Landes. The j integral as a fracture criterion. In *Fracture Toughness: Part II*. ASTM International, 1972.

M.L. Benzeggagh and M. Kenane. Measurement of mixed-mode delamination fracture toughness of unidirectional glass/epoxy composites with mixed-mode bending apparatus. *Composites science and technology*, 56(4):439–449, 1996.

N.V. Bhat and P.A. Lagace. An analytical method for the evaluation of interlaminar stresses due to material discontinuities. *Journal of composite materials*, 28(3):190–210, 1994.

T.J. Boone, P.A. Wawrzynek, and A.R. Ingraffea. Simulation of the fracture process in rock with application to hydrofracturing. *International Journal of Rock Mechanics and Mining Sciences & Geomechanics Abstracts*, 23(3):255–265, 1986.

R. Borg, L. Nilsson, and K. Simonsson. Simulating dcb, enf and mmb experiments using shell elements and a cohesive zone model. *Composites Science and Technology*, 64(2): 269–278, 2004.

P. Bose and J.N. Reddy. Analysis of composite plates using various plate theories-part 1: Formulation and analytical solutions. *Structural Engineering and Mechanics*, 6(6): 583–612, 1998.

G.T. Camacho and M. Ortiz. Computational modelling of impact damage in brittle materials. *International Journal of solids and structures*, 33(20):2899–2938, 1996.

P.P. Camanho, C.G. Davila, and M.F. De Moura. Numerical simulation of mixed-mode progressive delamination in composite materials. *Journal of composite materials*, 37 (16):1415–1438, 2003.

J. Cao, R. Akkerman, P. Boisse, J. Chen, H.S. Cheng, E.F. De Graaf, J.L. Gorczyca, P. Harrison, G. Hivet, J. Launay, et al. Characterization of mechanical behavior of woven fabrics: experimental methods and benchmark results. *Composites Part A: Applied Science and Manufacturing*, 39(6):1037–1053, 2008.

L.A. Carlsson, J.W. Gillespie, and R.B. Pipes. On the analysis and design of the end notched flexure (ENF) specimen for mode II testing. *Journal of composite materials*, 20(6):594–604, 1986.

N. Chandra, H. Li, C. Shet, and H. Ghonem. Some issues in the application of cohesive zone models for metal–ceramic interfaces. *International Journal of Solids and Structures*, 39(10):2827–2855, 2002.

D.J. Chen, D.K. Shah, and W.S. Chan. Interfacial stress estimation using least-square extrapolation and local stress smoothing in laminated composites. *Computers & structures*, 58(4):765–774, 1996.

W. Chen and T. Huang. Three dimensional interlaminar stress analysis at free edges of composite laminate. *Computers & structures*, 32(6):1275–1286, 1989.

M. Cho and J.S. Kim. Higher-order zig-zag theory for laminated composites with multiple delaminations. *Journal of Applied Mechanics*, 68(6):869–877, 2001.

H.Y. Choi and F. Chang. A model for predicting damage in graphite/epoxy laminated composites resulting from low-velocity point impact. *Journal of Composite Materials*, 26(14):2134–2169, 1992.

R.M. Christensen. Stress based yield/failure criteria for fiber composites. *International journal of solids and structures*, 34(5):529–543, 1997.

R.J.C. Creemers. Interlaminar shear strength criteria for composites. 2009.

J.R. Dana and R.M. Barker. Three-dimensional analysis for the stress distribution near circular holes in laminated composites. Technical report, DTIC Document, 1974.

B. Dattaguru, K.S. Venkatesha, T.S. Ramamurthy, and F.G. Buchholz. Finite element estimates of strain energy release rate components at the tip of an interface crack under mode i loading. *Engineering fracture mechanics*, 49(3):451–463, 1994.

B.D. Davidson, R. Krüger, and M. König. Effect of stacking sequence on energy release rate distributions in multidirectional dcb and enf specimens. *Engineering Fracture Mechanics*, 55(4):557–569, 1996.

A. De-Andrés, J.L. Pérez, and M. Ortiz. Elastoplastic finite element analysis of three-dimensional fatigue crack growth in aluminum shafts subjected to axial loading. *International Journal of Solids and Structures*, 36(15):2231–2258, 1999.

R. De Borst. Fracture in quasi-brittle materials: a review of continuum damage-based approaches. *Engineering fracture mechanics*, 69(2):95–112, 2002.

R. De Borst. Numerical aspects of cohesive-zone models. *Engineering fracture mechanics*, 70(14):1743–1757, 2003.

J. Degrieck and W. Van Paepegem. Fatigue damage modeling of fibre-reinforced composite materials: Review. *Applied Mechanics Reviews*, 54(4):279–300, 2001.

A. Dimitrov, H. Andrä, and E. Schnack. Efficient computation of order and mode of corner singularities in 3d-elasticity. *International Journal for Numerical Methods in Engineering*, 52(8):805–827, 2001.

D.S. Dugdale. Yielding of steel sheets containing slits. *Journal of the Mechanics and Physics of Solids*, 8(2):100–104, 1960.

J.J. Engblom and J.J. Havelka. Transient response predictions for transversely loaded laminated composite plates. In *AIAA, ASME, ASCE, AHS, and ASC, Structures,*

Structural Dynamics and Materials Conference, 30 th, Mobile, AL, pages 1256–1263, 1989.

J.D. Eshelby. The continuum theory of lattice defects. *Solid state physics*, 3:79–144, 1956.

F. Esrail and C. Kassapoglou. An efficient approach for damage quantification in quasi-isotropic composite laminates under low speed impact. *Composites: Part B*, 61:116–126, 2014a.

F. Esrail and C. Kassapoglou. An efficient approach to determine compression after impact strength of quasi-isotropic composite laminates. *Composites Science and Technology*, 98:28–35, 2014b.

C. Fagiano, M.M. Abdalla, and Z. Gürdal. Interlaminar stress recovery of multilayer composite shell structures for three-dimensional finite elements. *Finite Elements in Analysis and Design*, 46(12):1122–1130, 2010a.

C. Fagiano, M.M. Abdalla, C. Kassapoglou, and Z. Gürdal. Interlaminar stress recovery for three-dimensional finite elements. *Composites Science and Technology*, 70(3):530–538, 2010b.

M.L. Falk, A. Needleman, and J.R. Rice. A critical evaluation of dynamic fracture simulations using cohesive surfaces. *arXiv preprint cond-mat/0106304*, 2001.

H. Fan, W. Yang, B. Wang, Y. Yan, Q. Fu, D. Fang, and Z. Zhuang. Design and manufacturing of a composite lattice structure reinforced by continuous carbon fibers. *Tsinghua Science & Technology*, 11(5):515–522, 2006.

D.N. Fenner. Stress singularities in composite materials with an arbitrarily oriented crack meeting an interface. *International Journal of Fracture*, 12(5):705–721, 1976.

K. Gordnian, H. Hadavinia, G. Simpson, and A. Aboutorabi. Calculation of energy release rate in mode i delamination of angle ply laminated composites. In *ICCES: International Conference on Computational & Experimental Engineering and Sciences*, volume 1, pages 61–68, 2007.

M.A. Hamed, A. Nosier, and G.H. Farrahi. Separation of delamination modes in composite beams with symmetric delaminations. *Materials & design*, 27(10):900–910, 2006.

Z. Hashin. Failure criteria for unidirectional fiber composites. *Journal of applied mechanics*, 47(2):329–334, 1980.

C.T. Herakovich, A. Nagarkar, and D.A. Obrien. Failure analysis of composite laminates with free edges. 1979.

A. Hillerborg, M. Modéer, and P.E. Petersson. Analysis of crack formation and crack growth in concrete by means of fracture mechanics and finite elements. *Cement and concrete research*, 6(6):773–781, 1976.

E. Hinton and J.S. Campbell. Local and global smoothing of discontinuous finite element

functions using a least squares method. *International Journal for Numerical Methods in Engineering*, 8(3):461–480, 1974.

I. Hirai, Y. Uchiyama, Y. Mizuta, and W.D. Pilkey. An exact zooming method. *Finite Elements in Analysis and Design*, 1(1):61–69, 1985.

P.W. Hsu and C.T. Herakovich. A perturbation solution for interlaminar stresses in bidirectional laminates. In *Composite Materials: Testing and Design (Fourth Conference)*. ASTM International, 1977.

H. Hu and C. Wu. Analysis of energy release rate for cracked laminates. *Applied Mathematics and Mechanics*, 16(6):565–581, 1995.

C.Y. Hui and E.J. Kramer. Molecular weight dependence of the fracture toughness of glassy polymers arising from crack propagation through a craze. *Polymer Engineering & Science*, 35(5):419–425, 1995.

J.W. Hutchinson, M.E. Mear, and J.R. Rice. Crack paralleling an interface between dissimilar materials. *Journal of Applied Mechanics*, 54(4):828–832, 1987.

G.R. Irwin. Fracture i. *in Handbuch de Physik VI*, pages 558–590, 1958.

Z. Jin, G.H. Paulino, and R.H. Dodds. Cohesive fracture modeling of elastic–plastic crack growth in functionally graded materials. *Engineering Fracture Mechanics*, 70 (14):1885–1912, 2003.

R.M. Jones. *Mechanics of Composite Materials*. Taylor and Francis Inc., Virginia, 1999.

S.S.V. Kandula, J. Abanto-Bueno, P.H. Geubelle, and J. Lambros. Cohesive modeling of dynamic fracture in functionally graded materials. *International journal of fracture*, 132(3):275–296, 2005.

M.F. Kanninen. An augmented double cantilever beam model for studying crack propagation and arrest. *International Journal of fracture*, 9(1):83–92, 1973.

M.F. Kanninen. A dynamic analysis of unstable crack propagation and arrest in the dcb test specimen. *International Journal of Fracture*, 10(3):415–430, 1974.

T. Kant and M.P. Menon. Estimation of interlaminar stresses in fibre reinforced composite cylindrical shells. *Computers & Structures*, 38(2):131–147, 1991.

T. Kant and K. Swaminathan. Estimation of transverse/interlaminar stresses in laminated composites–a selective review and survey of current developments. *Composite structures*, 49(1):65–75, 2000.

G.A. Kardomateas. The initial post-buckling and growth behavior of internal delaminations in composite plates. *Journal of Applied Mechanics*, 60(4):903–910, 1993.

C. Kassapoglou. *Design and Analysis of Composite Structures With Applications to Aerospace Structures*. John Wiley and Sons, The Netherlands, 2010.

C. Kassapoglou and P.A. Lagace. Closed form solutions for the interlaminar stress field

in angle-ply and cross-ply laminates. *Journal of Composite Materials*, 21(4):292–308, 1987.

H. Khoramishad, A.D. Crocombe, K.B. Katnam, and I.A. Ashcroft. Predicting fatigue damage in adhesively bonded joints using a cohesive zone model. *International Journal of fatigue*, 32(7):1146–1158, 2010.

B.W. Kim and A.H. Mayer. Influence of fiber direction and mixed-mode ratio on delamination fracture toughness of carbon/epoxy laminates. *Composites Science and Technology*, 63(5):695–713, 2003.

H. Kim and K.T. Kedward. Modeling hail ice impacts and predicting impact damage initiation in composite structures. *AIAA Journal*, 38(7):1278–1288, 2000.

J.Y. Kim and C.S. Hong. Three-dimensional finite element analysis of interlaminar stresses in thick composite laminates. *Computers & structures*, 40(6):1395–1404, 1991.

A.J. Kinloch, Y. Wang, J.G. Williams, and P. Yayla. The mixed-mode delamination of fibre composite materials. *Composites Science and Technology*, 47(3):225–237, 1993.

K. Kishimoto, S. Aoki, and M. Sakata. On the path independent integral-j. *Engineering Fracture Mechanics*, 13(4):841–850, 1980.

R. Krueger. Virtual crack closure technique: history, approach, and applications. *Applied Mechanics Reviews*, 57(2):109–143, 2004.

R. Krueger and T.K. O'Brien. A shell/3d modeling technique for the analysis of delaminated composite laminates. *Composites Part A: applied science and manufacturing*, 32(1):25–44, 2001.

P.E.W. Labossiere and M.L. Dunn. Fracture initiation at three-dimensional bimaterial interface corners. *Journal of the Mechanics and Physics of Solids*, 49(3):609–634, 2001.

P.A. Lagace. *Delamination Fracture under Tensile Loading*. Technology Laboratory for Advanced Composites, Department of Aeronautics and Astronautics, Massachusetts Institute of Technology, 1983.

C.Y. Lee and J.M. Chen. Interlaminar shear stress analysis of composite laminate with layer reduction technique. *International journal for numerical methods in engineering*, 39(5):847–865, 1996.

D. Leguillon. A method based on singularity theory to predict edge delamination of laminates. *International Journal of Fracture*, 100(1):105–120, 1999.

L.B. Lessard, A.S. Schmidt, and M.M. Shokrieh. Three-dimensional stress analysis of free-edge effects in a simple composite cross-ply laminate. *International Journal of Solids and Structures*, 33(15):2243–2259, 1996.

D. Liu. Impact-induced delamination-a view of bending stiffness mismatching. *Journal of Composite Materials*, 22:1–24, 1987.

X. Lu and D. Liu. An interlaminar shear stress continuity theory for both thin and thick composite laminates. *Journal of Applied Mechanics*, 59(3):502–509, 1992.

S. Maiti and P.H. Geubelle. A cohesive model for fatigue failure of polymers. *Engineering Fracture Mechanics*, 72(5):691–708, 2005.

K.M. Mao and C.T. Sun. A refined global-local finite element analysis method. *International Journal for Numerical Methods in Engineering*, 32(1):29–43, 1991.

R. Massabo and B.N. Cox. Concepts for bridged mode ii delamination cracks. *Journal of the Mechanics and Physics of Solids*, 47(6):1265–1300, 1999.

L.N. McCartney. Mechanics of matrix cracking in brittle-matrix fibre-reinforced composites. In *Proceedings of the Royal Society of London A: Mathematical, Physical and Engineering Sciences*, volume 409, pages 329–350. The Royal Society, 1987.

C. Mittelstedt and W. Becker. Free-corner effects in cross-ply laminates: an approximate higher-order theory solution. *Journal of composite materials*, 37(22):2043–2068, 2003.

I. Mohammed and K.M. Liechti. Cohesive zone modeling of crack nucleation at bimaterial corners. *Journal of the Mechanics and Physics of Solids*, 48(4):735–764, 2000.

C.M.D. Moorthy and J.N. Reddy. Recovery of interlaminar stresses and strain energy release rates in composite laminates. *Finite elements in analysis and design*, 33(1): 1–27, 1999.

A. Mota and J.F. Abel. On mixed finite element formulations and stress recovery techniques. *International Journal for Numerical Methods in Engineering*, 47(1-3):191–204, 2000.

A. Mukherjee and B. Varughese. Design guidelines for ply drop-off in laminated composite structures. *Composites Part B: Engineering*, 32(2):153–164, 2001.

M. Naǵelsmit, Kassapoglou. C., and Z. Gürdal. AP-PLY: A new fiber placement architecture for fabric replacement. *SAMPE Journal*, 47(2):36–45, 2011.

M.H. Naǵelsmit. *Fibre Placement Architectures for Improved Damage Tolerance*. 2013.

J.A. Nairn. On the calculation of energy release rates for cracked laminates with residual stresses. *International journal of fracture*, 139(2):267–293, 2006.

A. Needleman. A continuum model for void nucleation by inclusion debonding. *Journal of applied mechanics*, 54(3):525–531, 1987.

T. Nishioka and S.N. Atluri. Path-independent integrals, energy release rates, and general solutions of near-tip fields in mixed-mode dynamic fracture mechanics. *Engineering Fracture Mechanics*, 18(1):1–22, 1983.

T. K. O'Brien. Characterization of delamination onset and growth in a composite laminate. In *Damage in Composite Materials: Basic Mechanisms, Accumulation, Tolerance, and Characterization*. ASTM International, 1982.

J.T. Oden and H.J. Brauchli. On the calculation of consistent stress distributions in finite element approximations. *International Journal for Numerical Methods in Engineering*, 3(3):317–325, 1971.

R. Olsson. Analytical prediction of large mass impact damage in composite laminates. *Composites: Part A*, 32:1207–1215, 2001.

R. Olsson. Closed form prediction of peak load and delamination onset under small mass impact. *Composite Structures*, 59(3):341–349, 2003.

R. Olsson. A survey of test methods for multiaxial and out-of-plane strength of composite laminates. *Composites Science and Technology*, 71(6):773–783, 2011.

A. R. Oskouei, A. Zucchelli, M. Ahmadi, and G. Minak. An integrated approach based on acoustic emission and mechanical information to evaluate the delamination fracture toughness at mode i in composite laminate. *Materials & Design*, 32(3):1444–1455, 2011.

F. Ozdil and L.A. Carlsson. Beam analysis of angle-ply laminate dcb specimens. *Composites Science and Technology*, 59(2):305–315, 1999.

N.J. Pagano. On the calculation of interlaminar normal stress in composite laminate. *Journal of Composite Materials*, 8(1):65–81, 1974.

K. Park, G.H. Paulino, and J.R. Roesler. Determination of the kink point in the bilinear softening model for concrete. *Engineering Fracture Mechanics*, 75(13):3806–3818, 2008.

K. Park, G.H. Paulino, and J.R. Roesler. A unified potential-based cohesive model of mixed-mode fracture. *Journal of the Mechanics and Physics of Solids*, 57(6):891–908, 2009.

P. Petersson. *Crack growth and development of fracture zones in plain concrete and similar materials*. Division, Inst., 1981.

R. B. Pipes and N.J. Pagano. Interlaminar stresses in composite laminates under uniform axial extension. *Journal of Composite Materials*, 4(4):538–548, 1970.

R.B. Pipes and N.J. Pagano. Interlaminar stresses in composite laminatesan approximate elasticity solution. *Journal of Applied Mechanics*, 41(3):668–672, 1974.

S.A. Ponnusami, S. Turteltaub, and S. van der Zwaag. Cohesive-zone modelling of crack nucleation and propagation in particulate composites. *Engineering Fracture Mechanics*, 149:170–190, 2015.

A. Puck and H. Schürmann. Failure analysis of frp laminates by means of physically based phenomenological models. *Composites Science and Technology*, 58(7):1045–1067, 1998.

H. Puck, A.and Schürmann. Failure analysis of frp laminates by means of physically based phenomenological models. *Composites Science and Technology*, 62(12):1633–1662, 2002.

A.H. Puppo and H.A. Evensen. Interlaminar shear in laminated composites under generalized plane stress. *Journal of composite materials*, 4(2):204–220, 1970.

W. Qian and C.T. Sun. Calculation of stress intensity factors for interlaminar cracks in composite laminates. *Composites Science and Technology*, 57(6):637–650, 1997.

Y.P. Qiu and G.J. Weng. A theory of plasticity for porous materials and particle-reinforced composites. *Journal of Applied Mechanics*, 59(2):261–268, 1992.

I.S. Raju and J.H. Crews. Interlaminar stress singularities at a straight free edge in composite laminates. *Computers & Structures*, 14(1):21–28, 1981.

I.S. Raju, J.H. Crews, and M.A. Aminpour. Convergence of strain energy release rate components for edge-delaminated composite laminates. *Engineering fracture mechanics*, 30(3):383–396, 1988.

R.L. Ramkumar and J.D. Whitcomb. Characterization of mode i and mixed-mode delamination growth in t300/5208 graphite/epoxy. In *Delamination and debonding of materials*. ASTM International, 1985.

J.R. Rice. A path independent integral and the approximate analysis of strain concentration by notches and cracks. *Journal of applied mechanics*, 35(2):379–386, 1968.

J.R. Rice and G.C. Sih. Plane problems of cracks in dissimilar media. *Journal of Applied Mechanics*, 32(2):418–423, 1965.

D.H. Robbins and J.N. Reddy. An efficient computational model for the stress analysis of smart plate structures. *Smart materials and structures*, 5(3):353, 1996.

K.L. Roe and T. Siegmund. An irreversible cohesive zone model for interface fatigue crack growth simulation. *Engineering fracture mechanics*, 70(2):209–232, 2003.

E.F. Rybicki and M.F. Kanninen. A finite element calculation of stress intensity factors by a modified crack closure integral. *Engineering Fracture Mechanics*, 9(4):931–938, 1977.

E.F. Rybicki and D.W. Schmueser. Effect of stacking sequence and lay-up angle on free edge stresses around a hole in a laminated plate under tension. *Journal of Composite Materials*, 12(3):300–313, 1978.

H. Saghizadeh and C.K.H. Dharan. Delamination fracture toughness of graphite and aramid epoxy composites. *Journal of engineering materials and technology*, 108(4): 290–295, 1986.

N.J. Salamon. An assessment of the interlaminar stress problem in laminated composites. *Journal of composite materials*, 14(1):177–194, 1980.

R.A. Schapery and B.D. Davidson. Prediction of energy release rate for mixed-mode delamination using classical plate theory. *Applied Mechanics Reviews*, 43(5S):S281–S287, 1990.

I. Sheinman and G.A. Kardomateas. Energy release rate and stress intensity factors for delaminated composite laminates. *International Journal of solids and structures*, 34 (4):451–459, 1997.

K.N. Shivakumar, P.W. Tan, and J.C. Newman. A virtual crack-closure technique for calculating stress intensity factors for cracked three dimensional bodies. *International Journal of Fracture*, 36(3):R43–R50, 1988.

P.O. Sjöblom, J.T. Hartness, and T.M. Cordell. On low-velocity impact testing of composite materials. *Journal of Composite Materials*, 22:30–52, 1988.

K. Song, C.G. Dávila, and C.A. Rose. Guidelines and parameter selection for the simulation of progressive delamination. 2008.

S.H. Song, G.H. Paulino, and W.G. Buttlar. A bilinear cohesive zone model tailored for fracture of asphalt concrete considering viscoelastic bulk material. *Engineering Fracture Mechanics*, 73(18):2829–2848, 2006.

C. Soutis. Fibre reinforced composites in aircraft construction. *Progress in Aerospace Sciences*, 41(2):143–151, 2005.

E.L. Stanton, L.M. Crain, and T.F. Neu. A parametric cubic modelling system for general solids of composite material. *International Journal for Numerical Methods in Engineering*, 11(4):653–670, 1977.

Z.C. Su, T.E. Tay, M. Ridha, and B.Y. Chen. Progressive damage modeling of open-hole composite laminates under compression. *Composite Structures*, 122:507–517, 2015.

C.T. Sun and S. Chattopadhyay. Dynamic response of anisotropic laminated plates under initial stress to impact of a mass. *Journal of applied mechanics*, 42(3):693–698, 1975.

C.T. Sun and M.G. Manoharan. Growth of delamination cracks due to bending in a $[90_5/0_5/90_5]$ laminate. *Composites science and technology*, 34(4):365–377, 1989.

C.T. Sun and R.K. Pandey. Improved method for calculating strain energy release rate based on beam theory. *AIAA journal*, 32(1):184–189, 1994.

C.T. Sun and S. Zheng. Delamination characteristics of double-cantilever beam and end-notched flexure composite specimens. *Composites Science and Technology*, 56(4): 451–459, 1996.

Z. Suo. Singularities interacting with interfaces and cracks. *International Journal of Solids and Structures*, 25(10):1133–1142, 1989.

Z. Suo. Singularities, interfaces and cracks in dissimilar anisotropic media. In *Proceedings of the Royal Society of London A: Mathematical, Physical and Engineering Sciences*, volume 427, pages 331–358. The Royal Society, 1990.

Z. Suo and J.W. Hutchinson. Steady-state cracking in brittle substrates beneath adherent films. *International Journal of Solids and Structures*, 25(11):1337–1353, 1989.

Z. Suo and J.W. Hutchinson. Interface crack between two elastic layers. *International Journal of Fracture*, 43(1):1–18, 1990.

S. Tang and A. Levy. A boundary layer theory-part ii: extension of laminated finite strip. *Journal of Composite Materials*, 9(1):42–52, 1975.

S.W. Tsai and E.M. Wu. A general theory of strength for anisotropic materials. *Journal of composite materials*, 5(1):58–80, 1971.

A. Turon, J. Costa, P.P. Camanho, and C.G. Dávila. Simulation of delamination in composites under high-cycle fatigue. *Composites Part A: applied science and manufacturing*, 38(11):2270–2282, 2007a.

A. Turon, C.G. Davila, P.P. Camanho, and J. Costa. An engineering solution for mesh size effects in the simulation of delamination using cohesive zone models. *Engineering fracture mechanics*, 74(10):1665–1682, 2007b.

V. Tvergaard. Effect of fibre debonding in a whisker-reinforced metal. *Materials Science and Engineering: A*, 125(2):203–213, 1990.

V. Tvergaard and J.W. Hutchinson. The influence of plasticity on mixed mode interface toughness. *Journal of the Mechanics and Physics of Solids*, 41(6):1119–1135, 1993.

M.J. Van den Bosch, P.J.G. Schreurs, and M.G.D. Geers. An improved description of the exponential xu and needleman cohesive zone law for mixed-mode decohesion. *Engineering Fracture Mechanics*, 73(9):1220–1234, 2006.

D. Vavrik and I. Jandejsek. Experimental evaluation of contour j integral and energy dissipated in the fracture process zone. *Engineering Fracture Mechanics*, 129:14–25, 2014.

A. Wang and F.W. Crossman. Edge effects on thermally induced stresses in composite laminates. *Journal of Composite Materials*, 11(3):300–312, 1977.

H. Wang, H. Ji, Y. Sun, and H. Miao. Discussion on convergence issues in abaqus/standard while carrying out damage and fracture analysis. In *Advanced Materials Research*, volume 189, pages 2247–2250. Trans Tech Publ, 2011.

J.T. Wang and I.S. Raju. Strain energy release rate formulae for skin-stiffener debond modeled with plate elements. *Engineering Fracture Mechanics*, 54(2):211–228, 1996.

S.S. Wang. Fracture mechanics for delamination problems in composite materials. *Journal of Composite Materials*, 17(3):210–223, 1983.

S.S. Wang and I. Choi. Boundary-layer effects in composite laminates: Part 2free-edge stress solutions and basic characteristics. *Journal of Applied Mechanics*, 49(3):549–560, 1982.

J.D. Whitcomb and K. Woo. Application of iterative global/local finite-element analysis. part 1: Linear analysis. *Communications in numerical methods in engineering*, 9(9): 745–756, 1993.

J.M. Whitney and C.T. Sun. A higher order theory for extensional motion of laminated composites. *Journal of Sound and Vibration*, 30(1):85–97, 1973.

J.G. Williams. On the calculation of energy release rates for cracked laminates. *International Journal of Fracture*, 36(2):101–119, 1988.

F.H. Wittmann, K. Rokugo, E. Brühwiler, H. Mihashi, and P. Simonin. Fracture energy and strain softening of concrete as determined by means of compact tension specimens. *Materials and Structures*, 21(1):21–32, 1988.

X.P. Xu and A. Needleman. Numerical simulations of fast crack growth in brittle solids. *Journal of the Mechanics and Physics of Solids*, 42(9):1397–1434, 1994.

Q. Yang and B. Cox. Cohesive models for damage evolution in laminated composites. *International Journal of Fracture*, 133(2):107–137, 2005.

Q.D. Yang, M.D. Thouless, and S.M. Ward. Elastic–plastic mode-ii fracture of adhesive joints. *International Journal of Solids and Structures*, 38(18):3251–3262, 2001.

X. Zhang, Y. Duan, X. Zhao, and D. Li. Effects of quasi-3d stacking architecture on interlaminar shear strength and void content of frp. *Journal of Applied Polymer Science*, 41076:1–9, 2014.

Z.J. Zhang and G.H. Paulino. Cohesive zone modeling of dynamic failure in homogeneous and functionally graded materials. *International journal of plasticity*, 21(6):1195–1254, 2005.

S. Zheng and C.T. Sun. A double-plate finite-element model for the impact-induced delamination problem. *Composites Science and Technology*, 53(1):111–118, 1995.

Z. Zou, S.R. Reid, P.D. Soden, and S. Li. Mode separation of energy release rate for delamination in composite laminates using sublaminates. *International Journal of Solids and Structures*, 38(15):2597–2613, 2001.

Acknowledgements

The thesis summarized the research work that I have carried out during the past four and half years of my PhD journey in the chair of Aerospace Structures and Computational Mechanics (ASCM) in the faculty of Aerospace Engineering of Delft University of Technology. I always felt that it would not be such a smooth and pleasant progress of my PhD study without the support and help from many people, the colleagues, collaborators, friends, families. I wanted to take this opportunity to express my sincere gratitude to them. What follows is not necessarily in order of importance.

First of all I want to thank Prof. dr. Zafer Gürdal and Prof. dr. Chiara Bisagni, the former giving me a chance of being a PhD in the group of ASCM and the latter being my promotor and supporting this thesis.

I would like to give sincerely special thanks to my daily supervisor Dr. Christos Kassapoglou for his continuous support, attention to details, patience and encouragement. I have benefited greatly from his guidance, suggestions and professionalism. The discussions were pleasant and often provided me with deep understanding of composites and rich ideas to tackle problems at hand. His incredible understanding of culture, encyclopedic knowledge and rigorous scientific attitude will have a positive impact on my professional and personal life, which is going to be a big fortune for me in my whole life.

Next, I would like to thank Dr. Mostafa Abdalla for the constructive suggestions and fruitful discussion on my research work. His lucid explanations of basic principles made the research work more effective.

Many thanks go to my former supervisor Prof. dr. Minghao Zhao at Zhengzhou University in China. He led me to a miracle world of mechanics and provided a lot of help and support during my master's studies. I am grateful for the financial support provided by the Chinese Scholarship Council.

My thanks also go to Christian Fagiano for his explanation of the stress recovery procedure and Mohamad R. (Farid) Talagani for his help on the convergence of J-integral in ABAQUS. I also want to thank Eddy van den Bos for his help and support in the process of learning CATIA and Martin Nagelsmit for his manufacture work of my specimen at NLR.

Gratitude goes to the technicians in the Delft Aerospace Structures and Materials Lab-

oratory (DASML), Berthil Grashof, Gertjan Mulder, Misja Huizinga, Frans Oostrum, Johan Boender, Lijing Xue and Marianne de Knegt... I am grateful for their assistance during my tests.

I would express my gratitude to all the committee members, Prof. dr. ir. R. Benedictus, Prof. dr. W. van Paepegem, Prof. dr. D. Saravanos, Dr. ir. E. Jansen, Dr. ir. J.J.C. Remmers and of course, Prof. dr. R. Curran for being part of my PhD committee and devoting time and effort to improve the quality of research work in this thesis.

It is a great pleasure to spend the time with my nice group members, who made this group be an international and friendly working place. Gratitude goes to Jan Hol and Laura Chant for their assistance in providing the computational resources and administrative support. Many thanks go to my officemates (former and present), Pooria, Sourena, Ke, Sathiskkumar, Rijk, Jayaprakash, Daniel, Zhi and Jaco for the interesting discussions. I also want to thank Sonell for her help on the issues of daily life and academic work. Special thanks to Miranda for her comments on the first four chapters of this thesis. Thank Professor Arbocz, Alan, Roeland, Sergio, Martin, Gillian, Julien, Attila, Ali, Dan, Luca, Zhenpei, Yujie, Darun, Fardin, Ines, Javier, Niels, Huy, Adriaan, Etana, Duo, Edgars, Lars, Fred, Javad, Darwin, Jurij, Louis, Erik, Kristofer, Mario, Mohammed, Noud, Paul, Terry, Sam, Jinghua, Yang, Lin, Lijian...for the good time that had spent with you all.

I also want to thank my friends, Jing, Lin, Yan, Jinglang, Huajie, Xiaojun, Huiyu, Qingbao, Xinchao, Yuan, Wenbo, Le, Hongkai, Yannian, Huajie, Liaojun, Wandong, Tian, Lei, Linfeng, Lei, Shuanghou, Xiaojia, Feijia, Ye...for the parties, interesting talk and the shared joy time with you. The sweet and sports time with Jinglang, Monica, Lu, Nil, Jacqueline, Bart, Manju, Yang, Mengshi, Shuyan and other friends in the swimming pool and sports center were a good memory of life in Delft.

Last but certainly not least, I would like to thank my family for their unconditional love and support. My utmost gratitude goes to my husband Chunxiao, he gave up his career in China and start an adventure in Delft with me. He always accompanied me, made me laugh when I felt blue, encourage me when I was depressed, accepted and tolerated my imperfect and helped me to be better than yesterday. I could not have made this thesis happen without him.

Curriculum Vitae

Weiling ZHENG

EDUCATION

2011-2016 Ph.D. Candidate

Chair of Aerospace Structures & Computational Mechanics

Faculty of Aerospace Engineering

Delft University of Technology, Delft, the Netherlands

Thesis: “Delamination Analysis of A Class of AP-PLY Composite Laminates”

Promotor: Prof. dr. C. Bisagni

Co-promotor: Dr. C. Kassapoglou

2008-2011 Master of Engineering

Solid Mechanics, Faculty of Engineering Mechanics

Zhengzhou University, Henan, China

Thesis: “A new Blister Method for the Mechanical Properties of thin film/substrate system”

Promotor: Prof. dr. M. Zhao

2006-2008 Bachelor of Administration

Business Administration, Faculty of Administration

Zhengzhou University, Henan, China

2004-2008 Bachelor of Engineering Mechanics

Solid Mechanics, Faculty of Engineering Mechanics

Zhengzhou University, Henan, China